Instituto Universitario para el Desarrollo Tecnológico
y la Innovación en Comunicaciones

Programa de doctorado
Doctorado en Cibernética y Telecomunicación

Contribution on the study of Underwater Wireless Optical links: Channel prediction and energy efficiency

Víctor Guerra Yánez

Dirigida por el Dr. **Rafael Pérez Jiménez**

Codirigida por el Dr. **José Alberto Rabadán Borges**

El Director **El Codirector** **El Doctorando**

Las Palmas de Gran Canaria
Abril de 2016

Si tuviese que agradecer literalmente a todos aquellos que han hecho posible que haya terminado por fin mi tesis doctoral, debería empezar diciendo algo como – *Agradezco a Sir Isaac Newton su esfuerzo y dedicación para que yo haya podido acabar mi doctorado* – Sin embargo, ya que si nos pusiésemos en ese plan tendría también que agradecer a Planck, Maxwell, Lord Rayleigh y todos los demás señores con barba que me dejo por el camino, he preferido acotar estos agradecimientos a un círculo, digamos, que implique una circunferencia menor.

Antes de empezar, quiero que conste que el orden de aparición no implica necesariamente una mayor o menor importancia, pero por si acaso me gustaría comenzar agradeciendo a *Lara*, mi mujer, su infinita calma y actitud cariñosa. Envidio su capacidad para hacerme sentir tranquilo, aún en momentos de estrés.

A *Giulia*, mi hija. Esa pequeña central nuclear de un metro de altura. Le agradezco simplemente su existencia, ya que es la motivación intrínseca de mi mundo.

Por supuesto a mis padres, *Mari Carmen* y *Víctor*, que siempre han apoyado mis decisiones. A mis hermanos *Carlos* y *Héctor*, por permitirme que de vez en cuando los hostigase con mis fotones, los cuales a veces eran coherentes, y otras no tanto. Y a mis abuelos, *Andrés* y *Luisa*, a los que tanto quiero.

A mis suegros, *Loli* y *Ángel*. Sin su ayuda no podría haber finalizado esta carrera de fondo.

No podría olvidar a *Omar*. El que soportó estoicamente el yugo de mi tutela en su Proyecto Fin de Carrera y mi inmisericorde látigo a la hora de obtener parte de los resultados de esta tesis. Estoy inmensamente agradecido por su tan valioso apoyo.

A mis directores *Rafa* y *Jose*. No podría imaginar unos mejores conductores para mi tesis. Por un lado la fuente inagotable de ideas que es *Jose*, así como su eterna predisposición a mancharse las manos con todo tipo de cacharros electrónicos. Y por otro lado, la experiencia, los amplios conocimientos y la motivación que ha sabido siempre generar *Rafa* en mi. Sin ellos, esta tesis no existiría. Y no me refiero a los aspectos legales de la afirmación.

No me perdonaría a mi mismo no nombrar a mi amigo *Crisanto* en estos agradecimientos. Gran parte de mi amor por la investigación se lo debo a él. Su pasión es contagiosa, y espero llegar tener al menos una fracción de su ímpetu. Además, es el único que me ganaba al Squash.

Por último, a mi otro compañero de galimatías matemáticos de tinta, *Cristo*. Con el que conseguí acaparar más del 90 % del gasto en rotuladores del instituto. Gracias por no coartar mi natural efervescencia creativa escuchando atentamente los a menudo sinsentidos que produce mi cerebro.

A todos, gracias.

Contents

Acronyms

ACV After Convergence Variability.
ADC Analog to Digital Conversion.
AOA Angle Of Arrival.
APD Avalanche PhotoDiode.
API Application Programming Interface.
AUV Autonomous Underwater Vehicle.
BER Bit Error Rate.
BJT Bipolar Junction Transistor.
BSF Beam Spream Function.
CDF Cumulative Density Function.
CDMA Code Division Multiple Access.
CI Convergence Iteration.
CLT Central Limit Theorem.
CPU Central Processing Unit.
CSK Color Shift Keying.
DC Direct Current.
DPIM Digital Pulse Interval Modulation.
DPSK Differential Phase Shift Keying.
DSP Digital Signal Processing.
ELF Extreme Low Frequency.
EM ElectroMagnetic.
FEC Forward Error Correction.
FEM Finite Elements Method.
FET Field Effect Transistor.
FPGA Field Programmable Gate Array.
FSK Frequency Shift Keying.
FSO Free Space Optics.
GEV Generalized Extreme Value.
GPU Graphics Processing Unit.
HF High Frequency.
HOV Human Operated Vehicle.
IMDD Intensity Modulated Direct Detection.
IMU Inertial Measurement Unit.
IOWCC Integrated OWC Circuit.
IR InfraRed.
LED Light Emitting Diode.
LMS Least Mean Squares.
LOS Line Of Sight.
LTI Linear Time Invariant.
LTV Linear Time Variant.
MAC Medium Access Control.
MCRT Monte Carlo Ray Tracing.
MIMO Multiple Input Multiple Output.
MMCRT Modified Monte Carlo Ray Tracing.
MOS Metal Oxide Semiconductor.
MPI Message Passing Interface.
NLOS Non Line Of Sight.
OBTS Optical Base Transceiver Station.
OFDM Orthogonal Frequency Division Multiplexing.
ONC Optical Network Controller.
OOC Optical Orthogonal Code.
OOK On Off Keying.
OWC Optical Wireless Communication.
PAPR Peak to Average Power Ratio.
PCA Power Control Algorithm.
PDF Probability Density Function.
PIN Positive Intrinsic Negative.
PMMA PolyMethyl MethAcrylate.
PMT PhotoMultiplier Tube.
PPM Pulse Position Modulation.
PSK Phase Shift Keying.
PWM Pulse Width Modulation.
RF RadioFrequency.
RGB Red Green Blue.
ROV Remotely Operated Vehicle.
RTE Radiative Transfer Equation.
RTV Random Variable Transformation.
SCPI Standard Commands for Programmable Instruments.
SDMA Spatial Division Multiple Access.
SER Symbol Error Rate.
SIMD Single Instruction Multiple Data.
SINR Signal Interference Noise Ratio.
SNR Signal Noise Ratio.
SSIM Structural Similarity Index Method.
TDMA Time Division Multiple Access.
TDS Total Dissolved Solids.
TTP Threshold Transmit Power.
UAC Underwater Acoustic Communication.
UMTS Universal Mobile Telecommunications System.
US Uncorrelated Scattering.
UV UltraViolet.
UWOC Underwater Wireless Optical Communication.
UWSN Underwater Wireless Sensor Network.
VLC Visible Light Communication.
VRTT Vector Radiative Transfer Theory.
VSF Volume Scattering Function.
WSS Wide Sense Stationary.
YB-WLED Yellow Blue White Light Emitting Diode.

Chapter 1

Introduction

Oceans cover 71 % of Earth's surface and more than 90 % of the biosphere. Besides its capital importance regarding global biodiversity and climatic smoothing, oceans are an important media that affects global economy. Marine transportation of cargo is performed by ship up to 85% , and almost 35 % of hydrocarbon extraction is performed at the seabed . Furthermore, a high amount of food supplies are gathered from oceans through fishing. Nonetheless, the fishing industry currently subdues the marine ecosystem to an over-exploitation situation. This fact, combined to pollution, acidification and the subsequent climate change, has led to a notable redistribution of the chlorophyll, as Boyce et al. concluded in [1]. Figure 1.1 depicts the evolution of chlorophyll's distribution since 1900, based on indirect estimation (transparency of seawater) until 1950 and on direct measurements since that decade (*in situ* measurements). The chlorophyll concentration is directly related to the phytoplankton amount, which is the basis of the marine ecosystem. The lower the phytoplankton, the lower the upper-layer forms of life (direct effect on the fishing industry and hence on the economy) and also the lower oxygen production and carbon sequestration (direct effect on clime). This current trend is the seed of a positive-feedback situation if the proper regulations and control strategies are not made. In this regard, there is an increasing interest in ocean monitoring applications, such as oxygen and phytoplankton measurements, which are usually related to the deployment of instrumentation *in situ*. These deployments are based on battery-powered isolated nodes and therefore, energy-efficient communication technologies are needed.

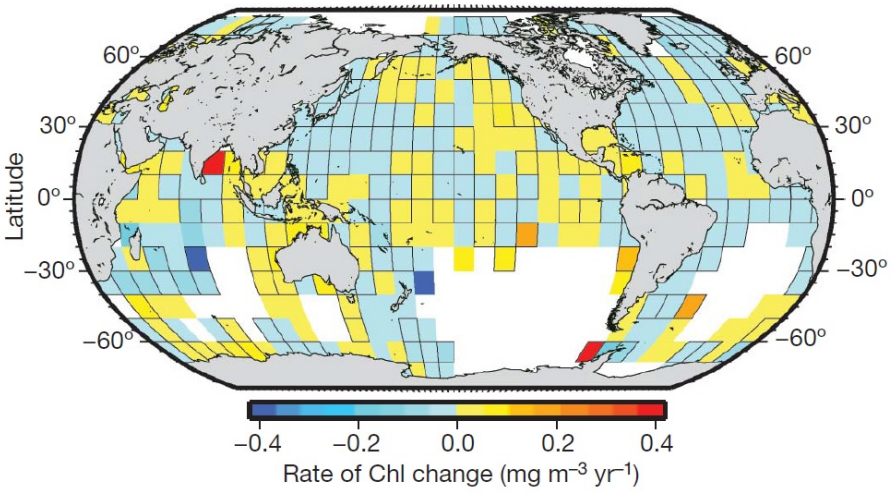

Figure 1.1: Mean change rate of the chlorophyll concentration since the early years of 1900. Extracted from Boyce et al.

Controlling the fishing industry is a "must" if an actual reversal of the current situation is intended. Fish farms are the current trend in production control and enhancement. Although the farming of carnivorous species such as Salmon does not reduce the actual pressure on wild fishing as they are normally fed with fish oil, there is a tangible relaxation on the non-carnivorous-species fishing. Nevertheless, fish farming may produce harmful effects on wild stocks of species such as the aforementioned Salmon, reducing the population dramatically. Offshore fish farms have a need on controlling and monitoring the production. The cages used in this kind of farms are usually located a few miles from the coast, needing buoys acting as communication hubs to perform telemetry.

Regarding hydrocarbon extraction, mining operations must be performed at very high depths, complicating communications with the surface's base station. These operations must be performed by robots, as the depth does not allow the presence of people unless HOV were used. When using telerobotic-based systems, tethering

is an added issue, as the tension and torsion forces may be extremely high. In this case, low-latency wireless communication technologies should be used to implement telemetry and telecommand.

There is an emergent activity also related to the mining industry, deuterium mining. Deuterium is an essential fuel for both Li-Hy batteries and the future's Fusion Reactor facilities. Deuterium is naturally created at very high pressures in the sea, which means very high depths. The used mining facilities will need a communication infrastructure linking the main extraction facilities to the deployed sensors and the sea-surface nodes.

All the aforementioned marine-related activities have strict connectivity requirements. Tethered solutions are not possible in every situation, as they limit the mobility and the cables may suffer from very high traction and torsion forces. In situations where mobility is required or at depths were cables are not feasible, wireless solutions offer an alternative. There are three main technologies regarding underwater wireless communications: radiofrequency, acoustic and optical communications. The following sections will discuss the advantages and disadvantages of each technology.

1.1 Underwater Radiofrequency Communications

Maxwell's equations define the propagation of EM signals in any type of medium. Equation set 1.1 shows the famous expressions. D is the displacement field, which is related to the electric field E as $D = \epsilon E$. H is the magnetizing field, which is related to the magnetic field B as $B = \mu H$. ϵ, σ, and μ are the electric permittivity, the conductivity, and the magnetic permeability of the material. Finally, ρ and J are the free charges and currents present in the scenario.

$$\begin{aligned} \nabla \cdot D &= \rho \\ \nabla \cdot B &= 0 \\ \nabla \times E &= -j\omega\mu H \\ \nabla \times H &= J + j\omega(\epsilon - \frac{\sigma}{j\omega})E \end{aligned} \tag{1.1}$$

Solving the equations for a plane wave scenario, it yields an expression of the form shown by Equation 1.2.

$$\vec{E}(r) = \vec{E_0} e^{-\gamma r} \tag{1.2}$$

Generally, the extinction of a plane wave is related to the loss tangent ($\tan\delta$), which is the ratio of the imaginary part and the real part of the complex electric permittivity (Equation 1.3). Furthermore, in a general material, the attenuation factor α, which is the real part of the propagation constant γ, can be expressed in terms of the loss tangent, as shows Equation 1.4.

$$\tan\delta = \frac{\sigma}{\omega\epsilon} \tag{1.3}$$

$$\alpha^2 = \frac{\omega^2\mu\epsilon}{2}\left(\sqrt{1+\tan^2\delta} - 1\right) \tag{1.4}$$

Figure 1.2 depicts the loss tangent for different types of seawater vs. frequency. It must be taken into account that both σ and ϵ depend on the frequency. It can be observed that the loss tangent is extremely high at HF and above, compared to ELF or visible light.

ELF (3 Hz - 30 Hz) and SLF (30 Hz - 300 Hz) radiofrequency systems were used after the end of World War II as an alternative to communicate with submarines. As the equivalent wavelength at such low frequencies is as high as thousands of kilometers, dipole antennae are not feasible. In order to propagate an effective power, ground dipoles must be used, which are huge facilities that comprise two electrodes deeply grounded and separated tens of kilometers in a low-ground-conductivity zone. USA (Project Seafarer), Russia (ZEVS) and India (INS Kattabomman base) are the only countries with known ELF stations. This kind of system has the advantage of allowing a virtual one-way connection at almost any place on the sea, but has several disadvantages. The power consumption to radiate a few watts of power is about 800 MW, whilst the throughput is limited to a few bits per minute and the communications is simplex.

The growing interest in underwater applications commented at the beginning of the chapter, has pushed the research on submarine radiofrequency communications during the last few years. Several authors have started to propose HF as an alternative to acoustic communications for different types of application. Al-Shamma'a et al. [2] performed several measures in seawater at different frequencies in the range of a few MHz, encouraged by the recovery of the results of Bogie in [3], where links up to 460 m at 7 MHz were reported. Two sets of experiments were carried out by the authors using loop antennae. In the first set, a laboratory-based experimental setup was implemented, and measured the near-field losses ranging from a few centimeters to 1 meter (Figure 1.3). The

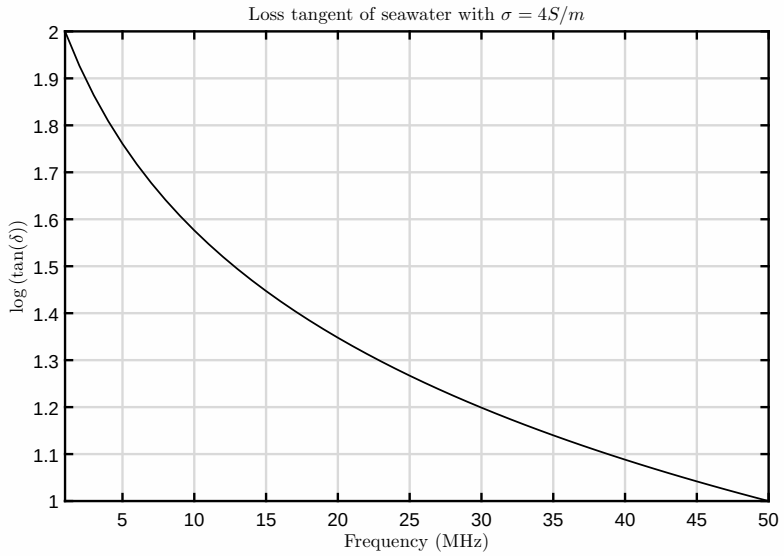

Figure 1.2: Loss tangent for seawater ($\sigma = 4\,\mathrm{S/m}$) from 1 MHz to 50 MHz

second experiment was carried out at Liverpool's dock, ranging from a few meters to 80 meters. Figure 1.4 depicts the results and the best exponential fit of the voltage amplitude.

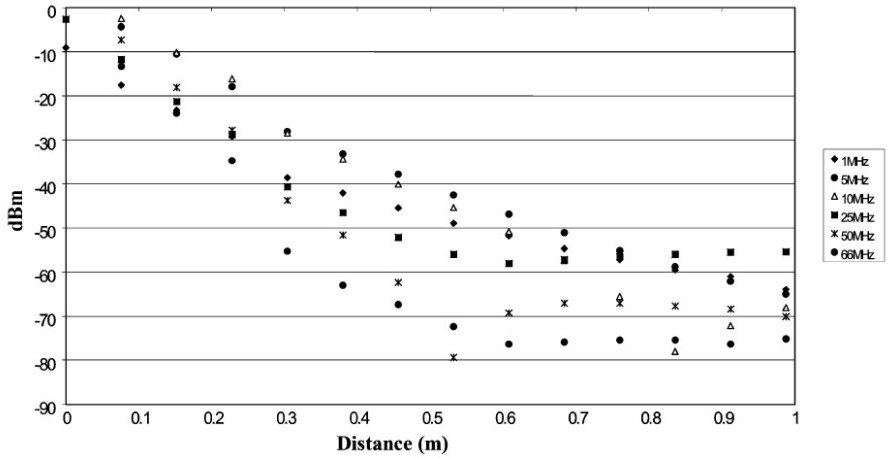

Figure 1.3: Results of the laboratory experiments performed by Al-Shamma'a et al.

The authors justified the observed results differencing the behavior of seawater molecules to near-field and far-field situations. For near-field excitation, due to the intensity of the electric field, ionization processes occurs and hence, conduction phenomena appear producing high attenuations. For far-field excitation, water molecules behave in a different manner and conduction is less important. These statements have not been verified yet. Regarding the repeatability of the experiments, Yoshida et al. observed similar discrepancies between the theoretical attenuation curves and the actual measurements [4] at 10 MHz. The analysis of the results suggests a mistake in the estimation of the losses, considering the attenuation due to seawater as a distance-independent phenomenon.

In order to adjust the theoretical value of the attenuation to the measurements of Al-Shamma'a et al., Uribe and Grote [5] adapted the attenuation factor α to introduce a dependence with distance. Equation 1.5 shows the introduced adjustment whilst Figure 1.5 depicts the fitted curve respect to Al-Shamma'a's measurements.

$$\alpha' = \alpha \frac{r_0}{r_0 + r} \tag{1.5}$$

As it can be observed, the attenuation factor decays exponentially with the link's distance r. r_0 is a parameter that models the near-to-far field effect. This approximation seems valid for the available data, but does not explain the phenomenon which occurs underneath. Furthermore, the exponential distance-dependent attenuation directly implies that there is virtually no attenuation for a sufficiently long distance. Al-Shamma et al. justified the decreasing extinction of the HF waves as an inherent reduction of the conduction current when the molecules of

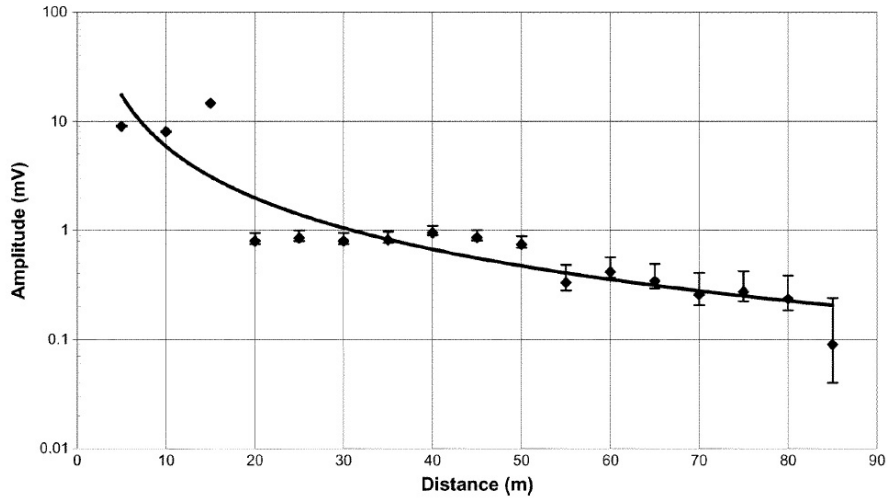

Figure 1.4: Results of the experiment carried out at Liverpool's Dock by Al-Shamma'a et al.

sea water are subject to low electric fields. Regardless this qualitative and evidence-free assertion, this issue needs more research.

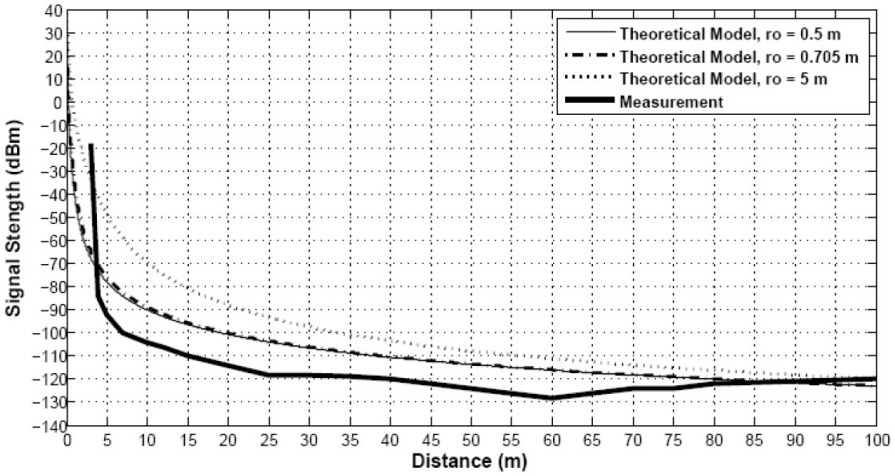

Figure 1.5: Fitted curve after introducing the modified α. Extracted from [5].

Finally, the authors summarized the applications of Underwater RF regarding data rate and distance, based on COTS devices. Table 1.1 reproduces their information.

Range	Data rate	Applications
$\leq$ 1 m	10 Mbps	Wireless Connector
10 m	1 Kbps	UWSN data download
50 m	1-5 bps	Divers Comms
200 m	0.1 bps	AUV Control, Telemetry, Navigation
2 Km	$\approx$ 1 b$\cdot$ min^{-1}	Seabed telemetry
10 Km	1-5 b $\cdot$ h^{-1}	Seabed telemetry

Table 1.1: Applications of Underwater RF

1.2 Underwater Acoustic Communications

Acoustic technology is the most extended communication technology for underwater applications. The propagation of acoustic waves through seawater suffers a extremely low attenuation compared to EM waves (RF or Visible Spectrum). However, the good propagation properties of mechanical waves in seawater, combined to the low propagation speed of 1500 $m \cdot s^{-1}$, produces a harmful effect in terms of bandwidth. Underwater acoustic channels

have strong multipath effects, presenting delay spreads ranging from tens to several hundreds of milliseconds [6]. Furthermore, the relative motion between emitter and receiver generates extreme Doppler distortion.

Regarding attenuation, the power of acoustic waves decays with distance by the absorption of the medium, phenomenon which depends on the frequency. In addition, as occurs in any radiative process, this kind of signal also suffers from spreading loss. Equation 1.6 expresses mathematically these two effects. d is the link's distance, referred to some reference distance d_r, $a(f)$ is the frequency-dependent absorption coefficient of the medium at frequency f. Finally, k is the spreading-loss coefficient, which ranges from 1 for cylindrical propagation to 2 for spherical propagation.

$$A(d, f) = \left(\frac{d}{d_r}\right)^k \cdot a(f)^{d-d_r} \tag{1.6}$$

Acoustic underwater ambient noise, $N(f)$, has a spectral distribution as the one depicted in Figure 1.6. This frequency dependency of the ambient noise, joint to the attenuation of the channel (Equation 1.6), has important implications on the design of underwater acoustic links, as the available bandwidth for a given SNR would depend on the term $(A(d, f)N(f))^{-1}$, as shows Equation 1.7.

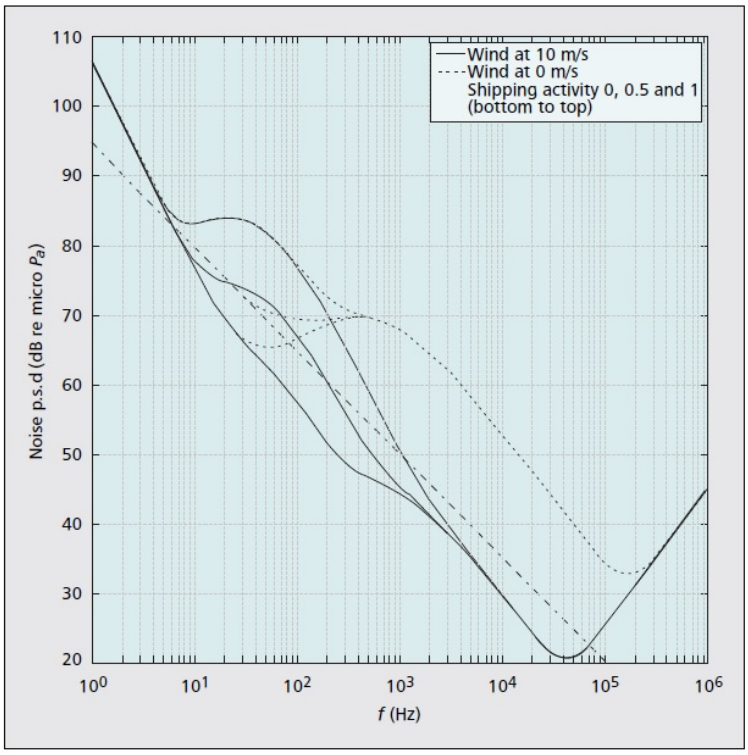

Figure 1.6: Underwater acoustic underwater noise. Extracted from [6].

$$SNR(d, f) = \frac{S(f)}{A(d, f)N(f)} \tag{1.7}$$

$S(f)$ is the spectral power density of the transmitted signal. Figure 1.7 shows the bandwidth of an acoustic link for different distances. It is absolutely intuitive that longer distances imply lower bandwidths (a few KHz).

Multipath in UAC is governed by two main effects, surface and bottom reflections and sound refraction. The last one is due to temperature, pressure and salinity gradients, which modify the refractive index of sound, bending the propagation direction according to Snell's law. Equation 1.8 shows the approximate frequency and time responses of UAC channels. Γ_i is the cumulative reflection coefficient along the i-th path, whose traveled distance is denoted by d_i. τ_i is the delay suffered by the i-th sound ray after traveling d_i.

$$\begin{aligned} H(f) &= \sum_i \frac{\Gamma_i}{A(d_i, f)^{1/2}} \\ h(t) &= \sum_i h_i(t - \tau_i) \end{aligned} \tag{1.8}$$

Regarding time variability, statistical characterization of UAC channels is an open topic yet. This variability is due to changes, at impulse-response time scale, on the geometrical (relative motion between Tx/Rx) and physical

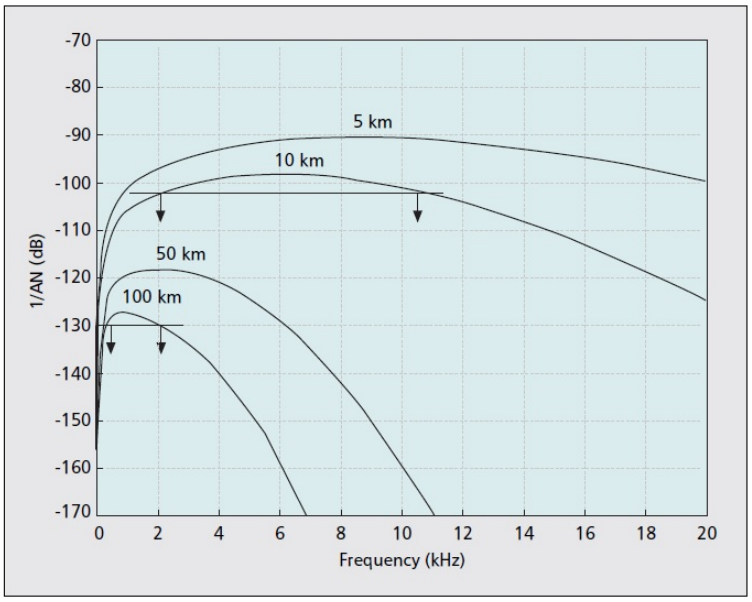

Figure 1.7: $(A(d,f)N(f))^{-1}$ product for different distances. Extracted from [6].

parameters of the link, such as the sea surface's agitation. Generally, coherence times up to hundreds of milliseconds may be considered.

Additionally to the physical constraints inherent to acoustic propagation, acoustic modems add several limitation to the design of acoustic networks. The power required by the transmitter to carry out the communication depends on the distance, but is normally in the range of tens of watts, whilst the power requirements on the receiver side are much more relaxed (about a few milliwatts). Power consumption is a critical issue in battery-powered isolated nodes, and energy efficiency is of capital importance. There are different ways to reduce the power consumption of the node, but the main ones are power control algorithms, retransmission-reduction techniques in random access networks, and bandwidth-adaptive systems.

Finally, marine mammals, such as dolphins and whales, have an audible spectrum that can cover up to almost 200 KHz. These animals use sound with both social and echolocation purposes, and the use of UAC under 200 KHz may be extremely harmful due to the high acoustic powers generally used. Furthermore, even though *a priori* non-harmful frequencies were used, due to Doppler effect, the actual spectral density that moving mammals may experience in an ensonified ocean could be harmful as well, as Siderius and Porter commented in [7].

1.3 Underwater Wireless Optical Communications

Underwater Wireless Optical Communications is a subgroup of Optical Wireless Communications. Unlike in FSO, the propagation medium presents absorption in UWOC. This absorption depends on the inherent properties of the seawater and the relative concentrations of algal and non-algal matter. Furthermore, whilst aerosols and gases produce scattering in FSO, UWOC suffers this spatial dispersion mainly from phytoplankton. Regarding turbulences, the refractive index gradients induced by temperatures changes in FSO are not enough to model this phenomenon in UWOC, since the refractive index of seawater depends on temperature, salinity and pressure. In addition, the wavelength dependency of the extinction coefficient (absorption plus scattering) generally defines a best wavelength that ranges within the blue-green window.

As it was commented above, underwater RF communications are power and bandwidth limited. The power consumption of ELF stations is absurdly high and the effective data rate is very low, but offers very good communication range. Regarding UAC, the available bandwidth can support a wide range of services, but is normally limited to a few thousands of bits per seconds. In the past few years, UWOC has demonstrated the best energy efficiency in terms of *bits per Joule* and a maximum range above 100 meters. Furthermore, the cost associated to the optical transceivers is much lower than the associated to UAC's hydrophones and drivers. However, due to the range limitation of UWOC, the current trend is to use hybrid opto-acoustical solutions, where long range telemetry is acoustically performed whilst low range, low latency and high bandwidth communication is carried out optically.

The recent proposals of UWOC as data interface for Underwater Wireless Sensor Networks is highly supported by the availability to download huge amount of long-term collected data in a fraction of time respect to acoustic transceiver. Furthermore, the use of optical interfaces lengthens the life of the deployed nodes. However, although the maximum allowed misalignment error has been demonstrated to be lower than expected due to the beam spreading of light, it stills lower than the case of UAC. Moreover, the low latency of the UWOC links allows a

natural remote operation of underwater vehicles. The latency of an UWOC link can be even better than the latency of a fiber-tethered link, since the refractive index is lower in seawater than in plastic or glass, but this enhancement is usually weighed by the necessity of retransmission in the untethered scenario.

There are several current challenges in UWOC regarding energy efficiency and channel modeling. Several contributions where the impulse response is modeled as in a LTI scenario can be found in the literature, but the UWOC channel is clearly LTV and only a few authors address this issue in laser-based links. Moreover, there is a lack of contributions regarding energy efficiency in UWOC, which is of capital importance in scenarios where battery replacement is normally prohibited by the huge cost of the operation.

In this dissertation, a statistical approach of the channel's main parameters (bandwidth, gain and coherence time) is performed. The analysis is based using theoretical approximations and simulation results. Two different scenarios are analyzed due to their applicability in UWSN: underwater-to-underwater and underwater-to-air links. Furthermore, a statistical model for big opaque particles is proposed. The proposal is focused on shallow water scenarios where the coastal currents generate a cloud of particles in sandy seabeds. Regarding energy efficiency, the use of different modulations and encodings, as well as power control algorithms is explored.

Chapter 2

Motivation, Hypotheses and Contributions

This chapter comprises the statements to be proven through experimentation in this thesis, the main objectives that have motivated its actual development, and the contributions that have been made during the development of this work.

2.1 Motivation

The topic of this thesis emerged as the natural evolution of the research lines of the *Photonic Technology and Communications Division* of the *Institute for Technological Development and Innovation in Communications*, of the University of Las Palmas de Gran Canaria.

The group has been focused during the last few years in IR and VLC, concretely in simulation engines [8] and the development of proof-of-concept prototypes for different applications using the aforementioned technology, such as video streaming using VLC [9] or in-flight optical communications (VLC downlink with IR uplink) [10][11].

In this work, since it is the first in a novel area for the group, several fronts have been treated. In first place, a thorough analysis of the current state-of-the-art research was mandatory in order to detect the main weaknesses and hence, opportunities to work in. As it will be commented in Chapter 3, energy-efficient strategies have not been studied in depth, and different approaches are proposed during the following chapters. Furthermore, stochastic models to carry out performance predictions according to link's parameters are not available yet, and a slight contribution in this regard is made.

Summarizing, the main objectives of this thesis are:

- Carry out a thorough analysis of the current state-of-the-art research.
- Propose strategies to enhance the energy efficiency of UWOC systems.
- Study the feasibility of performing stochastic modeling in UWOC links.

2.2 Hypotheses

This thesis departs from two fundamental hypotheses, which are enumerated below. The first one regards channel modeling, whilst the second addresses energy efficiency in UWOC.

Hypothesis 1 ***On the channel.*** *The Underwater Wireless Optical Communications channel is linear and time variant but Wide Sense Stationary with Uncorrelated Scattering (WSSUS).*

- The variability of the UWOC channel, enclosed within the time-variant impulse response $h(t, \tau)$, is due to the different scattering and reflective phenomena that occur during propagation. This variability, if emitter and receiver are at fixed positions, possesses a invariant mean value. Furthermore, the power contributions incoming from scattering events are mutually uncorrelated due to the independence of the locations where these scatterings are produced.
- In a scenario with suspended matter, the movement of the particles amid the link generates a variability on the received power that reduces the SNR. In order to verify this hypothesis, both simulation and experimental approaches have been used.

- Underwater-to-air links are also variable due to the changing shape of the seawater surface. Furthermore, the optical power that arrives the receiver can be estimated by the energy of the illuminated seawater surface area which impacts on the receiver. This illuminated area changes with time, following the shape of the sea waves spectrum.

Hypothesis 2 ***On the energy efficiency.*** *The energy efficiency of an Underwater Wireless Optical link can be improved by means of power control algorithms, the use of the best transmission wavelength, and energy-efficient encodings and modulations.*

- Generally, UWOC links are performed in the blue-green region of the visible spectrum, since the minimum absorption is usually located between these wavelengths. However, taking into account the better response of long-wavelength emitters and receivers, the worse propagation of redder wavelengths is compensated by these better efficiencies, defining a critical distance at which it is better to perform a red transmission than a blue one.
- Power control algorithms are a well-known strategy to optimize SNR in highly interfered environments. Furthermore, underwater remote sensor nodes , which are battery-powered, have prohibitively expensive replacement costs. Hence, strategies to reduce the power consumption are mandatory in this kind of device, and power control algorithms can be energy-optimized.
- Modulations and encodings are the lowest level of the communications stack. Taking into account the electrical characteristics of the optical emitters, nonlinear current drivers are a better option than linear ones. Therefore, modulations which need linear transmission can be quantized to allow the use of energy-efficient nonlinear drivers.

All these hypotheses will be discussed along this document. Section 2.3 presents a summary of the contributions presented in this thesis.

2.3 Contributions

To serve as a guide to those who read this work, a summary of the contributions made by this work is presented.

- **Chapter 3.** A thorough analysis of the current state-of-the-art research is presented. This in-depth analysis has been structured attending to an intuitive taxonomy and tries to serve as the starting point of this work.
- **Chapter 4.** A Monte Carlo Ray Tracing algorithm for UWOC is presented. Unlike other authors who employed Henyey-Greenstein scattering phase functions to model scattering due to particles, in this work, Mie scattering has been used since it models the phenomenon more accurately. The influence of each channel parameter on the impulse response is also analyzed. Furthermore, the algorithm was parallelized using both multiprocessor and GPU implementations
- **Chapter 5.** A model of underwater-to-air communications is presented, focusing on the channel availability.
- **Chapter 6**
  - Using the aforementioned Monte Carlo Ray Tracing algorithm, a statistical approach of both channel gain and bandwidth is made.
  - An empirical formula to predict the BSF is obtained.
  - After a rectangular approximation of the impulse response, a definition of Fresnel zone is performed in terms of received energy, allowing the reduction of the volume of interest in channel simulation. This simplification also allows the prediction of the channel bandwidth.
  - A statistical study to model the influence of opaque particles such as sand grains is presented in this work. The approach is based on geometrical relationships and some approximations, but may serve as baseline for further work.
- **Chapter 7**
  - In this chapter, the influence of moving particles on the SNR is demonstrated. The movement of particles produces a random variation on the received signal that can be modeled as a normal distribution of variance related to the density of particles.
  - The coherence time of a near-surface link and its relationship with the wind stress are obtained. Besides the wind speed, other parameters are taken into account, such as depth and wavelength.

  - The validity of the WSSUS approximation of a near-surface link is demonstrated through experimentation.

- **Chapter 8**
  - The use of red wavelength instead of blue under certain channel restrictions is justified in terms of energy efficiency. As red emitters are more energy-efficient than blue ones, and Si-based receivers are more sensitive to longer wavelengths, below a critical distance is better to perform the transmission in red, despite the higher attenuation of the medium at this frequency.
  - A power control algorithm with wavelength switching (red-blue) is presented and evaluated. The use of PCA is mandatory to reduce the power consumption of isolated underwater nodes. In this case, several enhancements are proposed to the classic Newton-Raphson gradient-descent algorithm (equivalent to a LMS algorithm).
  - The use of PWM combined to nonlinear drivers is explored as an efficiency-enhancement strategy for Optical OFDM. It will be discussed that due to the higher efficiency of nonlinear drivers, PWM modulation of OFDM samples could be an alternative to reduce the power consumption and hence, longer the lifespan of nodes which transmit OFDM signals.

2.4 Organization of the document

After commenting the motivation, the hypotheses and contributions that are the baseline of this work, the next chapters are organized as follows.

In Chapter 3, a profound analysis of the evolution of the research in UWOC is presented. The analysis comments most of the available contributions in UWOC regarding different aspects: channel modeling, modulations and encodings, energy efficiency, network layer, applications and surveys.

In Chapter 4, the UWOC channel is studied in detail. The different phenomena that affect underwater optical propagation are discussed in this chapter. Furthermore, a Monte Carlo Ray Tracing algorithm using Mie's scattering model is presented. Furthermore, a parallelization scheme is also presented to reduce the computation time.

Chapter 5 is dedicated to underwater-to-air links, especially in the discussion of the channel availability related to the seawater-air interface motion. The studied scenario has important implications in shallow-water sensor reading and UUV-to-air communications.

In Chapter 6, a statistical approach of the channel gain and bandwidth is developed. Massive data obtained from the implemented simulator of Chapter 3 is introduced in a decision algorithm to infer the best-fit option within a battery of possible probability distribution functions. Furthermore, a qualitative relationship between the distribution parameters and the channel's geometrical and physical parameters is commented.

In Chapter 7, the results of a near-surface underwater transmission are presented. Using these results, the WSSUS consideration of the varying channel is demonstrated and the coherence time of the channel is also calculated.

Chapter 8 comments different energy-efficient strategies. The use of red wavelengths instead of blue ones is justified for short-range links, and a power control algorithm with wavelength-switching capabilities is also presented and analyzed.

Finally, in Chapter 9, several conclusions are extracted and future research lines are exposed and commented.

Chapter 3

Underwater Wireless Optical Communications: a thorough analysis

In the past few years, there has been a growing interest in submarine applications, such as surveillance, telecommand of robots, ocean monitoring and military communications. The development and enhancement of visible range emitters and receivers has led to an increment on research works related to the use of LED and laser devices to establish communication links in the underwater medium. Nowadays, Underwater Wireless Optical Communications (UWOC), may be considered an independent topic apart from Free Space Optics (FSO) and Visible Light Communications (VLC). This independence has been encouraged by the particularities of the underlying communication channel, and the novelty of the field has attracted the attention of research groups worldwide. This growing interest can be observed at Figure 3.1 where the number of contributions in the field over time is analyzed.

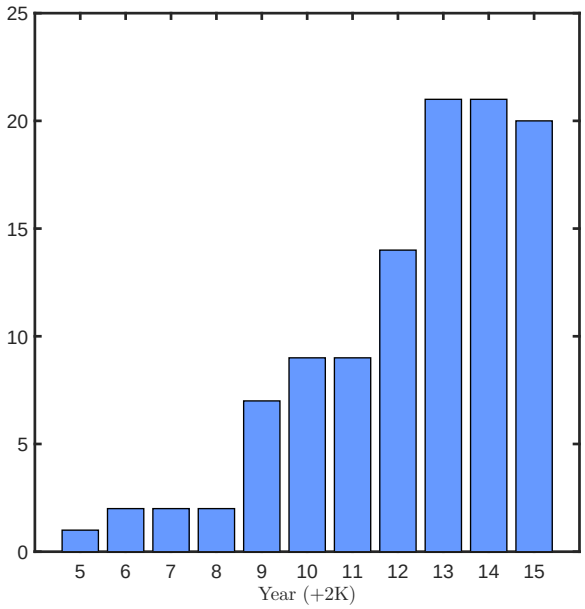

Figure 3.1: Evolution of the number of papers available in the IEEE database related to UWOC

To have a better understanding of the actual research interests within UWOC, the contributions have been classified in six different categories:

- Channel modeling
- Modulations and Encodings
- Energy efficiency
- Network layer
- Applications
- Surveys

Figure 3.2 depicts the distribution of the research attending the the aforementioned classification. Note that the distribution is qualitative as each paper may belong to several categories.

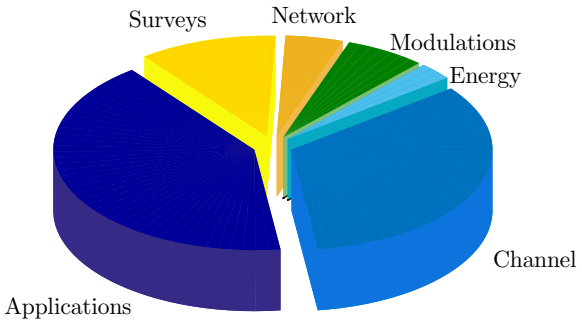

Figure 3.2: Distribution of publications per category in UWOC

As it can be observed, Applications and Channel modeling are the main interests. Due to the novelty of the topic and the complexity of the channel, there were a need of contributions supporting the feasibility of links and a mathematical apparatus to predict the behavior of the channel. Nonetheless, the lack of publications regarding energy efficiency seems contradictory taking into account the necessity of energy-saving techniques in scenarios where the actors are normally battery-powered nodes. Finally, there are several surveys in this topic, but are normally incremental and their scope is reduced in time. In this work, a deeper analysis is made increasing the time range as the topic is affordable in size yet.

3.1 Channel modeling

As it was commented above, channel modeling has been one of the main interests in UWOC since its origin. In order to provide a more accurate view of this issue, this category has been subdivided in three subtypes: physical effects, stochastic modeling and channel response.

This issue has suffered an evolution that is depicted in Figure 3.3. It can be observed that the last two years (2013-2015) comprise more than three quarters of the contributions in this aspect. It is common to perform experimental evaluations before establishing the mathematical background of a novel subject, as the scientific method underscores. In this aspect, UWOC has suffered the same treatment, centering the efforts in proving the feasibility of the technology. This will be further discussed in Section 3.5.

The following subsections comment the contributions in the three abovementioned subcategories.

3.1.1 Physical effects

Within this category are the publications that try to model or empirically evaluate the effects of different underwater phenomena. The main effects that have a significant weight in UWOC are:

- Turbulence
- Scattering and Absorption
- Fauna and optical fouling
- Misalignment

The following subsections analyze the most relevant contributions up to the date at each enumerated topic. Fauna has an unpredictable behavior from the communications' point of view. The pass amid the link of fishes and mammals has the potential to produce long-duration deep fading events, but normally, it is not considered and there are no works in this regard.

Turbulence

Turbulence is of capital importance in laser-based systems, as the energy is concentrated in a small solid angle. Islam et al. performed an experimental evaluation in a laboratory-controlled scenario [12], finding out that turbulent regimes affect the received SNR depending on its salt concentration. Furthermore, other conclusion of

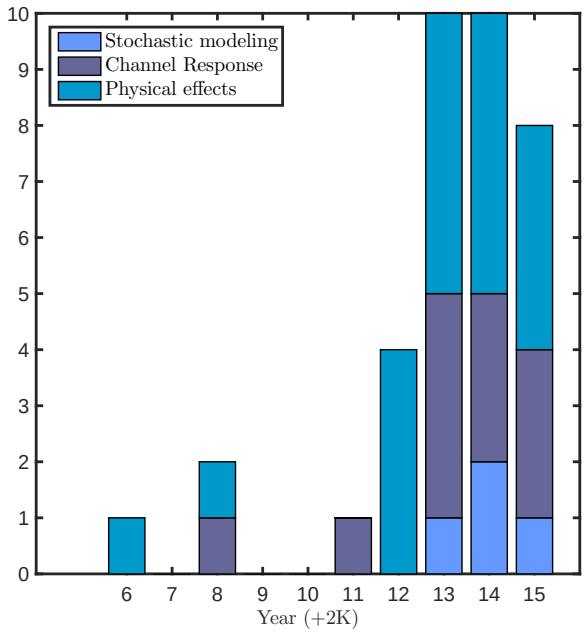

Figure 3.3: Evolution of the contributions regarding Channel Modeling

the experiment was that the lower the bandwidth, the lower the influence of the turbulence, as it was expected theoretically.

Hou and Matt [13] studied the propagation of images in a turbulent scenario. Although the scope of the article is not related to communications, the obtained results can be extrapolated to the UWOC domain. After using OpenFOAM to model turbulence conditions in a water tank, a degradation statistic was obtained. The structure similarity index metric (SSIM) is used to measure the statistical differences between two images, commonly an undistorted one and a distorted version [14]. In this case, the results showed that extreme turbulence regimes degraded the images up to 50 %. As each group of pixels can be considered as a traditional photodiode, this results may be easily extrapolated to a UWOC scenario. This SSIM degradation can be directly associated to a SNR decrement. Figure 3.4 reproduces the results obtained by Hou and Matt regarding the SSIM.

The SSIM index is calculated between two windows x and y as shows Equation 3.1.

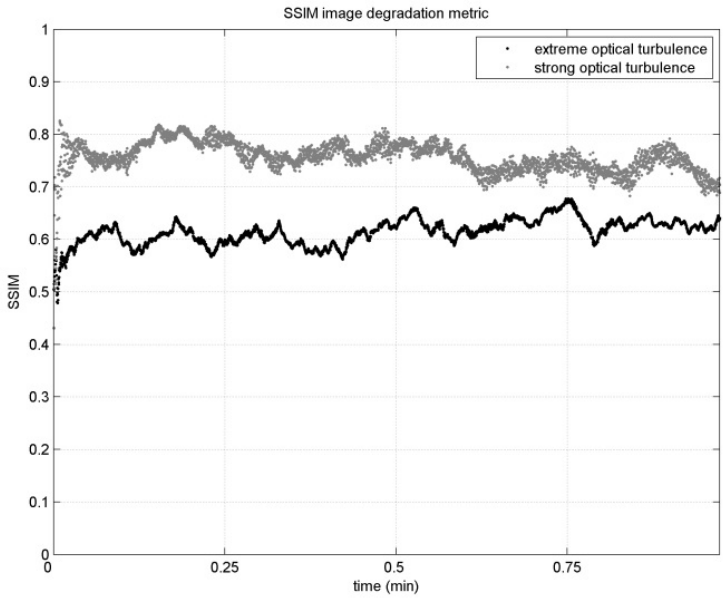

Figure 3.4: Time series of image degradation during Hou and Matt's lab experiment, under strong and extreme turbulence case

$$SSIM(x,y) = \frac{(2\mu_x\mu_y + c_1)(2\sigma_{xy} + c_2)}{(\mu_x^2 + \mu_y^2 + c_1)(\sigma_x^2 + \sigma_y^2 + c_2)} \tag{3.1}$$

μ_x and μ_y are the mean values of each image, σ_x^2 and σ_y^2 are variances, c_1 and c_2 are small constants used to avoid divisions by zero during the computation, but are negligible when analyzing the expression.

It is easy to demonstrate that the SSIM, in a Johnson noise-dominant situation, is related to the decrement of the SNR (ΔSNR) in the manner that shows Equation 3.2.

$$\Delta SNR \equiv \frac{C\mu_y^2}{SSIM} - 1 \tag{3.2}$$

Where C is a constant that relates the covariance, the mean values and the variances. It depends on the scenario but helps to simplify the analysis. Note that $N\mu_y^2$ can be associated to the electrical power after the optoelectrical conversion on a photodiode, as the whole area can be divided in a consistent partition comprised by the N pixels of the window.

Scattering, Absorption and Misalignment

Both scattering and absorption are the main power loss sources in UWOC. Scattering is the spatial dispersion of radiation after interacting with matter, whilst absorption is the decrement of the transported energy due to the conversion of photons in other kinds of energy. This effects has been thoroughly studied in UWOC, as it can be seen in the literature.

In 2006, Cochenour et al. studied the effects of multiple scattering in turbid water transmitting a RF signal using a laser in a coherent scheme [15]. In their experiments, the RF subcarrier recovery was unaffected by turbidity and the multipath effect due to the scattering was static during the transmission time. The authors suggested that several effects such as turbidity, misalignment and time variance should be investigated simultaneously to obtain a more accurate result.

Two years later, the same authors presented a work where the BSF (Beam Spread Function) of a scattered underwater link was modeled [16]. The principal contribution of this work was the simplification of the traditional Radiative Transfer Equation (RTE) to a less-complex approach using the Small Angle Approximation (SAA). This approach is only valid for laser-based links, as the energy is concentrated in a narrow solid angle. Both analytical predictions and measurements were performed. Figure 3.5 shows one of the results of their contribution. It can be observed that the received power is less sensitive to pointing errors as the link's distance increases, due to the effect of scattering.

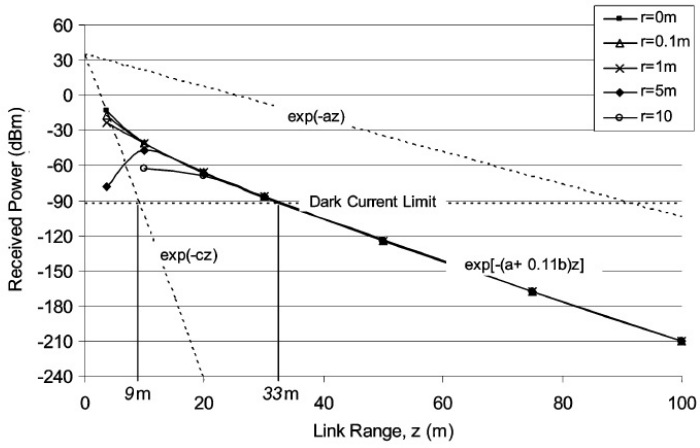

Figure 3.5: Received optical power versus link range for various transmitter/receiver pointing accuracies (r) with $c(\lambda) = 3.2/m$

In [17], Tang et al. obtained similar simulation results as those presented by Cochenour. The main contribution of this work is the analysis of the BER regarding the pointing offset and a closed form for the Threshold Transmit Power (TTP), which is the transmitted power needed to produce a certain SNR at the receiver. Gabriel et al. performed an experimental demonstration of Cochenour's predictions in [18].

Hagem et al. presented in [19] an analysis on the feasibility of an underwater link between a swimmer's goggles and a wrist-located blue-green emitter, in order to obtain feedback. The authors studied the scenario using two types of LED, one with a half-angle of 8° and other of 70°. After performing several tests varying the the pointing and the presence of air bubbles, they demonstrate the feasibility of a link with that restrictions. Figure 3.6 depicts

the received power without the presence of air bubbles. The straightforward conclusion of their work is that a short-distance link with a highly-variant channel gain due to movement is more reliable in terms of channel availability the wider the emitter is.

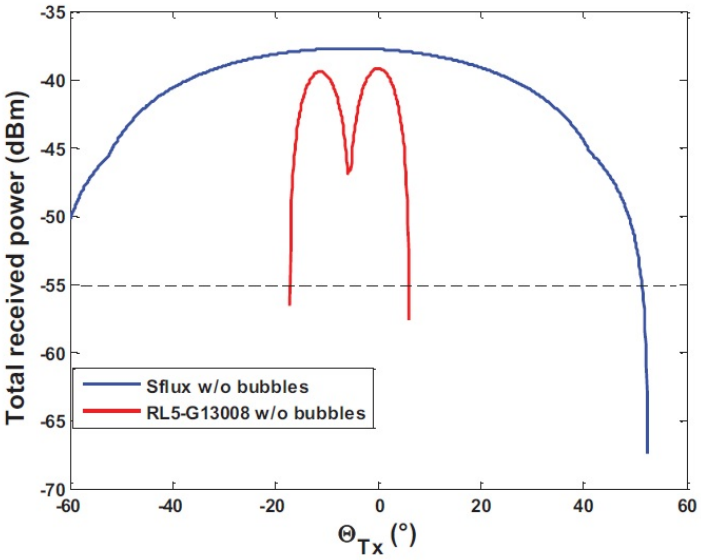

Figure 3.6: Total received power versus the pointing angle without the effect of air bubbles

The effect of a random sea surface for vertical links has been also studied by Dong et al. in [20]. The authors considered the effect of wind stress on the seawater surface and modeled it as a normal distribution. Actually, according to the measurements of Cox and Munk, presented in [21], the slope of the sea surface follows a distribution based on a Gram-Charlier series. However, this series may be approximated by a normal distribution without a significant loss of accuracy. After developing a numerical approximation, the authors conclude that the increment of seawater turbidity may diminish the BER performance degradation caused by the wind and enhances the link reliability with a tradeoff between turbidity and transmit power. In this work, the authors do not consider mechanical effects such as buoyancy and inertia on the floating emitter. Furthermore, the BER estimations are not realistic, as there would be periods of time in which the instantaneous BER could rise to a maximum. A better performance datum could be a combination between mean BER and its variance, or a combination between average BER and channel availability. Supported in this work, Zhang et al. derived a capacity-estimation formula for this kind of link in [22], but it is not a closed-form expression and must be calculated numerically for each scenario.

The same author presented in [23] a closed-form expression to obtain the angle-of-arrival (AOA) distribution in an underwater link. These results suggest that more turbid waters widen the AOA, whilst shorter links narrow this distribution.

Liu et al. studied in [24] the effects of wavelength (400 nm - 600 nm), chlorophyll concentration, receiver's FOV and misalignment on the received power. This work extracts straightforward conclusions very common in the literature.

An study related to communications in swarms using UWOC was performed by Tabacchiera et al. in [25]. The study proposes a system model, but the most remarkable aspect of this paper is one of the results. Although it may be seem straightforward, the channel extinction may be considered to produce a bandwidth-limiting effect on the receiver. Figure 3.7 illustrates this effect. For a given transmission power, if a concrete SNR is desired, the receiver's gain should be increased and hence, the link's bandwidth reduced.

Other contributions

Other contributions not classified in the above subsections look into purely reflective links, noise modeling, considerations on vertical links or experimental characterization of air-to-underwater links.

In [26], Arnon and Kedar proposed reflective underwater links using laser diodes and photomultiplier tubes (PMT) as photon counting-based receivers. Figure 3.8 depicts the scenario. Regardless the associated costs of the proposed scheme, this contribution was the first in address this kind of links. The authors considered a quiet surface for simplicity in the analysis, but in a real scenario, the seawater surface is normally a combination of a seawave spectrum and a noisy term due to wind stress. Tang et al. [27] introduced the aforementioned effects in a link as the one described by Arnon and concluded that highly-variant surface slopes degrade dramatically the BER performance on a reflective link, whilst the BSF due to scattering particles reduces this effect. This last is explained by the same conclusions extracted from Cochenour in [16]. In this case, the misalignment is due to the

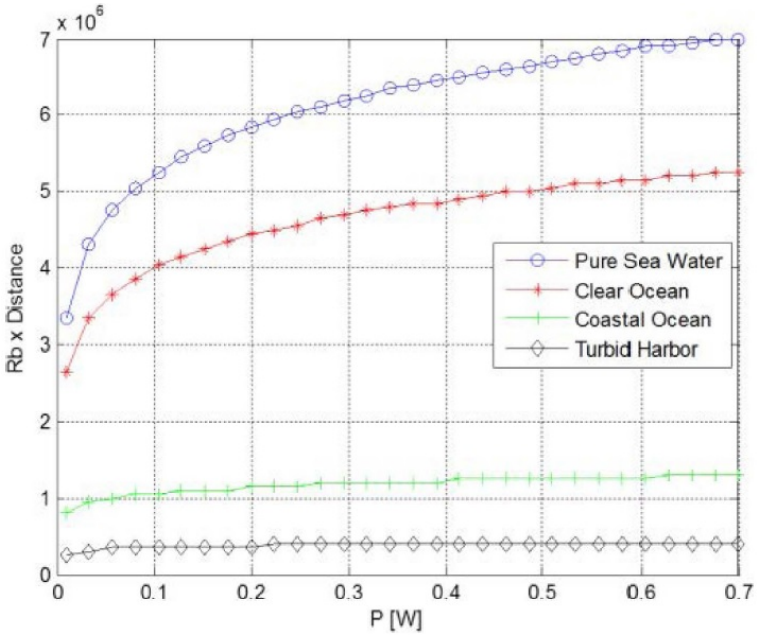

Figure 3.7: Bandwidth-distance product for different types of seawater regarding the transmission power.

variation on the reflected angle. Choudary et al. studied the same scenario in [28], analyzing different particle concentrations.

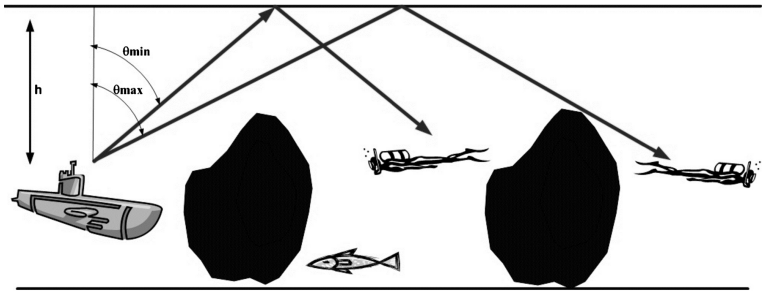

Figure 3.8: Underwater reflective link proposed by Arnon and Kedar [26]

Johnson et al. studied the particularities of vertical underwater links in [29]. The variation of both refractive index and extinction coefficient with depth may imply a significant offset between predictions and reality if their effects are not considered. Figure 3.9 depicts the depth profiles of both extinction and refractive index for three different chlorophyll-concentration profiles (S1, S3 and S6), based on the surface concentration $C_{chl-surf}$. This profiles were adapted and studied by the same authors in [30]. In this paper, the Z_∞ depth is defined as the depth from which the attenuation in UWOC reaches its global minimum of $0.0092m^{-1}$ at 430 nm. Table 3.1 shows a simplified transcription from the original paper.

	$C_{chl-surf}$ (mg/m^3)	Z_∞ (m)
S_1	<0.04	415.5
S_2	0.04-0.08	309.6
S_3	0.08-0.012	282.2
S_4	0.012-0.2	264.2
S_5	0.2-0.3	200.7
S_6	0.3-0.4	226.8
S_7	0.4-0.8	169.1
S_8	0.8-2.2	111.5
S_9	2.2-4	-

Table 3.1: Z_∞ for different surface chlorophyll concentration profiles

Regarding noise modeling in low-input-power scenarios, Rashkin et al. proposed a different SNR estimation

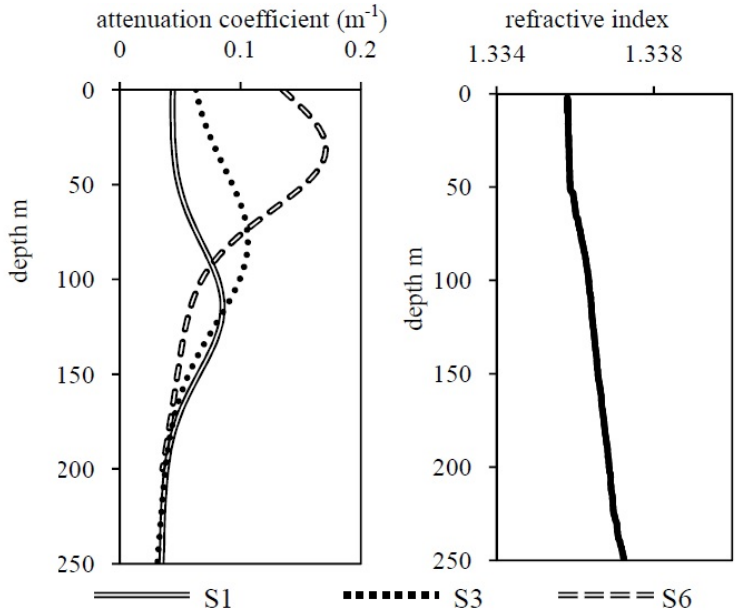

Figure 3.9: Variation of the refractive index and the extinction coefficient vs. depth

model [31]. Commonly, SNR is estimated with a normally-distributed assumption, but in the case of applications where PMT devices are needed, the photodetector's shot noise is not normally distributed but Poisson distributed. The correction proposed by the authors is based on a mean-value offset and a variance scaling, based on the received power. The performed experiments state that the new model is more accurate than the oversimplifications that are normally made, and that the estimation may represent a difference up to 7 dB.

In [32], Dy et al. explored the influence of the seawater surface movements on the received signal in an air-to-underwater link. The authors obtained qualitative results relating the surface agitation to the BER, concluding that the higher the wind stresses is, the worse the BER performance is. Actually, this conclusion is not valid for any kind of transmission, as the authors performed the experiments mixing a *desired* signal with a synthetic *noise* signal at the transmission side. The relationship between the amplitudes of the signals were identified to the desired SNR at the receiver. In a real case scenario, the noise terms would be the background illumination due to sunlight (for shallow water applications), the darkness current, the photogenerated shot noise and the Johnson noise. The authors do not take into consideration that both emitted signals would produce shot noise and that the receiver has a thermal noise baseline. A more accurate nomenclature to their experimental framework would be Signal-to-Interference-and-Noise Ratio (SINR).

3.1.2 Channel response

Channel response modeling is a critical aspect in any field related to communications. The obtained models are usually intended to predict the channel gain and bandwidth of any scenario. This predictions based on geometrical parameters and in the physical properties of the medium may be more or less accurate depending on the variability of the channel. In the case of the UWOC channel, shallow-water links are the most variable due to the high presence of chlorophyll, particles, fauna, and the effect of sunlight and the seawater surface. The deeper a link is, the more stable the impulse response is, as the presence of submarine currents is less important. The following contributions summarize the research of the last few years (up to the date of this work) in the modeling of the UWOC impulse response.

Analytical solutions

Jaruwatanadilok was one the first authors in obtaining an estimation of the impulse response for UWOC links [33]. In this work, the authors solves numerically the Vector Radiative Transfer Equation (VRTT) of an only-underwater scenario with a constant particle distribution. Figure 3.10 depicts the obtained impulse responses for 30 and 50 meters.

In [34], Li et al. applied a fast numerical solution to the RTT equation and estimated the path loss of an UWOC link. The main conclusion states that this kind of solving is much faster than a Monte Carlo integration scheme, conserving the accuracy.

Finally, Jamali and Salehi developed the mathematical apparatus to calculate the BER performance in MIMO UWOC links. The authors consider that the fading coefficients behave as log-normal variables, but there is no

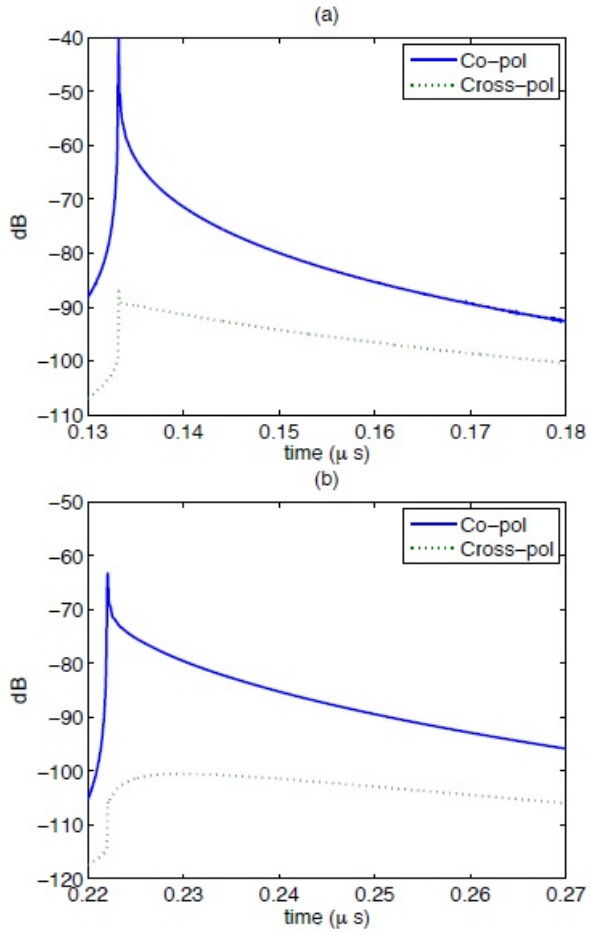

Figure 3.10: Impulse responses of an UWOC channel (up - 30 meters and down - 50 meters) obtained by Jaruwatanadilok

evidence in the literature to assure that. A random variable follows a log-normal distribution if its logarithm follows a normal distribution. Commonly, if the received power is the product of multiple variables, the last condition is satisfied by the Central Limit Theorem (CLT). In the case of UWOC links, this is neither clear nor straightforward.

Monte Carlo simulation

Gabriel et al. presented a Monte Carlo-based simulator in [35]. The authors consider the multiple scattering of photons, using the Henyey-Greenstein function as scattering function [36]. This function, which can be observed in Equation 3.3 is assigned as probability density function of the angular deviation of the photons after interacting with a particle. The authors obtained several curves showing the influence of distance, receiver's diameter and water type on the impulse response. Finally, the authors assume that the link does not suffer from Inter-symbol Interference (ISI), conclusion that directly contradicts the conclusions of Jaruwatanadilok. Two years later, the authors presented a very similar paper and relaxed the ISI conclusion [37].

$$p_\theta = \frac{1-g^2}{2\left(1+g^2-2gcos\theta\right)^{3/2}} \tag{3.3}$$

θ is the output angle and g is a parameter which defines the behavior of the scattering function. It ranges from -1 to 1 and defines the function from backscattering through isotropic to forward scattering. One of the main reasons of using this function is that its integral has inverse and hence, may be used in Monte Carlo methods without complication. Nevertheless, as Zhao and Sun demonstrated in [38], the approximation of Mie scattering through a Henyey-Greenstein function may result in very large errors.

Jasman and Green presented in [39] other Monte Carlo solution to obtain the impulse response of an UWOC link. In their case, the authors concluded that for a 10 meters link using LED sources, a bandwidth of 100 MHz can be achieved in harbor water.

Jagadeesh et al. presented in [40] an study of the channel impulse response in an NLOS situation. The authors considered a noiseless receiver in order to only examine the multipath effect in a 1 Gbps simulated transmission, which is a very unrealistic approximation. It can be observed that turbid environments like coastal water take

advantage of scattering regarding received power, for moderate distances, as it can be observed in Figure 3.11. However, this highly-scattered environment does not allow link distances as long as a clear water scenario.

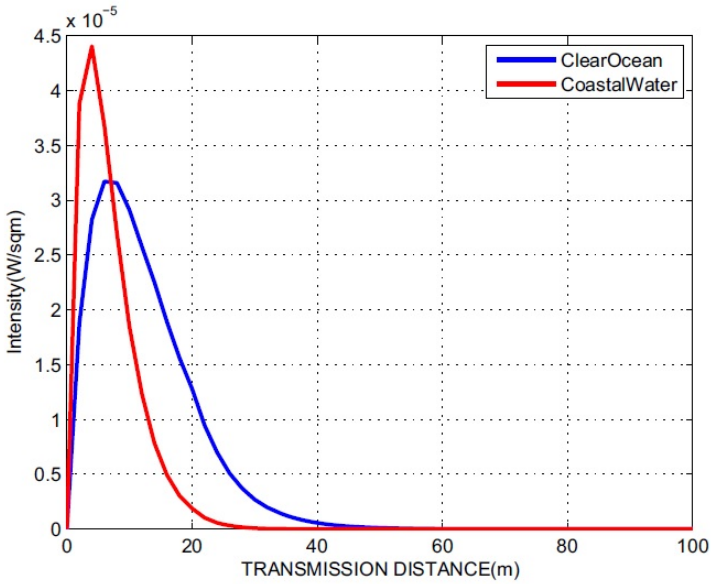

Figure 3.11: Received intensity in a NLOS scenario (coastal and clear water)

Curve fitting of the Impulse Response

Tang et al. presented in [41] a curve fitting of the LOS UWOC impulse response. The double gamma function was tested for turbid environments with a great error performance. Figure 3.12 depicts the one of the experiments whilst Equation 3.4 shows the mathematical expression of the fitting function.

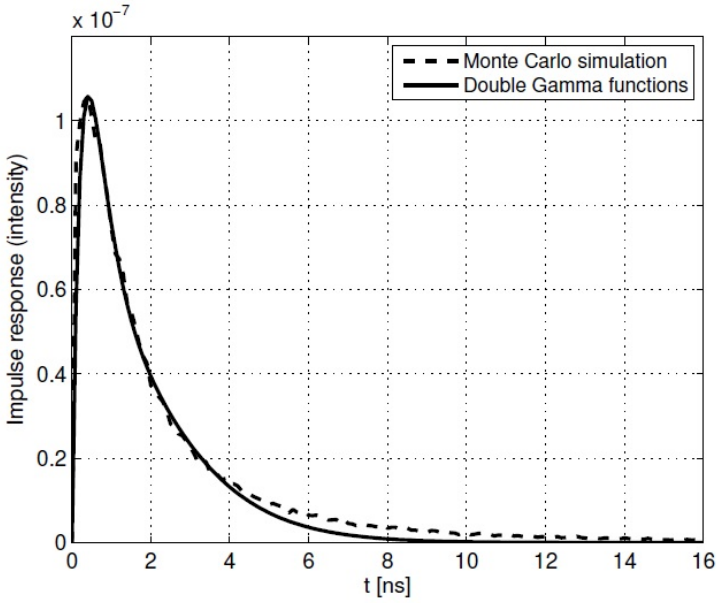

Figure 3.12: Double Gamma fitting of the UWOC impulse response in a turbid environment

$$h(t) \approx a(t-t_0)e^{-b(t-t_0)} + c(t-t_0)e^{-d(t-t0)} \tag{3.4}$$

a, b, c and d are constants to be determined, and t_0 is the propagation delay, which is determined by $t_0 = Ln/c_0$. L is the link's distance, n the refractive index of seawater and c_0 the speed of light in vacuum.

The same authors continued their research on this topic in [42], estimating the BER performance and the bandwidth using the parameter estimation of the double gamma approximation. Calculating the bandwidth through

the double gamma impulse response is as easy as applying the Fourier Transform to 3.4. Equation 3.5 shows the result.

$$H(j\omega) = \left(\frac{a}{(j\omega + b)^2} + \frac{c}{(j\omega + d)^2} \right) e^{j\omega t_0} \tag{3.5}$$

The double gamma approximation was proven to be very accurate to the simulations, but the relationship between its parameters and the physical and geometrical characteristics of the link has not been studied yet.

Finally, Dong et al. examined the possibility of a closed-form impulse response modeling in a MIMO-based UWOC link [43]. The approximation was based on a weighed superposition of double gamma functions, as it is the straightforward solution. In this version of the double gamma approximation, the author slightly modified Equation 3.4 to fit a 2x2 MIMO impulse response, adding two new parameters yielding Equation 3.6.

$$h(t) \approx a(t - t_0)^{\alpha} e^{-b(t-t_0)} + c(t - t_0)^{\beta} e^{-d(t-t_0)} \tag{3.6}$$

Other contributions

Cochenour et al. defined an experimental method to measure the temporal dispersion in laser-based UWOC links [44]. The authors demonstrate that Beer-Lambert's law is not accurate enough to establish a baseline in NLOS link design. Other effects such as multiple scattering , which generates temporal dispersion and hence, a reduction on the available bandwidth, should be considered. An interesting conclusion is that widening the FOV of the receiver enhances the input power but lowers the bandwidth in scattered environments. Furthermore, this sensitivity is dramatically reduced for off-axis links. These last conclusions have a significant impact on the link designer, which must know the geometrical parameters of the link.

Dai et al. studied in [45] the behavior of IR and UV light in seawater. The authors proposed a scattering model for this wavelength bands and contrasted it empirically. The results have direct application in seawater parameter monitoring and the sensing of chemical oxygen in water treatment facilities. The direct impact in communications in reduced, as these bands present distance-limiting attenuations.

3.1.3 Stochastic modeling

An accurate stochastic model is the main objective that channel modeling must try to achieve. The scientific method states that after observing a phenomenon a sufficient amount of times, a generalization may be performed with an accuracy directly related to the times the phenomenon was observed. It is logical that the efforts in UWOC channel modeling have been focused on simulation and experimental evaluations, but a critical mass has been reached and the production of probabilistic estimations and stochastic models should be the next milestone to fulfill.

Tang et al. studied the temporal statistics of a laser-based link in a turbulent scenario [46]. After considering Kolmogorov's turbulence approximation and Taylor's frozen turbulence hypothesis, which are widely valid for regions below 100 meters in oceanic environments, the authors studied the temporal correlation of the irradiance between two points. Figure 3.13 shows this correlation for link between 30 and 50 meters with two different turbulent regimes defined by the average vertical water speed through the link's axis.

It can be observed that the coherence time, which is the time at which this correlation function decays 3 dB, is almost independent of the distance and is highly affected by the turbulence's regime. Furthermore, the authors conclude that the correlation is more affected by salinity fluctuations than by temperature variations within the weak turbulence region. This is due to the higher sensitivity of the refractive index to salinity.

In [47], Zhang et al. developed a numerical method to calculate the spatial and temporal probability function of a LOS UWOC link, considering up to one single scattering event per photon. The final mathematical expression is the result of directly applying Random Variable Transformation (RVT) to the link's equations. The same authors continued this research line and presented in [48] a more generalized version of the aforementioned work, considering an integer number of scatterings. The authors do not depict any figure of the resulting probability density functions (pdf) and use the method as an alternative to the Monte Carlo simulation path loss estimation.

3.2 Modulations and Encodings

Modulations and encodings are a critical aspect in any communications link. The way the information is sent in a changing environment defines the BER, the effective throughput and has also influence on the channel availability.

Cochenour et al. studied in [49] the use of phase-coherent laser-based systems in turbid environments. The paper explores the use of different M-PSK schemes within a water tank. As it is usual in their contributions, the authors used different concentrations of Maalox to generate synthetic turbidities. The conclusions suggest that for relatively short distances (below 100 meters), coherent schemes are a feasible alternative in UWOC. However,

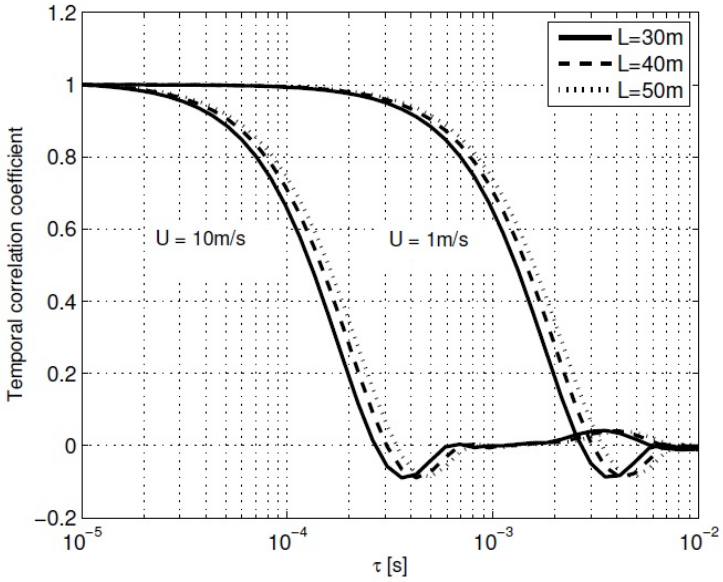

Figure 3.13: Correlation function of a laser-based link in a turbulent scenario

the authors also manifest the necessity of further work in long-range environments in order to establish a clearer relationship between SNR, multipath and BER.

Sui et al. studied in [50] different modulation approaches for turbid environments. Unlike Cochenour's group, the authors performed a simulated study considering only extinction in their framework. This work neglects the stochastic nature of the underwater environment, and only considers attenuation. The compared schemes are OOK, FSK, DPSK (coherent), 4-PPM and 8-PPM. In[51], the same authors proposed a variation of a PPM schemes named SPPM (Shorten PPM). Nevertheless, the results does not suggest any real improvement respect to PPM, as it presents a lower spectral efficiency and BER performance, and it has higher power requirements.

In [52], Yu et al. explored the use of FEC (Forward Error Correction) codes in UWOC. As the latter work, the random behavior of the channel response is not considered and its PDF (Probability Density Function) is defined as a Dirac's delta. The results show the reduction of the BER after using this codes.

The use of Optical OFDM in UWOC was experimentally explored by Minev et al. in [53]. The authors thoroughly describe the experimental setup and the OFDM scheme. The tested distances ranged from 0.5 meters to 3 meters, which is a very short distance to present a significant multipath effect so as to justify the use of OFDM. Furthermore, the authors obtained this conclusions observing that the ISI was negligible, as the delay spread is much lower than the symbol time. Figure 3.14 depicts the BER vs E_s/N_0 curve of the experiment.

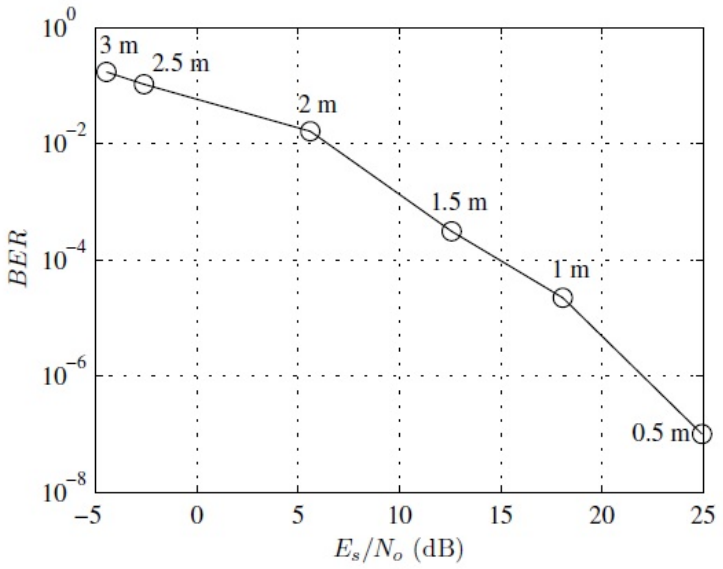

Figure 3.14: BER curve of the experiment performed from 0.5 to 3 meters

Gabriel et al. carried out an comparative work [54], similar to the one presented by Sui. In this case, the authors considered OOK, PPM, PWM and DPIM. The main conclusion of this paper is that although DPIM presents a higher demodulation complexity, its spectral efficiency is the highest and must be considered when designing an UWOC link. The authors remark the low PAPR of DPIM, but considering the associated transmission electronics, this aspect presents no actual advantage, as ON/OFF schemes may be driven by MOSFET-based circuits.

The use of Spread Spectrum techniques has been also considered for UWOC. Akhoundi et al. presented an analytical model and a experimental evaluation of a CDMA system using OOC (Optical Orthogonal Codes) in [55]. One of the key aspects of the paper is the definition of the Optical Base Transceiver Station (OBTS), which comprises a series of photodiodes and LED, and the Optical Network Controller (ONC), that manages part of the network in a cellular way. The proposed system can be observed in Figure 3.15 Both downlink and uplink are defined to use OCDMA. Figure 3.16 shows a diagram of the experimental setup used to validate the system.

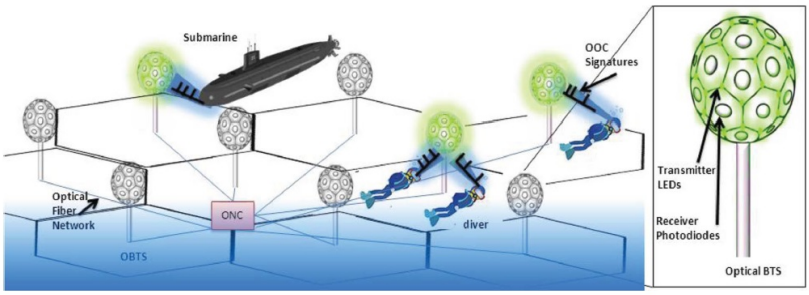

Figure 3.15: Cellular OCDMA underwater network

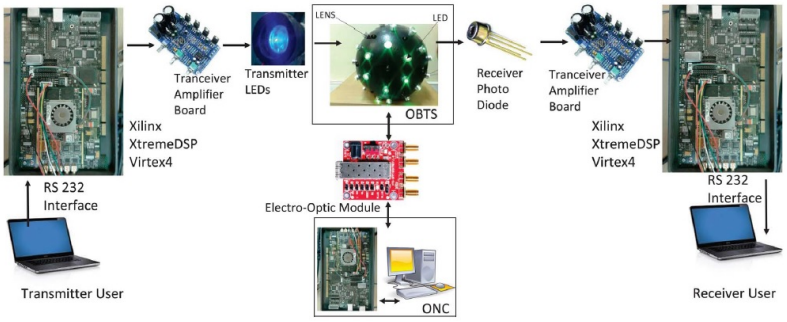

Figure 3.16: Experimental setup used to validate the proposed OCDMA underwater network. Virtex 4 FPGA's were used to implement the system.

This contribution does not deeply explore the use of different Spread Spectrum techniques, but is more focused on the network description and the MAC layer behavior.

3.3 Energy efficiency

Energy efficiency is one of the more important aspects when considering UWOC, and much more when considering UWSN. The use of energy-efficient strategies to longer the life of the batteries in autonomous nodes is of capital importance as the battery replacement is often much expensive than simply deploying new nodes.

Srinivasan et al. proposed a joint source-channel coding technique to reduce the average energy per symbol in [56]. Even though the authors propose the scheme for UWOC, the scheme is suitable for any sensor network.

BaniHassan et al. presented in [57] a power control algorithm based on the previous work of their group in Optical CDMA networks [55]. The authors propose two different approaches to perform power control. The first strategy consists on sectoring to reduce the emitted power, so as to enhance the energy efficiency by limiting the emission to a determined solid angle. The other strategy is to define rings. This discretization allows a better power control assigning a transmission power to each ring. The authors also consider a joint ring-sector strategy. The ring-system is defined as open-loop, as the nodes estimate their position in a received power-basis. The main issue of this proposal is that each node must know the extinction coefficient of the medium. Furthermore, this coefficient changes in time and the method does not takes this into account. The authors estimate that in a combined scheme, up to 15.5 dB of power can be saved in cells with 50 m of radius.

3.4 Network layer

Network layer is important when considering UWSN. Fading events may occur in UWOC, and may produce harmful effects in the connectivity of the network. The following lines comment different contributions that have been made during the last few years.

Liu presented in [58] a paper where a topology-recovery strategy was presented. The author proposed the technique for an ultrasound-based network, but the proposal can be easily extrapolated to the optical domain. The recovery procedure is based on two main steps. When the connectivity is destroyed, the reference node increments its transmission power. If this action does not solve the problem, then one of the mobile elements of the network (an AUV i.e.), is moved toward the location of the lost node.

Hu and Fei proposed in [59] a multilayer routing protocol for hybrid opto-acoustical networks. In this paper, the use of reinforcement learning, specifically Q-learning, is explored as an alternative in routing decision for multihop UWSN. The proposed network topology consists in an acoustic backbone and optical clusters conformed by remote optical nodes. The upper-layer (acoustic) nodes manage the optical clusters allowing fast intra-cluster routing. The results suggests that this layering strategy allows a lower latency network as well as a more energy-efficient alternative. Figure 3.17 shows the packet delivery rate, the delay and the inter-layer overhead respect to the packet rate. It can be observed that the delivery rate is almost independent of the packet rate in a layered system. Furthermore, the delay remains below the unlayered case at any packet rate.

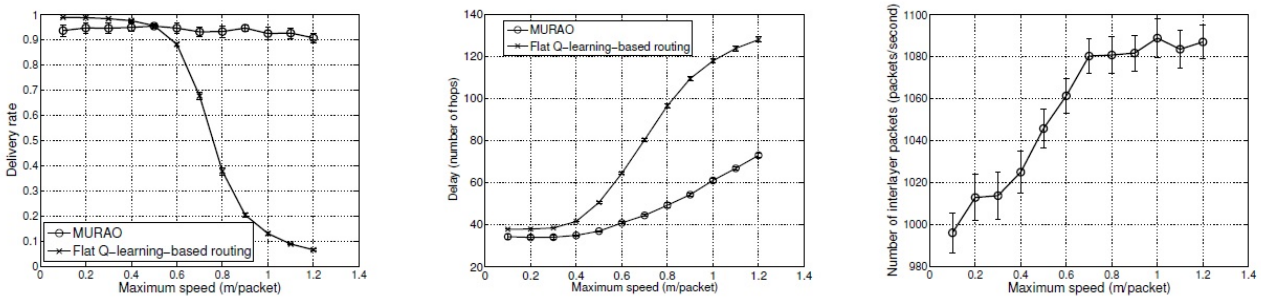

Figure 3.17: Delivery rate (left), delay (center) and inter-layer overhead (right) vs packet rate in an interlayer Q-learning routing scenario.

Mora et al. implemented in [60] an ad-hoc multihop optical network using a TDMA-based MAC layer. The network is dynamically conformed using a tree-based management strategy. The main disadvantage of the system is that every node has the full information of the network, which may incur in large delays and less energy efficiency.

A connectivity analysis was performed by Vavoulas et al. in [61]. The authors studied the node density requirements (number of nodes per linear meter) in order to establish a k-connectivity network. This requirements depend on the emitted optical power, the channel path loss and the wavelength. Furthermore, the authors considered an isotropic radiation patter, which is mostly improbable in an optical wireless transceiver. Figure 3.18 depicts some of the obtained results.

3.5 Applications

As it was mentioned at the beginning of this chapter, the development of a topic is normally bound to the theoretical analysis and the push of the experimental evaluations. In this section, different applications of the UWOC technology are presented. The following taxonomy has been applied in order to sort the papers.

- Hardware design
- Underwater Wireless Sensor Networks
- Applications for mobile systems
- Other applications

3.5.1 Hardware design

Anguita et al. implemented an IEEE 802.15.4 compatible PHY and MAC layer. In [62] presented the physical layer, which was implemented in a Spartan 3 FPGA, using LED devices and PPM modulation. Figure 3.19 shows the experimental setup used to validate the system.

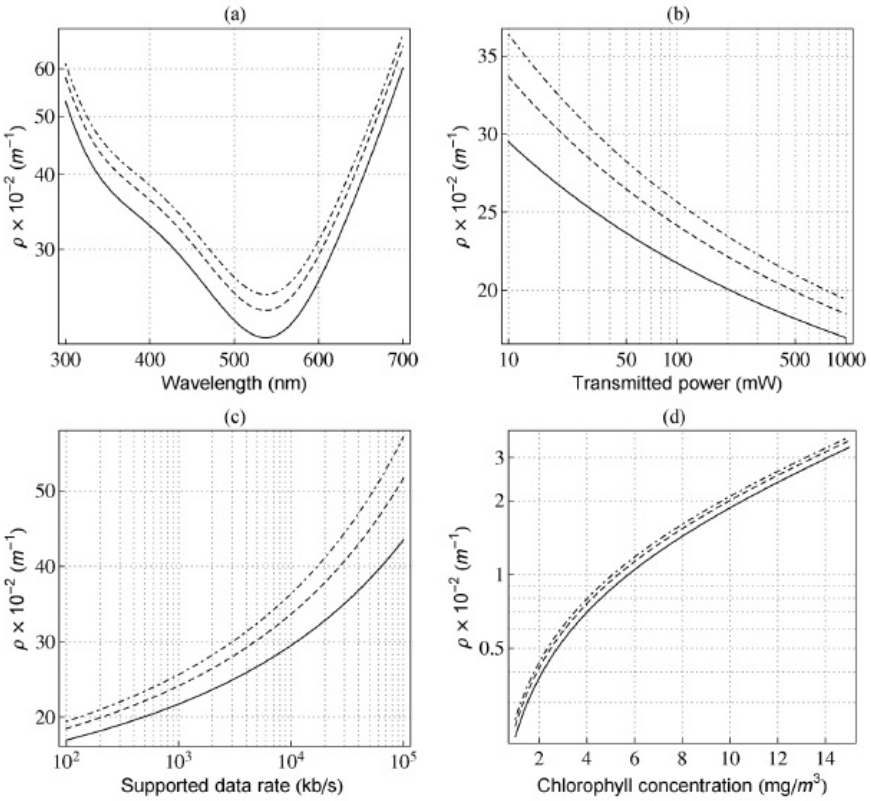

Figure 3.18: Required node density to achieve node isolation probability equal to 10^{-4} versus (a) operating wavelength, (b) transmitted power, (c) datarate, and (d) chlorophyll concentration for $BER = 10^{-3}$ (dashed–dotted line), $BER = 10^{-6}$ (dotted line), and $BER = 10^{-9}$ (continuous line).

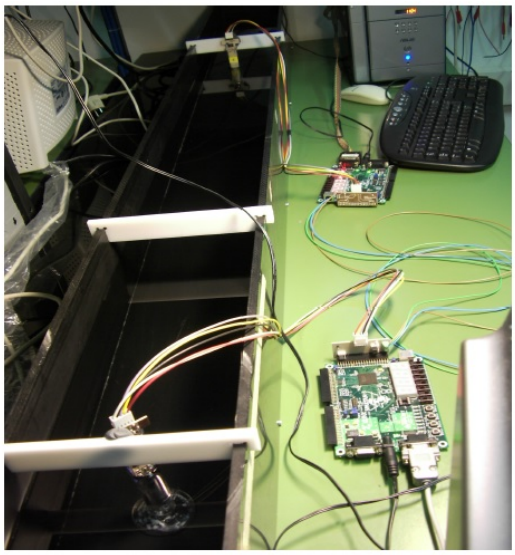

Figure 3.19: Experimental setup used by Anguita et al. to validate their FPGA implementations

The corresponding MAC layer implementation was presented in [63], transforming the former transmitter from directional to omnidirectional, as shows Figure 3.20. The proposed MAC protocol was CSMA/CA. Finally, the whole system was evaluated in [64]. Figure 3.21 depicts the block diagram of the system. The main contribution of this works is the application of an existing standard to the underwater medium.

Doniec and Rus presented AquaOptical II in [65]. This bidirectional system is based on an array of LED and an avalanche photodiode to perform transmission and reception respectively. The system achieved a 2.28 Mbps using DPIM encoding at a distance of 50 meters with a estimated SNR of 5.1 dB. Figure 3.22 shows the design of this transceivers.

In [66], this device was used to perform a robust underwater video-streaming link. Doniec et al. performed

Figure 3.20: Used planar emitter

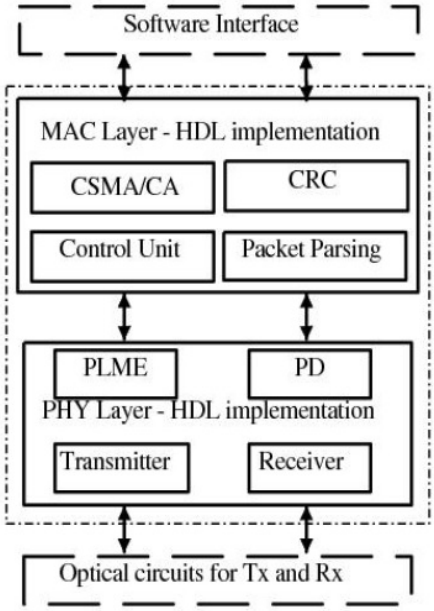

Figure 3.21: Block diagram of the IEEE 802.15.4 compatible VHDL implementation

tests up to 40 meters, using different video frame encodings, qualities and speeds. Figure 3.23 shows the obtained results regarding the interval between packets.

Destrez et al. implemented an hemispheric LED emitter using 12 LED [67]. The main objective of the work was to emulate an hemispheric radiation pattern, but also electronic design considerations regarding both emitter and receiver are presented. Even though the authors theorize speeds up to 50 Mbps, the experiments were performed at 1 Mbps using a traditional OOK encoding, showing poor BER performance at distances above 2.5 meters.

Swathi and Prince presented in [68] an study regarding considerations on UWOC transceiver design. The authors enumerate the influence of each design parameter into the system performance, but the main conclusion is that the authors propose the use of adaptive transceivers to take advantage of the channel's characteristics. Although the authors do not expose it literally, this means the use of wavelength-selectable emitters. Depending on the suspended-matter concentration and link's distance, an optimum wavelength may be estimated.

In [69], Tang et al. presented different considerations on the use of APD receivers in UWOC. The main tradeoff of using APD is their inner gain, and a more compact size and higher quantum efficiency compared to PMT. An

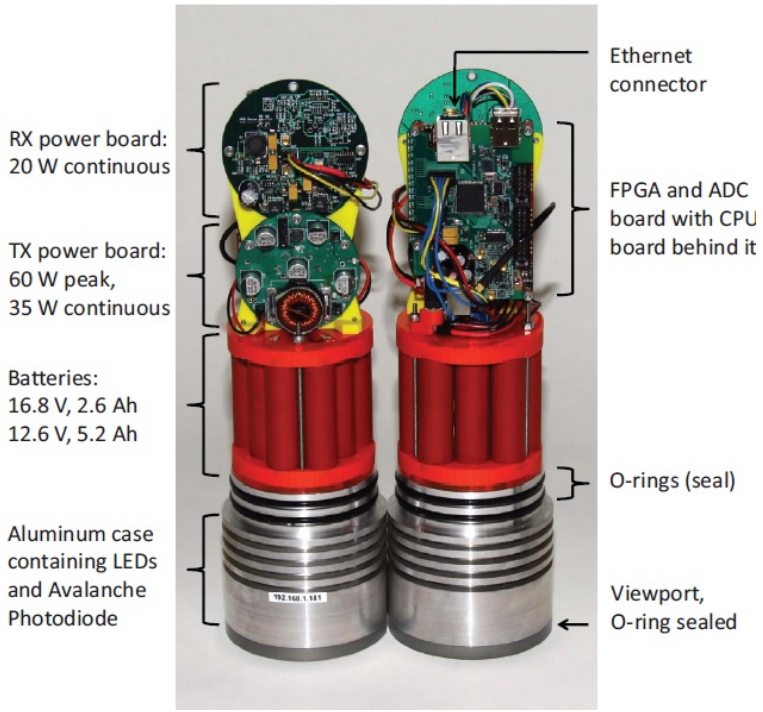

Figure 3.22: Aquaoptical II transceivers

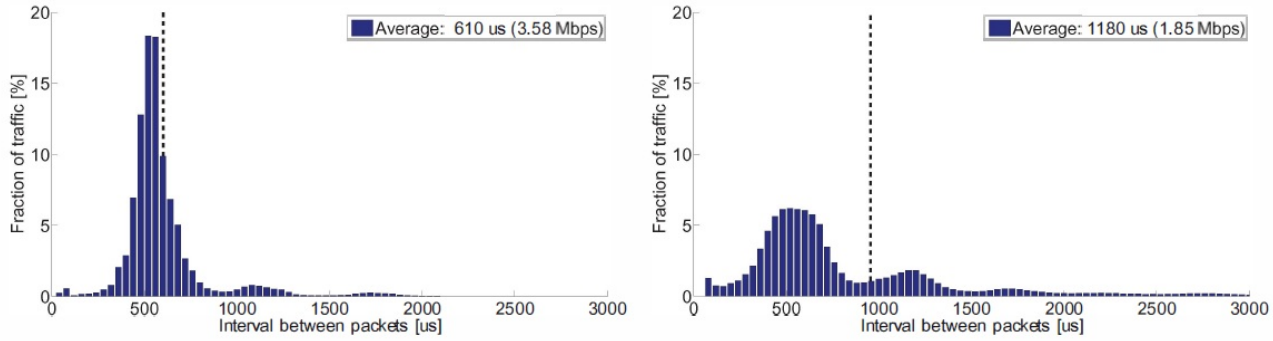

Figure 3.23: Interval between packets for links ranging from 10 to 25 meters (left), and for links ranging from 25 to 40 meters (right).

interesting gain control scheme is presented in order to maximize the SER. As the gain of an APD affects the SNR, for each scenario there is an optimal gain that maximizes this parameter. The authors presented a closed-form expression of the optimal gain, which depends on several parameters. Figure 3.24 depicts the optimal gain for a given example scenario. It can be observed that the optimal gain depends almost only on the link range.

Tian et al. implemented an UWOC link as the one shown in Figure 3.25 [70]. The LED driver is based on a non-inverting topology followed by a BJT-based switch. The receiver side implements a transimpedance amplifier followed by an inverting second stage. The tests, performed in a swimming pool, demonstrated communication distances between 20 and 30 meters.

Cossu et al. demonstrated a 2.5 meters link using a 40 dBm optical source at 470 nm in clear water [71]. Two receiver schemes were used, one based on APD and other in a PIN photodiode. This work does not provide any novel aspect regarding hardware design, but the authors performed an analysis of the impact of daylight into the BER performance. As the experiment were carried out in a pool, the near-surface condition of the link made it very sensitive to the Sun's position, as Figure 3.26 shows.

3.5.2 Underwater Wireless Sensor Networks

In 2006, Farr et al. proposed a laser-based underwater wireless optical modem [72]. In this work, the authors proposed the use of wireless optical technology using visible-light to establish a link in the underwater medium. The work covers the main aspects in the design of a link of this characteristics: transmitter devices, optics,

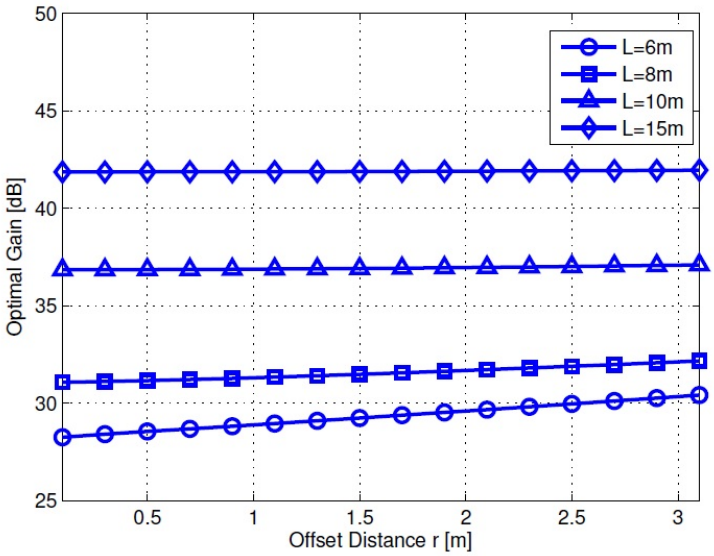

Figure 3.24: Optimal APD gain to maximize SER in a given scenario. The offset distance is the distance from the emitter's axis.

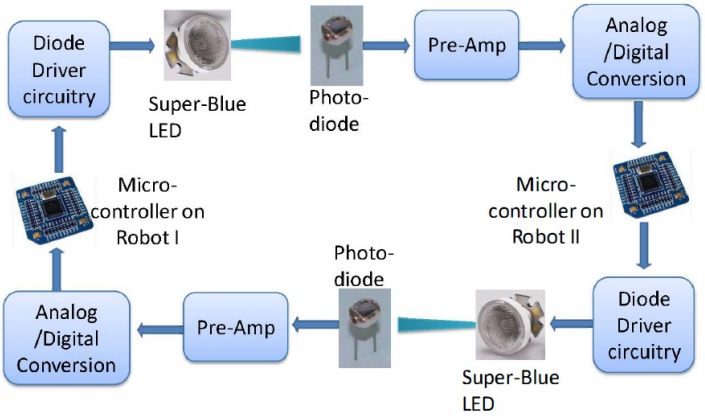

Figure 3.25: Block diagram of the system implemented by Tian et al.

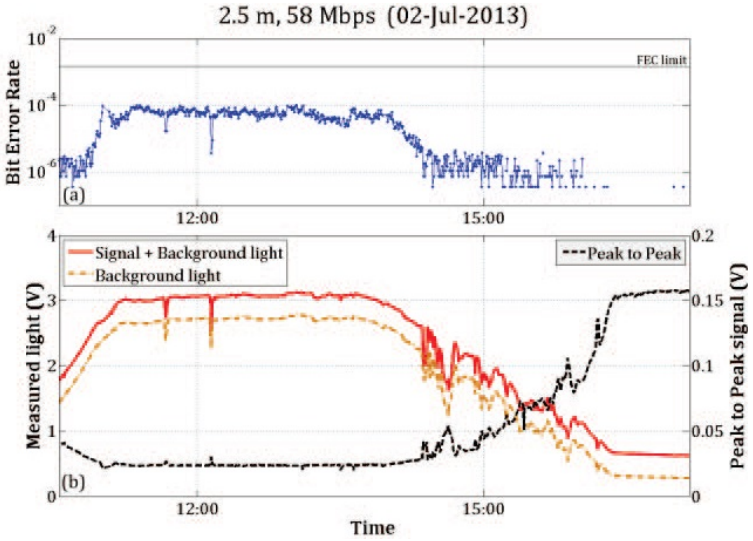

Figure 3.26: Impact of daylight in the BER performance for a near-surface link

receiver design, phenomena, application scenarios, etcetera. The work proposes three different solutions to establish communications between a vehicle and a fixed node, using combinations of directional and omnidirectional emitters

and receivers. As it is usual in the literature, the proposed receiver is PMT-based.

Simpson et al. implemented an underwater node that retrieves data from an ultrasonic receiver, encodes it using a return-to-zero Reed-Solomon code and transmits it using a high-power LED [73]. The authors demonstrated the feasibility of low-power and cost-effective UWSN nodes achieving datarates up to 5 Mbps.

The works presented by Anguita et al. regarding hardware implementations where evaluated by simulation in terms of achievable data rate in [74]. Medium-related aspects such as turbidity were considered in the simulations. Figure 3.27 depicts the obtained maximum data rate for the aforementioned planar emitter.

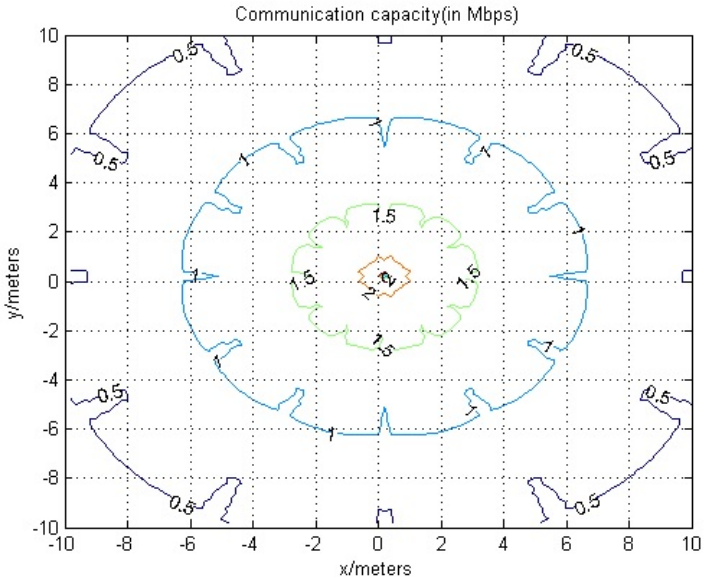

Figure 3.27: Maximum achievable data rate of Anguita's planar emitter

Farr et al. deployed an UWSN node in the northeast Pacific Ocean [75]. The main objective of the experiment was to gather geochemical data, but due to the high amount of data to collect, ultrasonic link were not feasible. The implemented system had an ultrasonic channel for telecommand, whilst the optical channel was used to download data up to 5 Mbps at a distance of 61 meters. Figure 3.28 depicts a concept artwork of the operation.

Johnson et al. made other contribution on hybrid optical-acoustical network approaches [76]. The authors expose the advantages of using an acoustical downlink and highly-directive optical uplinks at the UWSN nodes. However, the authors claim that this kind of structure presents several disadvantages, such as power-limited range and sensitivity to refractive gradients (as it is a vertical link). As Cochenour demonstrated in his experimental works, due to the BSF, misalignment and refractive gradients decrease their effect with distance. Finally, the power limitation of laser emission due to fauna's eye-safety is mentioned in this paper, being the first work in address this issue regarding UWSN.

3.5.3 Applications for mobile systems

Fung et al. implemented an UWOC system for robotic swarms in [77]. The robots carried out a multi-channel algorithm in order to propagate the information within the swarm. The communications was performed transmitting a serial port at 115 Kbps through a green laser. The authors complaint about the necessity of pointing in the system. Nonetheless, at the tested distances, an LED-based system would have been a trade-off regarding reliability. The use of laser devices was justified imposing the necessity of long range communications. However, only at actual long distances with significant particle concentrations, laser-based system relax their maximum misalignment error as Cochenour suggested in [16].

Doniec et al. evaluated the use of UWOC for robot operation [78]. The aim of the experiment was to perform a cable replacement to control the robot. Normally, this kind of robots are tethered to a base station, limiting the maximum range of operation and its maneuverability. The obtained delays were not distinguishable from a tethered version of the experiment. Furthermore, the implemented optical devices were capable of establishing a 200-meters link in air at night, a 30-meters link in a pool, and a 7-meters link in a high-turbidity harbor environment. The merit figure used by the authors to measure the quality of the link was the packet delay since the last update of the IMU. Figure 3.29 depicts the obtained results for two different environments: low SNR and high SNR.

Gao and Guo presented in [79] an implementation of a remotely operated microrobot. The robot implementation were intended to work under the command of a mother submarine. Nonetheless, the authors used infrared light to perform communication, limiting the maximum allowed distance of operation to a few dozens of centimeters.

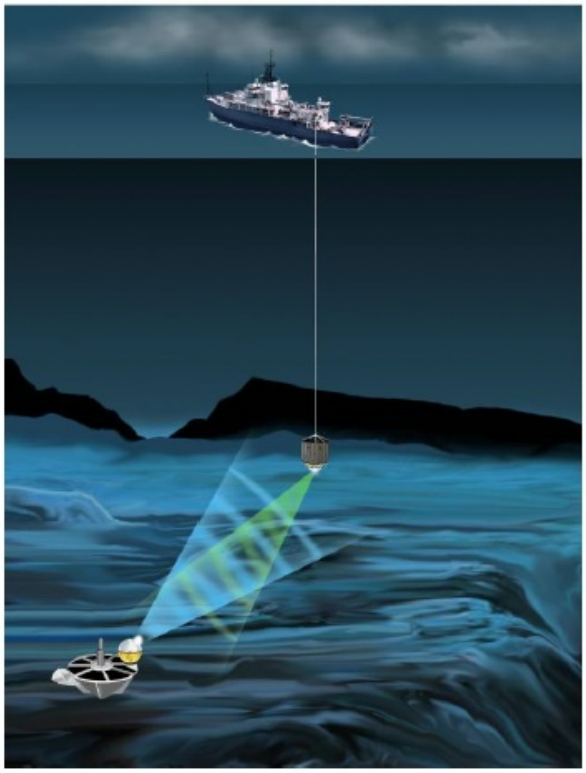

Figure 3.28: Concept of the system implemented by Farr et al.

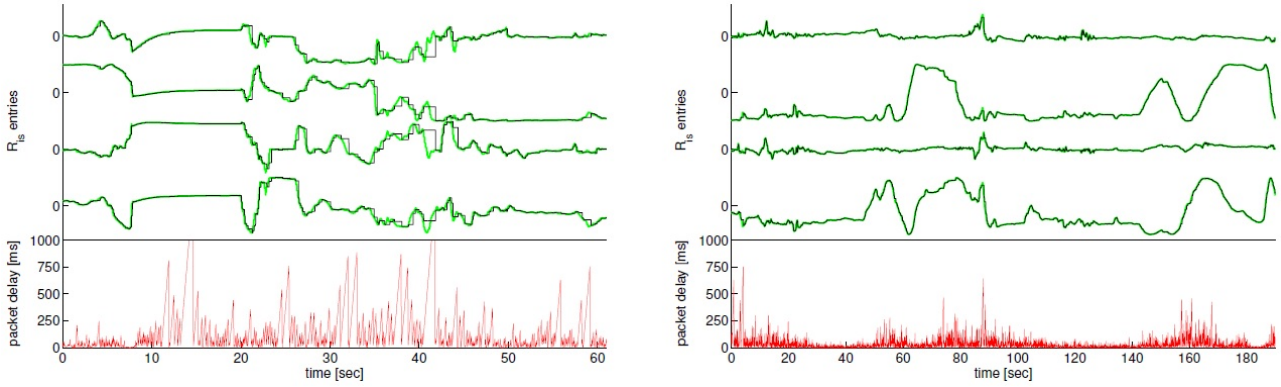

Figure 3.29: Packet delay for two different environmental conditions

Rust and Asada proposed a dual use of visible light to provide positioning plus communication to a robot for nuclear reactor inspection [80]. The positioning system is based on the signal strength and an estimation of the angle based on a photodiode array at the gateway station. Furthermore, incoming data from the ROV's IMU is used to filter the estimations. The system has not been tested in an real scenario, but has only been treated under simulations. The use of UWOC in a heavy water environment has not been reported yet, and possible the extinction coefficient would be different from the distilled water estimations present in the literature. In addition, effects such as Cherenkov radiation must be taken into account as background noise terms if a minimum link quality is intended to be provided.

Bowen et al. implemented an untethered ROV based on a hybrid optoacoustical approach [81]. The need of high bandwidth and low latency for ROV manipulation makes optical communication the best alternative. In this work, the communications system of a Nereus ROV was modified to include an optical subsystem. Although the uplink was implement with the ultrasonic modem, a TDMA half-duplex access protocol was proposed to eliminate the necessity of the acoustic part, which adds a significant latency to the system.

In [82], Han et al. evaluated through simulation the performance, in terms of energy efficiency and throughput, a hybrid optical-acoustical system for AUV communications and positions, as it is usual in the literature. The proposed scheme does not provide a significant enhancement of the throughput respect to the lower energy efficiency due to the use of the acoustic part. Regarding positioning, optical-based systems are not addressed, and the

technological review of the paper only cites a work made by Liu et al. [83] where the location was performed by acoustic trilateration.

Sun et al. presented in [84] the results of an experiment based on an UWOC laser-based link. The laser was continuous-wave driven at 50 mW and the modulation was carried out using a crystal after a polarizer. The receiver, which was at a distance of 5 meters, was PMT-based. The evaluation consisted in transmitting a high-speed RS232 signal. The maximum achieved bandwidth was almost 4 MHz with an associated BER of $3 \cdot 10^{-6}$. The authors propose the system to be mounted into a ROV, but the signal generation strategy is quite inefficient, whilst the misalignment or maximum expected link range are not discussed.

The same authors used the latter experimental setup to test the feasibility of an analog video transmission through seawater using laser radiation for AUV [85]. The authors claim that the seawater scattering would affect the color information as it is carried at the high frequencies of a PAL signal, due to the delay spread. As it has been demonstrated several times in the literature, the UWOC channel presents bandwidths much higher than the 5 MHz spectrum associated to a PAL signal, even using LED. In addition, the authors does not take into account the Mach-Zehnder modulator's bandwidth of 5 Mhz, which may interfere into the obtained results.

In [86], Farr et al. carried out a series of experiments communicating a CORK optical underwater node, which was commented in the previous section, and a ROV. The authors obtained an effective data rate of 1 Mbps up to 138 meters, in a vertical link. The emitted optical power of the 470 nm LED array emitter was approximately 20 W. Figure 3.30 depicts the ROV's trajectory, the received optical power and the achieved data rate.

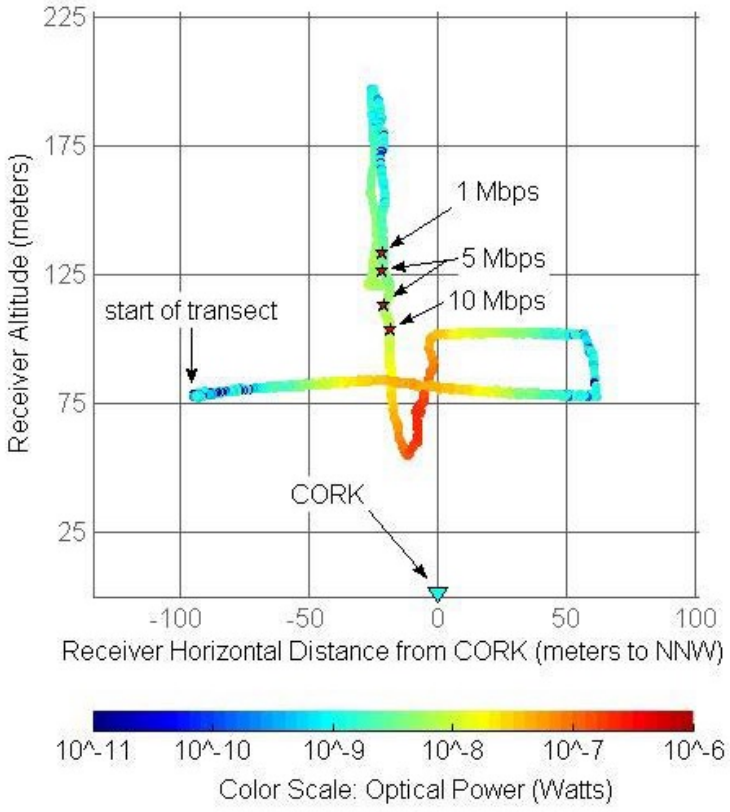

Figure 3.30: Trajectory, data rate and received optical power obtained by Farr et al.

An interesting benchmark comprising RF, acoustic and optical ROV telecommand systems is presented in [87]. Campagnaro et al. try to demonstrate the feasibility of a fully optical telecommand platform for ROV. Figure 3.31 depicts the comparative results of different modems. As it can be seen, both optical and acoustic outperform RF at every operation range.

Moriconi et al. presented in [88] a work addressing the use of a hybrid optical-acoustical approach for underwater swarms. Optical-acoustical systems are a *leit motiv* in the literature, as they highly increase the data rate at medium distances, but allow tracking and low data rate communication at very long distances. This paper makes a thorough analysis of both acoustical and optical channels, but does not introduce any enhancement neither regarding optical communications nor network-layer.

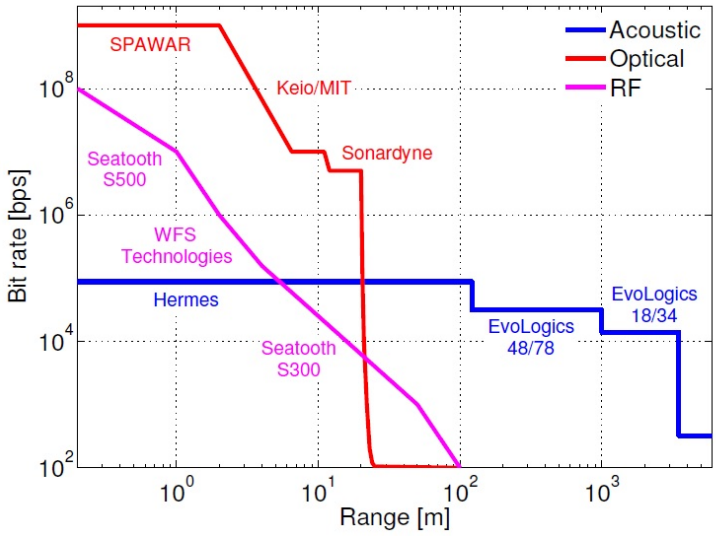

Figure 3.31: Benchmark of the RF, acoustic and optical telecommand systems of 2014.

3.5.4 Other applications

Atmosphere-to-ocean systems are a recurrent topic in literature [89] [90] [91] [92] [93]. Normally, the main idea is to establish a link between an aircraft and an underwater receiver. In this case, plus to the underwater phenomena, the typical FSO effects are also present, turning the communication even more difficult. In this regard, Dong and Quinji presented a work where the impact of different types of environments on the communication were analyzed [94]. Different types of cloud and three distinct kinds of seawater were taken into account. The main conclusion is that the presence of nimbostratus or harbor seawater highly affects communication.

Regarding this kind of links, Stokes et al. proposed in [95] an adaptive data rate controller protocol. The strategy tries to minimize the effect of the clouds and submarine depth on the SER (Symbol Error Ratio), reducing the number of bits per symbol according to an estimation of the SNR. As this systems must act in a closed-loop way, an uplink is needed to update the transmission configuration according to the estimations. This paper does not specify the kind of uplink, but it is of capital importance due to the associated difficulty.

Telerobotic mining was addressed by Baiden and Bissiri in [96]. In this work, the authors expose their recent advances in mining-robot telecommand and telemetry. The actual problem in deep-sea open-pit mining is that only robots can perform such operations. Figure 3.32 depicts a representation of the application scenario, where untethered robots are commanded by an operator using a visible light underwater network.

A work with the same scope was later presented in [97] by Barroso et al. In this paper, the telerobotic mining issue is proposed to be solved using blue LED emitters and OFDM. There are three main contributions in this paper. The first one is the use of IOWCC (Integrated Optical Wireless Communications Circuits) as the modulation base, instead of the traditional tee-based LED arrangement. This kind of systems present higher bandwidths than discrete-component systems. The second one is the implementation of a predistortion in FPGA to compensate the IOWCC frequency response. Finally, the last contribution is based on the use of Wavelength Shift (WS) fibers to fabricate lenses. This type of fiber is doped with fluorescent materials, which absorb high energy (and hence, short wavelength) photons and emit two or more low energy (long wavelength) photons. The correct proportion of these materials in the doped fiber allows the adjustment of the photodiode's incident photons to be in the right wavelength to maximize the optoelectrical conversion. Furthermore, lenses made of WS fibers would be cost-effective as the substrate can be PMMA (plastic fibers).

Hagem et al. performed the experimental evaluation of an IrDA-based swimmer's feedback sensor [98]. This work is the implementation of the proposal presented in [19], which was mentioned in Section 3.1. A similar work was also presented by the same authors in [99].

The same authors implemented an FSK-based UWOC link between a swimmer's wrist and his goggles [100]. The system transmitted the acceleration data of the strokes using an FSK scheme using carriers at 10 KHz and 12 KHz. Unlike the above work, where IR light were used, in this system, a green emission is used to minimize the absorption of the medium.

SDR (Software Defined Radio) was tested by Cox et al. in [101]. The authors proved the feasibility of both LED and laser-based systems in an experimental setup. Several tests were performed using simplex and duplex configurations. The use of laser increments the link's performance due to the higher bandwidth and the absence of misalignment. The authors describe a discrepancy between Beer-Lambert's predictions and the actual measured power. An exponential fit is proposed in order to include effects such as receiver's aperture into the prediction.

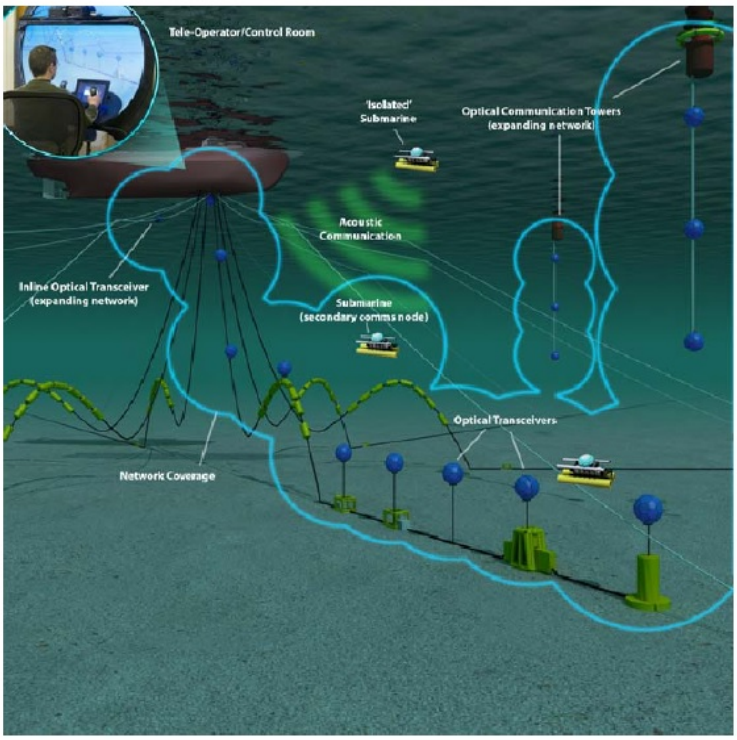

Figure 3.32: Concept of the Underwater Wireless Optical Network described by Baiden and Bissiri

The obtained fitted expression can be observed at Equation 3.7.

$$P_{rx} = ae^{c(\lambda)\alpha 3.66} \tag{3.7}$$

The 3.66 factor is the distance at which the link was performed. $c(\lambda)$ is the extinction coefficient and α is the correction factor introduced by Cox. There is a lower prediction-error in the laser-based experiments than the LED-based ones. This is due to the lower influence of the different spatial contribution (because of scattering) in the laser tests.

In [102], Mizukoshi et al. reported a 968 Mbps link using an IM/DD-OFDM scheme at 405 nm. The experiment was performed in a 2-meters water tank with clear water using a laser diode and a APD. The OFDM scheme comprises 64 16-QAM subcarriers with power allocation in order to minimize the laser response. This effect can be observed in Figure 3.33. If bit-loading techniques were used, low-frequency subcarriers would be benefited from the better SNR response.

UWOC has been also proposed into a water-type classification procedure. In [103], Szili et al. measured several water types at red, green and blue wavelengths, ranging from 30 cm to 60 cm and obtaining a fitted curve. The curve's parameters would serve as the input of a classical classifier. The authors does not perform any validation of the procedure, but to discern between salty water and mineral water, the obtained parameters should suffice.

Lu et al. evaluated in [104] the use of semiconductor lasers in UWOC. The experiments were carried out in tap-water-filled tank of 30 cm of length, and the results does not vary significantly from the obtained in air, as it is expected.

3.5.5 Summary

Figure 3.34 summarizes the experimental results available in the literature. The results are plotted as points in a plane whose axes are best-obtained range and highest data rate.The markers' inner color is related to the emitted wavelength, whilst their shape and outer color are related to the source type (LED or laser) and the used modulation scheme respectively. Farr et al. performed the longest link in an actual scenario, whilst Mizukoshi et al. obtained an almost-Gbps link using OFDM in a laboratory experimental setup. It must be taken into account that only Doniec et al. [78], Barroso et al. [97] and Farr et al. [86] performed their experiments in a real scenario.

3.6 Existing surveys

Several authors have published different surveys commenting the advances and challenges in UWOC. Due to the novelty of the topic, the contributions have not covered a wide enough time span. In this section, some contributions

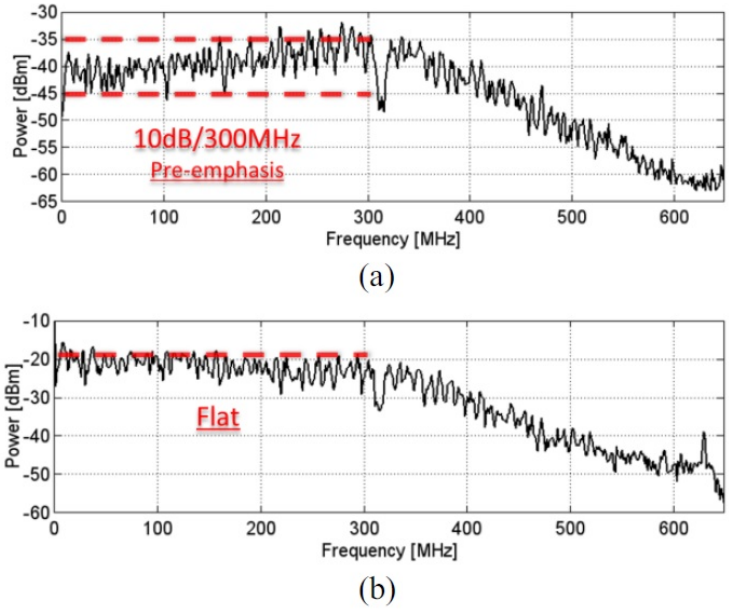

Figure 3.33: Power allocation scheme used to compensate the laser diode response.

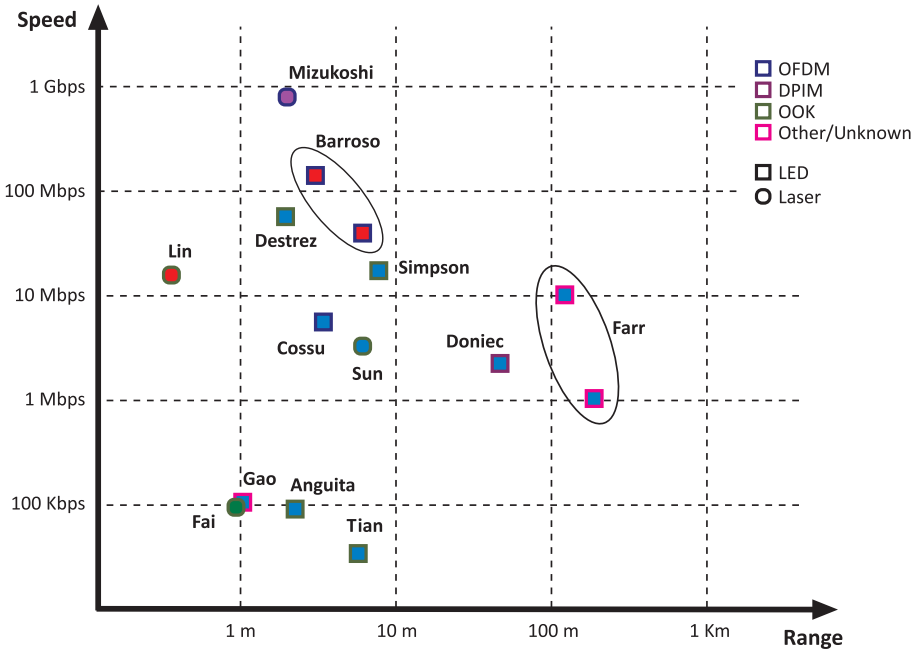

Figure 3.34: Summary of the application results in the literature expressed in a speed-range basis

are analyzed.

In 2005, Giles and Bankman studied the basic considerations of UWOC link designing in [105]. The main equations regarding RTT were exposed and the implications of the use of different light sources and received were also treated.

Anguita et al. analyzed in [106] the challenges and advances in their optical UWSN framework. The authors propose the use of the IrDA PHY layer to transmit the data from the upper layers. Furthermore, as the majority of authors, Anguita et al. focused on emissions at 420 nm. This paper is a melting pot of the contributions made in [62],[63] and [64].

Advances in environmental monitoring were presented in [107] by Camilli et al. The authors expose the necessity of reducing the power budgets due to the limited endurance of batteries, attending to an economical criterion. The cost of Watt per hour ranges from $10 to $100, considering replacement and recovery operations. Therefore, introducing energy-efficient strategies is mandatory.

A brief analysis of the state-of-the-art ROV technology was also performed. As the endurance of batteries is of high interest in order to enhance the duration of ROV missions, a very interesting solution is proposed.

In a data muling scenario, AUVs gather data from the network and transport the huge amounts of information to the base station at the surface. To increment the duration of the mission, each UWSN node may act as an information producer and as a wireless charging station. This proposal is directly opposite to the costs claim commented above, but it would be only feasible if efficient energy harvesting techniques were investigated. Currently, low-speed hydrokinetic turbines are under research and are a promising alternative to harvest energy in UWSN deployments [108].

Hagem et al. performed a review in UWOC, oriented to provide swimmer's feedback [109]. The review is focused on providing comments regarding physical-layer aspects (modulations, emitters and receivers). Furthermore, the analysis also offered a brief summary of different experimental evaluations available in the literature.

In [110], Johnson et al. presented a survey on UWOC channel modeling. Propagation of light in the underwater medium may be described by the RTT equation. Different kinds of solutions have been proposed in the literature, ranging from analytical solutions to different types of numerical approximations. Although all the common approximations work well for homogeneous media, there are different effects that occur in the real world which are not normally included in the simulation frameworks. For instance, the composition variability in terms of suspended matter (chlorophyll, particles, etcetera) includes heterogeneity in the medium, and may notably affect to the expected output. Moreover, large scale refractive-index changes are not taken into account when simulating vertical links, whilst the beam-steering effect produced by the differences of pressure, salinity and temperature may imply fading-affected situations.

Khalighi et al. addressed the remaining challenges in UWOC [111]. Channel modeling of horizontal links is one of the most studied topics in UWOC, but vertical links have not been treated the same way. Furthermore, turbulence modeling is an open topic and may be introduced in the study of shallow water environments. Other two aspects that remain almost unexplored are energy-efficient encodings and modulations, and misalignment-mitigation techniques.

3.7 Remaining challenges

After performing a profound analysis of the current state-of-the-art research, several conclusions may be extracted. First of all, there is a lack of contributions regarding energy efficiency in UWSN. This kind of architectures normally comprise battery-powered autonomous nodes, whose substitution is commonly prohibitively expensive. These contributions can be made at three different levels: physical, access and network layer.

- Energy-efficient network layer proposals are already present in the literature. Multihop network topologies need several optical interfaces and the discovery procedures are usually very power-demanding, but are the only solution when the main node does not have the possibility of conforming a star-like connectivity, which is the most addressed topology in the literature.

- UWOC MAC layer uses normally a TDMA scheme in the uplink to establish communication between the deployed nodes and the main node, which is normally an AUV, a ROV or a tethered transceiver. SDMA has been proposed too, sectorizing the transceivers using hemispherical arrangements, reducing the emitted power by the number of sectors. Finally, CDMA has been also proposed joint to power control algorithms. Nonetheless, this kind of medium access is power-demanding and in highly-populated networks, the effective SINR may notably decrement the link's quality. Regarding power control algorithms, there are few contributions in this regard. Nevertheless, the use of this type of techniques seems straightforward and the power-saving possibilities are high enough to take this into consideration.

- Different encodings and modulations has been proposed in UWOC. PPM-based encodings, such as M-PPM and DPIM, are the most extended due to their high energy efficiency. In the VLC literature, OFDM is presented as an efficient alternative to transmit data. Nevertheless, the computing requirements, the synchronization difficulty and the poor efficiency of linear LED (or laser) drivers, reduce its application to systems where power sources are not an issue, which is not the case of UWOC. The use of wavelength-selectable transceivers is a very interesting option for systems where there is certain distance variance, as well as the use of WS fibers to enhance the system's sensitivity.

The mathematical background of UWOC has been widely studied, but there is a weakness in channel performance prediction. There are accurate horizontal-link simulators, but does not exist an affordable stochastic model. There are not studies addressing the relationship between the channel's parameters (geometry and medium) and the expected performance of the link. Furthermore, vertical links are the main scenario in UWOC applications, and there is a need of mathematical analysis in this regard.

Finally, the cost-efficiency of the systems is normally not analyzed. The fact of introducing an optical transceiver has a direct impact on the initial costs, but has also a positive counterpart in the lifespan of the nodes. This enhancement must be analyzed in terms of *a priori* costs, lifespan, link's performance, etcetera.

Chapter 4

Impulse Response of the Underwater Wireless Optical Channel

The impulse response of a linear and invariant system defines the frequency response of a system. However, UWOC is not an invariant channel precisely, but a very variant one, whose variance depends on the characteristics of the surrounding medium. Although variant channels are characterized in statistical terms (Delay spread and Doppler spread generally), a simulation procedure to obtain statistically independent realizations of the underneath stochastic process is presented. These realizations would serve as input in a statistical-inference engine in an effort to obtain the distributions of the power delay profile and the Doppler spread profile. Chapters 6 and 7 will take into account the whole randomness of the impulse response.

Propagation of light underwater is a specific case of radiative transfer. Normally, this medium is considered homogeneous for simplicity, but in the simplest approximation, its homogeneousness is statistical. Particles are not structured in a crystalline network within seawater, but are randomly distributed following a 3D uniform distribution. This approximation does not takes into account neither the possible flocculation of algae nor the effects of turbulences in the particle distribution. Nevertheless, this approximation is still valid for channel modeling purposes, whilst these mentioned effects can be introduced as stochastic phenomena superposed to the main distribution. The next sections would introduce Radiative Transfer Theory, the underwater phenomena that affect UWOC links, Monte Carlo integration and the simulation procedure proposed in this work. Finally, several results are obtained and a parallelization of the algorithm is also commented.

4.1 Radiative Transfer Theory

Radiative transfer theory states the mathematical background of radiation propagation in absorbing and dispersive media. The first works in this regard were performed by Lord Rayleigh in 1871 on the illumination and polarization of the sunlit sky. Nonetheless, the governing equations had to wait three quarters of century for their formulation and solution. This subject has been principally investigated by astrophysicist, but in the late 60's, this problem caught the attention of particle physicists, since the same problems arise in the theory of neutron diffusion. In UWOC, this theory has also an important role regarding channel modeling, as the underwater medium can be considered as an absorbing and dispersive medium.

The equation of transfer [112] for isotropic media and parallel propagation in the z-axis is:

$$\frac{\cos\theta}{\kappa(\omega)\rho}\frac{\mathrm{d}I(\omega,z,\theta,t)}{\mathrm{d}z} = I(\omega,z,\theta,t) - \mathfrak{I}(\omega,z,\theta,t) \tag{4.1}$$

Where $\kappa(\omega)$ is the mass scattering coefficient at frequency ω, ρ is the density of the medium, $I(\omega,z,\theta,t)$ is the intensity of radiation at distance z and direction defined by θ. Finally, $\mathfrak{I}$ is the source function, which has the form:

$$\mathfrak{I}(\omega,z,\theta,t) = \frac{1}{2}\int_0^{\pi} p\left(\theta,\theta'\right) I(\omega,z,\theta',t)\sin\theta'\mathrm{d}\theta' \tag{4.2}$$

Note that the latter expression is the result of an integration respect to the azimuthal component. Due to the symmetry of the problem, this simplification is straightforward. $p(\theta,\theta')$ is the scattering phase function, which will be described in detail in the following sections. Simplifying, this function defines how a medium spatially disperses light.

Equation 4.1 is an integro-differential equation, whose analytical solution is conditioned by the existence of a simple algebraic formula of the scattering phase function. In astrophysics, this phase functions takes normally simple forms to allow an easy integration. Nonetheless, in UWOC, this phase functions would depend on the

submerged particles within the medium, and only numerical solutions are feasible. The Schuster-Schwarzschild approximation [113] proposes the division of Equation 4.1 into two main streams (inward and outward directions), but this algebraic artifact can be generalized into $2n$ directions as follows:

$$\frac{\cos\theta_i}{\kappa(\omega)\rho}\frac{\mathrm{d}I(\omega,z,\theta_i,t)}{\mathrm{d}z} = I(\omega,z,\theta_i,t) - \frac{1}{2}\sum_j a_j p(\cos\theta_i,\cos\theta_j) I(\omega,z,\cos\theta_j,t) \quad /i = \pm 1,...,\pm n \tag{4.3}$$

a_j is the j-th Gauss-Legendre quadrature weight. This last simplification is valid for any $\mathcal{C}^{(1)}$ phase function which can be expressed as a (2n-1)-order polynomial. This system of linear differential equations can be easily solved numerically. Nonetheless, the accuracy of the solution depends on the number of directions involved in the calculation. Furthermore, the division using the Gauss-Legendre quadrature can be reformulated using other type of numerical scheme, for instance, Monte Carlo. This integration scheme will be discussed during Section 4.3.

4.2 Channel characteristics

The RTE defines the propagation of EM waves through spatially-dispersive media. Seawater is conformed by molecules of water and a mixture of biological matter (phytoplankton in the vast majority) and dissolved salts. Depending on the concentration of each type of additive, the effects on the propagation differ. The following subsections comment each effect separately.

4.2.1 Absorption

Absorption is a wavelength-dependent process where electromagnetic energy is converted into other types of energy, typically heat or chemical. It is of capital importance because it defines the decay of the propagating energy through seawater, and hence, has a direct impact on the amount of photons that arrive the receiver. Since seawater is a mixture of different elements apart from pure seawater, the overall absorption can be expressed as a sum of partial absorptive contributions (Equation 4.4).

$$a(\lambda) = \sum_{i=1}^{N} C_i a_i(\lambda) \tag{4.4}$$

Generally, the considered absorptive contributions are: pure seawater ($\alpha_w(\lambda)$), phytoplankton ($\alpha_\phi(\lambda)$), gelbstoff ($\alpha_g(\lambda)$, decaying organic matter) and non-algal matter ($\alpha_n(\lambda)$). Figure 4.1 depicts the spectral response of these components.

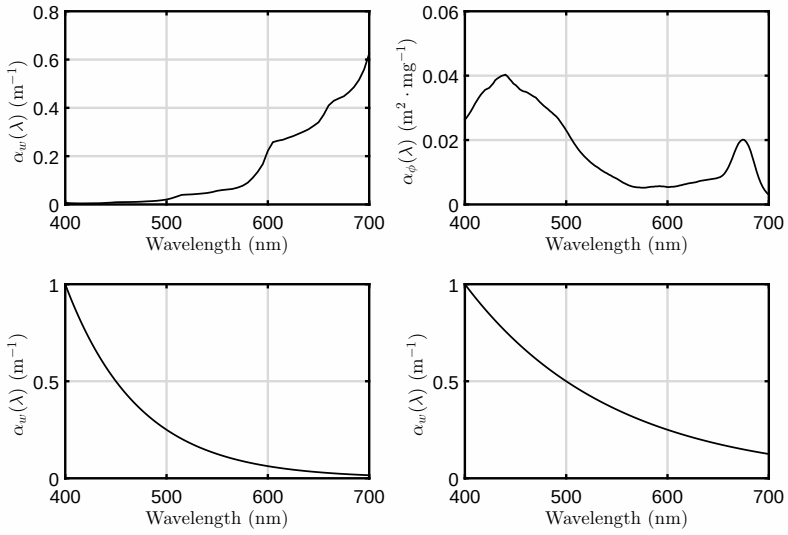

Figure 4.1: Absorption spectra of each element that conform seawater. Seawater (NW - [114]), Phytoplankton (NE - [115]), Gelbstoff (SW - [116]) and Non-algal matter (SE - [117])

The concentration of each of the components conform the overall absorption spectrum. Figure 4.2 depicts an example of absorption spectra for open ocean and coastal waters.

It must be taken into account that the relative concentrations are depth dependent, as Johson et al. studied in [29]. This fact has a direct impact on the design of vertical links, where the light rays cross different concentration

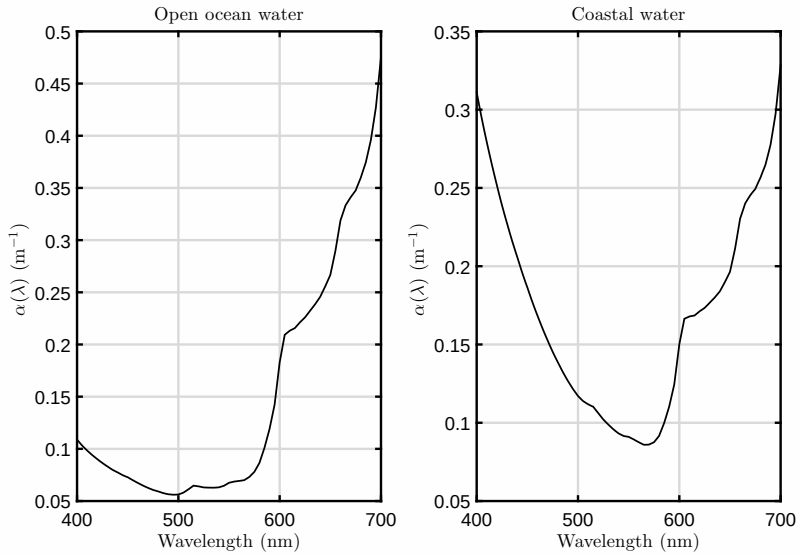

Figure 4.2: Absorption spectra of open ocean (left) and coastal water (right).

layers. Finally, Haltrin [118] derived a model describing the absorption in terms of a single parameters, chlorophyll concentration, C_ϕ. Equation 4.5 illustrates the expression.

$$\alpha(\lambda) = \alpha_w(\lambda) + \alpha_\phi(\lambda)\left(\frac{C_\phi}{C_\phi^*}\right)^{0.6} + \alpha_f(\lambda)C_f e^{-k_f\lambda} + a_h(\lambda)C_h e^{-k_h\lambda} \tag{4.5}$$

$C_\phi^* = 1\,\mathrm{mg}\cdot\mathrm{m}^{-3}$. $\alpha_\phi(\lambda)$, $\alpha_f(\lambda)$ and $\alpha_h(\lambda)$ are the phytoplankton, fulvic acid and humic acid absorption spectra respectively. C_f and C_h are the fulvic and humic acid concentrations, and k_f and k_h their spectral decaying constants.

4.2.2 Scattering

Scattering is a physical process in which energy is spatially dispersed due to light-matter interaction. Figure 4.3 illustrates this phenomenon.

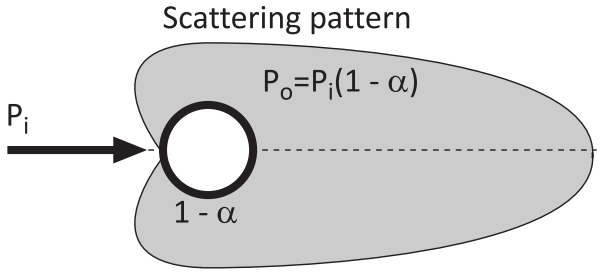

Figure 4.3: Representation of the scattering phenomenon

Depending on the relative size of the scattering centers, different approaches may be used to model the phenomenon. The relative size of a particle, a, is the relationship between its diameter and the wavelength of interest (Equation 4.6). D is the diameter of the particle, λ the wavelength in vacuum and n_w the refractive index of the surrounding medium.

$$a = \pi\frac{Dn_w}{\lambda} \tag{4.6}$$

For very small relative sizes ($a << 1$), Rayleigh scattering is used to model this phenomenon. For near unitary relative sizes ($a \approx 1$), Mie's approximation of Maxwell's equations is used to describe scattering. Finally, very high relative sizes ($a >> 1$) produce very small scattering effects and their behavior can be explained by geometric optics.

In this work, since the scattering centers are usually conformed by phytoplankton, and the wavelengths of interest are next to the size of these particles, only Mie scattering is going to be considered.

Mie scattering

Mie's theory is the most general solution to the elastic scattering problem. Its applicability ranges from Rayleigh's approximation for small particles to geometric optics on the limit, but is limited to spherical particles. However, the spherical assumption is not a problem regarding the error bias it may produce in a communications estimation problem.

Lets consider a spherical particle of diameter D and refractive index $m = n_r - j\kappa$. The imaginary part of the refractive index is related to the absorption coefficient of the material ($a_{mat}(\lambda)$) through Equation 4.7.

$$\alpha_{mat}(\lambda) = \frac{4\pi\kappa}{\lambda} \tag{4.7}$$

Although Mie's theory defines the scattering process taking into account the polarization state, and since this work is oriented to the use of unpolarized radiation (LED emissions), this introductory formulation is presented in its horizontal-vertical averaged version. In a spherical coordinate system, the relationship between the scattered intensity and the incident intensity after scattering, is related to a function $\sigma'_{scat}(\theta)$ as shows Equation 4.8.

$$I_{scat}(\theta) = I_0 \frac{\sigma'_{scat}(\theta)}{r^2} \tag{4.8}$$

Note that there is no azimuthal (ϕ) dependency as the surrounding medium is isotropic and the incident light is unpolarized. Taking into account the energy transformations involved in the process, the extinction cross section σ_{ext}, the scattering cross section σ_{scat} and the absorption cross section σ_{abs} are related by Equation 4.9.

$$\sigma_{ext} = \sigma_{abs} + \sigma_{scat} \tag{4.9}$$

Furthermore, the differential cross section $\sigma'_{scat}(\theta)$ and the cross section σ_{scat} are related by a integration over 4π steradians. In Mie's equations, the differential cross section can be expressed as a combination of terms. Equation 4.10 starts the mathematical description.

$$\sigma'_{scat}(\theta) = \frac{\lambda^2}{8\pi^2}(i_1 + i_2) \tag{4.10}$$

In this formulation, the intensity functions are calculated from an infinite series given by:

$$\begin{aligned} i_1 &= \left| \sum_{n=1}^{\infty} \frac{2n+1}{n(n+1)} \left[a_n \pi_n(\cos\theta) + b_n \tau_n(\cos\theta) \right] \right|^2 \\ i_2 &= \left| \sum_{n=1}^{\infty} \frac{2n+1}{n(n+1)} \left[a_n \tau_n(\cos\theta) + b_n \pi_n(\cos\theta) \right] \right|^2 \end{aligned} \tag{4.11}$$

The angular dependent functions π_n and τ_n of Equation set 4.11 are expressed in terms of the Legendre polynomials by:

$$\begin{aligned} \pi_n(\cos\theta) &= \frac{P_n^{(1)}(\cos\theta)}{\sin\theta} \\ \tau_n(\cos\theta) &= \frac{\mathrm{d}P_n^{(1)}(\cos\theta)}{\mathrm{d}\theta} \end{aligned} \tag{4.12}$$

Finally, the parameters a_n and b_n are defined in terms of the Ricatti-Bessel functions Ψ and ξ as shows Equation set 4.13.

$$\begin{aligned} a_n &= \frac{\Psi_n(a)\Psi'_n(ma) - m\Psi_n(ma)\Psi'_n(a)}{\xi_n(a)\Psi'_n(ma) - m\Psi_n(ma)\xi'_n(a)} \\ b_n &= \frac{m\Psi_n(a)\Psi'_n(ma) - \Psi_n(ma)\Psi'_n(a)}{m\xi_n(a)\Psi'_n(ma) - \Psi_n(ma)\xi'_n(a)} \end{aligned} \tag{4.13}$$

Finally, after integrating the differential scattering cross section over the sphere, the resulting scattering cross section may be expressed as:

$$\sigma_{scat} = \frac{\lambda^2}{2\pi} \sum_{n=0}^{\infty} (2n+1) \left(|a_n|^2 + |b_n|^2 \right) \tag{4.14}$$

The above equations express the angular dependence of scattering and hence, the volume scattering function. As it was commented, this function only depends on elevation and has revolution symmetry for spherical particles immersed in an isotropic medium such as seawater. Figure 4.4 depicts the phase function of a particle for a given wavelength and refractive index.

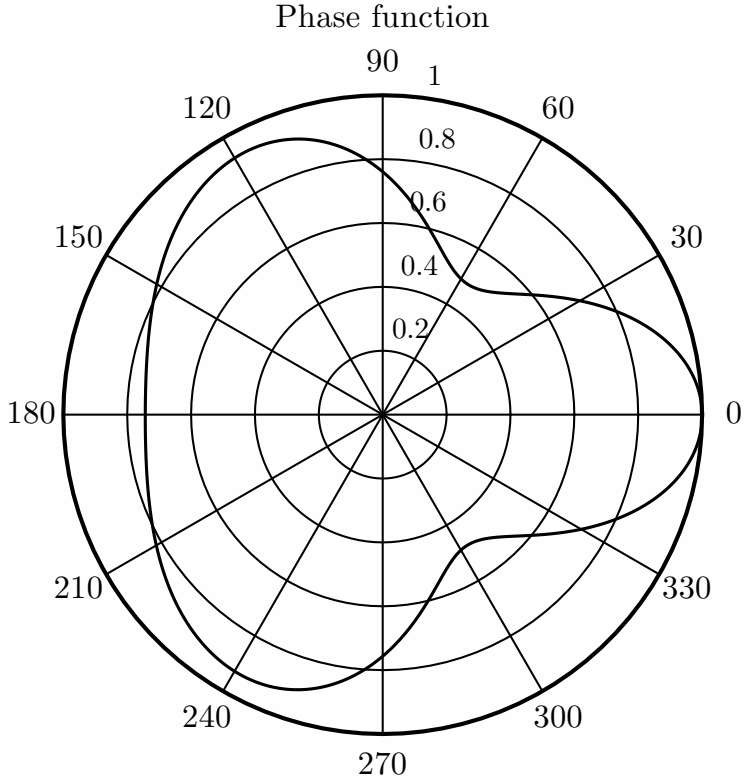

Figure 4.4: Phase function of a Mie scattering for a particle with unitary normalized size

Volume Scattering Function

The volume scattering function is the differential scattering cross section per unit volume. Using the above nomenclature, the VSF $\beta(\theta, \lambda)$ can be expressed as the volume derivative of the scattered intensity, respect to the incident intensity per unit area.

$$\beta(\theta, \lambda) = \frac{\mathrm{d}I_{scat}(\theta, \lambda)}{E_i(\lambda)\mathrm{d}V} \tag{4.15}$$

Where $E_i(\lambda)$ is the incident irradiance. This function is important because it takes into consideration the particle concentration of the medium and integrating it over all direction yields the scattering coefficient $b(\lambda)$. This coefficient and the absorption coefficient presented above conform the overall extinction coefficient as:

$$\begin{aligned} c(\lambda) &= a(\lambda) + b(\lambda) \\ b(\lambda) &= 2\pi \int_0^{\pi/2} \beta(\theta, \lambda) \sin\theta \, \mathrm{d}\theta \end{aligned} \tag{4.16}$$

The VSF can be rewritten as the product of the scattering coefficient $\beta(\lambda)$ and a phase function $\tilde{\beta}(\theta, \lambda)$ which defines the angular distribution of the scattered radiation. This phase function can be characterized by the asymmetry parameter g or mean cosine, which is the average of the cosine of the scattering angle over all scattering directions (Equation 4.17).

$$g = 2\pi \int_0^{\pi} \tilde{\beta}(\theta, \lambda) \cos\theta \, \sin\theta \, \mathrm{d}\theta \tag{4.17}$$

This parameter models the "shape" of the phase function and has been widely used in simulation schemes through the Henyey-Greenstein approximation as it was commented in Chapter 3. This approximation of phase

functions is not able to model the "peaky" nature of Mie's scattering for relative sizes near to one. In addition, Zhao and Sun demonstrated in [38] the poor accuracy of this approximation. Nonetheless, several authors use Henyey-Greenstein function (Equation 3.3) because its integral has inverse and can be used in a closed form to generate random directions in a Monte Carlo integration scheme.

4.2.3 Refractive Index

The refractive index of a material is the relationship between the speed of light in it, respect to the speed of light in vacuum. This parameter defines the delay of communication, and also has an important role in the behavior of reflections (Snell's law) and turbulences. Generally, the refractive index of seawater, noted by n_w, depends on temperature, salinity and wavelength. The wavelength-dependence implies chromatic dispersion, but due to the use of monochromatic sources and the reduced range of UWOC links, this effect can be neglected. Actually, this effect can be neglected even if wideband emitters, such as YB-WLED, were used, due to the effect of absorption. Several authors have empirically fitted this dependence after performing different measurements. McNeil [119], in Equation 4.18, and Matthäus [120], in Equation 4.19, performed two different attempts to obtain a mathematical expression of the refractive index of seawater within the visible spectrum.

$$n_w(\lambda, S, T) = 1.3247 - 2.5 \cdot 10^{-6} T^2 + S\left(2 \cdot 10^{-4} - 8 \cdot 10^{-7} T\right) + \frac{3300}{\lambda^2} - \frac{3.2 \cdot 10^7}{\lambda^4} \tag{4.18}$$

$$\begin{aligned} n_w(\lambda, S, T) =& 1.447824 + 3.011 \cdot 10^{-4} S - 1.8029 \cdot 10^{-5} T - 1.6916 \cdot 10^{-6} T^2 - 0.489\lambda + 0.728\lambda^2 - 0.384\lambda^3 - \\ & S\left(7.9362 \cdot 10^{-7} T - 8.06 \cdot 10^{-9} T^2 + 4.249 \cdot 10^{-4}\lambda - 5.847 \cdot 10^{-4}\lambda^2 + 2.812 \cdot 10^{-4}\lambda^3\right) \end{aligned} \tag{4.19}$$

Temperature T is in Celsius degrees, salinity S is in ‰, and the wavelength in micrometers. Figure 4.5 depicts the refractive index of seawater at 15° and 30 ‰ of salinity for each wavelength. From the above equations , it can be observed that the refractive index of seawater is more sensitive to salinity than to temperature fluctuations.

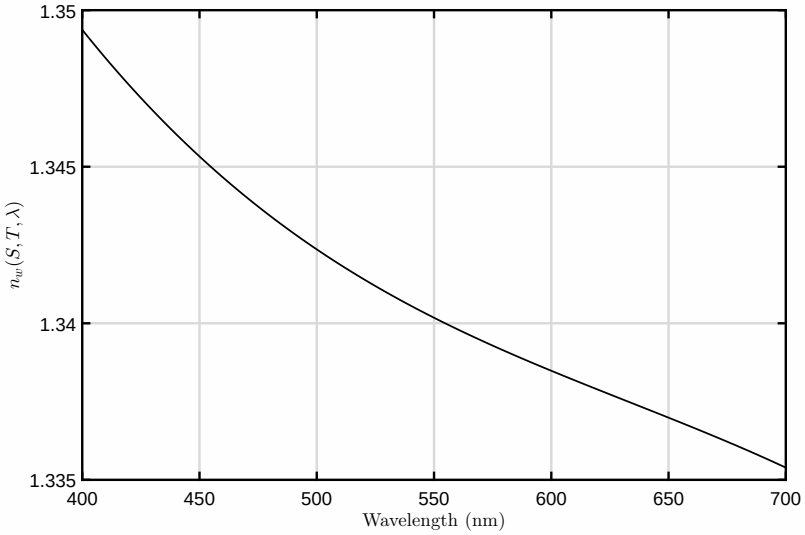

Figure 4.5: Refractive index vs wavelength for seawater at 15° and 30 ‰ of salinity

Johnson et al. studied the relationship between depth and refractive index in order to estimate the expected bending of the light rays [121], and its effect regarding the pointing between emitter and receiver. However, this estimation departs from a unrealistic hypothesis, since it considers a stratified scenario regarding refractive index. This assumption directly implies an also stratified distribution of temperature and salinity, whilst an actual scenario cannot be considered as a laminar perfectly-separable scenario. Regardless this physical unrealism, due to the lack of literature analyzing this issue, their approximation may be considered as a valid starting point.

4.2.4 Turbulences

Optical turbulence is a rapid change of the seawater's refractive index. These sharp changes may occur at any depth, and are normally attributed to temperature variations. Unlike turbulences in FSO, the power spectrum of the refractive index depends on both temperature and salinity. Therefore, the traditional Kolmogorov power

spectrum may present errors modeling turbulences in oceanic environments, as Tang et al. stated in [46]. After introducing the effect of salinity, it yields the power spectrum proposed by Nikishov et al. [122]:

$$\Phi(\kappa) = C_0 \epsilon^{-1/3} \kappa^{-11/3} \frac{\chi_T}{\omega^2} \left[1 + 2.35(\kappa\eta)^{2/3}\right] \phi(\kappa) \tag{4.20}$$

$C_0 = 3.88 \cdot 10^{-9}$,ϵ is the dissipation rate of turbulent kinetic energy per unit mass and ranges from 10^{-8} to $10^{-2}\, m^2 s^{-3}$, and χ_T is the rate of mean-square temperature dissipation ranging from 10^{-10} to $10^{-4} K^2 s^{-1}$. These constants and ranges are based on the measurements provided by Korotkova et al. [123]. κ is the scalar spatial frequency, $\eta = 10^{-3}$ is Kolmogorov's micro-scale and ω is a parameter that defines the dominance of the turbulence respect to salinity (ω near to 0) or temperature (ω near to -5). Finally, $\phi(\kappa)$ is a function of the form presented in Equation 4.21.

$$\phi(\kappa) = \omega^2 e^{-A_T \delta} + e^{-A_S \delta} - 2\omega e^{-A_{TS} \delta} \tag{4.21}$$

$A_S = 1.9 \cdot 10^{-4}$, $A_T = 1.863 \cdot 10^{-2}$ and $A_{TS} = 9.41 \cdot 10^{-3}$. $\delta = 8.284(\kappa\eta)^{4/3} + 12.978(\kappa\eta)^2$. After numerically solving this equation for a general case ($\omega = -2$), the resulting power spectrum presents two peaks which are related to temperature and salinity fluctuations (Figure 4.6).

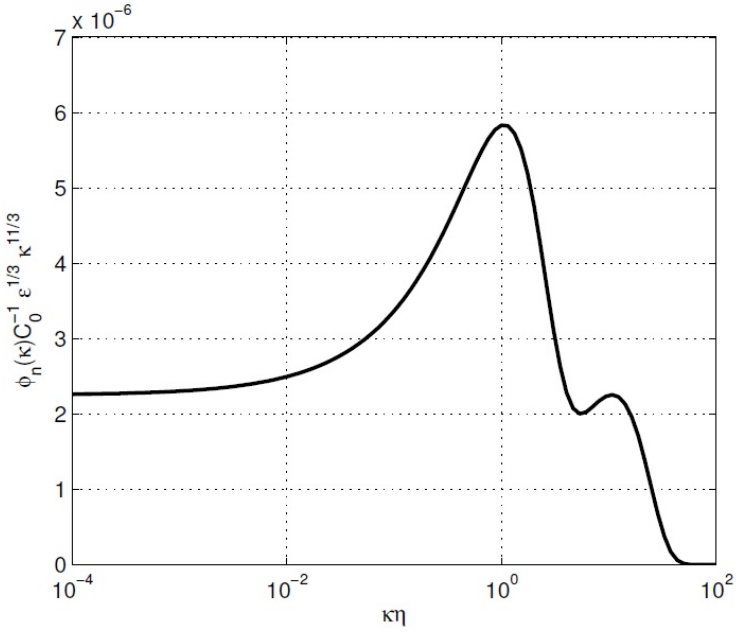

Figure 4.6: Turbulence power spectrum obtained by Tang et al. [46] for $\omega = -2$

As it can be observed, the oceanic turbulence power spectrum is very different from Kolmogorov's $-11/3$ power law used in FSO. There are two main aspects of interest regarding turbulence analysis in communications. The first one is the turbulence variance related to the link's range (Rytov's variance σ_I^2), and the second one is the temporal correlation.

Rytov's variance, also known as scintillation index, was studied by Farwell in his PhD dissertation [124]. Farwell concluded that for gaussian-like laser emissions, the scintillation index takes the form presented in Equation set 4.22.

$$\begin{aligned}
\sigma_I^2(r, L) =& \sigma_{I,l}^2(0, L) + \sigma_{I,l}^2(r, L) \\
\sigma_{I,l}^2(0, L) =& 8\pi^2 k^2 L \int_0^1 \int_0^\infty \kappa \Phi(\kappa) \exp\left[-\frac{\Lambda L \kappa^2 \xi^2}{k}\right] \left[1 - \cos\left(\frac{L\kappa^2}{k} \xi \left(1 - \xi(1 - \Theta)\right)\right)\right] \mathrm{d}\kappa \mathrm{d}\xi \\
\sigma_{I,l}^2(r, L) =& 8\pi^2 k^2 L \int_0^1 \int_0^\infty \kappa \Phi(\kappa) \exp\left[-\frac{\Lambda L \kappa^2 \xi^2}{k}\right] [I_0(2\Lambda r \xi \kappa) - 1] \mathrm{d}\kappa \mathrm{d}\xi
\end{aligned} \tag{4.22}$$

$\xi = 1 - \frac{z}{L}$ is a normalized distance variable and k the wavenumber. $I_0(x)$ is the zeroth order modified Bessel function whilst Λ and Θ are the output plane parameters. For an incident plane wave, these last parameters are 0 and 1 respectively. Introducing this condition into Equation 4.22, it yields:

$$\sigma_I^2(L) = 8\pi^2 k^2 L \left(\int_0^\infty \kappa \Phi(\kappa) \mathrm{d}\kappa - \int_0^1 \int_0^\infty \kappa \Phi(\kappa) \cos\left(\frac{L\kappa^2}{k} \xi\right) \mathrm{d}\kappa \mathrm{d}\xi \right) \tag{4.23}$$

Farwell left the analysis at this point, but taking into account the shape of the sinc in the second term, the integral may be approximated to the first root of the sinc, hence:

$$\sigma_I^2(L) \approx 8\pi^2 k^2 L \int_{\sqrt{\pi\frac{k}{L}}}^{\infty} \kappa\Phi(\kappa)\mathrm{d}\kappa \tag{4.24}$$

To obtain an approximation of the scintillation index, the integrals resulting of the product $\kappa\Phi(\kappa)$ are of the form shown at Equation 4.26. Depending on the condition of Equation 4.25, δ can be approximated to the squared term or to the 4/3 power. These two approximations could be applied depending on the shape of the $\kappa\Phi(\kappa)$ product. In the end, the approximations define an upper and a lower bound to the power dependence of the scintillation index.

$$\delta \approx \begin{cases} 12.978(\kappa\eta)^2 & / \kappa\eta > 9.12 \\ 8.284(\kappa\eta)^{4/3} & / \kappa\eta < 1.3 \cdot 10^{-5} \\ 8.284(\kappa\eta)^{4/3} + 12.978(\kappa\eta)^2 & / \text{otherwise} \end{cases} \tag{4.25}$$

$$\int_{\sqrt{\pi\frac{k}{L}}}^{\infty} \kappa^{-a} e^{-b\kappa^c}\mathrm{d}\kappa = \frac{b^{\frac{a-1}{c}}}{c}\Gamma\left(\frac{1-a}{c}, b\left(\pi k\right)^{c/2} L^{-c/2}\right) \tag{4.26}$$

Where $\Gamma(s,x)$ is the upper incomplete Gamma function, and $\Gamma(s,x) = (s-1)\Gamma(s-1,x) + x^{s-1}e^{-x}$. Taking into account the decaying nature of the exponentials involved in the latter expressions, the Rytov's variance of the ocean turbulent channel would directly depend on the higher power of the link's range L. Taking into account the approximations made in Equation 4.25, the dependence of the scintillation index respect to the link's range can be approximated to:

$$\sigma_I^2(L) \propto L^{\alpha} \quad /\alpha \in (3/2, 11/6) \tag{4.27}$$

After imposing Taylor's frozen turbulence hypothesis, which implies that the temporal statistics are related to the spatial statistics, Tang et al. analyzed the temporal correlation of a laser-based emission under weak turbulence regime. They obtained that the correlation is almost independent on the link's distance, whilst is highly dependent on the speed of seawater.

These formulae were obtained considering plane wave propagation, coherent radiation and neglecting the effect of scattering. If scattering were considered, the correlation between points would change due to the BSF. Furthermore, if the radiation were non-coherent, such as LED, Rytov's variance would be dramatically reduced since interference effects would not occur. Furthermore, collimated and coherent emissions would suffer from beam wander with a higher probability, whilst LED emissions not.

4.2.5 Surface reflections

The ocean surface can be modeled as a superpositions of traveling sea waves, usually modeled by a sea wave spectrum, plus a noisy term which depends on the wind stress. This stress produces a random variation on the seawater's surface, whose PDF follows a Gram-Charlier series as Cox and Munk demonstrated in [21]. The variation of the surface is usually modeled azimuthally uniform, and the variance of the slope depends on the wind speed. The relationship that can be obtained from Cox and Munk's work regarding wind speed is presented in Equation 4.28. Actually, the variance for the crosswind direction and the upwind direction slightly differ, but for the purposes of this work the omnidirectional approximation is valid.

$$\sigma_{surf}^2 = 0.003 + 0.00512 v_{wind} \quad /1 < v_{wind} < 14\mathrm{m}\cdot\mathrm{s}^{-1} \tag{4.28}$$

In an underwater-to-underwater scenario, random surface reflections may introduce delayed additional power contributions in a horizontal link. Figure 4.7 depicts the scenario under consideration. After a reflection, the direction of the output ray $\hat{v}_{ref}$ can be expressed as a linear combination of both surface normal vector $\hat{n}_{surf}$ and incident direction $\hat{v}_i$.

$$\hat{v}_{ref} = \hat{v}_i - 2 < \hat{v}_i, \hat{n}_{surf} > \hat{n}_{surf} \tag{4.29}$$

After the impact, part of the incident power is reflected and part is transmitted. The amount of energy which is reflected, $R_{Fresnel}(\theta_i)$, follows Fresnel's equation (Equation 4.30). Additionally, for incident angles above certain limit (critical angle), there is no transmission of energy and total internal reflection occur. This happens because the light rays travel to a medium with a lower refractive index, in the opposite case, there is no critical angle and always part of the energy is transmitted.

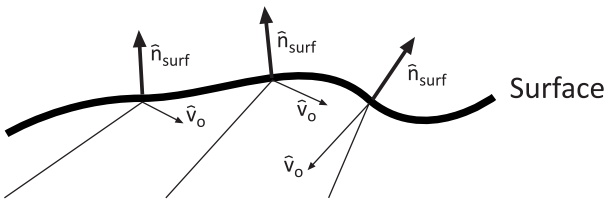

Figure 4.7: Reflection of light rays on the seawater surface

$$R_{Fresnel}(\theta_i) = \frac{1}{2}\left[\left(\frac{\sin(\theta_t - \theta_i)}{\sin(\theta_t + \theta_i)}\right)^2 + \left(\frac{\tan(\theta_t - \theta_i)}{\tan(\theta_t + \theta_i)}\right)^2\right] \tag{4.30}$$

θ_t is the refracted angle, which follows Snell's law $n_{air} \sin\theta_t = n_w \sin\theta_i$.

4.2.6 Seabed diffusion

Diffusive effects are a common phenomenon which is produced due to the scattering of light on a surface. There are many scattering functions which model the diffusion depending on the presence or not of specular components, such as Phong or Torrance. However, as the seabed is normally compound by sand, rock or coral extensions, a Lambertian approximation is a compromise solution. Equation 4.31 shows the reflectivity of a Lambertian scattering, whilst Figure 4.8 depicts the scenario.

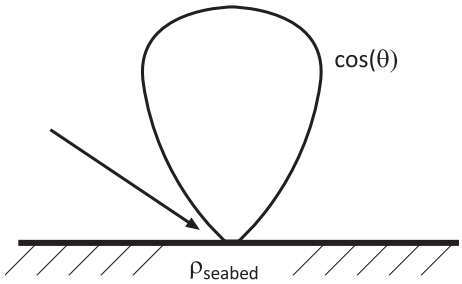

Figure 4.8: Light scattering due to seabed diffusion

$$R_{seabed}(\theta, \theta_i, \rho_{seabed}) = \rho_{seabed} \cdot \cos\theta_i \cdot \cos\theta \tag{4.31}$$

4.2.7 Optical fouling

Optical fouling is the deposition of matter, normally algae and phytoplankton, over the transparent shielding of optical emitters in UWOC applications. This deposition has a direct effect on the effective power radiated to the medium. Depending on the matter spectral response, the deposition density and its thickness, the power loss can be modeled as an exponential decay (Equation 4.32). The fouling resistance, β, is the rate at which the thickness of the fouling, $\tau(t)$ increases. α depends on the fouling density and the type of particle, whilst β depends on the type of particle, the water speed, the temperature of the surface and the bulk water temperature [125].

$$P_{tx,eff} = P_{tx} e^{-\alpha(\rho_{fouling},\lambda)\tau(t)} \tag{4.32}$$

There are different types of fouling resistances depending on the nature of the deposited matter. Generally, linear, falling and asymptotic curves are used to model this phenomenon. The behavior of the fouling rate is related to the deposition rate and the removal rate, being the difference of both. Normally, biological matter follows an asymptotic curve, and Equation 4.33 shows the mathematical description of the thickness in terms of the fouling resistance.

$$\tau(t) = \tau_{max}\left(1 - e^{-\beta t}\right) \tag{4.33}$$

τ_{max} is the asymptotic maximum of the thickness. Including Equation 4.33 into Equation 4.32, it yields:

$$P_{tx,eff} = P_{tx} e^{-\alpha(\rho_{fouling},\lambda)\tau_{max}\left(1-e^{-\beta t}\right)} \tag{4.34}$$

Figure 4.9 depicts, for illustrative purposes, the effect of fouling in the effective emitted power. $\alpha_{fouling}$ can be expressed in terms of the mass density of chlorophyll and its absorption spectrum, using Equation 4.5.

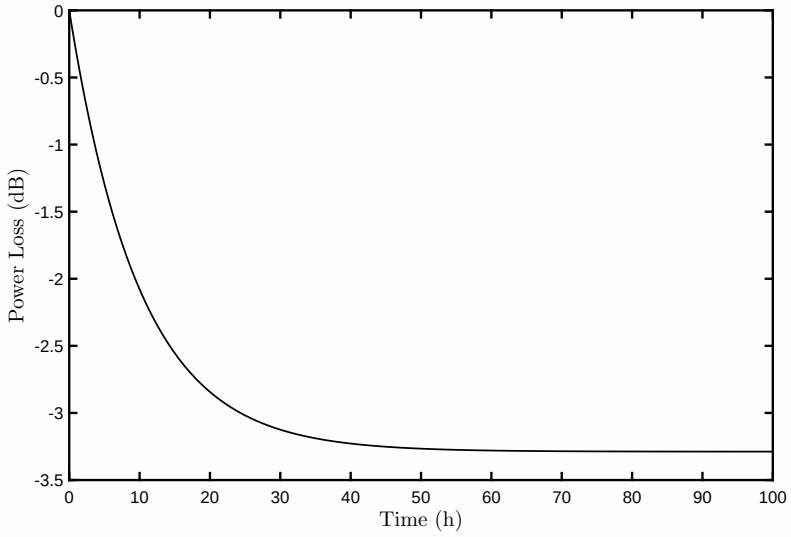

Figure 4.9: Effect of optical fouling on the effective emitted power. $P_{tx} = 1\,\mathrm{W}$, $\beta = 0.1\,\mathrm{h}^{-1}$, $\tau_{max} = 10^{-}2\,\mathrm{m}$ and $\alpha(\rho_{fouling}, \lambda) = 75.71\,\mathrm{m}^{-1}$ with $C_\phi = 1\,\mathrm{g}\cdot\mathrm{m}^{-3}$

4.2.8 Fauna

The effects of fauna on the performance of an UWOC link have not been studied in depth yet. Nonetheless, it would presumably depend on the concentration of fauna, the size of the individuals, its mobility and its awareness respect to the used wavelength.

4.3 Simulation of the UWOC impulse response

The RTT equation is difficult to solve, and the task becomes harder when the random nature of the scattering by particles is introduced. However, Monte Carlo integration offers a simple and computationally efficient alternative to obtain a solution to the time-dependent RTT equation in any scenario. Analytical solutions can be obtained without taking into account neither the randomness of the medium nor the effect of the seawater surface or seabed, as Jaruwatanadilok carried out in [33]. The main objective of this simulation process is to obtain a representation of the UWOC impulse response and perform an analysis relating physical parameters to communication-performance parameters, such as channel gain and bandwidth.

4.3.1 Simulated scenario

The simulated scenario consists in a three-dimensional volume bounded in the Y and Z axes. The Y-limits are the seabed and the seawater surface, whilst the Z-axis boundaries are the emission and reception planes. The phenomena included in the simulation process are absorption, scattering by particles, diffusive effects on the seabed and surface reflections. Turbulences and fauna have not been considered because of their stochastic nature. In a stochastic model, these effects can be included as multiplicative factors, since they present statistical independence. Furthermore, LED emission is considered and hence polarization and coherence are neglected, easing the calculation. Figure 4.10 depicts the effects considered in the simulation as well as the geometry of the problem. It can be observed that the emitter point is the coordinate origin. Therefore, the depth of the link is parametrized as a positive value, whilst the seabed's depth is a negative value.

4.3.2 Monte Carlo integration scheme

Monte Carlo integration is a numerical integration technique which randomly generates points within the integration domain. Let's consider the general multidimensional definite integral in the domain $\Omega \in \mathbb{R}^n$ shown at Equation 4.35.

$$I = \int_\Omega f(\vec{x})\mathrm{d}\vec{x} \tag{4.35}$$

The integration domain has a hyper-volume V of the form:

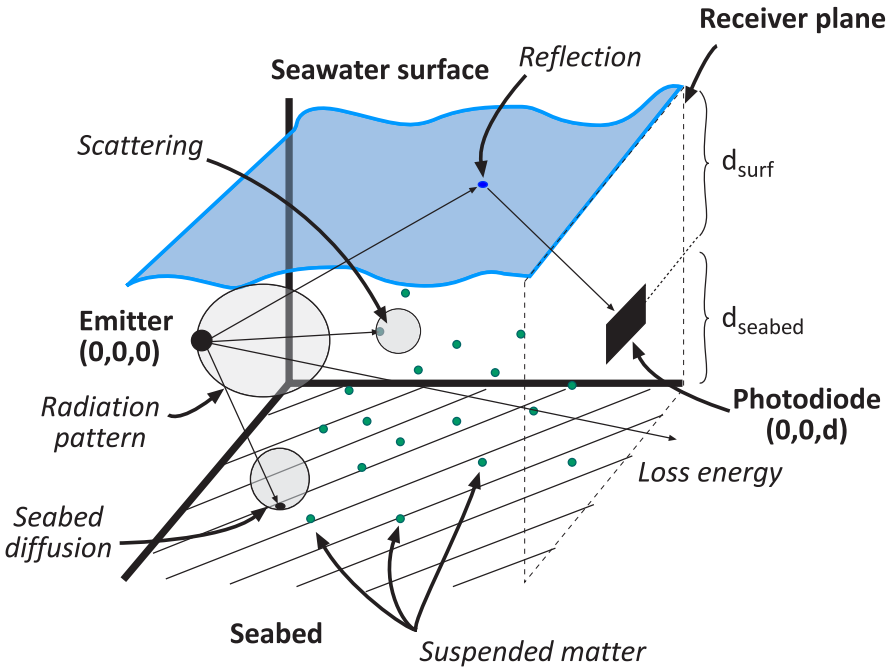

Figure 4.10: Simulated scenario

$$V = \int_{\Omega} \mathrm{d}\vec{x} \tag{4.36}$$

Finally, Monte Carlo integration states that the integral of Equation 4.35 can be approximated to a summation of the form:

$$I \approx \frac{V}{N} \sum_{i=1}^{N} f(\vec{x}_n) \tag{4.37}$$

Where $\vec{x}_n$ are random sample points within the domain Ω. This type of integration is particularly useful when dealing with complex problems such as the one under consideration in this work. The UWOC impulse response can be approximated using a Monte Carlo approach over the RTT equation (Equation 4.1). This leads to an expression of the form:

$$h(t) \approx \sum_{i=1}^{M} P_i \delta \left(t - \frac{n_w(\lambda)}{c_0} d_i \right) \tag{4.38}$$

Where P_i is the weighed contribution of the i-th arriving ray, d_i is the traveled distance, and M is the number of effective contributions to the impulse response. Equation 4.39 shows how P_i is obtained, and Equation 4.40 defines the delay suffered by an arriving ray.

$$P_i = \frac{P_{tx}}{N} e^{-\alpha(\lambda) d_i} \prod_{j=1}^{N_h} L_j \tag{4.39}$$

$$d_i = \sum_{j=1}^{N_h} d_j \tag{4.40}$$

N is the number of rays generated at the emitter. Intuitively, the radiation pattern is divided in N differential solid angles, resulting in a random generation of directions over the emitter's hemisphere. Each ray is then scattered in many directions depending on the multiple random collisions due to particles and the seabed. Note that $M \neq N$ because after each collision with particles, a new bundle of rays is generated. N_h is the number of hops (collision events) that a ray has made before arriving the receiver, d_j is the traveled distance after the j-th collision, and L_j is the j-th power weighing applied to a ray. These last weights are classified as follows.

$$L_j = \begin{cases} A_{pd}\cos\Psi/d_j^2 & \text{Impact on the receiver} \\ R_{Fresnel}\left(<\hat{v}_j,\hat{n}_{surf}>\right)/d_j^2 & \text{Impact on the seawater surface} \\ \rho_{Seabed}<\hat{v}_j,\hat{n}_{seabed}>\cos\theta/d_j^2 & \text{Impact on the seabed} \\ R_{Mie}(\theta)/d_j^2 & \text{Impact with a scattering particle} \end{cases} \tag{4.41}$$

A_{pd} is the receiver's area, Ψ is the angle of arrival to the receiver and $R_{Mie}(\theta)$ is the scattering pattern of the particles defined by Mie's theory. In this case, the Monte Carlo integration has been performed randomly generating output angles at the emitter and after each collision. The following subsection will discuss this random ray generation.

The proposed simulation procedure performs the calculation of the impulse response through a Modified Monte Carlo Ray Tracing algorithm (MMCRT). Traditional MCRT algorithms perform the integration generating N random rays at the source point and propagating the contributions of each ray, but only a random ray produces a useful contribution when it "casually" impacts on the receiver. Unlike MCRT, the MMCRT algorithm generates a deterministic ray and N-1 random rays, ensuring a faster convergence of the solution. The deterministic ray is generated in the direction defined by the emitting point and the receiver. This procedure has been used in different indoor OWC simulation algorithms [8][126].

In a MMCRT algorithm, all the generated rays have a power equal to the whole radiated power over the number of generated rays. However, the random generated directions follow the radiation pattern of the source to emulate higher radiation densities at privileged directions. In the case of the emission, this rays will follow a m-order Lambertian pattern; whilst in the case of a scattering, the scattering pattern (Lambertian for seabed, and Mie for collision with particles). In order to generate the random directions, two spherical angles must be obtained. As the medium is isotropic and the considered particles are spherical, all the radiation patterns involved in this simulation have azimuthal symmetry ($f_\phi(\phi) \sim U(0,2\phi)$). Regarding the elevation angle θ, its PDF has the shape of the radiation pattern. The generation of random elevation angles follows the traditional random number generation presented in Equation 4.42.

$$\theta = F^{-1}(r) \;\; /F = \int_0^\theta f_{\theta'}(\theta')\mathrm{d}\theta',\, , \; r \sim U(0,1) \tag{4.42}$$

Where $f_\theta(\theta)$ is the energy-normalized radiation pattern. The energy normalization is needed to conserve the shape of the scattering phase function (or emission pattern) while complying Kolmogorov's probability theory. Since the scattering functions are hardly integrable, an iterative interpolation process after sampling $f_\theta(\theta)$ is performed to obtain random elevation angles.

4.3.3 Collision with particles

In this work, a uniform distribution of particles of density ρ_{part} (m^{-3}) has been considered. In the real world, particles are not uniformly distributed at a local scale due to the effects of marine currents and mass transportation. Nonetheless, this approximation is valid in a large scale basis. When considering an uniform distribution of spherical particles, the collision distance on a straight line follows an exponential distribution whose parameter μ is the product of the particle's scattering cross section and its density in particles per unit volume (Equation 4.43).

$$f_d(d) = \mu e^{-\mu d} \;\; /\mu = \sigma_{scat} \cdot \rho_{part} \tag{4.43}$$

Where d is the collision distance and $f_d(d)$ its PDF. After a collision, scattering is produced and that point behaves as a new emitter which follows the scattering pattern defined by Mie's theory. This will be taken into consideration when defining the simulation procedure.

4.3.4 Description of the simulation procedure

The proposed algorithm can be reduced to the following high-level operations (Algorithm 1). The operations of the initialization step will not be discussed since they are simple operations. Nevertheless, function **growAndHarvestTree(ray)** is commented in the following subsection.

Routine **bhmie()** calculates Mie's scattering using Bohren-Huffman's algorithm [127]. Due to the tree-like nature of the algorithm, a simple recursive algorithm was implemented in first place. However, since the algorithm was intended to be embedded in a GPU, a stack structure was needed to control the execution in an iterative fashion. The used stack was conformed by an array of structures containing the state of the propagated ray until the last collision event, and two boolean variables indicating if the calculation of the derived random and direct rays had finished.

Algorithm 1 MMCRT UWOC Simulator

inputData(): *Reads the simulation parameters from a configuration file*
getAbsorption(): *Calculates absorption using Equation 4.4*
getRefractionIndex(): *Calculates the refractive index of seawater using Equation 4.19*
bhmie(): *Calculates Mie's scattering phase function for the given particle*
initializeParams(): *Initializes a global parameters structure*

ray ← directRay
growAndHarvestTree(ray): *Performs the calculation of each contribution*
for N-1 Random rays **do**
    ray ← newRandomRay:
    growAndHarvestTree(ray)
end for
writeResults(): *Writes the calculated impulse response to a CSV file*

Function growAndHarvestTree()

Algorithm 2 describes the iterative process to calculate the contributions of each ray. The geometry of the problem can be observed in Figure 4.11. As it was commented above, each impact produces a multiple-branch situation where one of the branches is based on a deterministic direction.

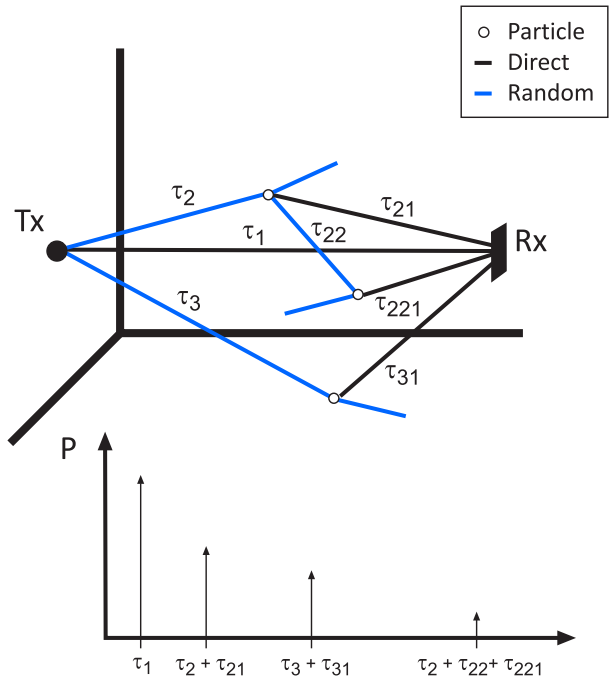

Figure 4.11: Geometry of the problem

MAXHOPS is the maximum number of allowed collisions per ray. This static final global variable is used to control the memory used by the program. Considering a problem where each scattering event produces N_s rays, the maximum number of stack-saved rays would be $N_s^{MAXHOPS}$. The actual memory size used by the simulation would be **sizeof**$(Ray) \cdot N_s^{MAXHOPS}$. Furthermore, MAXHOPS must be, at least, the value shown in Equation 4.44. If MAXHOPS were fixed to a lower value, there would be probably no contributions due to the premature discard of rays.

$$MAXHOPS \geq \left\lceil \frac{d_{link}}{E[d_j]} \right\rceil = \lceil d_{link} \cdot \mu \rceil \tag{4.44}$$

d_{link} is the link's range. This condition can be interpreted in a reverse way to estimate the maximum concentration of particles allowed in the simulation. Operating over Equation 4.44 it yields:

$$\mu_{max} < \frac{MAXHOPS}{d_{link}} \tag{4.45}$$

Algorithm 2 growAndHarvestTree

```
loop
    if Rays in the stack then
        if Random and Direct rays calculated then
            pop(): Retrieves a ray from the stack
        else
            if currentHop > MAXHOPS then
                return
            end if
            calculateDistanceAndType(): Calculates the next collision distance following Equation 4.46
            if Ray is not lost then
                switch type do
                    case Surface
                        Mark random as done (a surface reflection is not scattering)
                        save(): Saves the current ray in the stack
                        Change direction and weight
                    case Receiver
                        sumContribution(): Adds power at position pos = ⌊τ_ray(fs) − τ_min(fs)⌋
                        pop()
                    case Seabed or Particle
                        if Direct done then
                            Mark direct as done
                            save()
                            Change direction and weight
                        else if All random rays done then
                            Mark random as done
                            save()
                            Change direction and weight
                        end if
                end switch
            else
                pop()
            end if
        end if
    else
        return If Random and Direct rays calculated
    end if
end loop
```

For a given range, the maximum concentration allowed directly depends on the parameter MAXHOPS. If higher concentrations were of interest, this parameter should be increased. Nonetheless, this increase would led to a higher computation time and memory usage.

Routine **sumContribution()** adds the power of the j-th ray at the position defined by $pos = \lfloor \tau_{ray}(fs) - \tau_{min}(fs) \rfloor$. Note that the sampling time of $h(t)$ has been fixed to 1 femtosecond, which is a sufficiently high sampling bandwidth for the simulation purposes. τ_min is the delay related to the direct ray, which implies the minimum distance between emitter and receiver. Finally, the size of the array used to store the contributions has a size N_T that is the division of the integration time and the sampling time. When a ray is propagated and its associated delay surpasses the integration time, it is prematurely discarded.

To estimate the computational complexity of the problem, the following assumptions have been made:

- Only scattering events are considered.
- N initial rays are generated.
- After each scattering, each incident ray generates N_s random rays.
- Each ray is propagated until its maximum allowed number of hops, MAXHOPS.

Using Equation 4.44 and taking into account the last assumptions, in BigO notation, the algorithm has a computational complexity $\mathcal{O}\left(N \cdot N_s^{\lceil d_{link} \cdot \mu \rceil}\right)$, which is a polynomial problem of type $\mathcal{O}(n^m)$, where m is defined by the link's range, the scattering cross section of particles and the density of particles.

Calculation of the collision distance

This subsection corresponds to the process performed by routine **calculateDistanceAndType()**. The collision of a ray can be of five types: arrival to the receiver, surface impact, seabed impact, particle impact and loss. The type of the collision is obtained regarding the positive element which implies minimum distance in Equation 4.46.

$$d_j = \min_{\forall \hat{d}_j > 0} \left\{ d_j^{(surf)}, d_j^{(seabed)}, d_j^{(rx)}, d_j^{(particle)} \right\} \tag{4.46}$$

$$d_j^{(surf)} = \frac{y_{surf} - y_j}{< \hat{v}_j, \hat{e}_2 >}$$

$$d_j^{(seabed)} = \frac{y_j - y_{seabed}}{< \hat{v}_j, \hat{e}_2 >}$$

$$d_j^{(rx)} = \frac{z_{rx} - z_j}{< \hat{v}_j, \hat{e}_3 >}$$

$$d_j^{(particle)} \sim f_d(d)$$

The position of the receiver is $\vec{r}_{rx} = (x_{rx}, y_{rx}, z_{rx})$, $\hat{e}_i$ is the canonical basis, and $\vec{r}_j = (x_j, y_j, z_j)$ is the position of the j-th ray. If the minimum distance is the one associated to the receiver's XY plane and the ray is a random ray, then it is discarded since it would surpass the receiver. In a more general implementation, the ray would not have been discarded, but in this case, backscattering due to particles is practically inexistent. When the traveled distance is determined, the position of the ray is updated as $\vec{r}_{j+1} = \vec{r}_j + d_j \hat{v}_j$

To illustrate the method, Figure 4.12 shows an scenario where all the aforementioned distances are depicted.

Change of direction

When Mie scattering occurs, the spatial dispersion is oriented in the direction of the incident energy. In order to generate the random rays after the scattering event, a change of basis (rotation) is needed since the spherical angles (θ, ϕ) are related to the previous direction. Matrix $\mathbf{B}$, which defines the change of basis, is obtained after applying a Gram-Schmidt orthogonalization process using $\hat{v}_j$ as the seed vector of the transformed space. This vector must act as the z-component in the new domain, since the elevation angles are defined after it. Equation 4.47 illustrates the process carried out to randomly modify the direction of a ray.

$$\hat{v}_{j+1} = \mathbf{B}^T \cdot \left[S^{-1}\left((0, \theta, \phi) + S\left(\mathbf{B} \cdot \hat{v}_j\right)\right)\right] \tag{4.47}$$

$S(\hat{v}_{cart})$ performs the conversion from rectangular to spherical coordinates, whilst $S^{-1}(\hat{v}_{sph})$ carries out the inverse operation. Finally, $\mathbf{B}$ is an orthogonal matrix, and hence $\mathbf{B}^{-1} = \mathbf{B}^T$. Vector $(0, \theta, \phi)$ is the randomly-calculated scattering direction modification.

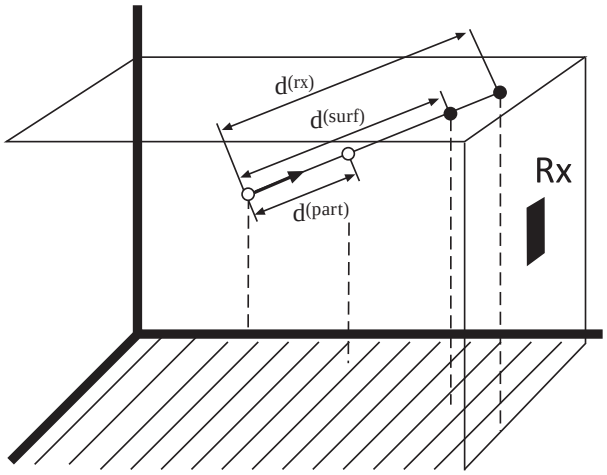

Figure 4.12: Example of collision distance calculation

4.3.5 Parallelization of the algorithm

As it has been commented above, the proposed MMCRT algorithm performs the same operation to each ray, which consists on calculating the temporally dispersed contribution of each emitted ray on the receiver. Furthermore, each ray is independent as there are no interaction between emitted rays. These two facts are the main requirements of any problem to be parallelized. A parallelization is a software implementation in which different tasks are performed at the same time. There are three major parallelization classes: multiprocessor (OpenMP), multicomputer (MPI) and GPU (CUDA, OpenGL). In this work, only multiprocessor and GPU approaches have been tested under the restrictions of the UWOC impulse response calculation problem.

OpenMP

OpenMP [128] is a multiplatform API that supports shared memory multiprocessing. This multiprocessing is normally performed by the parallelization of for-loops, assigning chunks of the for-range to each available CPU core. The computation model is based on a fork-join scheme, where the master thread blocks execution until the last "forked" thread ends. OpenMP offers different types of scheduling on the distribution of iterations of the parallelized for loop.

- No scheduling. Each thread receives $\left\lceil \frac{N}{\#Threads} \right\rceil$, expect the master thread, which receives also the rest.
- Static scheduling. The total iterations are divided in "chunks" of length N_{chunk}. Each thread executes in blocks of N_{chunk} iterations until all the iterations are done. When a chunk is finished, all the threads are synchronized to execute the following set at the same time.
- Dynamic scheduling. The same as static regarding the distributions of threads, but without the synchronization between threads.

The actual parallelization of the problem was based on the inclusion of two simple directives into the original sequential code. Firstly, the directive `#pragma omp parallel for private(ray, theta, phi)` was introduced just before the main for-loop (the one which performs the generation of the N-1 random rays). The variables `ray,theta` and`phi` were declared private because OpenMP considers all the variables as shared if the opposite is not specified. Moreover, these are the only variables used by the routine **growAndHarvestTree()** to perform the calculation. The rest of variables can be shared as they are read-only. The other sentence was introduced just before the **sumContribution()** routine, as it performs a writing operation on a shared memory space. This last sentence, `#pragma omp critical`, controlled the execution marking the operation as a critical section (semaphore-based execution control).

In any shared-memory program, critical sections are mandatory to prevent the data from being corrupted. Nonetheless, the actual probability of simultaneous access to a specific memory position of an array of N_T elements in a M-processor scenario is:

$$p_{access}(N_T, M) = \sum_{i=2}^{M} N_T^{-i} \left(1 - \frac{1}{N_T}\right)^{M-1} \tag{4.48}$$

Where ${N_T}^{-1}$ is the probability to access a determined memory position assuming an uniform distribution. Assuming N_T very high, Equation 4.48 can be reduced to Equation 4.49, which is a geometric series of ratio N_T^{-1}.

$$p_{access}(N_T, M) \approx \sum_{i=2}^{M} N_T^{-i} \approx N_T^{-2} \tag{4.49}$$

As it can be observed, the simultaneous-access probability tends to N_T^{-2}, which in the case of a 10^5-elements array would tend to 10^{-10}. This approximation does not takes into account the actual distribution of the memory access, and taking into account the actual physical problem, the first elements of the array would present higher access probabilities.

GPU

GPU's are parallel processors designed to accelerate image rendering in computer graphics. There is no a standard architecture for GPU, and in the literature, their components are normally described in terms of the terminology inherited from graphics segmentation. Terms such as *rasterizer, shader*, etcetera are very common. Nonetheless, as a simplification of the GPU architecture, these devices comprise two or more *multiprocessors*, which are compound by several *cores*, which finally have ALU's of different complexities inside.

Each multiprocessor have a relatively small amount of shared memory between cores. Furthermore, there is a global memory that is shared by all the GPU components. When data is transferred between the host's CPU and the GPU, it is stored or retrieved from this memory space by default.

In this work, a NVidia Tesla M2050 [129] was used as GPU platform. Figure 4.13 depicts its architecture. Host and GPU memory are communicated through a DMA, controlling transactions at high speeds. This GPU is conformed by groups of processors that execute the same instruction with different data at the same time. This operation form is known as SIMD. Each multiprocessor has a shared local memory and a Special Function Unit, used for the calculation of transcendent functions (trigonometric, logarithms, etc...).

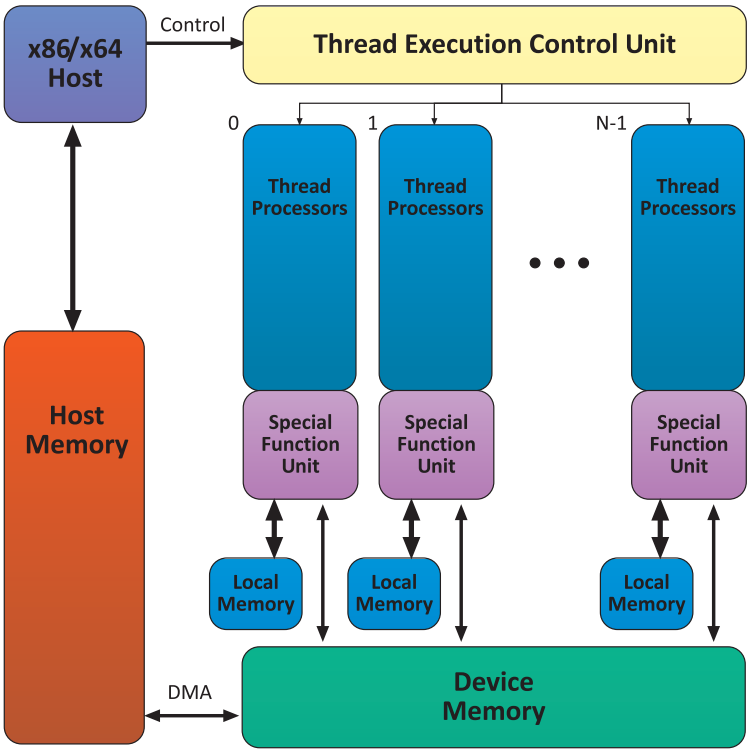

Figure 4.13: NVidia Tesla M2050 architecture

NVidia's CUDA technology has API's for different programming languages such as C/C++, Fortran, Java, Python and .NET. This SDK allows high-level programming using the GPU drivers with high transparency to the programmer. Regarding the actual programming using CUDA and GPU, several considerations must be taken into account.

- Memory allocation. In CUDA 2.0, GPU memory must be allocated using **cudaMalloc()** prior to its utilization. Furthermore, transactions between host and GPU must be performed through **cudaMemcpy()**.

- GPU parallel code. Parallel computed code must be embedded within a CUDA *kernel*. This code executes its inner instructions in the GPU using N blocks of threads and M threads per block. Calls to kernels must be carried out as `kernel <<<Blocks,Threads>>>(args)`.
- Device functions. GPU code cannot use host-defined functions. In order to introduce auxiliar functions into the GPU, these must be defined as `__device__`.
- Avoid conditional branches. As the used GPU executes the code using SIMD, when a conditional branch occurs (actually a dependence on data), some threads are deactivated and queued, blocking the execution.
- Kernels are not blocking. When the host calls a kernel, the GPU starts the computation and the host is not blocked, allowing the possibility to perform some calculations until the GPU ends. The host only is blocked when a device-to-host memory operation is requested.

The actual parallelization was performed defining the initial random ray generation (for loop) as a kernel, whilst function **growAndHarvestTree()** as a device function. Furthermore, CUDA 2.0 did not offer a random number generator in GPU. Because of that, a simple random number generator of period 2^{20} [130] was implemented as a device function. Each thread is initialized with a host-generated random seed. Finally, all the host-version functions which used **memcpy()** operations were transformed to a literal version (for loop with write sentence) since the GPU ignored host-defined operations.

4.4 Simulation results

In this section, several results are obtained from the implemented algorithm. As communication-performance characteristics, channel gain and bandwidth are calculated from the obtained $h(t)$. Nonetheless, unlike indoor OWC channels, where the impulse response may be considered fixed; in the case of UWOC, the scenario is continuously varying due to movement of particles and the seawater's surface. Furthermore, the pointing between underwater emitters and receivers is not perfect and presents a variation which depends on the marine currents. This effect has been neglected for simplicity, but as well as turbulence and fauna, it can be included as a multiplicative factor in an stochastic description of the UWOC channel.

Channel gain is defined as:

$$H(0) = \int_0^\infty h(t)\,\mathrm{d}t \tag{4.50}$$

In the case of the Monte Carlo integration, using Equation 4.38 and including it into Equation 4.50,it yields Equation 4.51. From an implementation-related viewpoint, this magnitude can be obtained as the sum of all the contributions saved in the 1-femtosecond-sampled $h(t)$ array.

$$H(0) \approx \sum_{i=0}^{N_T-1} P_i \tag{4.51}$$

Regarding bandwidth, it is related to delay spread by Equation 4.52.

$$B \approx \frac{1}{5\tau_{rms}} \tag{4.52}$$

Where τ_{rms} is the delay spread of the impulse response, defined by Equation set 4.53

$$\begin{aligned} \tau_{rms} &= \sqrt{\frac{1}{H(0)}\int_0^\infty (\tau-\bar{\tau})^2 h(\tau)\mathrm{d}\tau} \\ \bar{\tau} &= \frac{1}{H(0)}\int_0^\infty \tau h(\tau)\mathrm{d}\tau \end{aligned} \tag{4.53}$$

The actual implementation uses the same concept as Equation 4.51, converting integrals to sums as shows Equation set 4.54

$$\begin{aligned} \tau_{rms} &\approx 10^{-15}\sqrt{\frac{1}{H(0)}\left(\sum_{i=1}^{N_T-1} i^2 P_i\right) - \bar{i}^2} \\ \bar{i} &\approx \frac{}{H(0)}\sum_{i=1}^{N_T-1} iP_i \end{aligned} \tag{4.54}$$

In order to analyze the effect of the geometrical and physical link's parameters on the impulse response, a baseline scenario was defined. Table 4.1 shows the parameters.

Parameter	Value
Receiver's position	(0,0,5 m)
Photodiode's area	$A_{pd} = 20\,\text{mm}^2$
Directivity	$m = 1$
Transmitted power	1 W
Wavelength	470 nm
Particle radius	$500\,nm$
Particle refractive index	1.25 (lossless)
Concentration of particles	$3.3 \cdot 10^1 1\text{m}^{-3}$
Distance to surface	5 m
Agitation of the surface	$\sigma^2_{surf} = 0.0081$ ($v_{wind} = 1\,\text{m} \cdot \text{s}^{-1}$)
Distance to seabed	5 m
Seabed's reflectivity	$\rho_{seabed} = 0.5$
Number of rays	10^6
MAXHOPS	12

Table 4.1: Parameters of the baseline scenario

After modifying the parameter of interest, several runs of the simulation are performed in order to average the results. Concretely, to obtain a trend of the influence of each parameter, 100 runs were carried out per specific scenario. The results regarding the impact of each aforementioned parameter on the impulse response are discussed in the following subsections. The swept interval of each parameter will be presented, sample images of the impulse response at the two boundaries will be depicted, and finally, a curve showing the influence on both channel gain and bandwidth will be also presented and commented.

Furthermore, the obtained channel gain $H(0)$ has been calculated taking into account the emitter's radiation pattern but normalizing respect to the photodetector's area. Therefore, the units of the calculated $H(0)$ are W/m^2.

4.4.1 Effect of the link's range

In this case, the link's range has been swept from 1 meter to 10 meters. The impulse responses associated to the boundaries of the interval can be observed in Figure 4.14. The broadening of the response is clearly observed, whilst the reduction of the overall power is evident.

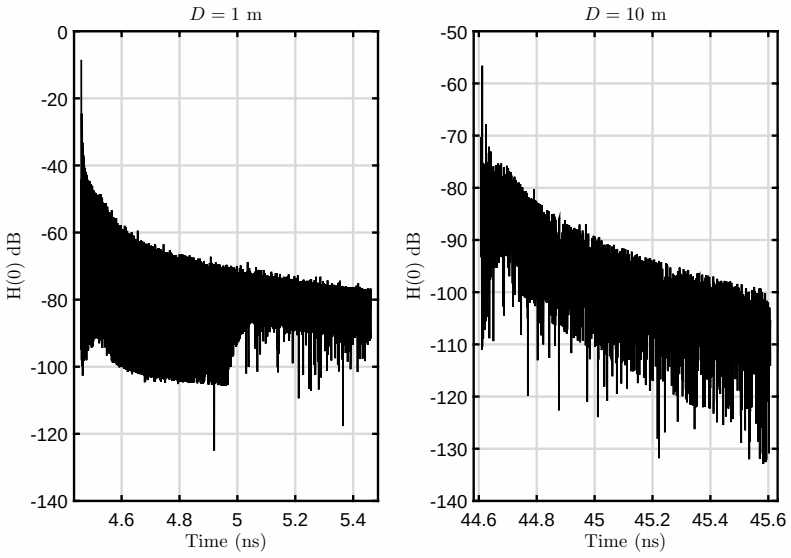

Figure 4.14: Impulse responses at different ranges

The exponential decay of the light intensity can be observed in Figure 4.15. This decay also affects the bandwidth, which also is diminished due to the greater amount of multipath components due to multiple scattering. It can be stated that there is an important exponential dependency of both parameters with the link's range.

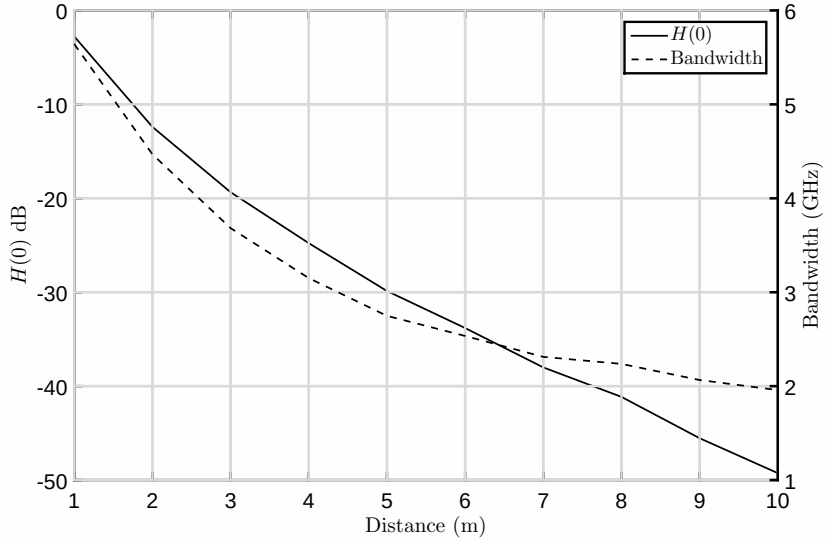

Figure 4.15: Dependency of $H(0)$ and B with d_{link}

4.4.2 Effect of the link's depth

A priori, the link's depth should have a significant importance since it defines the strength of the reflective components of the impulse response. Nonetheless, the mean value of the channel gain does not reflect a clear relationship with the link's depth, nor the bandwidth does. Figure 4.16 illustrates the boundaries of the swept range whilst Figure 4.17 shows the dependency of $H(0)$ and B with the link's depth.

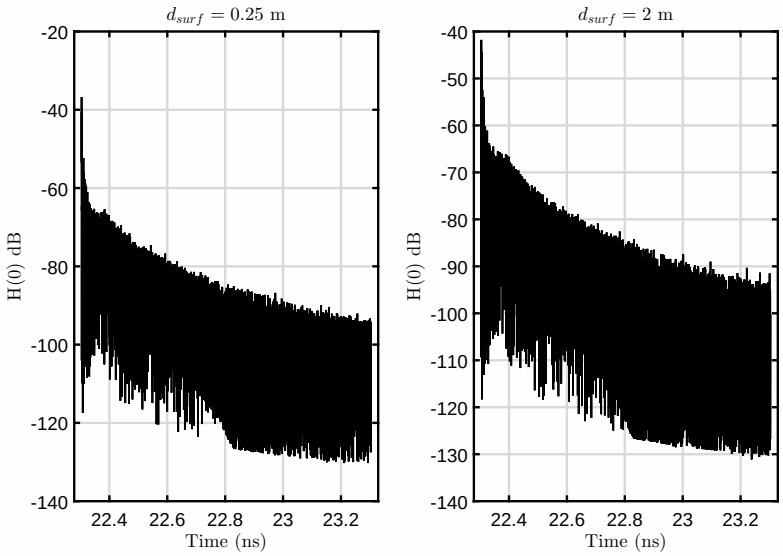

Figure 4.16: Impulse responses at different depths

The random nature of the impulse response will be discussed in detail in Chapter 6, but a Wilcoxon test to compare medians has been performed in order to analyze the influence of the depth on the studied channel parameters. The analysis yields a p-value of 0.0508 between the obtained values at $d_{surf} = 0.25$ meters and $d_{surf} = 2$ meters, which assures with almost a 5 % of confidence that the link's depth has influence on the channel gain. In the case of the bandwidth, the tests returns a p-value of $3.5 \cdot 10^{-6}$, which implies almost certainty about the dependency.

4.4.3 Effect of the surface agitation

The wind speed produces an azimuthally-symmetric random slope on the seawater surface. This random variation has several effects. On the one hand, a variable surface has more probability to produce reflections directly to the receiver, whilst a quiet surface only has a small illuminated area whose reflections produce power contributions.

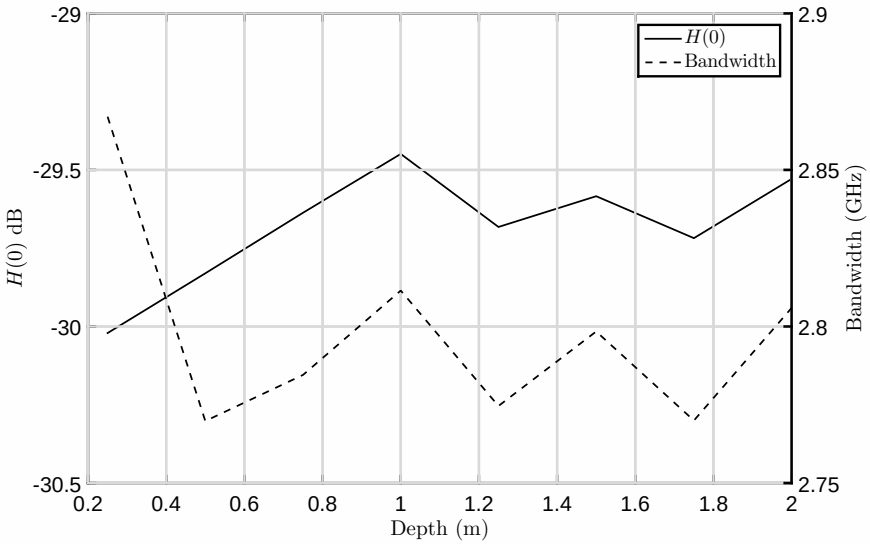

Figure 4.17: Dependency of $H(0)$ and B with d_{surf}

On the other hand, the delay associated to the main geometrical reflective component (defined by Snell's law) are "spread" as the agitation increases, since the Beam Spread Function of the medium (due to multiple scattering) widens the effective surface area with significant contributions. Figure 4.18 depicts the impulse responses for the boundaries of the swept wind speed. Note that the circled areas involve the main reflective component delay. In this case, due to the geometry of the scenario, is located close to 22.4 nanoseconds.

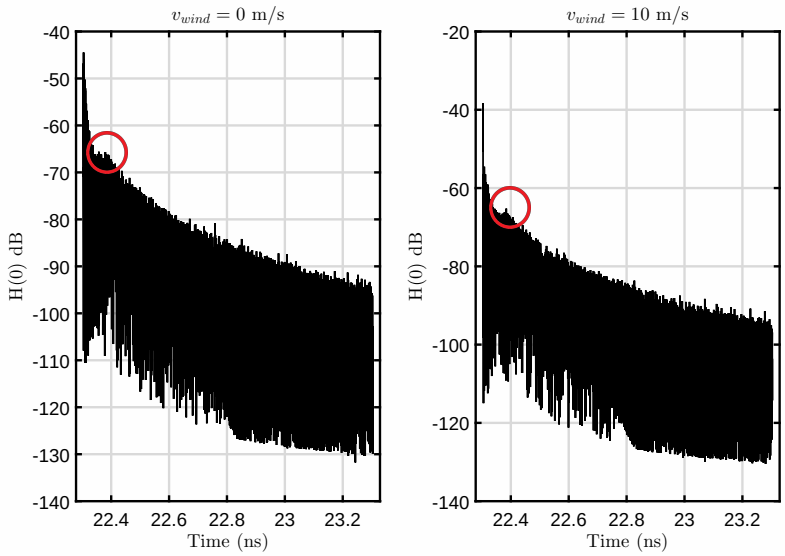

Figure 4.18: Impulse responses at different wind speeds for a depth of 0.25 meters

Figure 4.19 shows the detail of the circled area. For a still seawater surface, the geometrical reflective components are located surrounding the theoretical delay. Nonetheless, for a agitated surface, this components are spread.

Regarding the influence of the wind speed on the channel parameters, as the wind speed increases, the bandwidth and the channel gain increase too. This trend is absolutely compliant with the above discussion on the spreading of the reflective components.

4.4.4 Effect of the distance to seabed

The seabed was modeled as a Lambertian scatter, whose reflectivity ranges in the interval $[0, 1]$. Figure 4.21 illustrates the effect of the distance to seabed on the impulse response. A secondary spike can be observed next to 22.6 nanoseconds at the close-to-seabed scenario. This delay implies a traveled distance of 5.067 meters. Taking into account the geometry of the problem, there are two impact points on the projection of the pointing vector

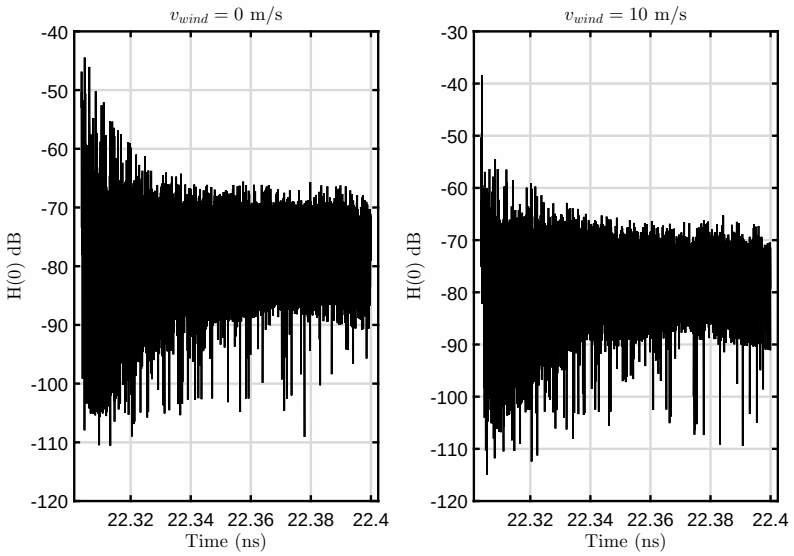

Figure 4.19: Detail of the circled area of Figure 4.18

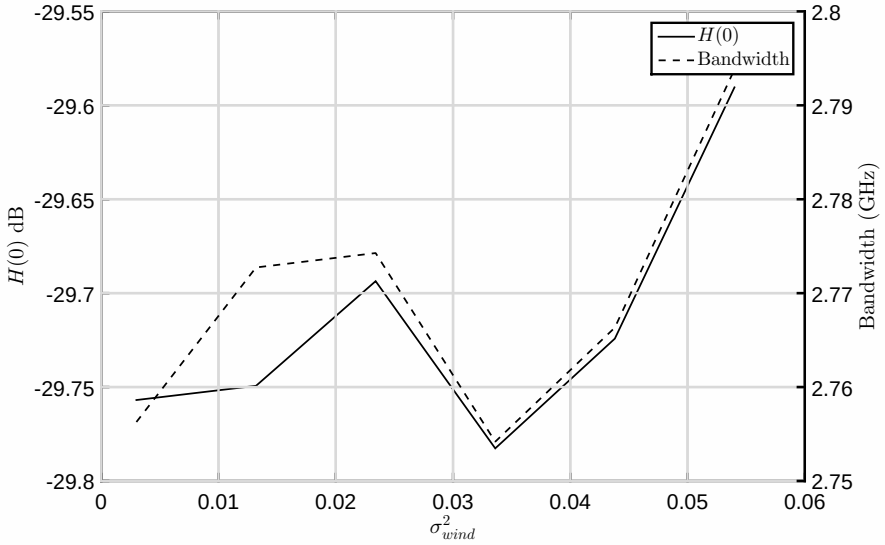

Figure 4.20: Dependency of $H(0)$ and B with v_{wind}

over the seabed that generate contributions with this delay: 4.5 meters and 0.5 meters (There is actually an ellipse on the seabed whose associated delay is 22.6 nanoseconds). Since the radiation pattern and the diffusion pattern are the same, the weighing of both main diffusive contributions are also the same by trigonometry.

It can be observed that for 2 meters, there is no apparent contribution of the seabed. The effect of the distance to seabed is shown in Figure 4.22. As it is obvious, the bandwidth is increased as the distance to seabed is incremented. However, there is not an appreciable impact on the channel gain. As it was done above, a Wilcoxon test was carried out to prove the influence of the distance to seabed on the channel gain. In this case, the test returned a p-value of 0.65, being impossible to assure that the distance to seabed has influence on the channel gain.

4.4.5 Effect of the seabed's reflectivity

In the previous subsection, it was demonstrated that the distance to seabed does not have a significant impact on the channel gain. In this case, for $d_{seabed} = 0.25$ meters, the expected impact of the reflectivity on the channel gain would be presumably the same. Figure 4.23 depicts the impulse response of the aforementioned scenario for a totally absorbing seabed and a very reflective one. There is no difference between the right graph of Figure 4.23 and the left graph of Figure 4.21.

Figure 4.24 depicts the obtained mean channel parameters respect to the seabed's reflectivity. There is no significant impact on any of the parameters, and the Wilcoxon test returns a p-value above 0.9 for both cases.

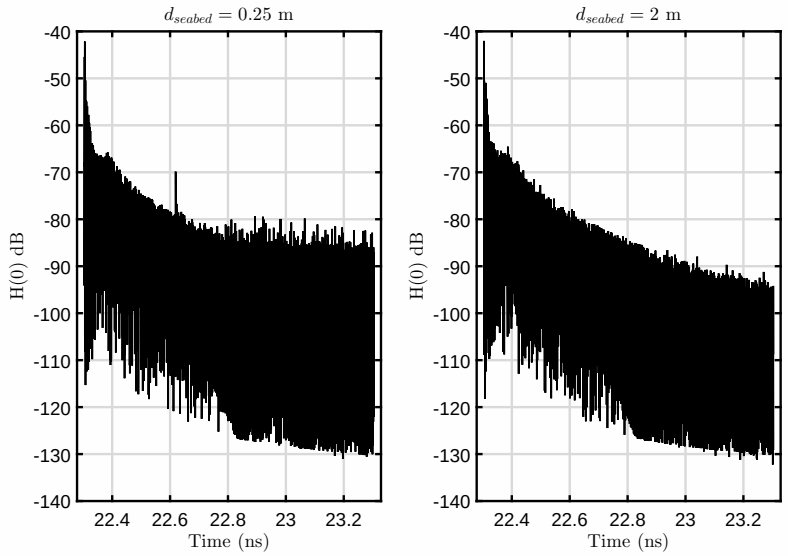

Figure 4.21: Impulse responses at different distances to the seabed

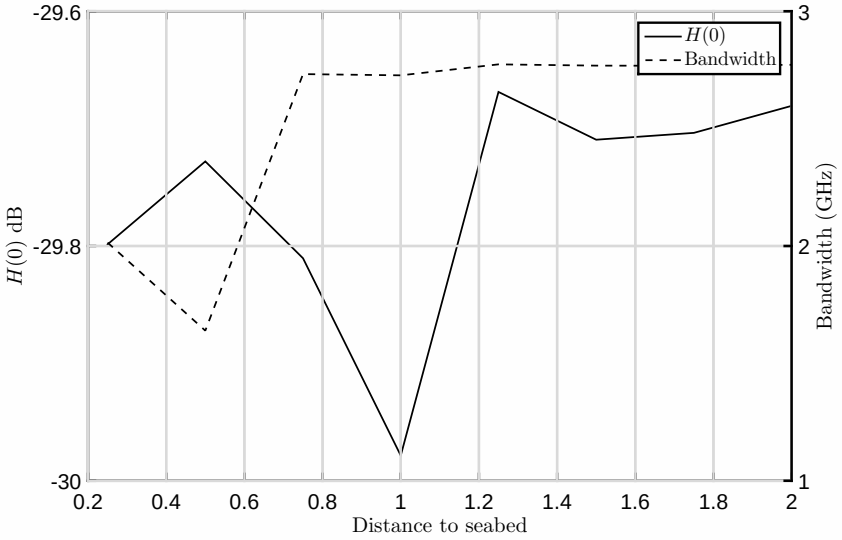

Figure 4.22: Dependency of $H(0)$ and B with d_{seabed}

However, only lambertian-scattering seabed has been tested and in further research, the use of other diffusion patterns should be tested.

4.4.6 Effect of the emitter's directivity

The emitter directivity is related to the concentration of the emitted energy in a narrower solid angle. It is logical that a more directive emitter would generate a better response on the receiver, whilst the multipath would be considerably reduced due to the decrement of the illuminated volume of water. Figure 4.25 depicts the impulse response for a pure lambertian emitter (left graph) and for an emitter with $\theta_{1/2} = 12°$. It is easily noticed that the directive emitter presents a narrower and more energetic impulse response.

The relationship between directivity and the channel parameters is presented in Figure 4.26. A log-like dependency can be easily extracted from the available data. In the limit, channel gain and bandwidth tend to the parameters of a laser-like link, which is defined by the BSF.

4.4.7 Effect of the wavelength

The wavelength directly affects attenuation, scattering and propagation delay. Since the redder wavelengths are more attenuated than the ones in the blue-green region, the channel gain is directly affected by the behavior of the

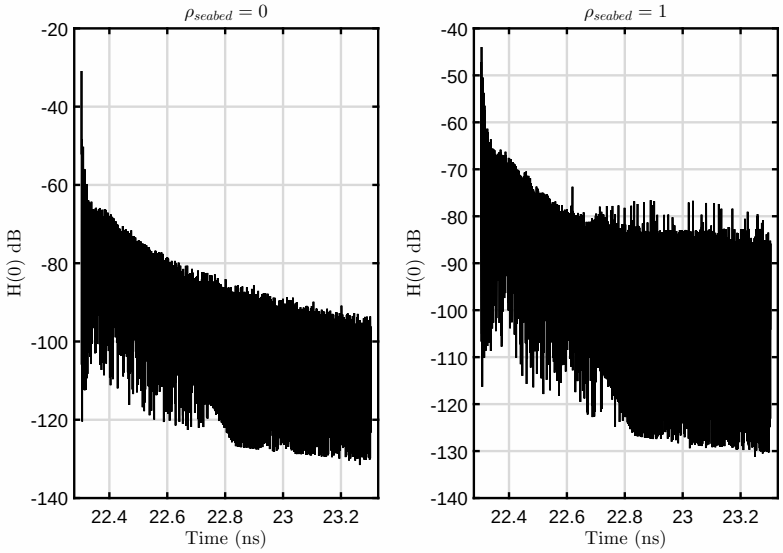

Figure 4.23: Impulse responses at different seabed reflectivity coefficients for distance to seabed of 0.25 meters

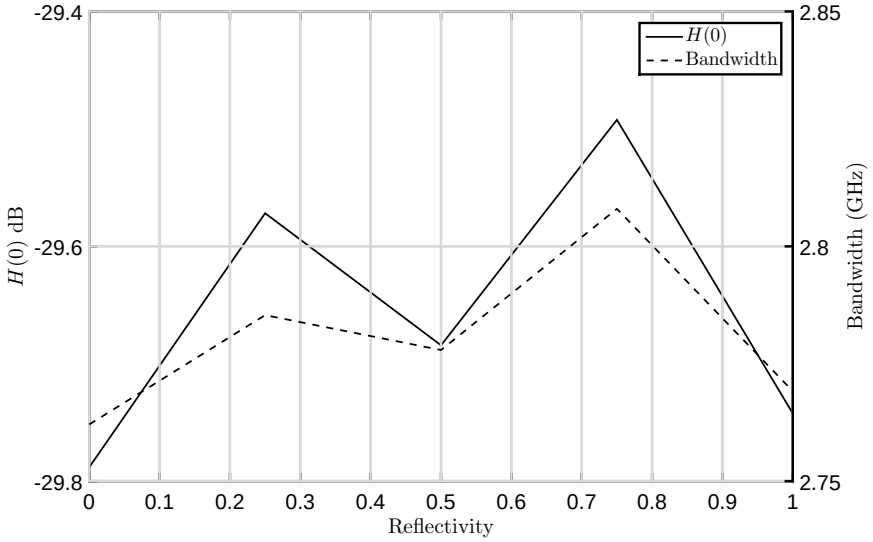

Figure 4.24: Dependency of $H(0)$ and B with ρ_{seabed}

attenuation coefficient. Furthermore, the refractive index of seawater is higher for longer wavelengths. Therefore, the excess delays are higher in a red-emission scenario, reducing the bandwidth. Figure 4.27 depicts the impulse response for a 470 nm and a 660 nm emission, whilst Figure 4.28 illustrates the aforementioned dependency of the parameters.

4.4.8 Effect of the particle size

As it was commented in Section 4.2.2, the normalized size of a particle directly affects the shape of the scattering phase function. The lower the normalized size, the more similar the phase function to a Rayleigh scattering, which presents a very broad dispersive profile. However, the higher the normalized size, the narrower the phase function. In the limit, the phase function tends to a Dirac's delta, only affecting the propagation adding wavelength-dependent scalar losses. The left graph of Figure 4.29 illustrates the impulse response with a low normalized size, whilst the right one shows the channel response of a particle with normalized size close to 1.

Regarding the effects of the particle radius on the impulse response, small radii have broad phase functions, which have associated also broad BSFs. This broadening that has been commented several times in this document is the main reason of the relaxation of the pointing between emitter and receiver. In the presented scenario, a wide BSF produces a low channel gain but a high bandwidth, as shows Figure 4.30. Therefore, it may be concluded that the channel gain is inversely proportional to the particle radius whilst the bandwidth presents direct proportionality.

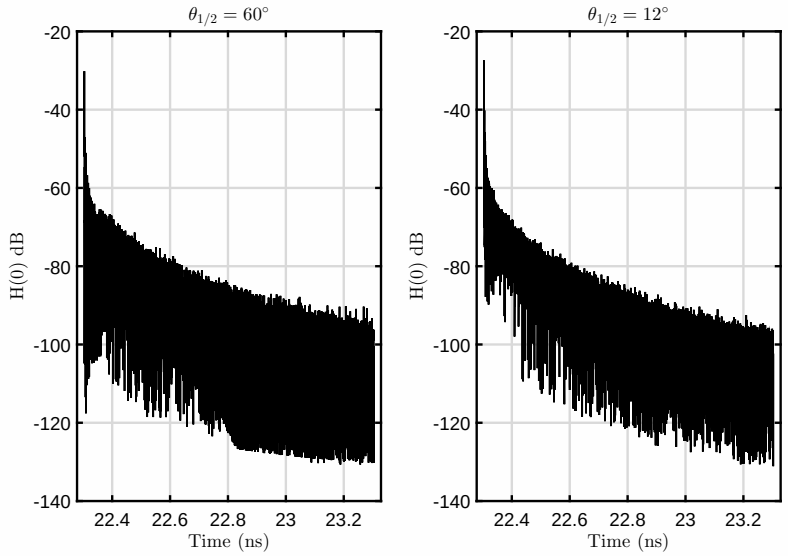

Figure 4.25: Impulse responses at different directivity values

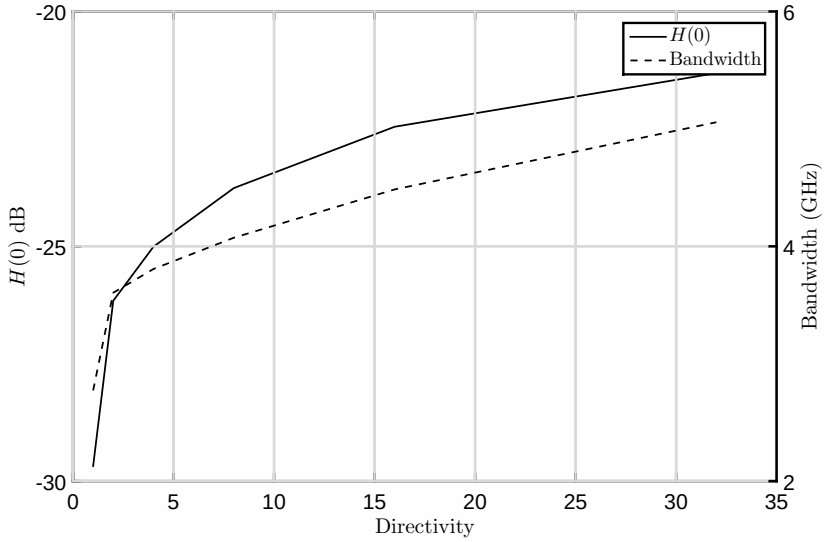

Figure 4.26: Dependency of $H(0)$ and B with the emitter's directivity

A local maximum can be observed in the channel gain curve. Its location depends on the particle concentration, which implicitly defines the scattering coefficient $b(\lambda)$. This effect has a special treatment in Chapter 6

4.4.9 Effect of the concentration of particles

As it has been commented, the concentration of particles joint to the scattering phase function defines the scattering coefficient. The total extinction is, hence, defined by the last two terms combined to the inherent optical absorption of the medium. As in the case of the particle radius, the concentration broadens the BSF since it defines the amount of scatterings per unit volume. Figure 4.31 illustrates the impulse responses associated to the boundaries of the swept range.

Figure 4.32 depicts the dependency of the channel parameters with the concentration of particles. For a particle radius of 100 nanometers, it can be observed that the channel gain increases in the swept range, but its concave curvature intuitively foresees a trend change. Regarding the bandwidth, it varies in a very narrow interval, but this parameter presents inverse proportionality.

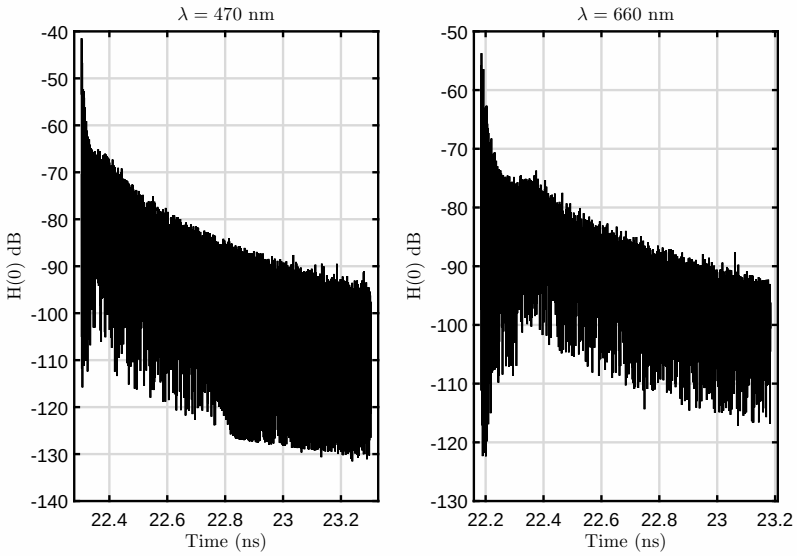

Figure 4.27: Impulse responses at different wavelengths

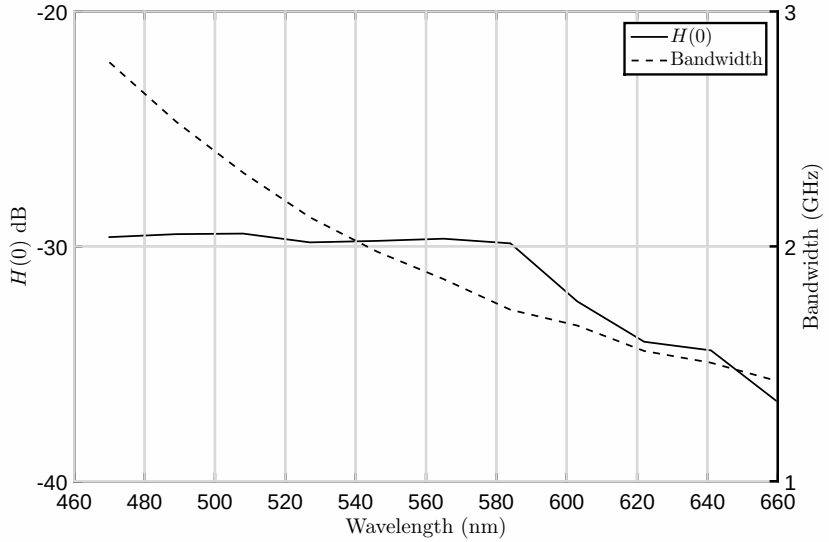

Figure 4.28: Dependency of $H(0)$ and B with the emitted wavelength

4.4.10 Parallelization speedup and efficiency

In this section, the speedups and efficiencies (speedup respect to number of physical processors) relative to the parallelization of the algorithm are presented. As a first result, the iterative version of the code respect to the initial recursive version offered an speedup of between 18 and 22. The simulation scenario presented as baseline scenario, was executed in an average time of 68381.74 ms. This result will also serve as the reference time to calculate the speedups.

OpenMP

Table 4.2 shows the speedups and efficiencies for different OpenMP schedulings and and number of threads. Using OpenMP without any type of scheduling is very inefficient. The tree-like structures generated during the calculation process have random widths and depths. Therefore, the execution times of each thread could highly differ, fixing the computation time to the slower one. Because of that, static and dynamic scheduling types were used, looking for an efficiency enhancement.

It can be observed that the chunk size does not affect static scheduling, as all the threads must be synchronized between the calculation of consecutive chunks. There is an efficiency enhancement respect to the no-scheduling case, but the synchronization problem still exists, even though at a lower scale.

Finally, dynamic scheduling offers the best solution due to the randomness of the execution time. Each time

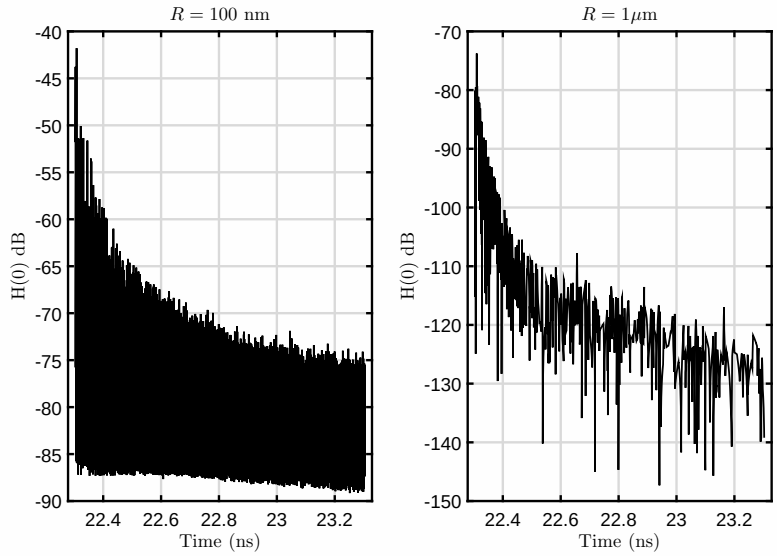

Figure 4.29: Impulse responses at different particles sizes

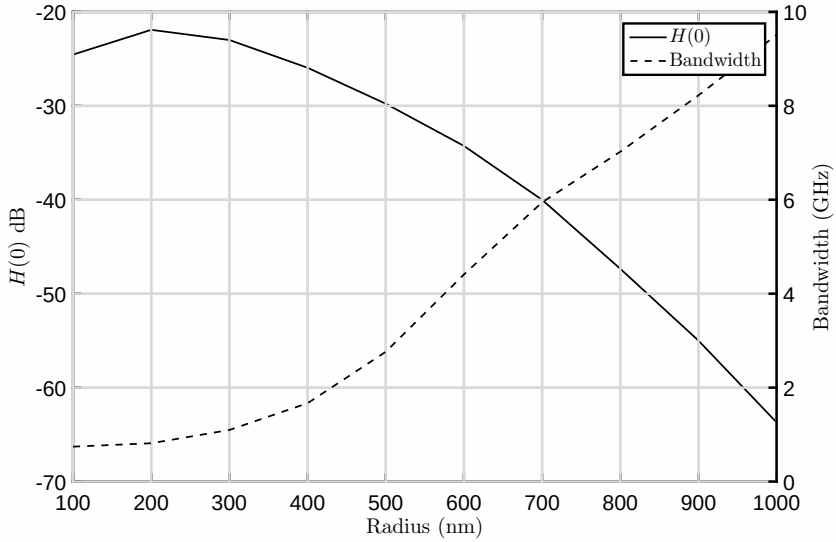

Figure 4.30: Dependency of $H(0)$ and B with the particle radius

a thread finishes the computation of a chunk of iterations, it retrieves a new chunk of iterations from the pool. Nonetheless, the maximum speedup for each configuration is very similar. The difference between the best configuration and the worst is approximately an 8 %, which depending on the problem, it may represent a significant amount of time. Furthermore, since the used host was based on a Xeon processor (8 physical threads and 16 virtual threads), the efficiency at 32 threads is also very similar.

CUDA

The used GPU has 448 cores to perform calculations. However, speedups next to the number of cores can not be achieved because, as it was commented above, GPU's operate in a thread-wise manner, and the code was programmed using conditional branches. Therefore, the majority of the multiprocessors will run only a single thread at a time. Regardless this limitation, the speedups obtained with this technology will surpass any multiprocessor architecture just by hardware brute force.

The results have been obtained using 2^N thread blocks and 2^M threads per block ($N \in [0, 10]$ and $M \in [0, 8]$), in an effort to visualize how the GPU deals with different memory configurations.

The total memory-transaction overhead was measured in 3 ms approximately. Hence, the CUDA kernel execution time and the whole algorithm execution time will be practically the same.

The efficiency of a parallel algorithm is measured respect to the number of active processors during the execution.

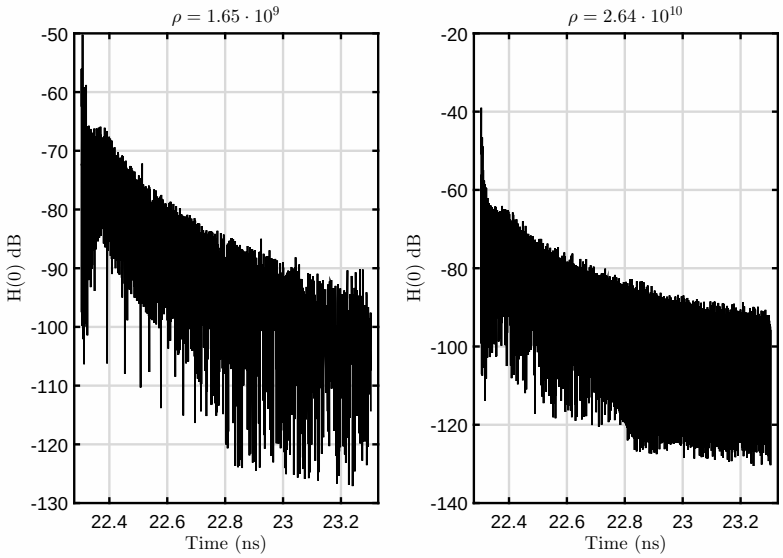

Figure 4.31: Impulse responses at different particle concentrations

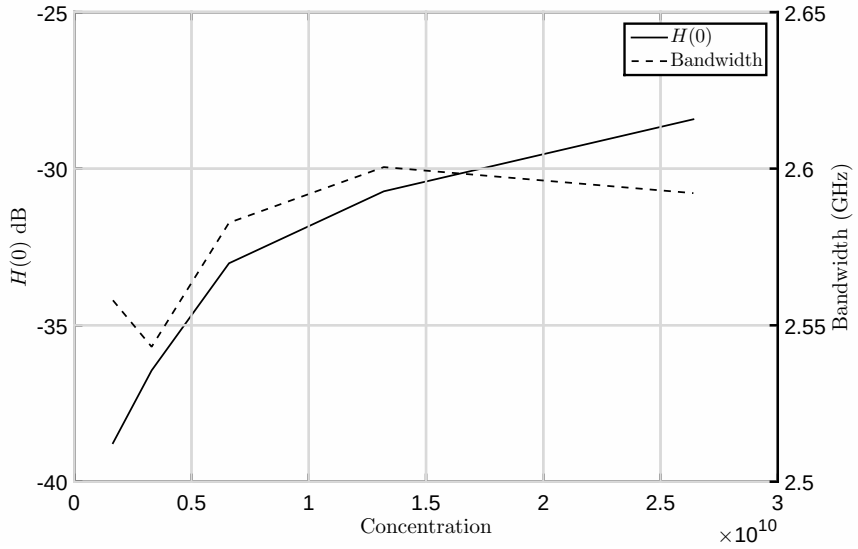

Figure 4.32: Dependency of $H(0)$ and B with the particle concentration

Nevertheless, the actual number of active cores is impossible to be measured using NVCC. Because of that, in order to provide an estimation of the GPU-code efficiency, the worst case scenario has been considered, fixing the number of used cores to the theoretical maximum of 448. The obtained results can be observed in Table 4.3.

As it was commented, the efficiency is very poor as expected, but the absolute speedup is beyond 42, which implies that 1 minute simulations turn to 1.5 seconds. This higher speedup is because that, even deactivating most of the cores, the number of GPU multiprocessors is higher than the number of cores in the case of OpenMP. The objective of this work was to obtain a significant speedup, since simulations of hundreds of runs were projected in order to obtain a statistical characterization of the problem. Therefore, efficiency may be enhanced but is out of scope.

For the extreme case of a single block of threads, the low efficiency of the code respect to the SIMD execution model of the GPU exceeds the speedup limit, carrying out the simulation slower than the sequential version.

Economical efficiency

In spite of the hardware inefficiency of the GPU respect to OpenMP regarding the parallelized algorithm, the absolute speedup is much higher that the obtained through OpenMP. Furthermore, is the economical efficiency of the parallelization were defined as states Equation 4.55, it could be demonstrated that GPU's offer also a better monetary alternative, even though when the parallelized algorithm does not fit the SIMD paradigm. Table

Scheduling	Chunk size	Number of threads	Speedup	Efficiency
No scheduling	1	2	1.21	0.57
	1	8	2.52	0.32
	1	32	3.62	0.12
Static scheduling	1	2	1.68	0.84
	1	8	2.69	0.33
	1	32	3.65	0.114
	10	2	1.65	0.82
	10	8	2.85	0.35
	10	32	3.75	0.12
	100	2	1.61	0.80
	100	8	2.78	0.35
	100	32	3.76	0.12
Dynamic scheduling	1	2	1.64	0.82
	1	8	2.56	0.31
	1	32	3.84	0.12
	10	2	1.76	0.88
	10	8	2.88	0.36
	10	32	3.84	0.12
	100	2	1.78	0.89
	100	8	2.72	0.34
	100	32	3.904	0.122

Table 4.2: Speedups and efficiencies of the OpenMP parallelization

Thread blocks	Threads per block	Speedup	Efficiency
1	128	0.58	$1.3 \cdot 10^{-3}$
	256	1.1	$2.5 \cdot 10^{-3}$
	512	1.78	$4 \cdot 10^{-3}$
32	1	1.1	$2.5 \cdot 10^{-3}$
	16	2.51	$5.6 \cdot 10^{-3}$
	128	17.53	$3.91 \cdot 10^{-2}$
	256	22.21	$4.96 \cdot 10^{-2}$
	512	21.0	$4.69 \cdot 10^{-2}$
1024	1	4.8	$1.07 \cdot 10^{-2}$
	16	10.1	$2.25 \cdot 10^{-2}$
	64	42.01	$9.38 \cdot 10^{-2}$

Table 4.3: Speedups and efficiencies of the CUDA parallelization for 1024, 512, 256 and 128 blocks

4.4 demonstrates this last conclusion, showing that a GPU is up to 4 times more economically efficient than a workstation.

$$\eta_{\$} = \frac{\max speedup}{cost} \tag{4.55}$$

Technology	Speedup	Cost (k$)	$\eta_{\$}$
Tesla M2050	42	2	21
Xeon 808 Westmere Workstation (2 Xeon Westmere E5620 [131])	4	0.8	5

Table 4.4: Economical efficiency of GPU and OpenMP for the parallelized algorithm. The cost is approximated to the cost of the used devices in 2012

4.5 Comparison with the literature

There are several implementations of underwater impulse response simulators. However, there is no simulator based on a Monte Carlo Ray Tracing. The most important contribution existing in the literature is the one presented by Gabriel et al. in [37]. In that work, the authors developed a simulator based on photon propagation, where the

photons scatter following a Henyey-Greenstein PDF. Nonetheless, as their method is purely statistical, it would have a higher computational cost to achieve effective photon contributions. On the contrary, the method presented in this work has lower convergence requirements since a deterministic direct ray is always generated after each scattering event. Furthermore, this work is the only current implementation (up to the date of this dissertation) of a parallelized MMCRT algorithm to obtain UWOC impulse responses.

Chapter 5

Considerations in Underwater-to-Air links

As is was commented in the previous chapter, underwater optical propagation is deeply affected by absorption and scattering, with magnitudes that can widely vary in different ocean water types. Scattering reduces both maximum link range and maximum data rate, since multipath effects become comparable to the bit time at certain datarates. Other important elements to consider are geometric factors as source beam divergence, propagation distance, receiver field of view, and misalignment. All these considerations should also be taken into account when the underwater-to-air interface is included. In addition, a change of medium which produces refraction, and the waves on the water surface must be also considered.

There are several applications in which a communication channel among underwater vehicles (or sensors) and surface devices is essential. Wind farms, off-shore energy plants or aquaculture facilities should be monitored and underwater sensors are needed. These sensors can collect data over long periods of time and the volume of stored data can be large and should be expected to grow as sensor technology becomes more complex. Although the techniques for underwater acoustic communication are well established and are practical in many cases, are limited to low speed transmission whilst free-space optical links have the potential to provide higher data rates than acoustic ones by several orders of magnitude.

In this chapter, a mathematical approach to the problem of modeling the underwater-to-air optical wireless channel is developed. This problem is studied in a channel availability estimation basis, calculating the maximum bandwidth and the link availability time percent. This simulation results presented were obtained using a scheme based on a MRT algorithm.

5.1 Sea waves propagation

Water wave motions without breaking can be modeled by the Navier-Stokes equations for incompressible Newtonian fluids, which represent the conservation of mass and momentum. Free surface boundary conditions, which ensure the continuity of the stress tensor over the surface, are necessary in determining the free surface location. Both the Navier-Stokes equations and the free surface boundary conditions are nonlinear. Consequently, even when the viscous and turbulence effects can be ignored, the computational effort required for solving a truly three-dimensional wave propagation problem, is normally prohibitive. Since this work is oriented to the achievement of a relationship between the propagation of sea waves and its influence on the received power in an underwater-to-air link, a linear model based on the Boussinesq approximation [132] has been considered. The Boussinesq approximation for a seawave propagating in the x-direction is represented in Equation set 5.1.

$$\begin{aligned} \frac{\partial \eta}{\partial t} + \frac{\partial}{\partial x}\left[(D+\eta)u\right] &= \frac{1}{6}D^3\frac{\partial^3 u}{\partial x^3} \\ \frac{\partial u}{\partial t} + u\frac{\partial u}{\partial x} + g\frac{\partial \eta}{\partial x} &= \frac{1}{2}D^2\frac{\partial^3 u}{\partial t \partial x^2} \end{aligned} \tag{5.1}$$

Where η is the wave height, D is the seabed's depth, which is constant, and u is the horizontal velocity at the seabed ($z = -D$). If the right-hand terms are neglected, it yields the Saint-Venant equations. If this equations are linearized making the approximations $\eta << D$ and $\partial u/\partial x \approx 0$, it yields Equation set 5.2.

$$\frac{\partial \eta}{\partial t} + D\frac{\partial u}{\partial x} = 0$$
$$\frac{\partial u}{\partial t} + g\frac{\partial \eta}{\partial x} = 0 \tag{5.2}$$

The performed approximations directly imply a small wave propagation over a lossless medium. In this case, it produced a pair of coupled equations that inherently represent a wave equation of the form.

$$\frac{1}{gD}\frac{\partial^2 \eta}{\partial t^2} = \frac{\partial^2 \eta}{\partial x^2} \tag{5.3}$$

This wave equation leads to a solution for the wave amplitude η of the type:

$$\eta(t, x) = \eta_0 \cos(\omega t - kx) \tag{5.4}$$

Where ω is the angular frequency of the traveling wave and k is the wavenumber ($k = 2\pi/\lambda_w$). The seawater surface is function of time and space, since it was defined by the above propagation equation. Its modeling is not trivial and is often defined probabilistically [133]. Even though this difficulty, a simple deterministic sea wave function is used in order to analyze the influence of the surface movement on communications. There are two main effects that are going to be considered in this chapter, where only monochromatic sea waves are taken into account: linear propagation and wind stress. For shallow waters, which is the introduced scenario, only long wavelengths will propagate without notable extinction. In this case, propagation speed $v_{seawave}$ is defined by the next formula, which is the propagation constant of Equation 5.3.

$$v_{seawave} = \sqrt{g \cdot D} \tag{5.5}$$

To consider the shallow water approximation as valid, the propagating sea wave may present a sufficiently long wavelength λ_w. This wavelength must satisfy the next condition, which is related to the frequency of the sea wave.

$$\lambda_w = 2\pi \frac{g}{\omega^2} \tanh\left(\frac{2\pi\eta_0}{\lambda_w}\right) \tag{5.6}$$

5.2 Underwater-to-air channel model

In this section, the mathematical model of an optical underwater-to-air link is presented. The movement of the sea surface has been modeled as a traveling monochromatic wave, but generally, the study can be generalized to any sea wave spectrum. Moreover, the seawater surface performs a lensing effect, narrowing or stretching the apparent receiver's amplitude respect to the emitter. Finally, the effect of wind stress in included in the same form as it was considered in Chapter 4. The scenario under consideration can be observed in Figure 5.1.

In this case, the coordinate origin has been located at the emitter point, but Equation 5.4 is still valid. The receiver has an area A_{pd} and is located at H meters from the surface.

5.2.1 Sea surface model

For the commented traveling plane wave scenario, the sea surface has the form:

$$S(x, t) = D + \eta_0 \cos(\omega t - kx) \quad \forall y \tag{5.7}$$

This surface defines a normal vector $\hat{n}(x, t)$ of the form:

$$\hat{n}(x, t) = \frac{\left(-\frac{\partial S(x,t)}{\partial x}, 0, 1\right)}{\sqrt{1 + \left(\frac{\partial S(x,t)}{\partial x}\right)^2}} \tag{5.8}$$

This normal vector has capital importance in the development of the mathematical approach of this chapter, due to its influence on the refracted angles of the outgoing light. The next chapter introduces a nonlinear change of basis, where this normal vector is introduced within the refraction phenomenon. Furthermore, some assumptions will be made to simplify the analysis of the problem.

If wind stress were considered, an additive noisy component would be added to Equation D.15. The behavior of this random component is defined by the normally-approximated Gram-Charlier series that was used in the previous chapter.

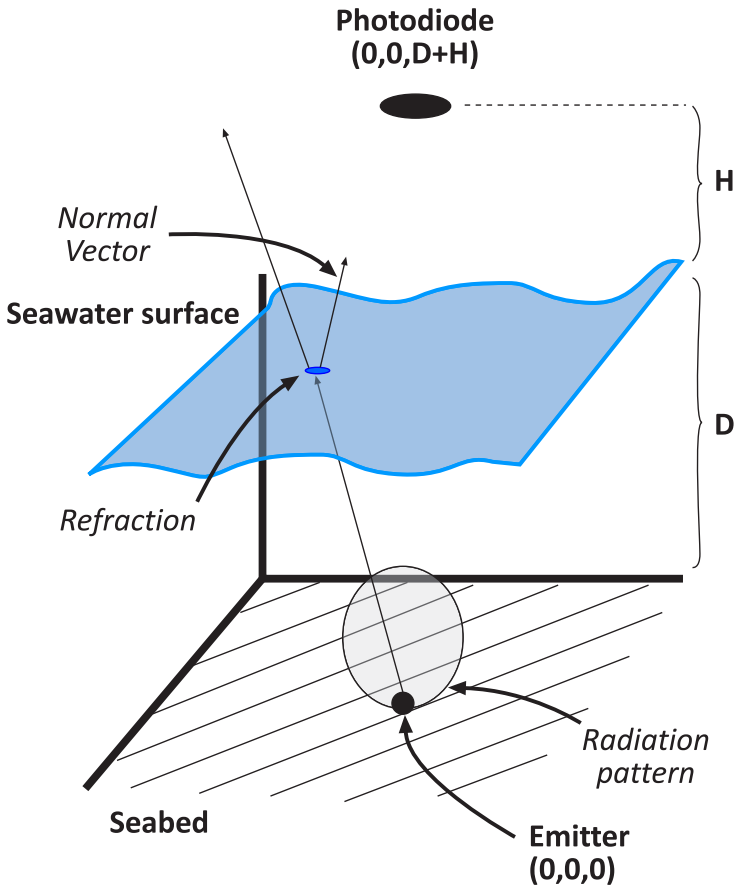

Figure 5.1: Underwater-to-air scenario under consideration

5.2.2 Received power

Wireless optical systems usually work following the intensity modulation and direct detection (IM/DD) paradigm. The optical power that arrives to the receiver is integrated through all the active area of the photoreceiver (usually a photodiode). If the optical power distribution over the receiver's area were defined by a solid angle Ω, the total received optical power, P_{rx}, would be:

$$P_{rx} = \int_{\Omega} P_{tx}(\Omega) \cos \Psi \, \mathrm{d}\Omega \tag{5.9}$$

Ψ is the relative angle between emitter and receiver, and $P_{tx}(\Omega)$ is the output radiance. As it can be seen, in order to obtain the received power, the optical power distribution must be known or estimated. For the proposed scenario, as there is a change of medium, the total optical power over the area A_{pd} located at the receiver's plane is equal to the optical power over an area A'_{pd} at the sea surface, since the air's extinction is negligible. Figure 5.2 helps to illustrate this lensing effect.

In this case, the optical power may be calculated at the sea surface as the amount of light that comes out of water and impacts on the receiver. On the following subsections this will be discussed in detail. Concreting Equation 5.9 for a lambertian emitter, and satisfying the same range restrictions that Barry et al. defined in [134], it yields Equation 5.10.

$$P_{rx} \approx P_{tx} \frac{m+1}{2\pi} \cos^m(\theta) T(\gamma_i) \frac{A'_{pd}}{D^2} e^{-c(\lambda)D} < \hat{r}, \hat{e}_3 > \tag{5.10}$$

$T(\gamma_i)$ is the Fresnel transmission coefficient for the incident angle with the surface γ_i. $\hat{r}$ is the unitary vector that defines the refracted direction of the LOS component. Note that the link is aligned respect to the z-axis, and due to the lensing effect, the solid angle that contains the effective contribution depends only on D and not on $(D + H)$. The influence of H is included in A'_{pd} as it will be commented in the next subsection.

5.2.3 Projection of the receiver's area

The refracted angles on the sea surface are governed by Snell's law. Considering each ray defined by a direction vector $\hat{v}$, and the incident surface point normal by $\hat{n}$, it is straightforward to demonstrate that the resulting refracted

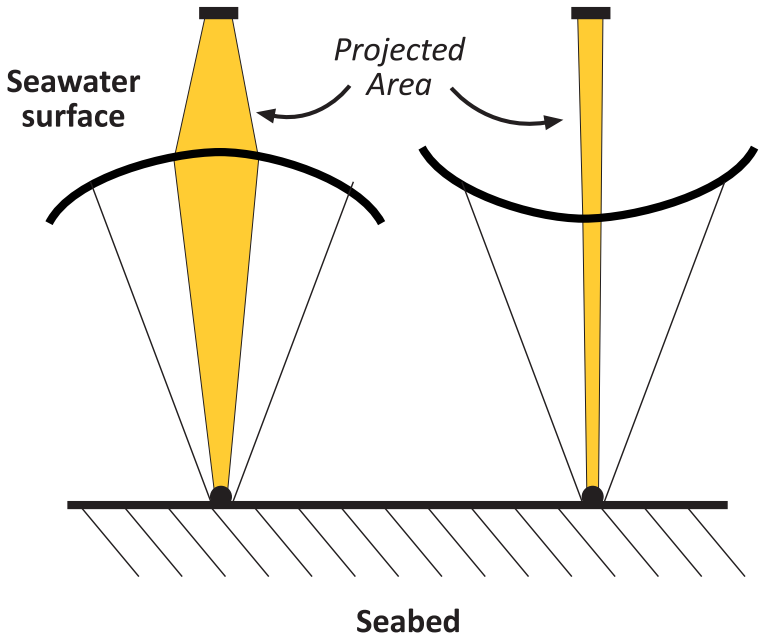

Figure 5.2: Lensing effect of the seawater surface

ray $\hat{r}$ may be defined as a linear combination of these vectors, as shows Equation 5.11. γ_r is the refracted angle.

$$\hat{r} = n_w \hat{v} + (\cos\gamma_r - n_w \cos\gamma_i)\,\hat{n} \tag{5.11}$$

The coefficients resulting from Snell's law can be expressed in terms of $\hat{v}$ and $\hat{n}$, yielding:

$$\hat{r} = n_w \hat{v} + \left(\sqrt{1 - n_w^2\,(1 - <\hat{v},\hat{n}>^2)} - n_w <\hat{v},\hat{n}>\right)\hat{n} \tag{5.12}$$

This last expression is computationally more efficient than Equation 5.11, since the scalar product $<\hat{v},\hat{n}> = \cos\gamma_i$ is easily calculated and does not imply the use of transcendent functions. As it was commented above, a change of basis has been used to refer the integration limits to a virtual photodiode located over the surface. It is supposed that do not exist neither spray nor particles between seawater and photodiode. The proposed change of basis is presented in the next expression.

$$\begin{aligned} x' &= x + \Delta x(x,y) \\ y' &= y + \Delta y(x,y) \end{aligned} \tag{5.13}$$

Figure 5.3 depicts the meaning of this nonlinear change of basis. Note that the terms $\Delta x(x,y)$ and $\Delta y(x,y)$ refer to the distance a ray travels in each direction before impacting the receiver's XY plane. This deviation depends on the receiver's height H and the refraction, as Equation set 5.14 shows.

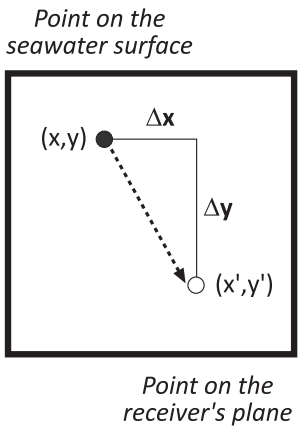

Figure 5.3: Graphical interpretation of the nonlinear change of basis

$$\Delta x(x,y) = [H - S(x,t)]\,\frac{r_x}{r_z}$$
$$\Delta y(x,y) = [H - S(x,t)]\,\frac{r_y}{r_z} \tag{5.14}$$

Finally, the projected area of the photodiode can be obtained in terms of the inverse transformation (Demonstration of the existence of inverse in Appendix A). Actually, due to the characteristics of the seawater surface, the rectangular area of the photodiode would not be projected as a rectangular area but as a curved one. However, due to the small-slope restriction imposed in this work, the error of assuming a rectangular projection will be negligible. Therefore, the projected area can be calculated using equation 5.15.

$$A'_{pd} \approx \left|x_L^{(2)} - x_L^{(1)}\right| \cdot \left|y_L^{(2)} - y_L^{(1)}\right| \tag{5.15}$$

Where $x_L^(i)$ and $y_L^{(i)}$ correspond to the projected corners of the photodiode after solving the nonlinear systems of equations:

$$\left.\begin{aligned} +x_L &= x_L^{(1)} + \Delta x(x_L^{(1)}, y_L^{(1)}) \\ +y_L &= y_L^{(1)} + \Delta x(x_L^{(1)}, y_L^{(1)}) \end{aligned}\right\}$$
$$\left.\begin{aligned} -x_L &= x_L^{(2)} + \Delta x(x_L^{(2)}, y_L^{(2)}) \\ -y_L &= y_L^{(2)} + \Delta x(x_L^{(2)}, y_L^{(2)}) \end{aligned}\right\} \tag{5.16}$$

Figure 5.4 shows the evolution of the average received power in the scenario defined in Table 5.1. The systems of equations were solved using the fixed point method.

Parameter	**Value**
Wavelength	3 m
Period	2 s
Wave height	25 cm
Depth	3 m
Receiver's height	2 m
Photodiode's area	9 cm^2
Emitter power	1 W
Directivity	$m = 1$
Extinction coefficient	$c(\lambda) = 0.305$

Table 5.1: Underwater-to-air baseline scenario

It can be observed that the energy loss due to the stretching of the projected area can imply a reduction of more than 3 dB for the example scenario. If wind were considered, each point of the sea water surface would behave following a normal distribution on its slope. The shear effect due to wind would produce a reduction of the received power and in this case, a pseudo-analytical solution as the presented above should not be used. The next section introduces the followed simulation procedure used to obtain the received power in a windy scenario.

5.3 Simulation procedure

Unlike the simulation of underwater-to-underwater links, underwater-to-air links are limited by the seawater surface. As it was commented in Chapter 4, when a light ray impacts on the surface, part of the energy is reflected, and the other part refracted. The direction of the refracted ray depends on the surface's normal vector and the incident ray's direction. Since there is no diffusive effects, the approach used to accelerate the convergence in underwater-to-underwater scenarios can not be used in this case. Therefore, a traditional MCRT algorithm was implemented to calculate the received power. Algorithm 3 shows the pseudo-code of the implemented simulator.

Routine **calculateImpact()** solves the next equation in ρ, which is the distance that a ray travels before impacting the surface in a direction defined by (θ, ϕ).

$$\frac{\rho}{\cos\theta} = D + \eta_0 \cos\left(\omega t - k\rho \sin\theta \cos\phi\right) \tag{5.17}$$

On the other hand, **calculateRefraction()** calculates the random incidence angle and the Fresnel loss. Finally, the output direction is projected to the receiver's plane using the transformation of Equation set 5.13.

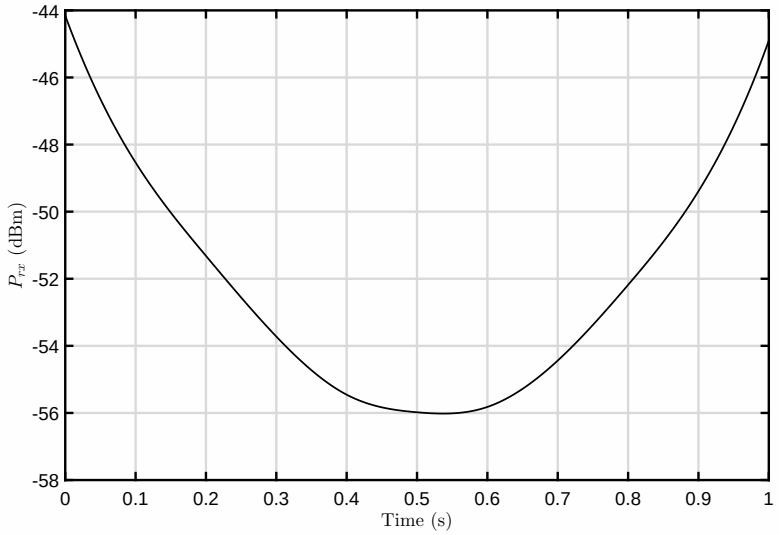

Figure 5.4: Evolution of the received power vs time for the parameters of Table 5.1

.

Algorithm 3 Underwater-to-air simulator

```
for N Random rays do
    ray ← newRandomRay:
    calculateImpact(): Calculates the impact on the surface
    calculateRefraction(): Calculates the output direction and Fresnel loss
    if Impacts on the receiver then
        Sum contribution
    end if
end for
```

5.4 Simulation results

In this section, several simulation results are presented in a similar way as in Chapter 4. In this case, the swept parameters are depth, receiver's height, sea wave height and wind speed (respect to the baseline scenario of Table 5.1). Furthermore, after commenting the influence of each parameter on the received power, the channel availability will be briefly discussed.

The channel availability is defined as the amount of time the received signal is over a threshold level S. This parameter is critical since it defines the probability to loss the connection. Expression 5.18 shows the mathematical description in terms of the PDF at each instant $f_X(X,\tau)$, and the sea wave period T.

$$T_{ch} = \frac{1}{T}\int_0^T \tau \int_S^\infty f_X(X,\tau)\,\mathrm{d}X\mathrm{d}\tau \tag{5.18}$$

The following curves represent only one half of the sea wave period. Due to the space-time symmetry of the seawater surface, one half of the period is enough to visualize the behavior of the received power.

5.4.1 Effect of the emitter's depth

The portion of the link which is performed underwater is subject to extinction. In this case, an extinction coefficient of 0.305 (Coastal water) has been selected. If this coefficient were varied, only the average received power would be diminished or increased, not the shape of the received power respect time. Hence, the main effect of the emitter's depth is the higher attenuation distance $c(\lambda)D$. In Figure 5.5, it can be observed that the received waveform is almost unchanged, but the offset level is defined by the attenuation distance $c(\lambda)D$.

5.4.2 Effect of the receiver's height

The height has direct influence on the lensing effect of the seawater. The higher the receiver is located, the wider the illuminated area during the concave periods of the sea surface that allow a bigger collection of light. Nonetheless,

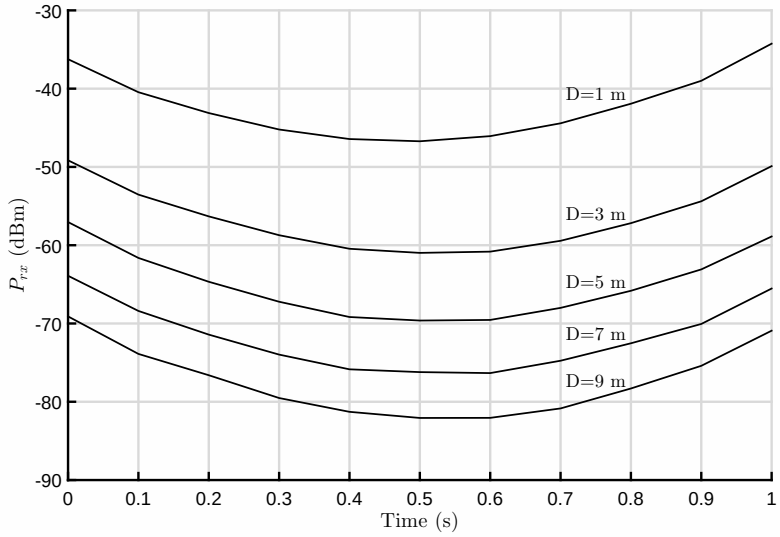

Figure 5.5: Effect of the emitter's depth on the received power

when the height increases, the maximum-minimum distance is also increased, since the lensing effect acts in an opposite way during convex periods. This effect can be observed in Figure 5.6.

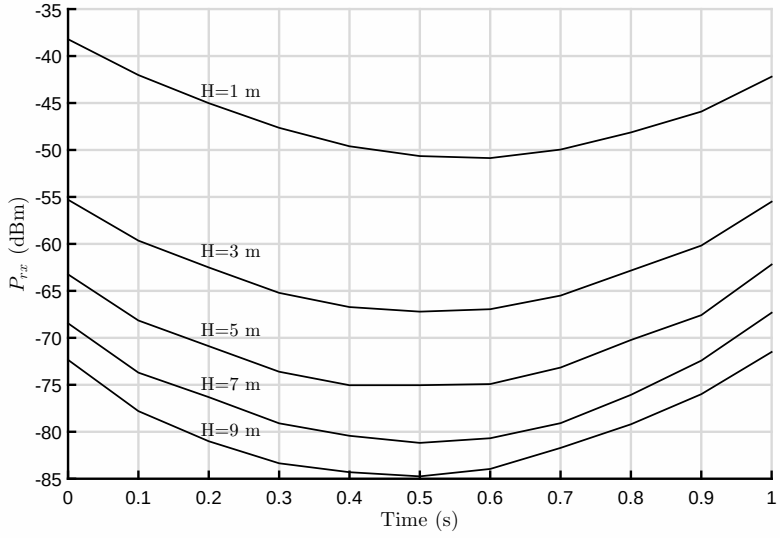

Figure 5.6: Effect of the receiver's height on the received power

5.4.3 Effect of the sea wave height

The sea wave height, joint to the wavelength of the sea wave, defines the slope of a monochromatic wave. This slope has a direct influence on the deviation of the illuminated area that contributes to the received power. As the sea wave height increases, the maximum slope is incremented proportionally and also the maximum deviation of the photodetector's projected area. Furthermore, this deviation has a Fresnel loss associated to the incidence angle. If this angle is increased, the minimum of the received waveform is reduced, as shows Figure 5.7.

Figure 5.8 depicts the trajectory that follow the corners of the photodiode over the surface, according to Equation 5.13. The effect commented above can be observed for two different values of η_0. Note that the higher η_0, the larger the perimeter of the curve.

Furthermore, Figure 5.9 illustrates the behavior of the projected area. It can be observed that high values of η_0 introduce fadings between the convex and concave situations, whilst lower values produce very small variations as expected.

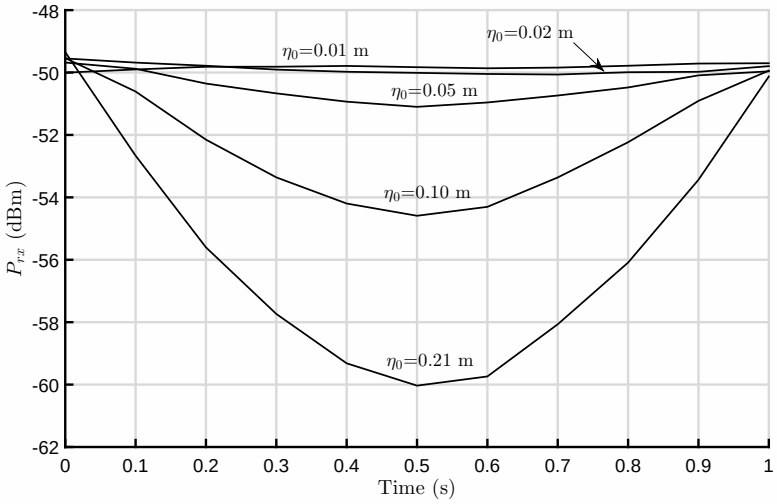

Figure 5.7: Effect of the sea wave height on the received power

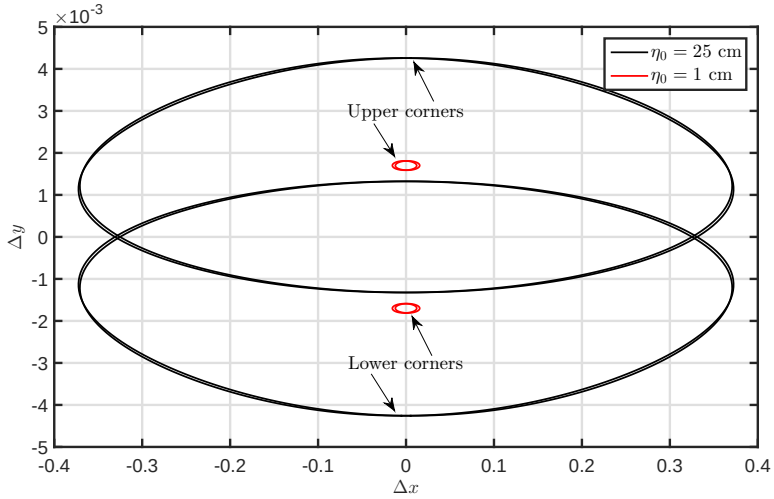

Figure 5.8: Trajectory followed by the corners of the photodiode over the seawater surface according to Equation 5.13

5.4.4 Effect of the sea wave wavelength

As it was commented above, wavelength and period are related through the dispersion relation. In order to correctly analyze the influence of the wavelength on the received power, this relation must be satisfied for each pair (T, λ). The expected effect due to wavelength is similar to the effect because of η_0. Figure 5.10 shows the influence of λ in normalized time units. As λ increases, the slope of the seawater surface is decreased, limiting the maximum deviation of the projected area.

5.4.5 Effect of the wind speed

The wind speed introduces a random noise on the sea surface slope due to stress. The noise variance is linearly related to the speed and is normally distributed on elevation and uniformly distributed on azimuth. The *a priori* effect of the wind speed would be a reduction of the peak-to-peak value of the received power, since each illuminated spot of the sea surface would have a probability to generate energy on the receiver. Figure 5.11 depicts the effect of wind speed on the received envelope.

5.4.6 Channel availability

The following figures depict the channel availabilities of the simulated scenarios respect to the receiver's sensitivity. This sensitivity is the minimum detectable optical power. In Figures 5.12 and 5.13, it can be observed that the

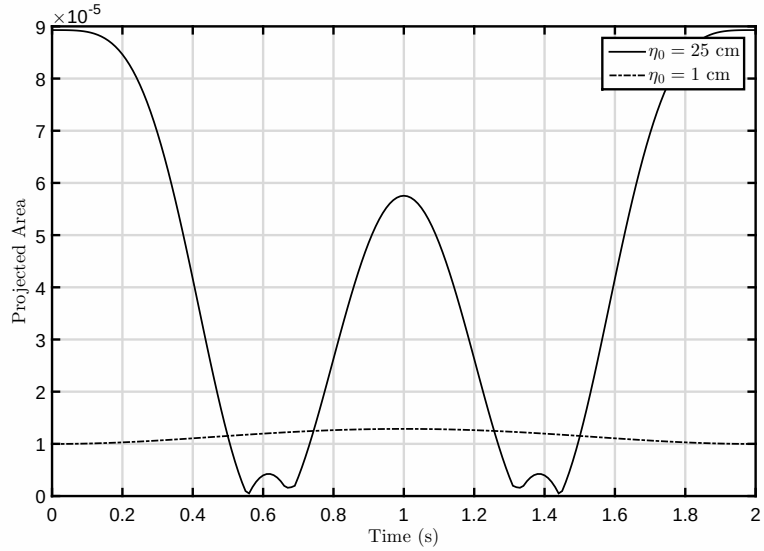

Figure 5.9: Projected photodiode's area vs. time for different values of η_0

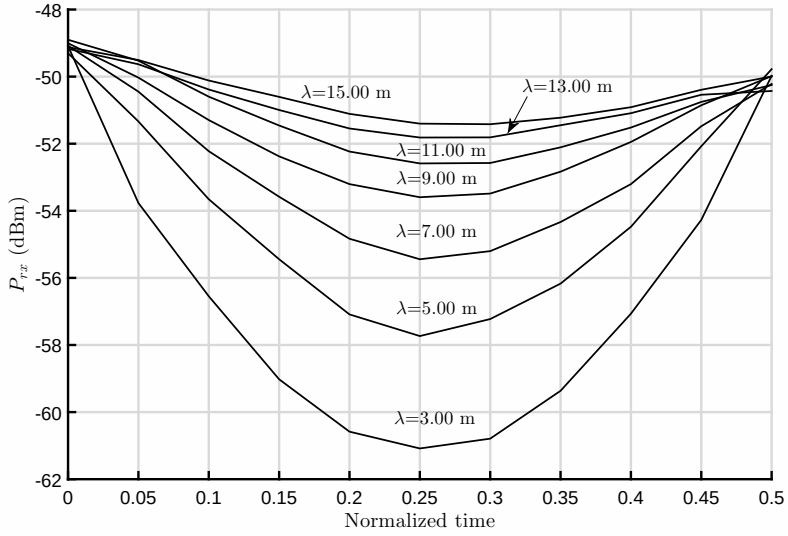

Figure 5.10: Effect of the sea wave wavelength on the received power

distance of emitter and receiver to the seawater interface increment the sensitivity requirements of the receiver. Furthermore, the relaxed slope of the curves denote large peak-to-peak variability on the received power.

Figure 5.14 illustrates the effect of the sea wave height on the channel availability. Large sea waves imply higher variations of the seawater's slope, and hence, a greater peak-to-peak variation on the received power. This effect is similar to the observed in Figure 5.15, where the increment of the sea wave wavelength relaxes the surface's slope and the sensitivity requirements.

Finally, in Figure 5.16, the effect of wind speed is depicted. As it was observed in the previous subsection, the shear effect of the wind on the surface produces a reduction on the mean received power, but also a decrement of the maximum power deviation. Therefore, wind speed helps to mitigate the refractive losses due to the changes on the surface's slope.

During this chapter, the problem of an underwater-to-air link has been addressed. It has been observed that the sea surface parameters have critical importance on the performance of the communications link, incrementing the sensitivity requirements on the receiver. Furthermore, it has been observed that the wind speed acts as a smoothing parameter, reducing the harmful effect of highly variable surfaces.

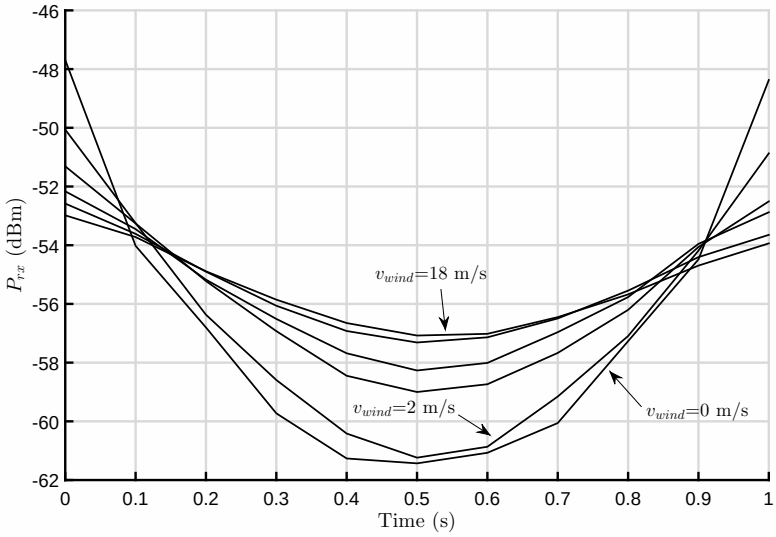

Figure 5.11: Effect of the wind speed on the received power

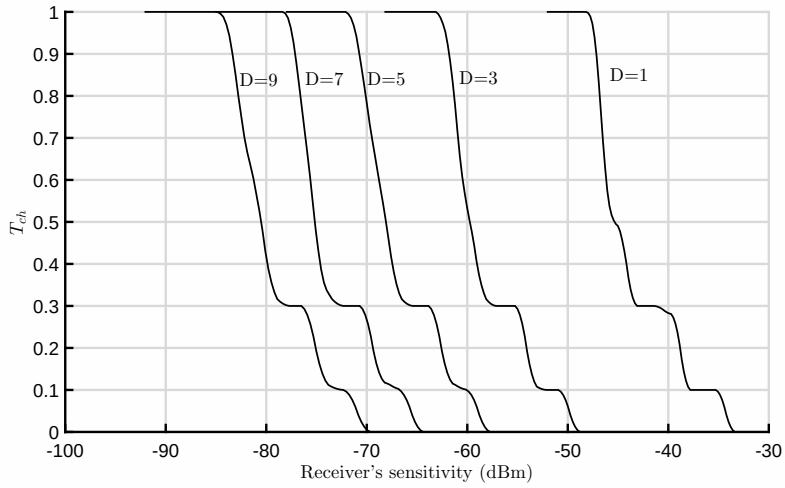

Figure 5.12: Channel availability for different depths

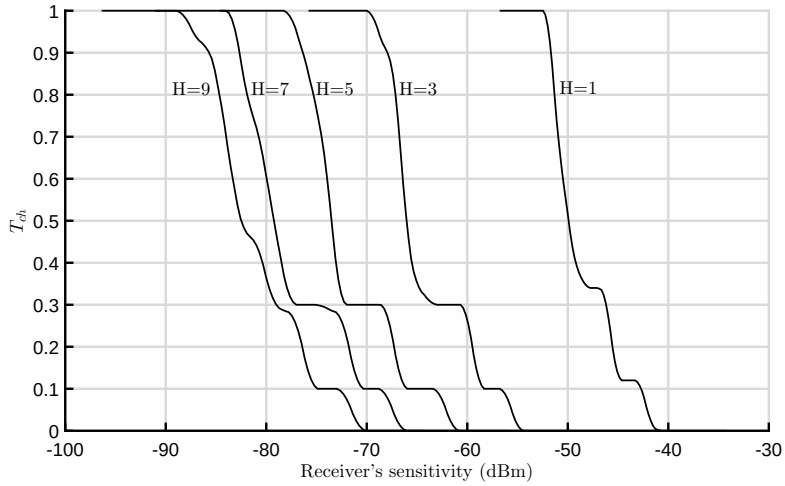

Figure 5.13: Channel availability for different receiver heights

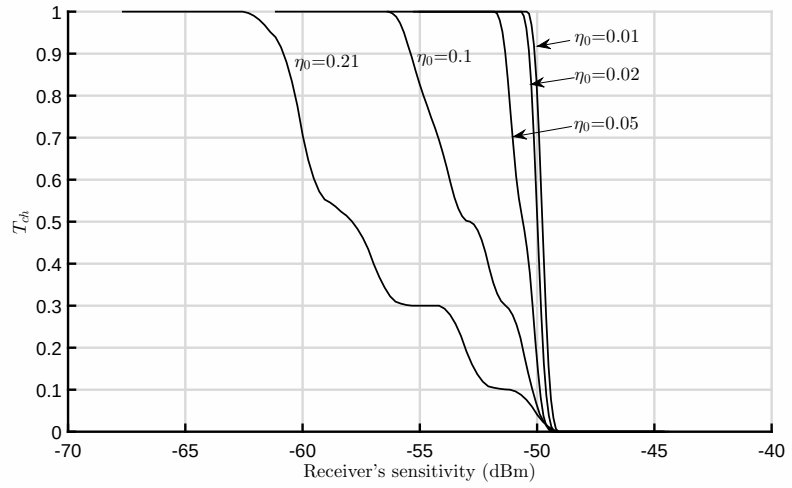

Figure 5.14: Channel availability for different sea wave heights

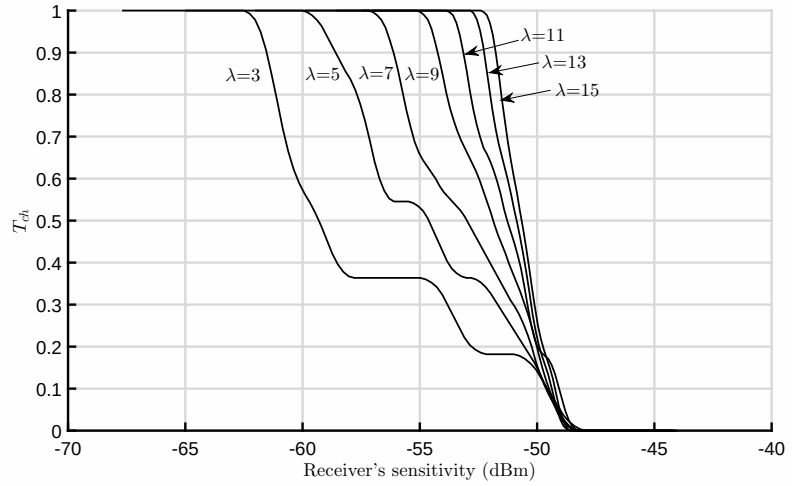

Figure 5.15: Channel availability for different sea wave wavelengths

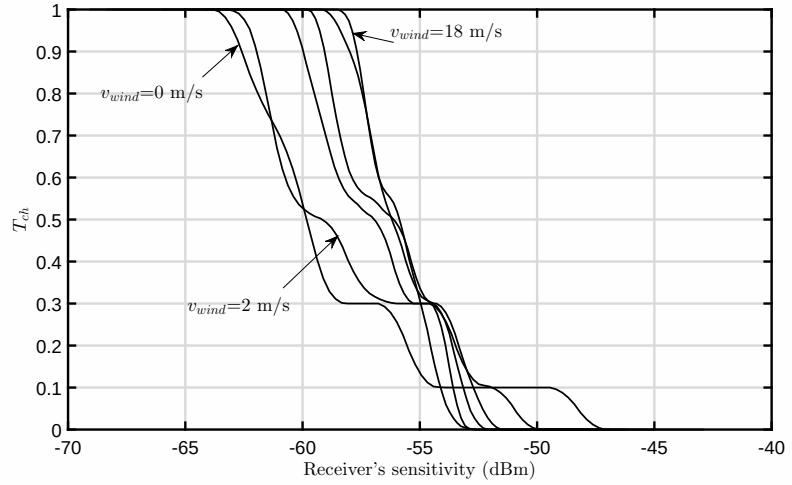

Figure 5.16: Channel availability for different wind speeds

Chapter 6

Statistical modeling of the Underwater Wireless Optical Channel

An UWOC link is fully characterized by its time-dependent impulse response. Generally, the values of the impulse response are samples of a random process defined in two variables: time and multipath delay. Therefore, an actual impulse response would present the form $h(t,\tau)$, where t is time and τ is delay. From this information, if the channel is WSSUS, the scattering function $S(f,\tau)$ of the channel can be extracted as:

$$S(f,\tau) = \mathfrak{F}_{\Delta t}\left\{E\left[h(t,\tau)h^*(t+\Delta t,\tau)\right]\right\} \tag{6.1}$$

The scattering function is the Fourier transform of the autocorrelation function on the variable Δt. f is the Doppler frequency and τ conserves its original meaning. From this function, two important statistical functions can be derived, the Power Delay profile $P(\tau)$ and the Doppler Spectrum $S(f)$. Equations 6.2 and 6.3 show the mathematical description of each function.

$$P(\tau) = \int_{-\infty}^{\infty} S(f,\tau)\,\mathrm{d}f = E\left[\left|h(t,\tau)\right|^2\right] \tag{6.2}$$

$$S(f) = \int_{-\infty}^{\infty} S(f,\tau)\,\mathrm{d}\tau \tag{6.3}$$

From $P(\tau)$, the delay spread can be obtained as it was performed in Chapter 4, and its inverse is related to the coherence bandwidth. Regarding $S(f)$, it allows the calculation of the coherence time by means of its inverse Fourier transform. In this part of the work, the WSSUS approximation is going to be assumed, but in Chapter 7 it will be demonstrated through experimentation. Furthermore, in this work, a statistical approach of both channel gain and bandwidth will be presented, since the implemented simulator only offers independent samples of $h(t,\tau)$ (no dependence with t). In the described situation, the mean delay spread could be approximated from:

$$P(\tau) \approx \frac{1}{N}\sum_i \left|h^{(i)}(\tau)\right|^2 \tag{6.4}$$

Where N is the number of random samples of $h(\tau)$. Note that τ has inverse meaning respect to the original formulation of Chapter 4. However, a statistical description of the delay spread and the channel gain is the main objective of this work, and the parameters obtained in Chapter 4 will be introduced into a statistical inference engine to perform a best fit analysis of their PDFs. As it was mentioned above, the variable t will be introduced into the analysis after obtaining actual measured data.

6.1 Brief analysis of the problem

The simulator presented in Chapter4 calculated the impulse response using a MMCRT algorithm. The resulting impulse response was conformed by the sum of a finite number of Dirac's deltas weighed by a factor that depended on the phenomena the ray suffered during its trajectory. The trajectory followed by each ray is randomly determined by the particle distribution. This particle distribution defines the scenario and hence, the power and delay of each contribution. Nevertheless, at each run of the algorithm, the positions of the particles randomly vary and are uncorrelated between iterations. This fact makes a delay-based simulation impossible, which is a requirement to obtain the scattering function $S(\tau,f)$. However, this simulator allows the calculation of the distributions of both $H(0)$ and τ_{rms}.

If a time-dependent simulator were implemented, the position of each particle (neglecting the effect of the surface due to its complexity) would be necessarily saved and modified at each iteration of the algorithm (only in a region of interest). In the case depicted in Figure 6.1, an initial distribution of uniformly distributed particles would be calculated, the impulse response obtained through Monte Carlo and then, the position of each particle updated introducing a mass transportation effect. For the presented scenario, the amount of memory-saved particles would be increased by the third power of the link distance. If only single scattering were considered, the actual parallel GPU implementation would be straightforward, as each ray would be governed by the same one-hop equation. This concept is not explored in this dissertation and is part of the future research lines.

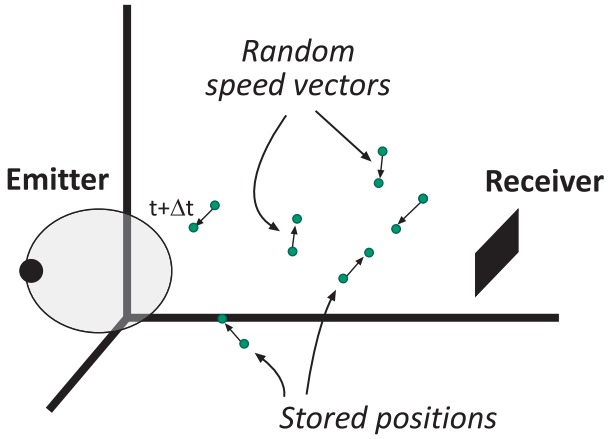

Figure 6.1: Scenario of a time-dependent Monte Carlo simulator

As it was observed in the results of Chapter 4, the impulse response presents a very steep shape, due to the dominance of the LOS component. This type of impulse response can be approximated to the sum of two rectangles as shows Figure 6.2. The first one contains the 95 % of the energy whilst the second represents the tail of the impulse response.

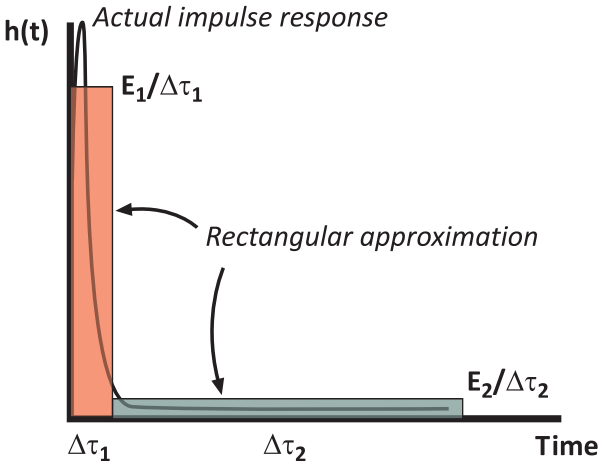

Figure 6.2: Approximation of the impulse response

Using this approximation, the channel gain and the bandwidth can be calculated in terms of E_1 and $\Delta\tau_1$.

$$H(0) \approx E_1 \tag{6.5}$$

$$B \approx \frac{\sqrt{12}}{5\Delta\tau_1} \tag{6.6}$$

These equations are obtained after imposing $E_1 >> E_2 \left(\frac{\Delta\tau_2}{\Delta\tau_1}\right)^2$ and $\Delta\tau_2 >> \Delta\tau_1$. Since the important contributions are defined within the interval $\Delta\tau_1$, the region of interest of a link would be determined by those delays below $\Delta\tau_1$. This limit is associated to a maximum distance d_{lim} described by:

$$d_{lim} = \Delta\tau_1 \frac{c_0}{n_w} \tag{6.7}$$

This distance limits the region of interest to an ellipsoid analogous to a Fresnel zone. Unlike radiofrequency-associated Fresnel zones, in this case the radius of the ellipsoid does not imply a phase shift of π but an important-contribution zone. The focuses of the ellipsoid are the emitter and receiver respectively and the radius of the ellipsoid takes the form:

$$r_{ellip} = \frac{1}{2}\sqrt{d_{lim}^2 - d_{link}^2} = \frac{1}{2}\sqrt{\left(\Delta\tau_1 \frac{c_0}{n_w}\right)^2 - d_{link}^2} \tag{6.8}$$

This zone can be introduced into the aforementioned time-dependent simulator in order to reduce the simulation volume and hence, reduce the number of particles and the memory requirements. Furthermore, this ellipsoid can be used to predict the influence or not of an obstacle amid the link, as it us usual in radio communications. The importance of this zone will be demonstrated in the following sections. Nonetheless, a statistical approach of $\Delta\tau_1$ is needed in terms of the channel parameters to perform this prediction.

6.1.1 Analysis of the statistical nature of the channel gain

Assuming that the received power is defined by the Monte Carlo integration scheme of Equation 4.38, each contribution of the channel gain takes the form:

$$P_i = K_i \frac{e^{-\alpha(\lambda)\sum_j d_j}}{\prod_j d_j^2} \tag{6.9}$$

The PDF of P_i can be approximated by the distribution of the product of $f(d_j)$ and $g(d_j)$, which correspond to the distributions of both numerator and denominator. Since each d_j is independent and equally distributed, the distribution of $1/\prod_j d_j^2$ is related to the n-th power of the inverse distribution of d_j. From random variable algebra, the inverse distribution is defined by Equation 6.10. Introducing the Exponential distribution of d_j in Equation 6.10 and taking the n-th power it yields Equation 6.11.

$$f_y(y) = \frac{1}{y^2} f\left(\frac{1}{y}\right) \tag{6.10}$$

$$g(x) \propto x^{-3/2k} e^{-\mu k/\sqrt{x}} \tag{6.11}$$

k is the number of collisions. Analyzing the numerator, since e^{-X} follows a Power Law distribution when X is exponentially distribution, the numerator would follow a distribution proportional to the n-th power of a power law distribution (Equation 6.12)

$$f(x) \propto x^{-k} \tag{6.12}$$

Although $f(x)$ and $g(x)$ are not independent since they depend on the same d_j terms, they are going to be considered independent for simplicity. Furthermore, as the number of collisions increase, the correlation between numerator and denominator decreases. Under this approximation, the product distribution would present the following proportionality:

$$h(x) \propto x^{-5/2k} e^{-\mu k/\sqrt{x}} \tag{6.13}$$

Nonetheless, the actual distribution of the total received power would be a summation of random variables following $h(x)$. Again, from the random variable algebra, the sum of independent random variables is proportional to the convolution of these variables. Formally, the total received power would take the form of Equation 6.14.

$$f_x(x) \propto \ast_{i=0}^{N-1} C_i x^{-3k_i} e^{-\mu k_i/x} \tag{6.14}$$

Where C_i are constants for each distribution and $*$ denotes convolution. If C_0 is much larger than the rest (highly directive link), the last equation may be reduced to the firs term, yielding:

$$f_x(x) \approx C_0 x^{-5/2k_0} e^{-\mu k_0/\sqrt{x}} \tag{6.15}$$

Note that k_0 is a random variable which defines the number of hops of a ray before impacting the receiver. This number is in $\mathbb{N}$ and is distributed following the recursive expression shown in Equation 6.16.

$$\begin{aligned} p(k=i) &= p\left(k=i-1\right) \cdot \frac{p\left(d_{col,i} > d_{link} - \sum_{j=0}^{i-1} d_{col,j} \middle| \sum_{j=0}^{i-1} d_{col,j}\right)}{p\left(d_{col,i} < d_{link} - \sum_{j=0}^{i-2} d_{col,j} \middle| \sum_{j=0}^{i-2} d_{col,j}\right)} \\ p(k=0) &= 1 - e^{\mu d_{link}} \end{aligned} \tag{6.16}$$

This last equation is defined by a stochastic kernel derived from a continuous-state Markov chain. Using Equation 6.16 and combining it with Equation 6.15, it yields the following final expression depending on μ, d_{link} and implicitly on $\alpha(\lambda)$.

$$p(x) \approx C_0 \sum_{j=0}^{\infty} p\,(k=j)\, x^{-5/2j} e^{-\mu j/\sqrt{x}} \tag{6.17}$$

The last equation can be generalized to an overall version considering only the most significant term. The following distribution function is proposed.

$$f_x(x) \approx C_0 x^{-a} e^{-b/\sqrt{x}} \tag{6.18}$$

This last equation is integrable in the domain $(0, \infty)$, yielding the following final version including the constant C_0 and a shift term x_m.

$$f_x(x) \approx \frac{1}{2}\frac{b^{2(a-1)}}{\Gamma\,[2(a-1)]}\,(x-x_m)^{-a}\, e^{-b/\sqrt{x-x_m}} \quad /x \in [x_m, \infty) \tag{6.19}$$

a, b and x_m are the parameters of the distribution, which is very similar to a Gamma distribution. This approximation will be included in the database of distributions used in Section 6.3. Nonetheless, the approximations made to achieve Equation 6.19 would probably make the distribution's goodness-of-fit very sensitive to big values of r_{ellip}. The following section introduces the statistical procedure followed to perform a best-fit approach of $H(0)$ and B.

6.2 Statistical procedure

As it has been already mentioned, one of the main objectives of this work is to perform a statistical approach of $H(0)$ and B to provide a preliminary prediction tool during the UWOC link planning stage. This type of information is very important since it allows a better power budget calculation and a maximum data rate estimation. One of the most important parameters in a statistical-inference problem is the sample size. This sample size depends on the variance of the underneath process, which is *a priori* unknown.

The implemented procedure is based on the following steps.

1. Generate N random impulse responses.
2. Obtain the N values of $H(0)$ and bandwidth.
3. Perform a Maximum Likelihood Estimation with every distribution in the database.
4. Reject or accept the fit based on a Kolmogorov-Smirnov goodness-of-fit test.

The sample size N depends on the variance of the unknown distribution. Instead of imposing a computationally-inefficient over-dimensioned sample size, an iterative process has been performed within processes 1 and 2 of the above procedure. This iterative process is based on an error minimization of the experimental cumulative distribution function. The minimization problem is defined in Equation 6.20.

$$\varepsilon_n = \frac{1}{n}\sum_{\Omega_n} \left| \tilde{F}^{(n)}(\Omega_n) - \tilde{F}^{(n-1)}(\Omega_n) \right|^2 \tag{6.20}$$

Where Ω_n is the support at iteration n, and $\tilde{F}^{(n)}(\Omega)$ is the ECDF. Two aspects must be taken into account. In first place, the support Ω_n is defined by the random samples X_i, and furthermore:

$$\Omega_n = \Omega_{n-1} \cup X_n \tag{6.21}$$

Since $\tilde{F}(\Omega_i)$ has a different support at each iteration, in order to carry out Equation 6.20, $\tilde{F}(\Omega_{n-1})$ is interpolated to the domain defined by Ω_n.

The evaluated distributions for the parameters of interest are reflected in Table 6.1.

6.3 Results obtained through simulation

In the current section, different results for the scenarios defined in Chapter 4 are presented. The number of impulse response samples was determined for an error below 10^{-3}. Moreover, in subsection 6.3.2 a qualitative relationship between the channel's parameters and the distribution's parameters is carried out.

Distribution	Parameters
Gamma	a, b
Birnbaum-Saunders	β, γ
Burr Type XII	α, c, k
Exponential	μ
Generalized Extreme Value	k, σ, μ
Log-Normal	μ, σ
Nakagami	μ, ω
Normal	μ, σ
Rayleigh	b
Rician	s, σ
Student's T	ν
Wald	μ, λ
Weibull	a, b
Proposed distribution	a, b, x_{min}

Table 6.1: Tested distributions

6.3.1 Channel gain and Bandwidth

After applying the procedure defined in the previous section, and using the distributions of Table 6.1, the following p-values for the baseline scenario have been obtained. It can be observed that only Burr, T-Location-Scale, Generalized Extreme Value and the proposed distribution present significant p-values for the channel gain. Therefore, this three distributions will be the only ones kept in the database of possible distributions. Regarding the bandwidth, the last four except the proposed distribution are the suitable distributions. Figure 6.4 depicts the histograms of the channel gain and the bandwidth for the baseline scenario.

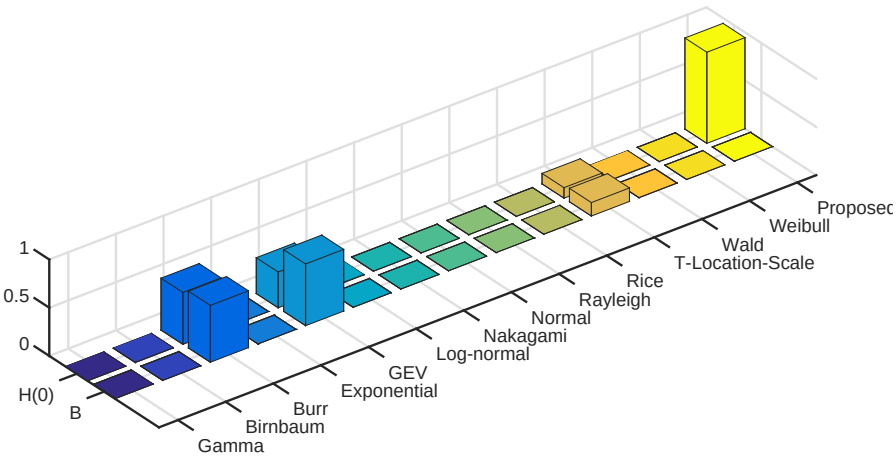

Figure 6.3: Obtained p-values for the baseline scenario

In order to obtain a more general approach, the percentage of scenarios covered by each distribution has been calculated. These percentages are calculated attending to those cases whose associated p-values are higher than a confidence α. Figures 6.5 and 6.6 depict these curves vs the parameter α.

It can be observed that channel gain is very accurately described by the proposed distribution, but it is even better modeled by a Generalized Extreme Value distribution. As it was commented above, the proposed distribution is sensitive to situations in which the energy is not concentrated around the emission axis. Observing the fitting results, it can be almost assured that both channel gain and bandwidth follow a Generalized Extreme Value distribution. The following subsection comments the relationship between the physical parameters and the distribution parameters.

6.3.2 Comments on the relationship between the distribution and the channel's parameters

The GEV PDF is described by Equation 6.22.

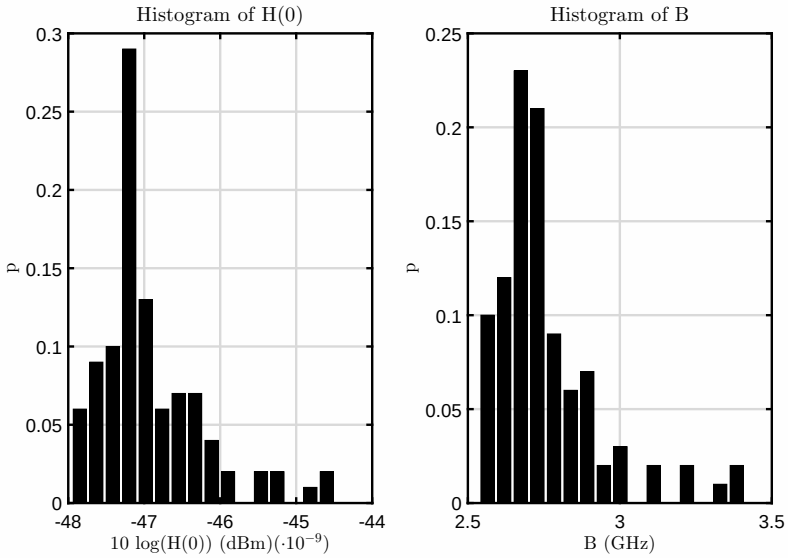

Figure 6.4: Histograms of the channel gain and the bandwidth for the baseline scenario

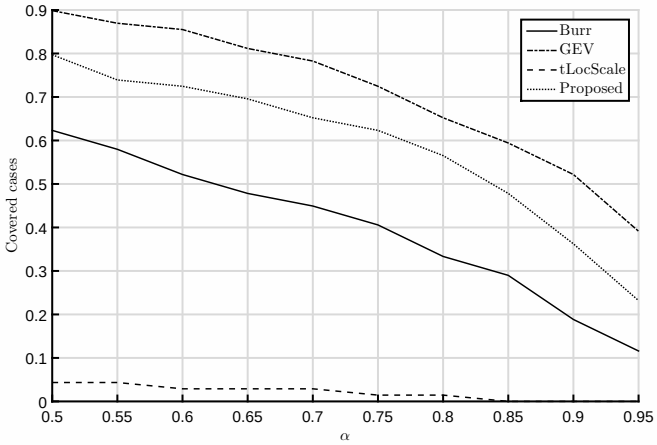

Figure 6.5: Percentage of well-described scenarios in terms of Channel gain vs α

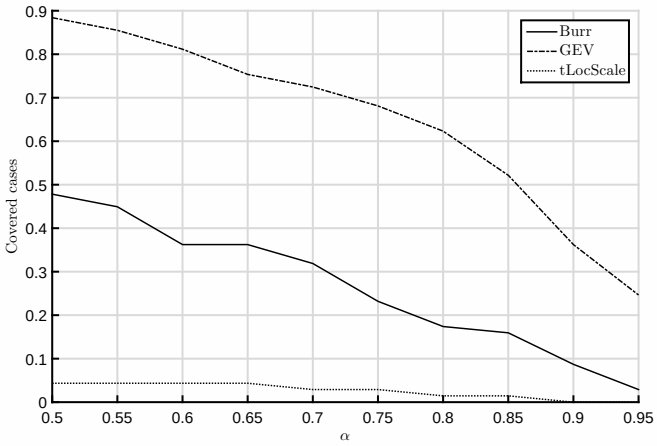

Figure 6.6: Percentage of well-described scenarios in terms of Bandwidth vs α

$$f_x(x) = \frac{1}{\sigma} t(x)^{1+\xi} e^{-t(x)}$$
$$t(x) = \begin{cases} \left(1 + \left(\frac{x-\mu}{\sigma}\right)\xi\right)^{-1/\xi} & \xi \neq 0 \\ e^{-(x-\mu)/\sigma} & \xi = 0 \end{cases} \tag{6.22}$$

Its mean value and variance are defined in Equation set 6.24.

$$E[x] = \mu + \frac{\sigma}{\xi}(\Gamma(1-\xi) - 1) \tag{6.23}$$

$$\mathrm{Var}(X) = \left(\frac{\sigma}{\xi}\right)^2 \left(\Gamma(1-2\xi) - \Gamma^2(1-\xi)\right) \tag{6.24}$$

Where μ is the location parameter, σ the scale parameters and ξ the shape parameter. This last parameter defines the support of the distribution. Since the channel gain can only present values on $\mathbb{R}^+$, and using the properties of the GEV, the shape parameter is bounded also in $\mathbb{R}^+$. From the Fisher-Tippett Theorem [135], the maximum of a large sequence of equally distributed random variables follows a Generalized Extreme Value distribution. Therefore, the channel gain follows a GEV distribution because its value can be considered as the maximum of the impulse response, due to its abrupt shape. Analyzing the parameters for increasing link ranges (Figure 6.7), it can be observed that both μ and σ, which primarily define the mean and variance of the distribution, present an exponential decay as the received power does. However, at very short distances, the model does not fit the data adequately, as the negative value of ξ suggests. In Figure 6.8, both μ and σ increase with the directivity. However, ξ decreases with the directivity and hence, higher directivity imply better SNR performance. The particle radius influence is depicted in Figure 6.9, where the effect of the BSF can be observed at the local maxima of μ and σ. Above this maximum value, the variance decreases as the scattering effect is also reduced. Finally, the effect of the particle concentration is shown in Figure 6.10. Recalling that the baseline particle radius was 100 nm, an increase in the number of particles per cubic meter produces not only a decrement on the mean received power, but also a decrement on the SNR. However, for the tested scenario, due to the small number of particles, the mean received power increases because of the BSF.

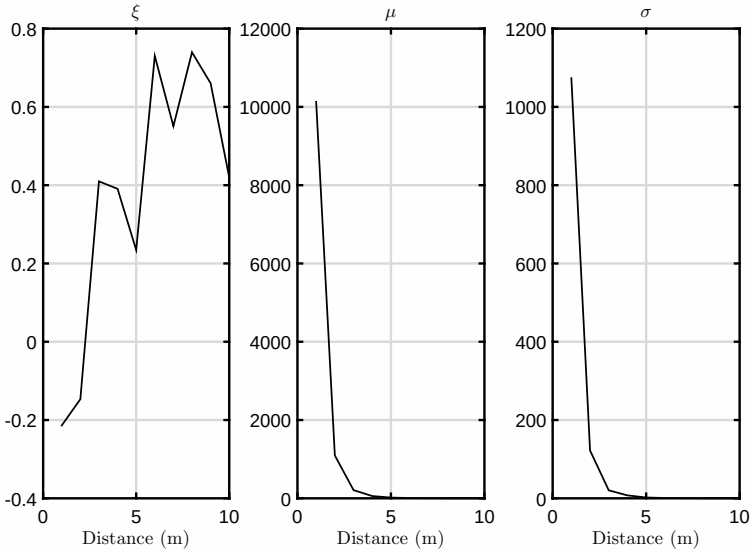

Figure 6.7: Evolution of the GEV parameters with the link range

6.4 Fresnel zones and Beam Spread Function

During Section 6.1, the concept of Fresnel zone appeared. In RF, Fresnel zones are volumes that have associated phase shifts below a certain limit. This manner, the first Fresnel zone is limited to those phase shifts under π, the second one to shifts below 2π and so on. Moreover, in the same section the Fresnel zone was defined as the illuminated volume at which its power contribution is related to the 95 % of the total received energy.

If the BSF of the channel $\xi(d, r)$ were known, with d the traveled distance and r the radius over the orthogonal plane of the direction of propagation, the received power could be approximated by Equation 6.25. Figure 6.11 depicts the situation.

$$P_{rx}(\theta') \approx 2\pi \int_0^{\theta'} P_{tx}(\theta)\xi(d_{link}\cos\theta, d_{link}\sin\theta)\left(\frac{A_{pd}\cos\theta}{d_{link}}\right)^2 \mathrm{d}\theta \tag{6.25}$$

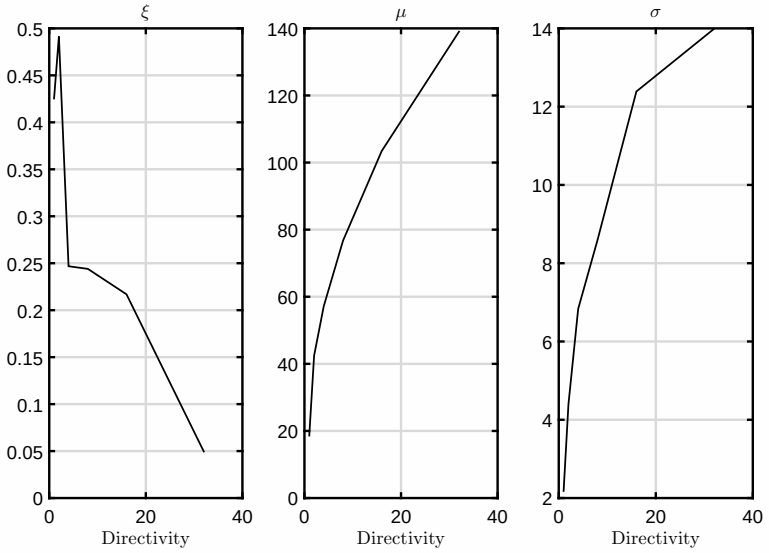

Figure 6.8: Evolution of the GEV parameters with the emitter's directivity

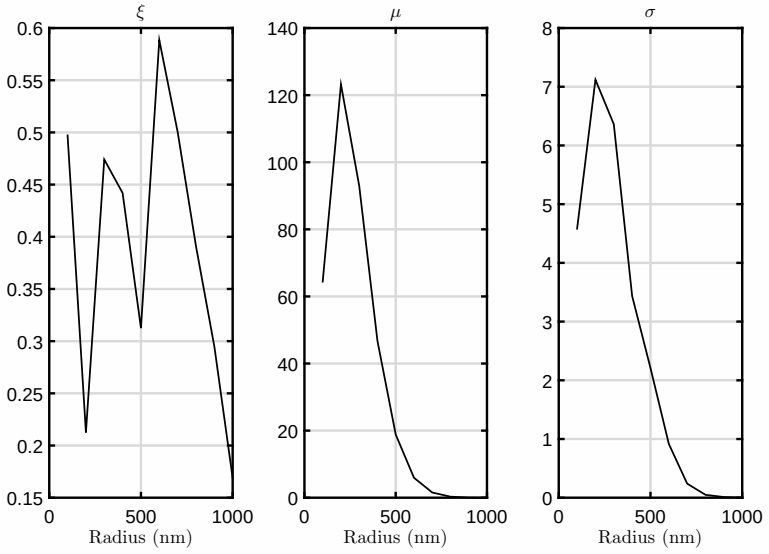

Figure 6.9: Evolution of the GEV parameters with the particle radius

Note that the BSF has generally units of watts per square meter. However, in this case, this BSF has been normalized and is expressed uniquely as m^{-2}. The radiant intensity $P_{tx}(\theta)$ has units of watts per steradian. Since $d\Omega \approx A_{eff}/d^2$, the equation is consistent in units with the squared A_{eff} term.

Note that $P_{rx}(\theta') = P_{rx}$ when $\theta' = \pi/2$, and the BSF has been considered azimuthally symmetric, which is a common assumption in homogeneous media. This nomenclature eases the following description regarding the calculation of $\Delta\tau_1$, which can be obtained in terms of a maximum elevation angle θ_{max}. This θ_{max} is the angle at which the integrated power is the 95 % of the total received power. Mathematically:

$$\theta_{max} = \underset{\theta}{\arg} \{P_{rx}(\theta) = 0.95 P_{rx}\} \tag{6.26}$$

Under the geometrical restrictions of the problem, this θ_{max} implies a hypothetical maximum traveled distance equal to $d_{link}\,(\cos\theta + \sin\theta)$. Introducing this distance into Equation 6.7 it yields the following approximation of the Fresnel zone's radius.

$$r_{ellip} \approx \frac{d_{link}}{2} \tan\theta_{max} \tag{6.27}$$

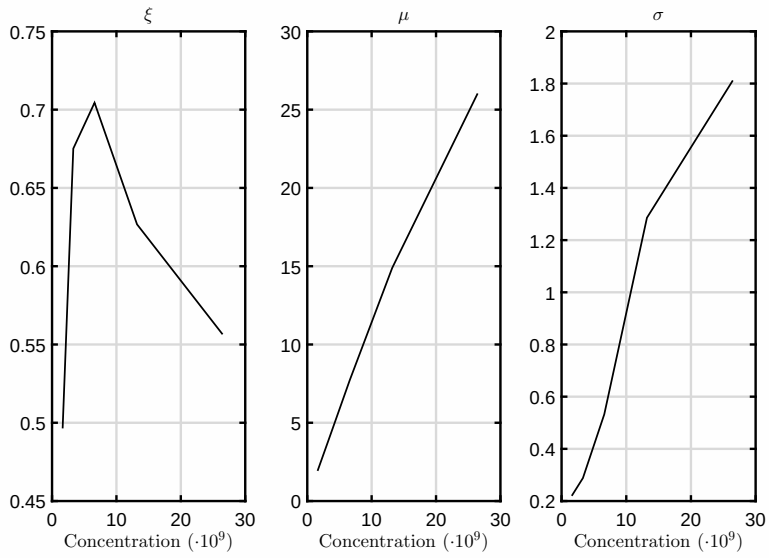

Figure 6.10: Evolution of the GEV parameters with the concentration of particles

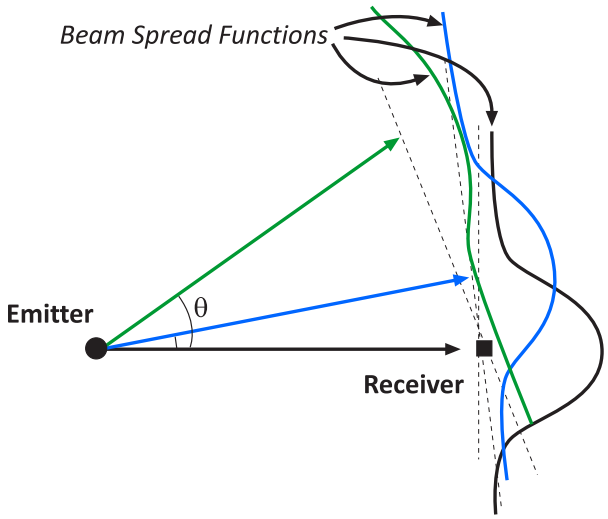

Figure 6.11: Integration of the received power using the Beam Spread Function

6.4.1 Beam Spread Function

The BSF describes the spatial dispersion of an infinitesimal solid angle respect to the traveled distance, which is related to the scattering particles of the medium. The BSF can be understood as the light intensity on a plane perpendicular to the propagation distance at each traveled distance d. If the medium is homogeneous, this BSF would present revolution symmetry respect to the propagation axis, and each point of the plane would be defined by a radius r in polar coordinates.

From Cochenour's work in [16], the BSF can be expressed in terms of the spatial frequency κ of the light intensity and the spatial Fourier transforms of both intensity and scattering. To simplify the calculation, the BSF is expressed as the following zeroth order Hankel transform.

$$\xi(d,r) = \frac{1}{2\pi}\int_0^\infty I(\kappa,d)S(\kappa,d)J_0(\kappa r)\kappa\,\mathrm{d}\kappa \tag{6.28}$$

For the approximation presented in Equation 6.25, the emitter's radiation pattern is divided in an infinite number or rays. At each direction, the spatial distribution of the incident light can be considered as a Dirac's Delta. Hence, $I(\kappa,d)$ is an unitary constant. Cochenour et al. divided the resulting BSF into a non-scattered term $\xi_{NS}(d,r)$ and a scattered term $\xi_S(d,r)$, but in this case this approximation is not used. The scattering term $S(\kappa,d)$ is defined in Equation 6.29

$$S(\kappa,d) = e^{-c(\lambda)d}e^{b(\lambda)\int_0^d P(\kappa(d-z))\,\mathrm{d}z} = e^{-c(\lambda)d}e^{b(\lambda)d\int_0^1 P(d\kappa\nu)\,\mathrm{d}\nu} \tag{6.29}$$

$P(x)$ is the Hankel transform of the scattering phase function and $\nu = 1 - z/d$. Introducing Equation 6.29 into Equation 6.28, it yields:

$$\xi(d,r) = \frac{e^{-\alpha(\lambda)d}}{2\pi} e^{-b(\lambda)d} \int_0^\infty e^{b(\lambda)d \int_0^1 P(d\kappa\nu)\,\mathrm{d}\nu} J_0(\kappa r)\kappa\,\mathrm{d}\kappa \tag{6.30}$$

This equation is numerically integrable. Figure 6.12 depicts $\xi(d,r)$ at different distances and scattering coefficients for isotropic scattering and a Henyey-Greenstein scattering with $g = 0.9$ respectively.

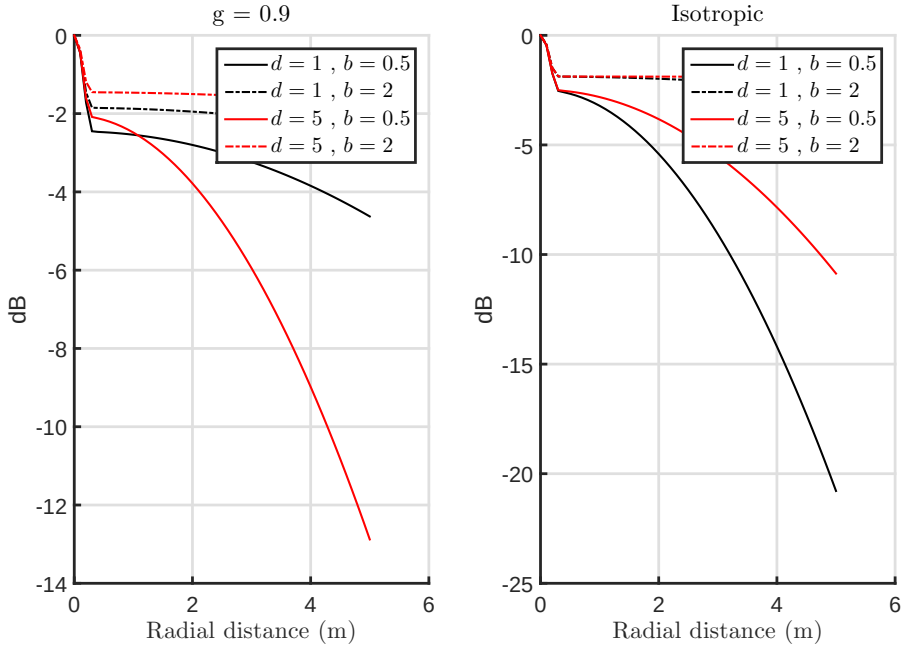

Figure 6.12: Normalized Beam Spread Function for isotropic scattering (right) and Henyey-Greenstein with parameter g = 0.9 (left)

It can be observed that the scattering coefficient and the phase function shape affect the width of the BSF. Furthermore, the obtained BSF may be approximated by the sum of two Gaussians in a wide range of distances and scattering coefficients. Under this assumption, a fitting analysis can be performed to obtain a relationship between $b(\lambda)$, g,d and the peak and width of $\xi(d,r)$. Sweeping $b \in (0,2)$, $g \in (0,1)$ and $d \in (1,10)$ the following relationships were obtained.

$$\xi(d,0) \approx 8.231 e^{-b(\lambda)(1-0.13g)\,d} \tag{6.31}$$

$$\eta \approx (1 - 6.6 \cdot 10^{-3} b(\lambda)) e^{\left(1 - e^{5 \cdot 10^{-4} g\, b(\lambda)}\right) d^2} \tag{6.32}$$

$$\sigma_1^2 \approx 4.6 \cdot 10^{-3} + 2.22 \cdot 10^{-4} b(\lambda) + 1.74 \cdot 10^{-4} e^{0.169 g\, b(\lambda)\, d} \tag{6.33}$$

$$\sigma_2^2 \approx (3.87g + 0.976 b(\lambda)^2) e^{(0.39 b(\lambda) - 0.663g)d} \tag{6.34}$$

With:

$$\xi(d,r) \approx \xi(d,0) \left(\eta e^{-\frac{r^2}{2\sigma_1^2}} + (1-\eta) e^{-\frac{r^2}{2\sigma_2^2}} \right) \quad / \sigma_1 < \sigma_2 \tag{6.35}$$

η is a weighing factor between the two gaussians. Generally, the BSF is formed by a very narrow component due to the privileged forward direction and a wide component due to the multiple scattering phenomena. Note also that the expression of $\xi(d,0)$ is completely compliant with the experiments of Cochenour [16]. This terms describes that the higher the average cosine of the particle's phase function, the lower the actual power loss in the forward direction due to beam spreading. Regarding σ_1^2, the obtained approximation can be enhanced since for lower values of $b(\lambda)$ (out of the swept ranges), the BSF must present a more abrupt behavior. The following R^2 goodness-of-fit values were obtained for the approximations presented in this section.

6.4.2 Analysis of the resulting Fresnel zones

Using the approximation obtained in the previous subsection, the analysis of the Fresnel zones can be reduced to the solution of Equation 6.25. Figures 6.13 and 6.14 illustrate θ_{max} for the cases presented in Figure 6.12, but for

Parameter	R^2
Two-Gaussian approximation of the BSF	$\{R^2_{max} = 1.0, R^2_{min} = 0.85\}$
$\xi(d, 0)$	0.99
η	0.989
σ_1^2	0.945
σ_2^2	0.955

Table 6.2: Goodness-of-fit R^2 values for the approximations presented in this section. The support was conformed by 400 data points.

a pure lambertian emitter ($\theta_{1/2} = \pi/3$) and a lambertian emitter with $m = 20$.

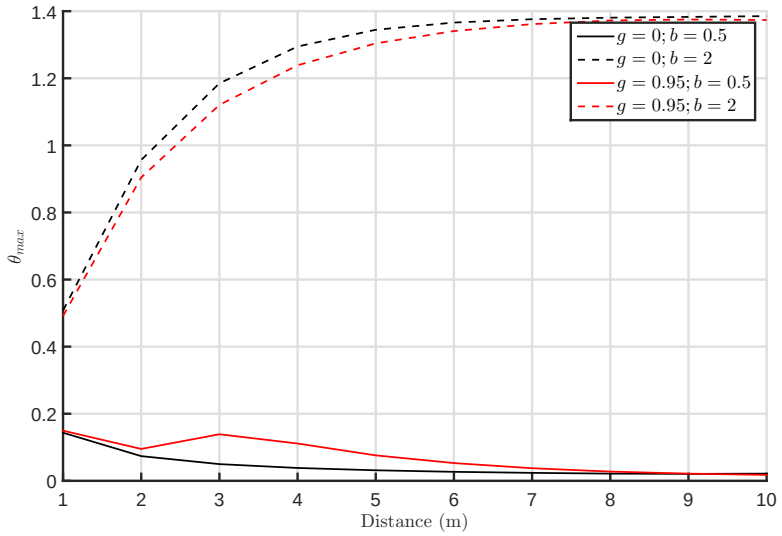

Figure 6.13: θ_{max} for both isotropic and Henyey-Greenstein scatterings at different distances for a pure lambertian emitter

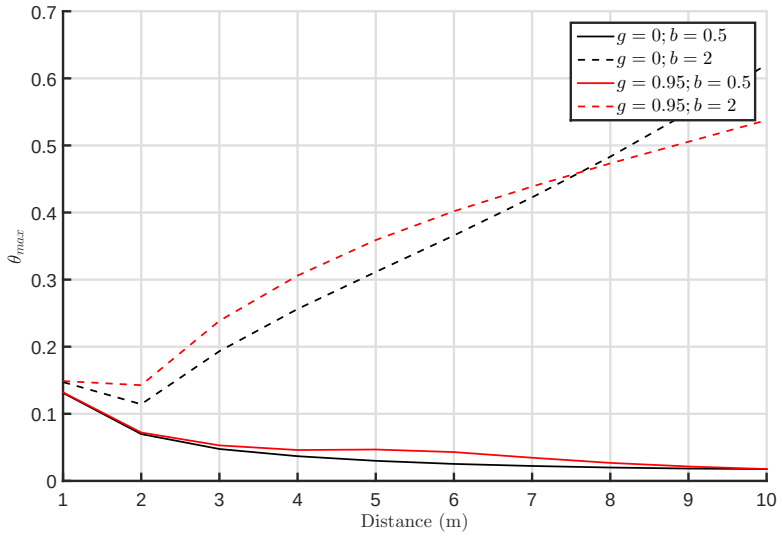

Figure 6.14: θ_{max} for both isotropic and Henyey-Greenstein scatterings at different distances for a lambertian emitter with $m = 20$

It can be observed that the directivity of the emitter is inversely proportional to θ_{max}, since the energy is concentrated in a smaller solid angle as the directivity increases. Furthermore, for small particle concentrations (low $b(\lambda)$),θ_{max} decreases with the distance regardless the directivity. This occurs because the scattered energy is very small and the majority of the energy remains on the forward direction. Finally, high concentrations invert

the relationship of θ_{max} with the link's range, increasing with the distance. Performing an analysis similar to the one carried out in the previous subsection, an approximate formula to predict the θ_{max} can be obtained. Equation 6.36 shows the result of the approximation, which was obtained with an R^2 value of 0.9604.

$$\theta_{max} \approx 0.2971 b(\lambda)\, g\, m\, d_{link} \left(1 - 6.8 \cdot 10^{-3} b(\lambda)\, g^2\right) e^{-0.157 m\, d_{link}} + 9 \cdot 10^{-4} m\, d_{link}\, b(\lambda)^2 \tag{6.36}$$

Using Equation 6.36 combined with Equation 6.27, r_{ellip} can be easily calculated. This approximation has three main applications. Knowing the Fresnel zone to a 95% of the received power and considering steep impulse responses, the maximum bandwidth can be directly calculated using Equations 6.36 and 6.7. On the other hand, this approximation allows the link designer to consider whether an obstacle affects the transmission or not. Finally, the simulation of UWOC links is reduced to a very small volume if only the significant ellipsoid is considered. As it was commented, the available bandwidth can be estimated using Equation 6.6 and introducing the definition of the Fresnel zone's radius.

$$\tilde{B} = \frac{c_0 \sqrt{12}}{5 n_w d_{link}} \cos\theta_{max} \tag{6.37}$$

The empirical formulae presented in this section have been obtained through simulation. Therefore, they may not accurately model reality and further research acquiring actual data from real scenarios should be carried out. Nonetheless, the obtained predictions seem to indicate a logical trend on the estimated bandwidths.

6.5 Statistical model for big opaque particles

Generally, the literature only treats the problem of scattering. Nonetheless, in certain scenarios, big opaque particles such as sand grains are part of the heterogeneous underwater medium. In coastal scenarios, under shallow water regimes, the forces of the seawater mass transportation on the seabed generate a random distribution of big opaque particles amid the link. In this section, a purely geometrical model to predict the influence of this particles is presented.

6.5.1 Definition of big opaque particle

A big opaque particle is a piece of matter whose spectral absorption is high enough to consider that there is no transmission and whose dimension assures that the diffraction is negligible. If a plane wave passes through a circular slit of radius R, the diffraction pattern $I(\theta)$ is determined by the following Airy disk:

$$I(\theta) = 4 I_0 \left(\frac{J_1\left(\frac{2\pi R}{\lambda} \sin\theta\right)}{\frac{2\pi R}{\lambda} \sin\theta} \right)^2 \quad / \forall \phi \tag{6.38}$$

The angle θ is defined from the center of the slit. However, since the interest of this work is focused on particles and not slits, from Babinet's principle it can be stated that the diffraction pattern of the particle is the same as the slit's except on the forward direction. For very high R/λ ratios, the overall diffracted intensity tends to zero, since:

$$\lim_{x \to \infty} \frac{J_1(x)}{x} = 0 \tag{6.39}$$

For near field, which occurs when the Fresnel number (Equation 6.40) satisfies $F >> 1$, the diffracted intensity is governed by the Kirchoff-Fresnel equation. The resulting near field patterns are also determined by the R/λ ratio and the result is similar to the far field case.

$$F = \frac{R^2}{d\lambda} \tag{6.40}$$

d is the distance from the particle to the plane of interest. Hence, a big opaque particle will only block the incident light producing a shadow in a far field situation. This shadow could be projected over the photodiode's area producing a power loss. The following subsection introduces the mathematical formulation of the power loss.

6.5.2 Mathematical formulation

Lets consider a LOS situation in an UWOC link, with an uniform distribution with density ρ of big opaque particles or radius R. If the emitter has a radius R_{tx} and the receiver a radius R_{rx}, the volume enclosed by the LOS emission would be:

$$V_w = \frac{\pi}{3} d_{link} \left| \frac{R_{tx}^3 - R_{rx}^3}{R_{tx} - R_{rx}} \right| \tag{6.41}$$

Figure 6.15 depicts the situation. The total volume is the difference of two conic volumes. It is intuitive to assume that the number of particles within V_w would follow a Binomial distribution. This distribution has a mean value of ρV_w. Furthermore, the hypothetical maximum number of particles of radius R in the volume V_w is $N_{max} = \lfloor 3V_w/(4\pi R^3) \rfloor$. From N_{max} and the mean of the distribution, it is straightforward to state that:

$$n \sim B\left(\rho \frac{4\pi}{3} R^3, N_{max}\right) \tag{6.42}$$

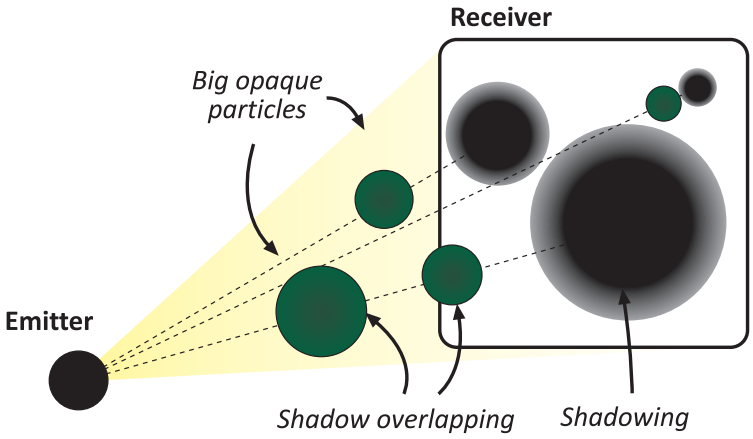

Figure 6.15: LOS component subject to the presence of big opaque particles

Observing Figure 6.15 it is logical to notice that if the emitter were a point source, the projected shadow of a close-to-the-emitter particle would tend to infinity. Hence, the theoretical analysis of the problem must be performed considering the emitter as an extended source. Generally, the power loss due to an opaque object over an area A_{rx} is determined by the linear projection of the object's cross section according to the slope of the cone determined by the two areas (Figure 6.16). Appendix B, demonstrates this assumption. The section of the cone defined by emitter and receiver at a distance d_i is defined by:

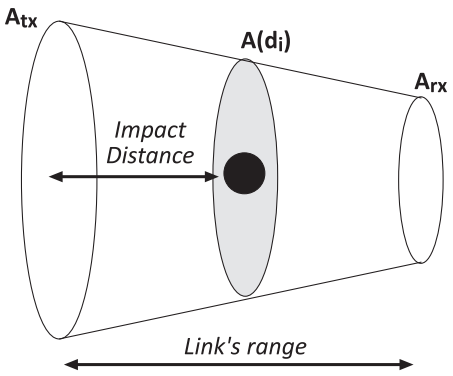

Figure 6.16: Power loss due to the effect of big opaque particles

$$A(d_i) = \pi \left(R_{tx} + \frac{d_i}{d_{link}} (R_{rx} - R_{tx}) \right)^2 \tag{6.43}$$

The power loss would be related to the amount of receiver's area that is shadowed by the particle. This amount can be expressed as a ratio between the particle's cross section and the area of Equation 6.43. The received power can be expressed as:

$$P_{rx} = P_{tx} \frac{m+1}{2\pi} \frac{A_{pd}}{d_{link}^2} e^{-c(\lambda) d_{link}} \zeta \tag{6.44}$$

Where ζ is a random variable that expresses the reduction of the photoreceiver's area as:

$$\zeta = 1 - \pi R^2 \sum_{i=1}^{n} \frac{\gamma_i}{A(d_i)} \tag{6.45}$$

Where γ_i is a variable that indicates the overlapping degree of each particle with the rest. This analysis neglects the effect of the beam spreading and should be included in further research. Probably, the analysis would be analogous to the current proposal but after applying an integration of the form of Equation 6.25. In that case, V_w should be increased to the volume of a truncated ellipsoid defined by the above-studied Fresnel zone and the emitter and receiver's areas. Furthermore, $A(d_i)$ must be transformed to the area of the intersected ellipsoid at d_i.

If the effect of γ_i were neglected, an unrealistic worse case scenario would be considered. In that situation, all the particles within V_w would produce shadowing and hence, the power loss would decay beyond zero. However, for a number of particles relatively small, this situation would present a very small probability. d_i follows a truncated exponential distribution from $d_i = 0$ to $d_i = d_{link}$. Finally, the resulting distribution of $A(d_i)^{-1}$ can be expressed as follows according to the random variable algebra (Equation 6.46). Figure 6.17 depicts the experimental CDF of the inverse area vs the approximation.

$$f_x(x) = K \cdot (\pi x)^{-3/2} e^{-\frac{\mu d_{link}}{R_{rx} - R_{tx}} \left((\pi x)^{-1/2} - R_{tx} \right)} \tag{6.46}$$

$$K = \frac{\pi \, \mu \, d_{link}}{2|R_{rx} - R_{tx}|} \tag{6.47}$$

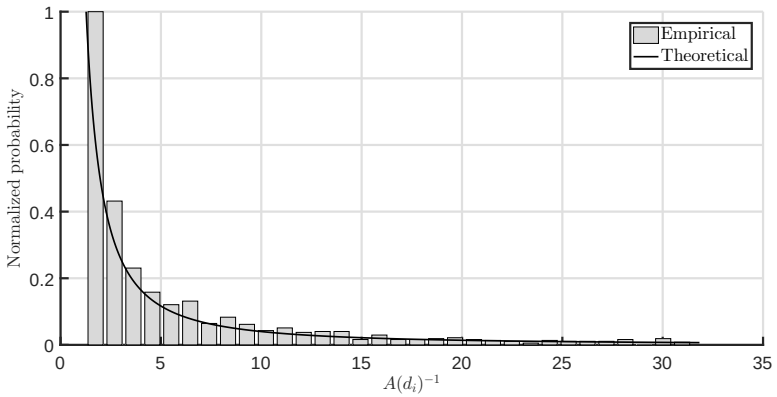

Figure 6.17: Comparison between the histogram and the PDF of Equation 6.46. $\rho = 10^-4$, $d_link = 5$ m, $R_{tx} = 5$ cm, $R_{rx} = 1$ cm, $R = 1$ mm.

Assuming a big number of particles and using Wald's equation, the PDF of ζ can be approximated to a normal distribution $\mathcal{N}(\mu, \sigma^2)$ with the following parameters.

$$\begin{aligned} \mu &\approx 1 - \pi R^2 E[n] \cdot E[x] \\ \sigma^2 &\approx \left(\pi R^2\right)^2 \left(E[n]\sigma_x^2 + E[x]^2 \sigma_n^2 \right) \end{aligned} \tag{6.48}$$

$E[x]$ and σ_x^2 are the expected value and variance of Equation 6.46 respectively. This approximation would present an error that increases as the number of particles decrease. Furthermore, since γ_i has been neglected, the estimated loss may become negative. Therefore, this approximation is valid for a middle-range average number of particles. Figure 6.18 depicts three example situations where an experimental CDF following equation 6.45 is compared to the normal approximation. The first scenario is an scenario with a reduced average number of particles, the second corresponds to a very polluted environment and finally the third presents a moderate number of particles.

As it was commented, the loss surpasses the threshold and becomes negative for the most polluted scenario. In order to fix this issue, the simulated PDF could be truncated at zero, introducing the left-side excess probability as a delta at the origin.

6.5.3 Influence of the link's parameters on the SNR

In a situation in which Johnson and shot noises could be neglected respect to the noise associated to this kind of particles, the SNR of the link would be defined by the quotient $E^2[\zeta]/\sigma_\zeta^2$. The baseline scenario of Table 6.3 is

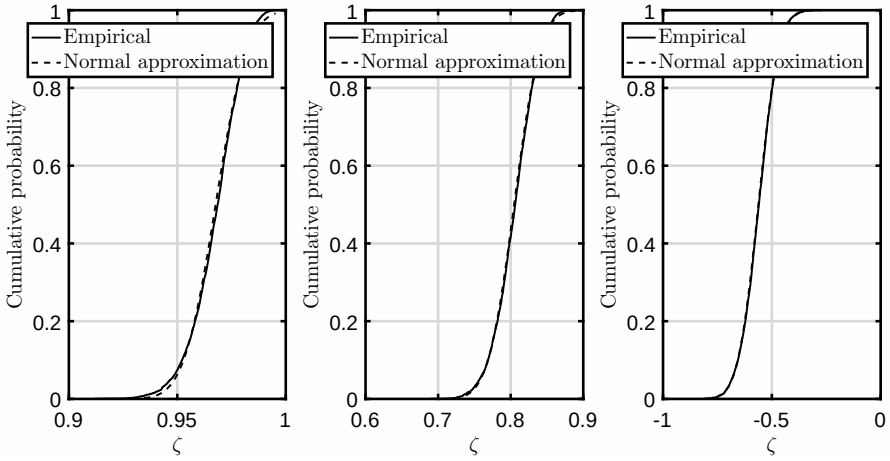

Figure 6.18: Comparison between the experimental CDF and the normal approximation in a link shadowed by big opaque particles. The left figure corresponds to a link in which the average number of particles is approximately 16, the center figure to 100 particles, and the right figure is associated to a very polluted environment with an average of 1000 particles within the volume. Note the precision of the normal approximation as the number of particles increase.

defined to analyze the influence of different parameters in a scenario with big opaque particles. Note that this SNR must be understood as a lower bound since the overlapping of shadows has not been considered.

Parameter	**Value**
R_{tx}	10 cm
R_{rx}	1 cm
R	1 mm
ρ	10^3 m^{-1}
d_{link}	5 m

Table 6.3: Baseline scenario to analyze the influence of the link parameters on the SNR

First of all, the influence of the link's range has been obtained through simulation. From the mathematical development presented above, the volume of water enclosed by emitter and receiver increases linearly with d_{link}. This increment is linked to a greater average number of particles, and hence, the SNR decreases. Figure 6.20 depicts the influence of the emitter radius. It can be observed that large emitters are subject to the influence of a higher amount of particles, shadowing the output power of the lamp. Furthermore, very small emitters are also highly influenced by this type of particles, since their emission surfaces are comparable to the particle cross section. Note that there is a local maximum at which the influence of the particles is minimized. This optimal emission area is of high importance in very turbid environments, where the maximization of the SNR is mandatory. In further research, the mathematical expression of the optimal emitter radius depending on the concentration, and the receiver and particle radii may be found. On the contrary, in Figure 6.21 it can be observed that bigger light collection areas diminish the influence of these particles, improving the SNR performance but saturating at certain level. The initial enhancement occurs because although there is a bigger amount of particles within the emission cone, the relationship between the receiver's area and the particle area increases rapidly. However, beyond a threshold radius the marginal improvement of the SNR is close to zero, since the increment on the area is compensated by the greater amount of particles. Figure 6.22 shows the influence of the particle radius. This parameter has the bigger influence on the SNR since the particle cross section to receiver area ratio rapidly increases. Finally, the influence of the concentration of particles can be observed in Figure 6.23. The concentration of particle has two main effects according to the theoretical analysis above. The first one is to increment the average number of particles, and the second one is to produce more collisions with particles at closer distances, reducing the effective output power of the lamp.

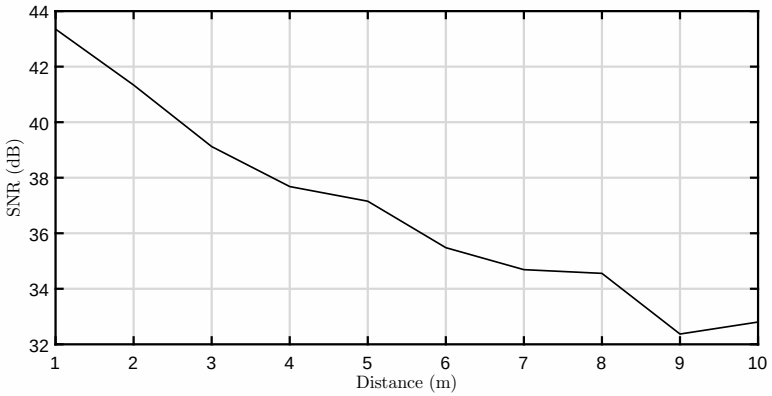

Figure 6.19: SNR of a link defined by the big opaque particle distribution vs the link's range

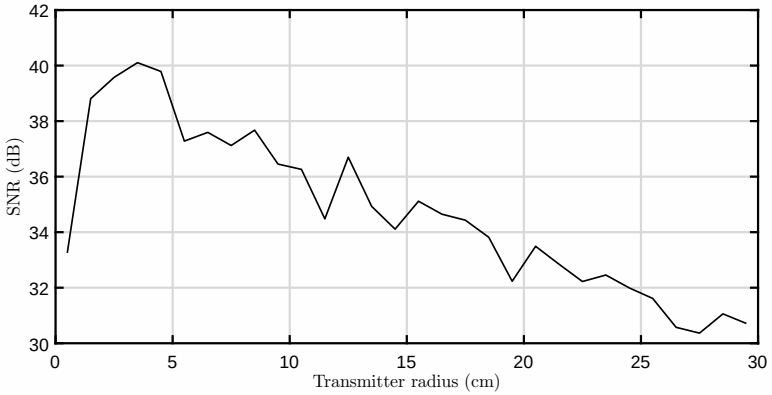

Figure 6.20: SNR of a link defined by the big opaque particle distribution vs the emission area

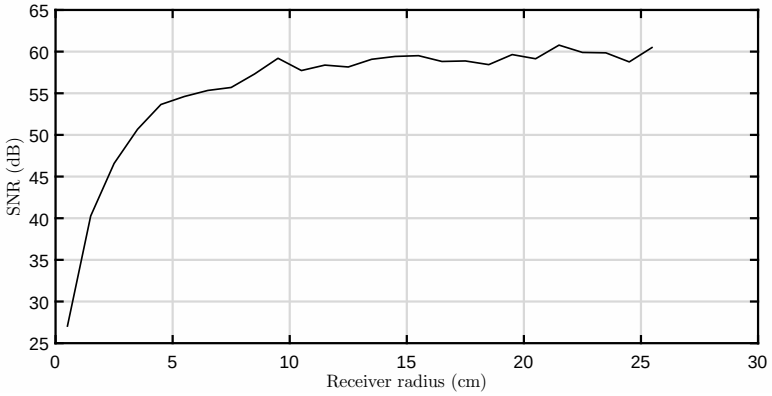

Figure 6.21: SNR of a link defined by the big opaque particle distribution vs the reception area

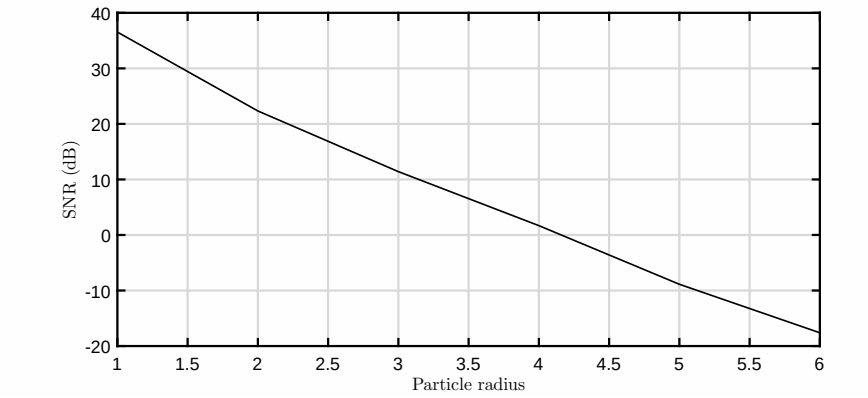

Figure 6.22: SNR of a link defined by the big opaque particle distribution vs the particle radius

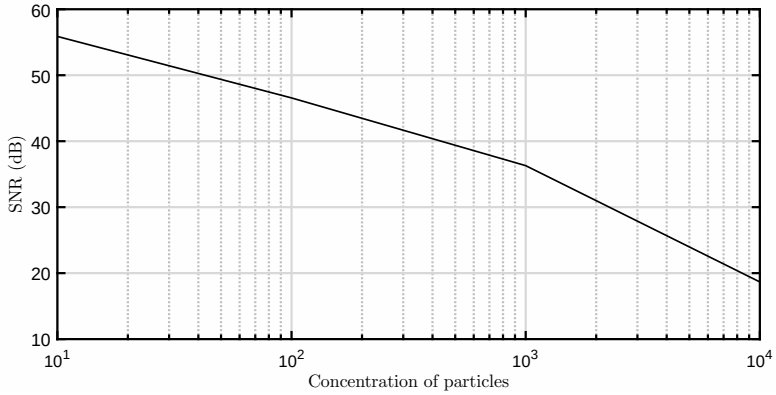

Figure 6.23: SNR of a link defined by the big opaque particle distribution vs the concentration of particles

Chapter 7

Measurements on a short-range Underwater Wireless Optical Channel

In this chapter, an experimental characterization of an underwater wireless optical link for near-surface or shallow water is presented. The wide-sense stationarity assumption, which has been used in the previous chapters, is discussed and demonstrated for this channel. Furthermore, estimated coherence times for different configurations are presented based on actual measurements. These tests have been carried out in a laboratory scenario with a controlled solution of suspended matter *(Arthospira platensis)* [136]. The used particle is a cyanobacteria that presents fluorescence for excitations below 450 nm. However, the experiments were performed at wavelengths above this limit. The effect of the particles on the received SNR and its variance, as well as the effect of the surface-reflected component are also estimated.

Nowadays, there are many ongoing applications requiring low-speed underwater wireless communications in shallow waters, as could be sensor interconnection in seaweed, aquaculture or wastewater treatment. For these facilities, RF systems are not well suited as they require large antennas and power consumptions. Underwater Wireless Optical Communications (UWOC) have been also considered so as to solve this problem, although they are subject to the variability of the underwater optical channel. The submarine currents, the misalignment between emitter and receiver, the wind stress over the seawater surface or the surrounding fauna are factors that directly affect the channel attenuation. Equation 7.1 shows the independent and time-dependent behavior of each term affecting the impulse response.

$$\begin{aligned} h(t,\tau) &= G(t,\tau)L_G(t,\tau) + R(t,\tau)L_R(t,\tau) \\ L_i(t,\tau) &= F_i(t,\tau)\cdot M_i(t,\tau)\cdot T_i(t,\tau)\ /i = \{G,R\} \end{aligned} \tag{7.1}$$

Where $h(t,\tau)$ is the channel impulse response, $G(t,\tau)$ is the line-of-sight (LOS) component of the link and $R(t,\tau)$ is the term which models the reflective components. $L_i(t,\tau)$ is a time-varying weighing function that comprises the other present phenomena. $F_i(t,\tau)$ is the effect of fauna in the received power, $T_i(t,\tau)$ is the turbulence effect, and $M_i(t,\tau)$ is the misalignment term. Note that the subindex indicates that each phenomenon affects either the LOS or the reflective NLOS component.

As it was suggested in Chapter 6, $G(t,\tau)$ presents a very small variability for uniformly distributed suspended matter, yielding an almost constant term. Gabriel et al. studied misalignment in [18], as well as Tang in [17]. It is straightforward to demonstrate that this variability depends on the mechanical stress suffered by the communication nodes due to mass transportation, as Dong et al. did in [20]. Finally, fauna is an unpredictable effect. For fauna-free scenarios like monitoring in wastewater treatment facilities, $F(t,\tau)$ can be neglected. Otherwise, the pass of fauna amid the link would produce an intense shadowing which would be traduced into an infinite loss during a random amount of time. There is no literature addressing this issue.

Introducing this considerations into Equation 7.1, it yields a simplified version where only reflective components have a time-dependent behavior (Equation 7.2). This component is only important for near-surface links, which is the situation that concerns this work. Furthermore, a very high bandwidth has been considered, as suggest the results of Chapters 4 and 6. This simplification is valid if the receiver's bandwidth is much lower than the physical bandwidth of the channel, which is true for most monitoring and sensor network applications.

$$h(t,\tau) \approx (G + R(t))\,\delta\left(\tau - d_{link}\frac{n_w}{c_0}\right) \tag{7.2}$$

As a general approach, the UWOC channel can not be assumed to be Wide Sense Stationary with Uncorrelated Scattering if all the terms of Equation 7.1 have significant weight. However, considering Equation 7.2, both conditions (stationarity and uncorrelated scattering) are satisfied as it will be demonstrated below.

In this work, an experimental setup to measure the channel variability of an UWOC link is presented. Furthermore, several results regarding SNR and coherence time for different configurations are obtained. A very high coherence bandwidth has been considered as the literature suggests, simplifying the calculation of the results.

7.1 WSSUS processes

Bello simplified the analysis of time variant systems in his seminal paper [137]. In his work, he defined the properties of linear time variant channels through the scattering function $S(\tau, \nu)$. Concretely, for WSSUS channels, the analysis of the scattering function is simplified. Wide sense stationarity is satisfied by a channel that complies with Equation 7.3, whilst uncorrelated scattering assumes that all the multipath energy comes from uncorrelated scatterers (Equation 7.4.

$$E[h(t,\tau)h^*(t',\tau')] = R_{WSS}(\Delta t, \tau, \tau') \tag{7.3}$$

$$E[h(t,\tau)h^*(t',\tau')] = R_{US}(t, t', \tau')\delta(\tau - \tau') \tag{7.4}$$

In a WSS channel, the autocorrelation function depends only on the time difference $\Delta t = t - t'$, whilst US channels present an autocorrelation defined by the delay difference $\tau - \tau'$, which imply that the channel coefficients are uncorrelated. This two conditions must be satisfied by the statistical definition of the impulse response in order to describe a WSSUS channel. Equation 7.5 shows the mathematical definition of the autocorrelation in this case.

$$E[h(t,\tau)h^*(t',\tau')] = R_{WSSUS}(\Delta t, \tau)\delta(\tau - \tau') \tag{7.5}$$

The autocorrelation function $R_{WSSUS}(\Delta t, \tau)$ fully describes the behavior of the channel in two variables. From this description, it is extracted that the WSSUS channels are stationary in time and frequency through the the autocorrelation function of the time-varying transfer function $L(t, f)$.

$$E[L(t,f)L^*(t',f')] = R_L(\Delta t, \Delta f) \tag{7.6}$$

The transfer function is the Fourier transform of $h(t, \tau)$ respect to τ. For a scenario in which the channel bandwidth is much higher than the application's necessities, the transfer function can be reduced to a single variable function $L(t)$. The scenario studied in this chapter complies with this approximation, since the maximum delay differences are low enough to consider the channel above a few GHz. The scattering function $S(\tau, \nu)$ is the 2D power spectral density of$R_L(\Delta t, \Delta f)$, but since $L(t, f) \approx L(t)$, the scattering function is of the form:

$$S(\tau, \nu) = S_\nu(\nu)\delta(\tau) \tag{7.7}$$

Note that after removing the dependency with f, it yields $L(t) = h(t)$. Regarding the demonstration of the time-frequency stationarity of the underlying process in a near-surface scenario, since the bandwidth is considered as very high, the frequency stationarity is directly satisfied. To demonstrate the time stationarity, it would suffice to prove that the expected value of $h(t)$ at any time t does not vary.

7.1.1 Coherence Time

The coherence time of a LTV channel is a statistical measure of the time range in which the channel impulse response can be considered constant. From the scattering function, the coherence time T_c is defined as the inverse of the Doppler spread σ_D, which is calculated as:

$$\sigma_D = \frac{1}{E\left[h(t)^2\right]} \int_{-\infty}^{\infty} (\nu - \bar{\nu})^2 S_\nu(\nu)\, \mathrm{d}\nu \tag{7.8}$$

In the case of the very high bandwidth channel considered, the coherence time can be also calculated as the time instant at which the correlation function of $L(t)$ decays 3 dB. Mathematically:

$$T_c = \arg\min_t E\left[|h(t)|^2\right] \tag{7.9}$$

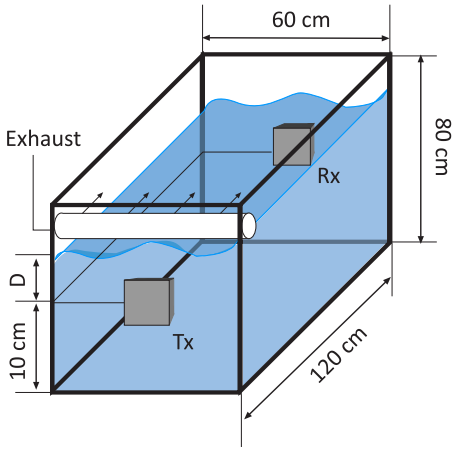

Figure 7.1: Diagram of the water tank

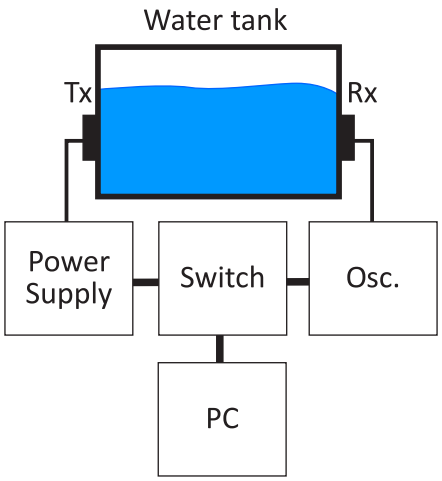

Figure 7.2: Instrumentation configuration of the experimental setup

7.2 Description of the experimental setup

The main objectives of this work are the demonstration of the WSSUS assumption validity on near-surface UWOC links, to measure the coherence time of the channel for different configurations and establish a relationship between the mobility of suspended matter and the SNR. This configuration depends on two variables: wind speed over the water surface and depth (distance to surface). Figure 7.1 shows the diagram of the water tank configuration whilst Figure 7.2 depicts the instrumentation setup.

The measurements have been carried out inside a water tank, whose walls have been optically isolated with a black matte covering. Furthermore, three water pumps submerged in the water were used to generate particle movement. Taking into account the negligible delay spread of the channel impulse response for a short-distance link, the measurements have been made with a DC current level applied to the emitter LED lamp. The setup's sizes and characteristics are shown in Table 7.1.

Both power supply and oscilloscope present Ethernet interface and are remotely operated through a network switch. Two different experiments have been performed. The first one is a measurement of the channel's variability due to the movement of suspended matter (*Arthrospira platensis*) in a situation where neither the surface nor the bottom contribute significantly to the received power. The second experiment explores the effect of the wind stress on the channel's variability. This stress is produced by an exhaust connected to a wind generator. The next section comments the obtained results and depicts the physical implementation of the experiments.

7.2.1 Emitter implementation

The emitter was implemented using CREE CLX6C-FKB [139] RGB LED devices. Figure 7.3 shows the implemented emitter, whilst Table 7.2 enumerates the main characteristics of the used LED. The electrical scheme used in this emitter was a simple 4-tee-4-series scheme as the one depicted in Figure 7.4. Since the driving was current-controlled

Driving current per LED	50 mA (both blue and red)
Wavelength	660 nm and 470 nm
Number of LED	16 (4 x 4 matrix)
Total emitted power	118 mW (red) - 96 mW (blue)
Photodetector	Thorlabs PDA36A [138]
Transimpedance gain	60 dB
Water tank dimensions	91 cm x 46 cm x 39 cm
Water's total dissolved solids (TDS)	456 ppm
Water temperature	25 °C
Sampling frequency	10 Ksps
Captured frame length	50 seconds
ADC bits	16 bits
Water pumps flux	800 l/h

Table 7.1: Characteristics of the experimental setup

by the power supply, only the electrical connections of the lamp itself were needed. This simple mount is allowed because the measurement of $h(t)$ is performed using a DC current level since the channel is considered flat for all the frequencies.

Peak blue wavelength	470 nm
Spectral width (blue)	28 nm
Optical efficacy (blue)	5 lm/W
Peak red wavelength	630 nm
Spectral width (red)	24 nm
Optical efficacy (red)	15 lm/W
Half angle	60°

Table 7.2: CREE CLX6C-FKB characteristics [139]

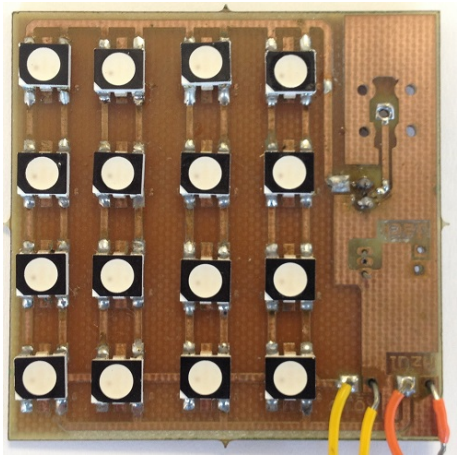

Figure 7.3: Implemented optical emitter

The used power supply was a Promax FA-851 [140], which presents SCPI TCP/IP interface to remotely control the device. SCPI is a common and simple interface to handle instrumentation [141], and has been extensively used during this experiment to automatize the measurements. As each LED has an independent anode per channel, the blue and the red channels are completely isolated, easing the emitter's setup. Regarding the measurement of the emitted optical power, an integrating sphere [142] connected to a LED tester [143] was used.

7.2.2 Receiver implementation

The used optical front-end is an amplified photodiode [138] which comprises a silicon photodiode of 13 mm^2 followed by a gain-adjustable transimpedance amplifier. The device can be observed in Figure 7.5. Furthermore, an InfiniVision 7012A Oscilloscope [144] was used as ADC. This allowed the implementation of an easy control

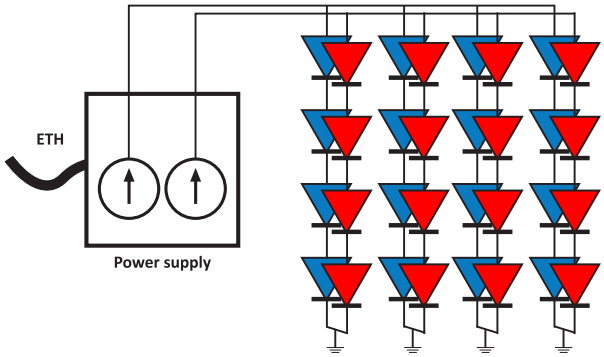

Figure 7.4: Electrical schematic of the emitter

software based on SCPI commands using reliable instrumentation. The responsivity of the photodiode follows the typical silicon's responsivity curve shown in Figure 7.6.

Figure 7.5: Image of the used amplified photodiode

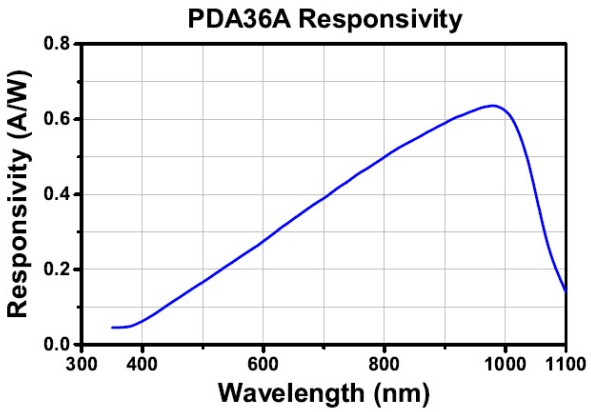

Figure 7.6: Responsivity of Silicon

7.2.3 Experimental methodology

To evaluate the influence of the suspended matter on the received power, two variables have been swept: particle concentration and mobility. In order to produce movement on the suspended matter, three pumps were submerged

inside the water tank at the positions depicted in Figure 7.7. The particle mobility statistic has been matched to the mean absolute value of the water flow through the LOS line, which was previously simulated using a FEM software [145] since an actual measurement was not feasible. The resulting water speed distribution can be observed in Figure 7.8. The average speed of the particles is $1\,\mathrm{cm}\cdot\mathrm{s}^{-1}$ for pumps with a water flow of 800 liters per hour. The output water speed is calculated assuming a small diameter, which allows a constant output flux approximation yielding an output speed of $0.31\mathrm{m}\cdot\mathrm{s}^{-1}$.

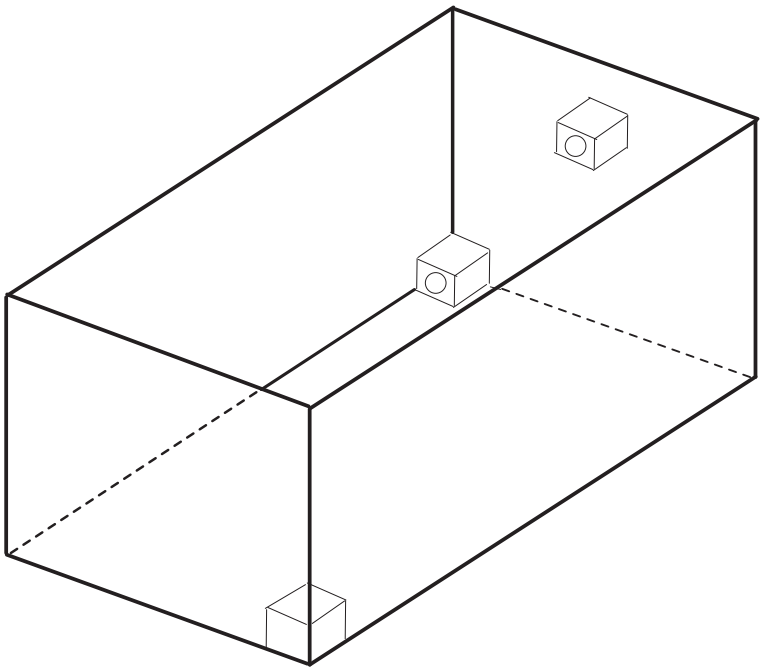

Figure 7.7: Positions of the water pumps used to agitate the scenario

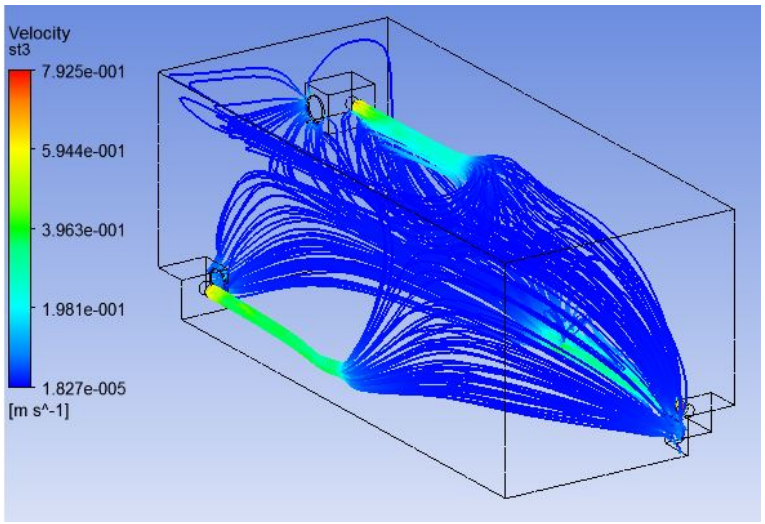

Figure 7.8: Water speed distribution of the experiment

The influence of the two variables on the received power has been analyzed using a two-way ANOVA test over an estimation of the electrical SNR, which can be observed at Equation 7.10. The received signal follows a Normal distribution for all the cases, as the result of the Kolmogorov-Smirnov test suggests.

$$SNR_{elec} \approx \frac{\mathrm{E}^2[V_{out}]}{\mathrm{Var}(V_{out})} \tag{7.10}$$

V_{out} is the voltage measured at the oscilloscope. Introducing the receiver chain in Equation 7.10, it yields Equation 7.11. P_{tx} is the emitted power, $\bar{H(0)}$ is the average channel gain, $R(\lambda)$ is the photodetector's responsivity, B is the receiver's bandwidth, q is the electron charge, I_d the dark noise, and σ_{ns}^2 represents all the non-shot noise contributions (Johnson noise and variability of the channel due to particles).

$$SNR_{elec} \approx \frac{\left(P_{tx}\overline{H(0)}R(\lambda)\right)^2}{\sigma_{ns}^2 + 2q\left(P_{tx}\overline{H(0)}R(\lambda) + I_d\right)B} \tag{7.11}$$

Note that the shot noise term is negligible due to the reduced bandwidth of operation and the small received power. The particle movement experiment may be affected by the distance of the emitter to the surface and the bottom of the tank. To minimize the effect of the reflections, the link's axis was fixed at the geometrical center of the tank, and the still water level was gradually incremented until the received power's variation was negligible. At this point, the link can be considered independent of the surface reflections. Regarding the bottom diffusive effect, since it was covered by an absorbing material, it is considered to not affect the link. In order to analyze the actual influence of the suspended matter, the darkness noise power of the receiver was calibrated as baseline.

The wind speed experiment was performed using clear tap water, since the presence of particles was not part of the designed experiment. The wind speed was measured using a digital anemometer at the middle of the water surface. The used wind generator presented only two different speeds: 8.1 $\mathrm{m \cdot s^{-1}}$ and 13 $\mathrm{m \cdot s^{-1}}$. Both wind speed and link's depth were swept to obtain long-duration waveforms on the receiver. Using the oscilloscope's retrieved data, the coherence time and the demonstration of the WSSUS approximation were obtained.

7.3 Results obtained through measurements

Figure 7.9 shows the actual implementation of the experimental setup. The results have been subdivided regarding the first and the second experiment commented above.

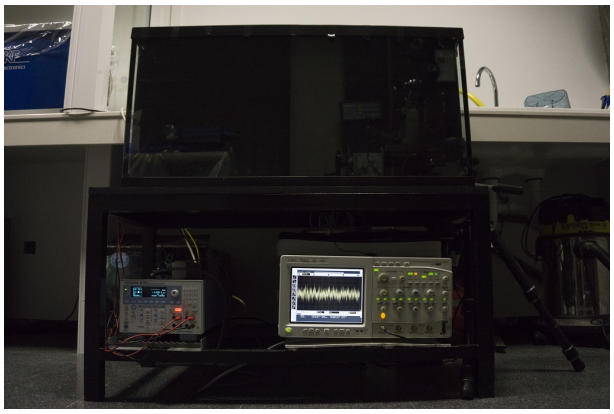

Figure 7.9: Instrumentation configuration of the experimental setup

As an example, Figure 7.10 depicts two captured frames. The left one is an only LOS scenario, whilst the right one is a near-surface link.

The following subsections present the demonstration of the WSSUS validity of a near-surface link, and the results obtained for the two aforementioned experiments, as well as comments on the effects of the wavelength and the wind speed.

7.3.1 Effect of the concentration and the movement of particles

Suspended matter contributes to the channel's power extinction in two different manners. If the particles are steady because of a null flow scenario, each emitter's outgoing ray suffers the same scattering events before arriving the receiver. On the other hand, if the particles present certain mobility, that almost-deterministic behavior is replaced by a random behavior whose mean value and variance depend on the evolution of the volumetric density of particles. In order to test this effects, two different particle mobilities and three different concentrations were used. Table 7.3 shows the parameters of the experiment.

Mobility	$\{0, 1\}$ $\mathrm{cm \cdot s^{-1}}$
Concentration of particles	$\{0, 6.12, 12.24\}$ $\mathrm{mg \cdot l^{-1}}$
Depth	30 cm

Table 7.3: Parameters of the particle mobility experiment

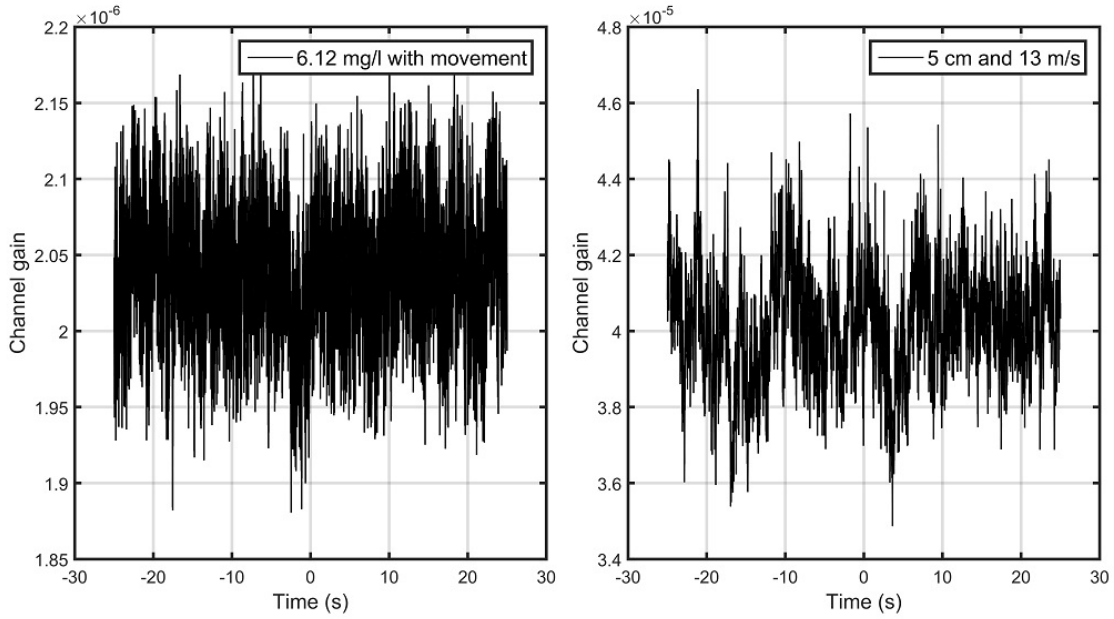

Figure 7.10: Captured frames for a LOS scenario with a concentration of 6.12 mg l^{-1} with agitated particles (left), and a near-surface link with an air flow of 13 m s^{-1} at 5 cm depth (right). Both are obtained with a 470 nm emission and are expressed in optical power units (W)

Figure 7.11 depicts the random nature of the SNR for red and blue wavelengths varying both particle concentration and mobility. As it can be observed there are 6 different scenarios, which are the combinations of mobility and particle concentrations. To statistically verify the influence of the particle mobility on the received power, an ANOVA test may be performed. To carry out the ANOVA test, a k-fold cross validation with 16 frames of 4096 samples has been used. The SNR of each frame is then estimated according to Equation 7.10. Afterwards it is tagged with its associated mobility and concentration, and finally used as input to the ANOVA test. As it is obvious, the test concludes that both mobility and concentration affect the electrical SNR.

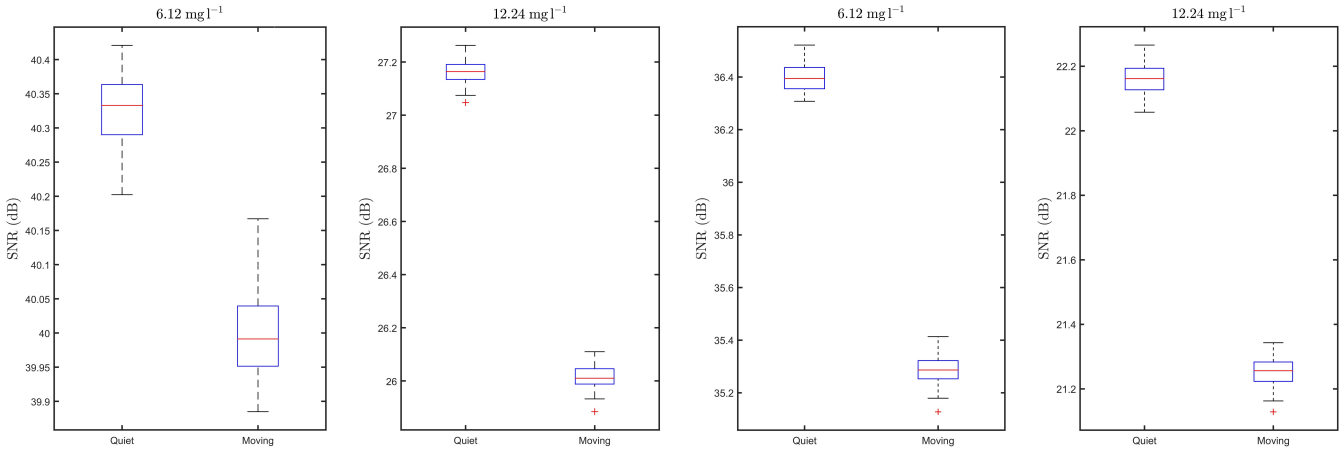

Figure 7.11: Boxplots of the SNR vs concentration and mobility for red (left) and blue (right) wavelengths

Taking into account the normality of the received power, which was demonstrated through a Kolmogorov-Smirnov test (Figures C.4 and C.10) a simple linear model is proposed to relate the mobility and concentration with the observed SNR decrement. Equation 7.12 expresses it mathematically for the channel gain, $H(0)$.

$$H(0)\,(\mathcal{C},\mathcal{M}) = \alpha\,(\mathcal{C},\mathcal{M})\,H(0)\,(\mathcal{C},0) + \mathcal{V}\,(\mathcal{C},\mathcal{M}) \tag{7.12}$$

$\mathcal{C}$ and $\mathcal{M}$ are the concentration and mobility respectively. α expresses the reduction of the mean received power and $\mathcal{V}$ is the channel variability term, which follows a normal distribution of the type $\mathcal{N}(0,\sigma^2_{ch}(\mathcal{C},\mathcal{M}))$. The variance due to the channel variability (extra noise due to particles moving) is related to the variance of $H(0)\,(\mathcal{C},\mathcal{M})$ as shows Equation 7.13.

$$\sigma_{ch}^2(\mathcal{C},\mathcal{M}) = \mathrm{Var}\left(H(0)(\mathcal{C},\mathcal{M})\right) - \alpha^2(\mathcal{C},\mathcal{M})\,\mathrm{Var}\left(H(0)(\mathcal{C},0)\right) \tag{7.13}$$

Finally, to obtain the dimensionless channel gain variability through the observed voltage signals, a simple conversion may be made as shows Equation 7.14. Note than α remains the same regardless the domain, as the voltage and the optical power are linearly related.

$$\begin{aligned}(G_{TZ}R(\lambda)P_{tx})^2\,\sigma_{ch}^2(\mathcal{C},\mathcal{M}) = \mathrm{Var}\left(V(\mathcal{C},\mathcal{M})\right) - \\ \alpha^2(\mathcal{C},\mathcal{M})\,\mathrm{Var}\left(V(\mathcal{C},0)\right)\end{aligned} \tag{7.14}$$

G_{TZ} is the transimpedance gain and $R(\lambda)$ the responsivity of the photodiode at the used wavelength. Table 7.4 summarizes the values of α and σ_{ch}^2 for each $(\mathcal{C},\mathcal{M})$ pair. Note that the variability of the red channel differs an order of magnitude respect to the blue channel measurements. This is because the dissolved alga presents an elevated concentration of chlorophyll, which implies a higher absorption at the red wavelength, reducing the effect of mobility.

Wavelength (nm)	**Concentration** ($\mathrm{mg\,l^{-1}}$)	α	σ_{ch}^2
660	0	0.99	$6.67 \cdot 10^{-18}$
660	6.12	0.92	$1.08 \cdot 10^{-15}$
660	12.24	0.96	$3.6 \cdot 10^{-15}$
470	0	1	$4.25 \cdot 10^{-12}$
470	6.12	0.89	$116.3 \cdot 10^{-12}$
470	12.24	0.91	$138.5 \cdot 10^{-12}$

Table 7.4: Values of α and σ_{ch}^2 for each concentration and wavelength for a mobility of $1\,\mathrm{cm\,s^{-1}}$

This reduction of the SNR in channels with moving particles may be important on the calculation of link budgets in UWOC. In order to avoid this effect, an extra power margin according the noise term presented above should be considered. These results are the sum of the turbulence effects (no concentration) and the influence of the particle density. Since this experiment was performed in laboratory, the Kolmogorov microscale would be higher than the expected in an open ocean environment. However, the concentration increment generates a reduction of the SNR much higher than the expected due to turbulences in short range links.

7.3.2 Effect of the wind speed

Near surface links are characterized by presenting a very important reflective component. Equation 7.15 shows the mathematical expression of the received power for this kind of links.

$$H(0) = H(0)_{LOS} + \int_x \int_y R(\hat{v}(x,y),\hat{n}(x,y))L(x,y)\,\mathrm{d}x\,\mathrm{d}y \tag{7.15}$$

The net reflective component is the sum of the contributions of all the points of the water surface. The surface plane can be divided forming a disjoint union of uncorrelated scatterers, whose fading behaviors are governed by their random normal vectors. The size of each uncorrelated region would depend on the wind speed and the propagating waves. $R(\hat{v}_i,\hat{n}_i)$ is the Fresnel loss due to the water-air interface, $\hat{v}(x,y)$ is the emission vector, which is bounded by the upper hemisphere of the radiation pattern; $\hat{n}(x,y)$ is the random normal vector of the seawater interface, and $L(x,y)$ depends on the product of the extinction loss and the approximation of the solid angle at the receiver ($\mathrm{d}\Omega \approx A_{pd}/d^2$). This last term would depend on the geometry of the link and goes to zero if the output ray does not impact on the receiver.

As it was commented in Chapter 5, $\hat{n}(x,y)$ depends on the wind speed and is commonly approximated by a normal distribution. The NLOS component of Equation 7.15 follows a Normal distribution since it can be understood as the sum of a high amount of independent Bernoulli processes (each scatterer has a probability p_{xy} to contribute to the overall received power), but its time-dependent evolution is unknown.

According to Equation 7.2, the reflective term $R(t)$ could be isolated since the LOS component does not vary significantly as it was shown in Subsection 7.3.1. Four different depths, three different wind speeds and two wavelengths were tested in this experiment. The resulting $R(t)$ signal was calculated and its probability distribution fits a normal distribution. Furthermore, its mean, variance and coherence time are shown at Table 7.5.

Regarding the coherence time, it must be taken into account that a very high bandwidth has been considered. This way, the time-frequency analysis is reduced to an only-time analysis, yielding a very simple calculation of the coherence time using Equation 7.9. The results of Table 7.5 are referred to signals expressed in watts. It

Wavelength (nm)	**Depth** (cm)	**Windspeed** ($\mathrm{m\,s^{-1}}$)	μ	σ^2	T_c (ms)
660	2	8.1	$0.231 \cdot 10^{-4}$	$0.116 \cdot 10^{-11}$	140
660	2	13	$0.21 \cdot 10^{-4}$	$0.064 \cdot 10^{-11}$	85.2
660	5	8.1	$0.256 \cdot 10^{-4}$	$0.164 \cdot 10^{-11}$	178.4
660	5	13	$0.222 \cdot 10^{-4}$	$0.075 \cdot 10^{-11}$	73.3
660	10	8.1	$0.247 \cdot 10^{-4}$	$0.176 \cdot 10^{-11}$	98
660	10	13	$0.233 \cdot 10^{-4}$	$0.1 \cdot 10^{-11}$	70.7
660	15	8.1	$0.25 \cdot 10^{-4}$	$0.132 \cdot 10^{-11}$	58.4
660	15	13	$0.237 \cdot 10^{-4}$	$0.078 \cdot 10^{-11}$	50.9
470	2	8.1	$0.294 \cdot 10^{-4}$	$0.25 \cdot 10^{-11}$	267
470	2	13	$0.24 \cdot 10^{-4}$	$0.1 \cdot 10^{-11}$	79.5
470	5	8.1	$0.355 \cdot 10^{-4}$	$0.475 \cdot 10^{-11}$	255.4
470	5	13	$0.321 \cdot 10^{-4}$	$0.215 \cdot 10^{-11}$	93.2
470	10	8.1	$0.417 \cdot 10^{-4}$	$0.331 \cdot 10^{-11}$	90.6
470	10	13	$0.375 \cdot 10^{-4}$	$0.226 \cdot 10^{-11}$	74.1
470	15	8.1	$0.424 \cdot 10^{-4}$	$0.326 \cdot 10^{-11}$	209.3
470	15	13	$0.398 \cdot 10^{-4}$	$0.165 \cdot 10^{-11}$	49.2

Table 7.5: Mean, variance and coherence time of $R(t)$ for each measured scenario

can be observed that the received reflective power contribution tends to increase in the considered depth interval. However, this trend changes abruptly above this depth, reducing its influence dramatically and being negligible above 22 cm.

The reduction of the coherence time with the increasing wind speed occurs because the number of uncorrelated regions on the surface is incremented. In other words, the spatial correlation between the points of the surface is reduced as the wind speed increases, incrementing the number of uncorrelated contributions on the receiver. Considering the near-surface UWOC link as WSSUS is obvious, since the scatterers (points on the surface) vary in a bounded region, and the emitter and receiver are at fixed positions, but the experimental demonstration can be found in the following subsection. Furthermore, all the obtained waveforms, correlations and probability density functions can be found in Appendix C.

7.3.3 Validity of the WSSUS assumption

In a wide sense stationary process, the expected value is constant. In order to demonstrate this property in a near-surface link, an ANOVA test was performed. The source signals were different frames built from the original 50 seconds time series as a concatenation of samples separated a multiple value of the coherence time (to create an uncorrelated vector). The result can be seen at Figure 7.12 for the red, 10 cm and 13 m/s scenario. As it was expected, the mean value of the process can be considered constant (p-value higher than 0.9 for all cases). The uncorrelation of the scatterers can be interpreted as a wide sense stationarity in the frequency domain. In this case, as the bandwidth is considered very high for all the scenarios, this property is directly satisfied.

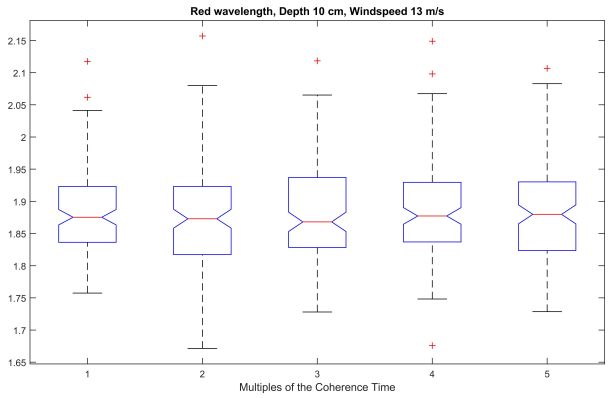

Figure 7.12: Result of the ANOVA test to demonstrate the WSS property of a near-surface link

Chapter 8

Strategies for energy-efficient transceiver design

Energy efficiency is one of the most important aspects in UWSN. The power consumption of battery-powered isolated nodes defines their lifespan, and taking into account the high replacement costs, it is a primary minimization objective. Generally, the power consumption of a node is a sum of partial contributions. The main consumptions are related to processing (CPU and control), communication interfaces and payload. This last aspect can widely vary depending on the purpose of the deployed node. For monitoring applications, the payload comprises sensors and acquisition circuitry, which can be normally neglected respect to communications. However, for applications where actuation is needed, the payload power consumption may be the primary source of energy usage. Regarding communications, for short-range links, UWOC has demonstrated to present the best *bits per Joule* efficiency, but for long-range links, UAC is still the best technology.

Energy efficiency can be improved in different manners. Using a layered approach, the best options to enhance the efficiency are the physical and the medium access layer. Regarding the physical layer, pulsed modulations are normally better alternatives than continuous waveforms such as OFDM or CSK. However, these types of signals can be Pulse Width Modulated in order to take advantage of high efficiency nonlinear drivers. Moreover, optical emitters and receivers present a better response to long wavelengths than to short ones. Although the best transmission windows are generally located at the blue-green region, the commented response of the devices makes red transmissions more energy-efficient below a critical distance d_{crit}. On the other hand, between PHY and MAC layers, power control algorithms are an interesting option to adapt the emitted power of the isolated nodes and hence, reduce the power consumption.

8.1 Signal to Noise ratio in UWOC

The SNR of an UWOC link is defined by Equation 8.1.

$$SNR(\lambda) = \frac{\left(P_{tx}H(0,\lambda)R(\lambda)\right)^2}{2q(P_{tx}H(0,\lambda)R(\lambda) + I_d + I_b)B + \frac{4KTB}{R_L}F_n} \tag{8.1}$$

P_{tx} is the emitted optical power, $H(0,\lambda)$ is the channel gain, $R(\lambda)$ is the responsivity of the photoreceiver at the wavelength λ, I_d is the darkness noise current, I_b is the background noise, q the electron charge, K is the Boltzmann's constant, T is the temperature in Kelvins, B is the bandwidth, R_L is the amplifier's gain and F_n its noise figure. In UWOC, the background noise is the sum of the effects of sunlight and the seawater blackbody radiation. Generally, the latter is neglected due to the low temperatures, whilst the first one losses importance as the depth increases. In this work, these noise sources are being neglected for simplicity in the analysis without loss of generality.

If the efficiency $\eta(\lambda)$ of the emitter were defined, the last Equation could be rewritten in terms of the power consumed by the transmitter. This efficiency is the product of the optical efficiency of the LED source $\eta_{opt}(\lambda)$ and the efficiency of the LED driver η_{driver}.

$$SNR(\lambda) = \frac{\left(\eta(\lambda)P_{tx}|_{elec}H(0,\lambda)R(\lambda)\right)^2}{2q(\eta(\lambda)P_{tx}|_{elec}H(0,\lambda)R(\lambda) + I_d + I_b)B + \frac{4KTB}{R_L}F_n} \tag{8.2}$$

If the ratio of the SNR induced by two different emitters with the same power consumption at two different wavelengths were introduced, the following merit figure could be defined.

$$\frac{SNR(\lambda_1)}{SNR(\lambda_0)} = \left(\frac{\eta(\lambda_1)H(0,\lambda_1)R(\lambda_1)}{\eta(\lambda_0)H(0,\lambda_0)R(\lambda_0)}\right)^2 \frac{2q\eta(\lambda_0)P_{tx}|_{elec}H(0,\lambda_0)R(\lambda_0) + \frac{4KT}{R_L}F_n}{2q\eta(\lambda_1)P_{tx}|_{elec}H(0,\lambda_1)R(\lambda_1) + \frac{4KT}{R_L}F_n} \tag{8.3}$$

Note that for shot-noise dominant scenarios (short distance) this merit figure is linear, but for Johnson dominant situations (long distance), the ratio becomes quadratic. However, in any of the two cases, the critical distance d_{crit} is defined as the distance at which the merit figure becomes one. Taking into account the conclusions of Chapters 4 and 6, the ratio of channel gains would depend on the difference of effective extinction coefficients, as shows Equation 8.4.

$$\frac{H(0,\lambda_1)}{H(0,\lambda_0)} \approx e^{-(c(\lambda_1)-c(\lambda_0)d_{link}} \tag{8.4}$$

Introducing Equation 8.4 into Equation 8.3 for the critical distance, it yields:

$$1 = \frac{\eta(\lambda_1)R(\lambda_1)}{\eta(\lambda_0)R(\lambda_0)}e^{-(c(\lambda_1)-c(\lambda_0))d_{crit}} \tag{8.5}$$

Solving the equation, the critical distance is of the form:

$$d_{crit} = -\frac{1}{c(\lambda_1)-c(\lambda_0)}\ln\left(\frac{\eta(\lambda_0)R(\lambda_0)}{\eta(\lambda_1)R(\lambda_1)}\right) \tag{8.6}$$

This critical distance describes the range from which it is better to transmit at wavelength λ_1 in terms of power consumption.

8.2 Optical transmitters and receivers

The transmission topology, the used encoding and the quantum efficiency of the light source are critical aspects regarding optical transmitters. On the other hand, optical receivers are determined by the opto-electrical device's NEP, the responsivity of the substrate and the amplifier's noise figure.

8.2.1 Current drivers

Optical transmitters generally comprise an LED lamp and a current driver, whose efficiency highly depends on the linearity requirements of the transmitted signal. Theoretically, a current driver performs a transconductance amplification since it converts an input voltage into a driving current. Linear drivers are normally implemented using bipolar junction transistors, whilst nonlinear drivers usually comprise MOSFET devices. The first ones need polarization in the active components, and that bias produces an energy leakage that can drop down the efficiency of the system below 50% easily. On the other hand, MOSFET transistors only consume energy during state transitions, allowing high speed drivers with efficiencies up to 95 % [146]. Nonetheless, these high impedance devices linearly increase their power consumption according to the storage of energy on the parasitic capacitors of the gate-source junction. Equation 8.7 shows the power consumption of a MOSFET.

$$P_{MOSFET} = \frac{1}{2}CV^2f \tag{8.7}$$

This term must be taken into account to calculate the efficiency of a MOSFET-based nonlinear driver. In Figure 8.1, a typical linear and a nonlinear driver can be observed. Equations 8.8 and 8.9 show the efficiency of both drivers. $\bar{I}$ is the average excitation current of the LED.

$$\eta_{linear} = \frac{V_D}{V_{cc} + \frac{P_{OPA}}{\bar{I}}} \tag{8.8}$$

$$\eta_{nonlinear} = \frac{V_D}{V_{cc} + \frac{1}{2}C\frac{V^2}{\bar{I}}f} \tag{8.9}$$

For frequencies above $2P_{OPA}C^{-1}V^{-2}$, the linear driver turns more efficient than the nonlinear one, but this limit is normally far enough to consider the nonlinear driver more efficient under any circumstance. In the case of nonlinear drivers, higher dynamic ranges are achievable since the transmitted signal is immune to nonlinear distortion. Nevertheless, linear drivers suffer from two types of dynamic range limitation. The first one is directly derived from the driving circuitry, and depends on the polarization. The other one is the inherent nonlinear behavior of LED devices.

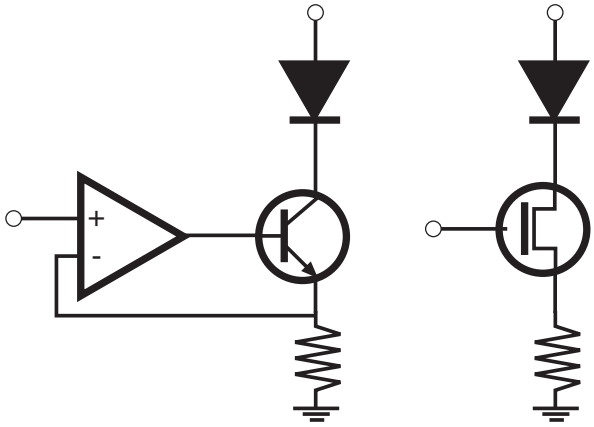

Figure 8.1: Linear (left) and nonlinear (right) current drivers

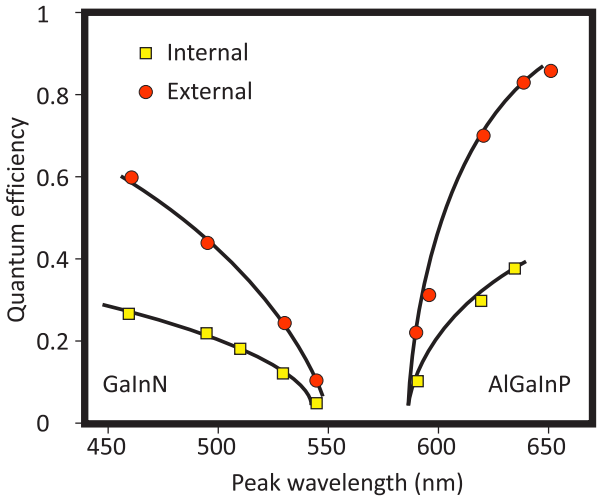

Figure 8.2: Quantum efficiencies for different types of substrate [147]

8.2.2 Optical emitters

The energy efficiency of optical emitters is measured in terms of their wall-plug efficiency. This efficiency is the ratio between the total radiated optical power and the electrical power consumed. Mathematically:

$$\eta_{opt}(\lambda) = \frac{P_{tx}}{V_D I_D} = \eta_{ext}(\lambda)\frac{hc}{q\lambda V_D} \tag{8.10}$$

$\eta_{ext}(\lambda)$ is the external quantum efficiency of the device., which is the ratio of the output photon flux and the injected electron flux. This ratio depends on the substrate and the manufacturing. However, the internal quantum efficiency is normally higher in AlGaInP (orange, red) devices than in GaN (blue) ones, as Figure 8.2 illustrates. It must be taken into account that $\eta_{opt}(\lambda)$ is not a constant, since V_D depends on the driving current I_D and $\eta_{ext}(\lambda)$ also presents nonlinearities for high values of I_D.

8.3 Power Control Algorithms

Power control is the selection of the transmission output power in a communications system, attending to an optimization criterion. This criterion is normally a combination of an energy minimization and the satisfaction of a minimum performance at the receiver. Traditionally, PCAs have been used to maximize the SNR whilst keeping the overall interference below a threshold in wireless communication channels, such as UMTS [148]. In this case, since all the signals are transmitted at the same time, each one spread by its corresponding orthogonal code, if there is no power control, the interference level may increase up to harmful levels, dramatically reducing the BER.

In the case of UWSN, PCAs are not proposed as SNR-improving techniques, but as energy-saving algorithms. BER is important since it partially defines the number of packet retransmissions, which is very power consuming. However, the possibility to adapt the transmission power to an optimum value in terms of energy, has more weight

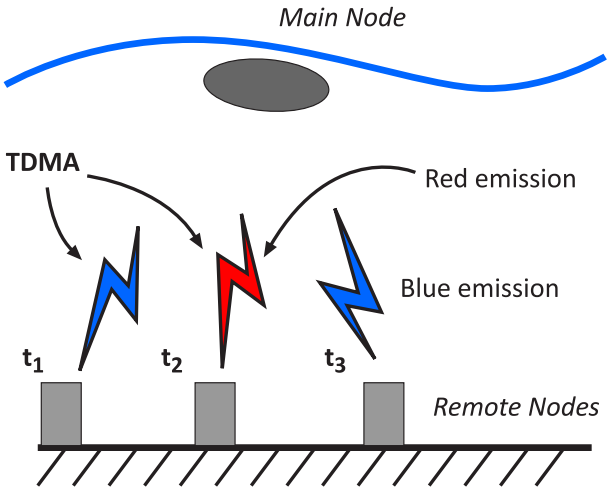

Figure 8.3: Scenario under consideration to study power control algorithms

in the design of optical UWSN nodes. Almost any energy-saving protocol or technique is justified in UWSN, because the extension of the nodes' lifespan dramatically reduces the replacement costs.

There are different taxonomies of power control algorithms, depending on the classification criterion. For instance, if each node takes its own decisions the algorithm is distributed whilst on the other case is centralized. If there is channel status exchange between nodes, *ergo*, there is a feedback of information, the algorithm is closed-loop. On the contrary, it is open-loop. Finally, depending on how is calculated the step size of the iterative power control process, the algorithms can be fixed-step, variable-step or adaptive-step.

In this work, a star-like network topology has been considered. This kind of network is a very general approach, but it is enough to study the impact of PCAs. Furthermore, a TDMA MAC protocol has been considered in order to simplify the optimization of the SNR and to isolate the study of the feasible N channels of a general scheme. Figure 8.3 represents the scenario under consideration, which may comprise a main energy-unlimited node and a bundle of remote nodes. This topology fits a buoy-nodes or a UAV-nodes scenario, depending on the mobility of the main node.

In addition, the studied algorithms are centralized and closed-loop. The centralization of the algorithms has been proposed to reduce the remote node's complexity. Furthermore, the estimation of the link's performance takes place at the main node's side whilst the uplink (main node to remote node) is always carried out at maximum power. The feedback of channel information is necessary to estimate with a lower error the needed transmit output power, but it also adds an error source that should be taken into account.

Generally, a power control algorithm is derived from an optimization problem of the type:

$$\begin{aligned} &\min \sum_i P_i \\ &\text{subject to:} \\ &\frac{(P_i g_{ii})^2}{\sigma_N^2 + 2qB\sum_j P_j g_{ij} + \sum_{j\neq i}(P_j g_{ij})^2} \geq K_i \end{aligned} \tag{8.11}$$

σ_N^2 is the sum of the receiver's inherent noise powers and K_i is the SINR threshold for the i-th channel. g_{ij} is the channel gain, including the responsivity, between the i-th receiver and the j-th emitter. Note that the quadratic term of the denominator is the optical interference term, whilst the linear term is the sum of all the shot noises due to both interference and wanted signals. These last two terms are nullified in the proposed scenario, due to the orthogonality of each channel after the use of a TDMA scheme, yielding the following simplified version of the convex minimization problem.

$$\begin{aligned} &\min P_i \\ &\text{subject to:} \\ &\frac{(P \cdot g)^2}{\sigma_N^2 + 2qBP \cdot g} \geq K \end{aligned} \tag{8.12}$$

Generally, the power is minimized iteratively, as shows Equation 8.13.

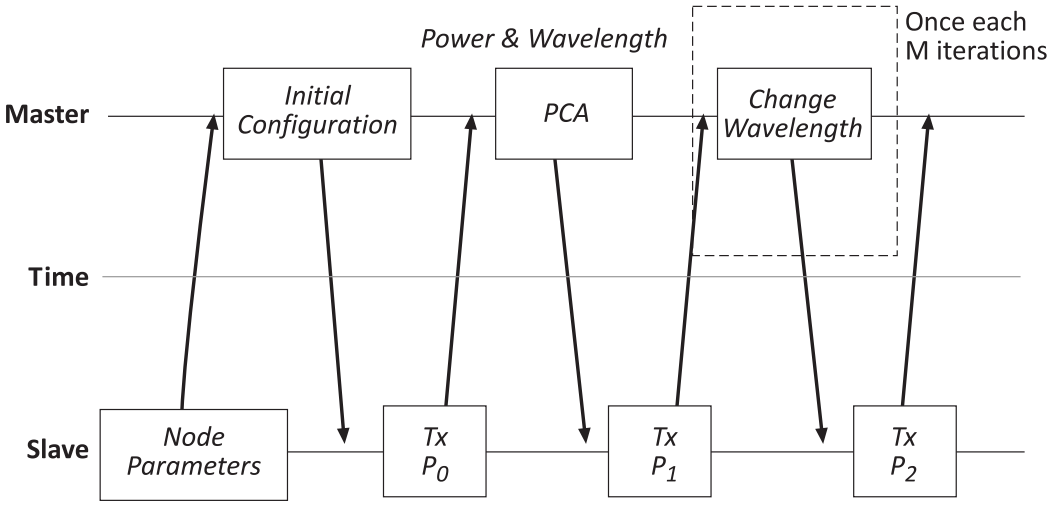

Figure 8.4: Sequence of the proposed UWOC power control algorithms

$$P^{(i+1)} = P^{(i)} + \Delta P^{(i)} \tag{8.13}$$

$P^{(i+1)}$ is the next transmission power and $\Delta P^{(i)}$ is the calculated step. Depending on how is this step calculated, the algorithm would be fixed-step, variable-step or adaptive-step. Other important aspect of the algorithms is how the SNR condition is estimated. The most common strategies are the following.

- **BER**. BER is directly related to the SNR through the complementary error function.As the modulation or encoding spectral efficiency increases, the BER becomes more sensitive to the SNR. The main disadvantage of this indirect estimation is the requirement of long integration periods to retrieve a sufficient amount of data to perform the calculation.
- **Direct SNR estimation**. The SNR is the ratio between the squared expected value and the variance of a signal. This estimation needs a high amount of samples to present a reliable confidence interval. However, if a soft signal detection were performed using a DSP or a FPGA, this estimation could be real-time performed.
- **Received power estimation**. For situations in which the shot noise could be neglected, the SNR condition can be directly calculated using Equation 8.14. Furthermore, this technique is suitable for low-power devices, since only a few amount of samples per frame are needed. Low pass filtering may be used to reduce noise before sampling, or a few samples from a long-duration synchronization header could be acquired to estimate the received power.

$$\begin{aligned} (P \cdot g)^2 &\geq K \cdot \sigma_N^2 \\ P \cdot g &\geq K^{1/2} \cdot \sigma_N \end{aligned} \tag{8.14}$$

Some of the proposed centralized algorithms need knowledge of the remote node's emission parameters: energy efficiency, allowed power codes, transimpedance conversion factor, etcetera. Therefore, an initialization stage to retrieve the necessary information is needed before the execution of the PCA. Figure 8.4 depicts the stages of the proposed PCAs.

8.3.1 Fixed-step algorithm

Fixed-step algorithms are the easiest approach to energy minimization. Depending on the result of Equation 8.14, the output power is incremented $N\delta$ or decremented $M\delta$. Mathematically:

$$\begin{aligned} P^{(i+1)} &= P^{(i)} + \Delta P^{(i)} \\ \Delta P^{(i)} &= \begin{cases} N\delta & P \cdot g < K^{1/2} \cdot \sigma_N \\ -M\delta & P \cdot g \geq K^{1/2} \cdot \sigma_N \end{cases} \end{aligned} \tag{8.15}$$

This algorithm is characterized by its low convergence speed and its low stability after reaching the optimum value. However, is very memory and computationally-efficient.

8.3.2 Variable-step algorithm

Variable step algorithms are the logical evolution of fixed step algorithms in an attempt to improve the speed. In this case, the step is gradually incremented on the direction defined by Equation 8.14. Mathematically:

$$\begin{aligned} P^{(i+1)} &= P^{(i)} + \Delta P^{(i)} \\ \Delta P^{(i)} &= (\alpha_i - \beta_i)\delta \\ &\begin{cases} \alpha_i = 0; \beta_i = \beta_{i-1} + 1 & P \cdot g < K^{1/2} \cdot \sigma_N \\ \alpha_i = \alpha_{i-1} + 1; \beta_i = 0 & P \cdot g \geq K^{1/2} \cdot \sigma_N \end{cases} \end{aligned} \tag{8.16}$$

This algorithm presents a higher convergence speed respect to fixed-step, but also a higher recovery speed after a channel loss. However, the stability after convergence is worse in this case. Fixed-step algorithms operate without memory, but variable-step algorithms need to store a one-sample history.

8.3.3 Adaptive-step algorithm

Adaptive-step algorithms modify the the power correction step $\Delta P^{(i)}$ at each iteration, depending on the received power and the distance to the optimum value. In order to obtain an adaptive method, a gradient descent strategy can be applied to Equation 8.14. For instance, a Newton-Raphson method may be used, defining an optimization function $F(P) = 0$ after the mentioned condition, yielding:

$$\begin{aligned} P^{(i+1)} &= P^{(i)} + \Delta P^{(i)} \\ \Delta P^{(i)} &= -\alpha \frac{F(P^{(i)})}{\frac{\partial F(P)}{\partial P}\Big|_{P=P^i}} \end{aligned} \tag{8.17}$$

α is a relaxation coefficient to smooth the convergence of the output power. From the optimization restriction, and naming $K_0 = K^{1/2}\sigma_N$, it can be demonstrated that:

$$\Delta P^{(i)} = -\alpha \frac{P^{(i)} g^{(i)} - K_0}{g^{(i)}} \tag{8.18}$$

Introducing Equation 8.18 in Equation 8.17, it yields the final form of the adaptive-step algorithm. Note that $g^{(i)}$ is the estimated channel gain at each iteration, this gain depends on the variability of the channel and defines the after-convergence variability of the algorithm.

$$P^{(i+1)} = (1 - \alpha)P^{(i)} + \alpha \frac{K_0}{g^{(i)}} \tag{8.19}$$

The resulting algorithm presents the same form as a LMS algorithm. Furthermore, it can be observed that this algorithm needs the estimation of the channel gain. Introducing an output power code in the header of the transmitted frame, the receiver would be able to estimate the channel gain according to the measured received power. However, this procedure introduces an extra error source, since low SNR situations could generate bit errors and hence, unrealistic channel gains. The convergence speed is the best in this algorithm, whilst the after-convergence variability depends on the channel gain estimations. However, to ensure that this algorithm converges, the damping factor must be bounded. Extending the iterative equation of the output power from $i = 0$ to $i = n+1$ it yields:

$$P^{(n+1)} = (1 - \alpha)^{n+1} P^{(0)} + \alpha K_0 \sum_{j=0}^{n} \frac{(1 - \alpha)^j}{g^{(n-j)}} \tag{8.20}$$

This last summation needs to be converging to ensure the stability. The simplest weak condition is to force each term to be smaller that the previous one. Mathematically:

$$\alpha g^{(i)} > \left| g^{(i+1)} - g^{(i)} \right| \tag{8.21}$$

It must be taken into account that $g^{(i)}$ is a random process that describes the behavior of the channel gain at uncorrelated instants. Intuitively, α can be adapted to the channel's random nature regarding the expected value of the last equation, yielding:

$$E[\alpha] > \frac{E\left[\left|g^{(i+1)} - g^{(i)}\right|\right]}{E\left[g^{(i)}\right]} \tag{8.22}$$

It can be observed that from Equation 8.22, α must be in the interval $(0, 1)$. Furthermore, both convergence speed and variability depend on α. Large values of α filter the output power and reduce the convergence time. On the other side, small values increment the variability and reduce the convergence speed. The following algorithm tries to obtain a compromise solution on both parameters.

8.3.4 Adaptive-damping-and-step algorithm

The last subsection introduced adaptive-step algorithms, but the convergence needs a high knowledge of the channel's variability. Regarding the observed variability of the UWOC channel and the wide range of phenomena that may occur, an adaptive-damping version of the last algorithm is proposed This algorithm adapts the damping factor α automatically. Analyzing Equation 8.22 it can be noticed that it expresses the variability of the channel. Hence, to reduce the variability of the algorithm, α can be iteratively modified with a parameter modeling this variability. Equation 8.23 shows the iterative formula.

$$\begin{aligned} \alpha^{(i+1)} &= \frac{\alpha^{(i)} + \xi^{(i)}}{2} \\ \xi^{(i)} &= \frac{2\sigma_i}{\mu_i + \sigma_i} \end{aligned} \tag{8.23}$$

μ and σ are the mean and standard deviation of the channel gain. ξ is the estimation of the channel's variability, where σ is always lower than μ due to the nature of the UWOC channel. The final value of $\alpha^{(i)}$ is then averaged with the estimated variability to obtain the next iteration value.

8.3.5 Wavelength switching

In Section 8.1, a merit figure to decide if a wavelength is more energy-efficient than other was presented. Assuming Red-Blue emitters on the UWSN remote nodes, a color code can be introduced in the transmitted frame's header and a comparison step between the power consumptions at each wavelength can be introduced between iterations of the algorithm. If the red emitter presents an efficiency $\eta(\lambda_1)$ and the blue one an efficiency $\eta(\lambda_0)$, the best emission wavelength can be extracted from the following inequality.

$$\eta(\lambda_1)^{-1} P(\lambda_1)|_{opt} g(\lambda_1) < \eta(\lambda_0)^{-1} P(\lambda_0)_{opt} g(\lambda_0) \tag{8.24}$$

This inequality relates the received electrical power and the power consumption of the emitter at each wavelength. During the decision process, the current tuple $(P^{(i)}, g^{(i)}, \eta(\lambda_i))$ is compared to a reference tuple (previously stored) at the other wavelength. Since the algorithm is subject to estimation errors, this procedure must be performed periodically. Note that g contains also the responsivity of the receiver.

8.3.6 Simulation results

In this subsection, several simulation results for different scenarios are obtained. In order to model the channel, a GEV distribution has been used according to the results of Chapter 6. In order to test the robustness of the algorithms, scenarios with different variabilities have been tested (Table 8.1). The emitter has a minimum output power of 10 mW and a maximum of 10 W, encoded in 8 bits.

Scenario	μ	σ	ξ
#1	10^{-3}	10^{-4}	0.2
#2	$2.5 \cdot 10^{-5}$	10^{-5}	0.3
#3	10^{-5}	10^{-6}	0.4

Table 8.1: Parameters of the tested scenarios

Two main statistics are obtained to describe the performance of each algorithm: convergence iteration (CI) and after-convergence variability (ACV). The convergence iteration is defined as the iteration at which the output power is below $1.1P^{(\infty)}$. The after-convergence variability is the variance of the output power after the convergence iteration. The following figures depict the behavior of the presented algorithms at each scenario. For simulation purposes $K_0 = 10^{-5}$.

Table 8.2 summarizes the obtained statistics for each scenario and algorithm on the form (CI/ACV).

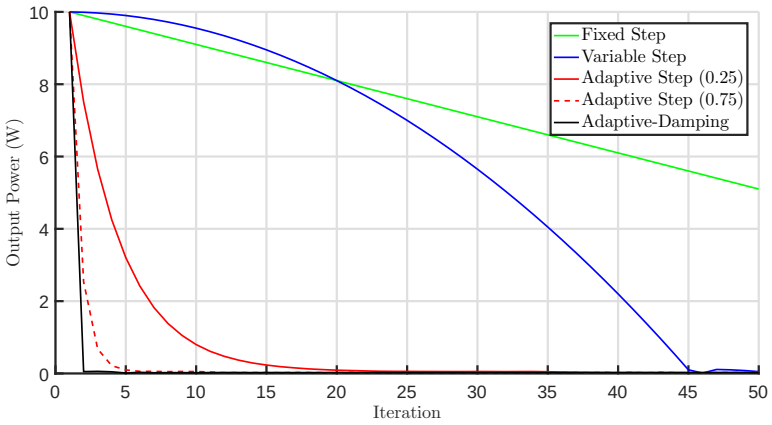

Figure 8.5: Evolution of the output power for Scenario #1

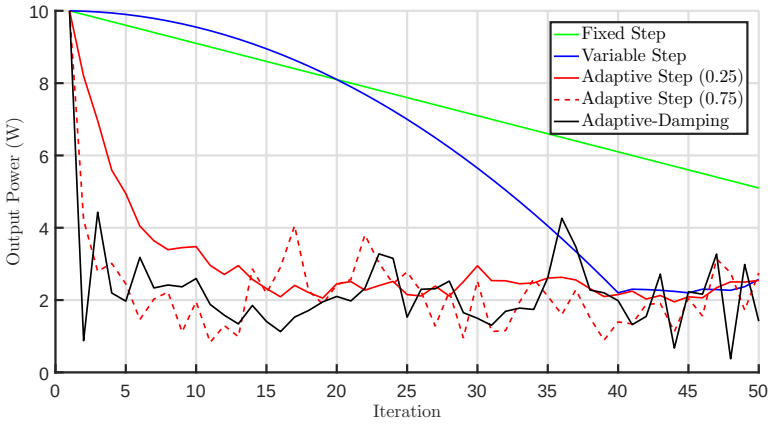

Figure 8.6: Evolution of the output power for Scenario #2

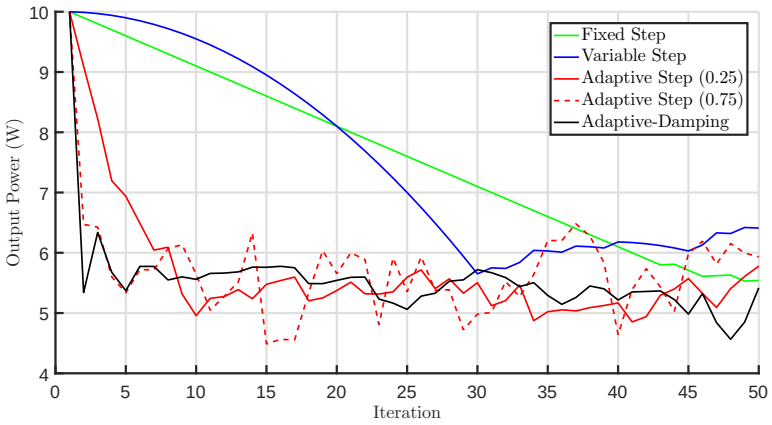

Figure 8.7: Evolution of the output power for Scenario #3

Scenario	FS	VS	AS ($\alpha = 0.25$)	AS ($\alpha = 1$)	ADAS
#1	$101/3.13 \cdot 10^{-4}$	46/0.001	$24/8 \cdot 10^{-7}$	$6//3.13 \cdot 10^{-6}$	$2/10^{-13}$
#2	107/0.016	55/0.1	59/0.115	6/0.48	2/0.0026
#3	45/0.05	30/0.024	9/0.103	4/0.445	$2/9.6 \cdot 10^{-4}$

Table 8.2: Simulations results summary

It can be observed that Fixed-Step and Variable-Step algorithms present a very reduced variability, however, their convergence iteration is several times greater than the adaptive algorithms. Regarding Adaptive-Step, the results suggest that the compromise between variability and speed is highly dependent on α. This dependency is eliminated using the Adaptive-Step-and-Damping algorithm. In addition, very low values of α may need a huge amount of samples to recover from a change in the mean channel gain (an increasing or decreasing link range in a AUV-to-node communication for instance). The proposed algorithm presents a the lowest variability although the calculation of the variability parameter was performed using only 5 samples.

Influence of the stored history size

The Adaptive-Step-and-Damping algorithm needs to store a certain amount of channel gain samples in order to calculate the damping factor according to Equation 8.23. Due to the variability of the channel, the calculated value of α is subject to a correct estimation of both μ and σ. The used estimators are shown in Equations 8.25 and 8.26.

$$\mu = \frac{1}{N}\sum_{j=1}^{N} g^{(i)} \tag{8.25}$$

$$\sigma = \sqrt{\frac{1}{N}\sum_{j=1}^{N}\left(g^{(i)}\right)^2 - \mu^2} \tag{8.26}$$

From a simple statistical analysis and assuming normality on the distribution (which is an obvious error), it can be shown that:

$$\mu \sim \mathcal{N}\left(E[g], \frac{1}{N}\mathrm{Var}(g)\right) \tag{8.27}$$

$$\sigma \sim NC - \chi_N\left(E[g], \mathrm{Var}(g)\right) \tag{8.28}$$

The sample mean follows approximately a normal distribution whose variance is directly reduced by the number of samples, whilst the standard deviation follows a noncentral χ distribution with N degrees of freedom. The variance of a noncentral χ distribution also decreases with the number of samples. Rearranging the terms of Equation 8.23, it can be shown that α follows a distribution which is related to the reciprocal of the ratio μ/σ. Therefore, the expected value of α can be approximated by:

$$E[\alpha] < \frac{2}{1 + E[\mu]/E[\sigma]} \tag{8.29}$$

Obviously, an error is being committed due to the nonzero correlation between mean and standard deviation. However, empirical observations of the correlation coefficients between the two variables suggest that the higher the degrees of freedom, the lower the correlation. Due to the elevated number of samples needed to accurately estimate the variance of σ, the variability of α is very sensitive to the actual variability of the channel. This aspect of the algorithm should be further investigated to make it more robust. Figure 8.8 shows the values of $E[\alpha]$ and $\mathrm{Var}(\alpha)$ for different history sizes. The values were obtained for Scenario #2, which is the more variable of the three studied. The actual variability parameter (Equation 8.23) at which α is associated was 0.8213. It can be observed that the higher the History Size, the better is estimated the variability of the channel. However, as the History Size increases, the delay between abrupt changes on the channel gain and the response increases.

Complexity comparison between algorithms

The complexity of the power control algorithm may be of capital importance for application with limited memory and computation resources. The presented memory complexity is presented in terms of the needed history size, whilst the computational complexity is detailed in sums, products and more complex operations (power, square root, division, etc...). Table 8.3 summarizes the complexities.

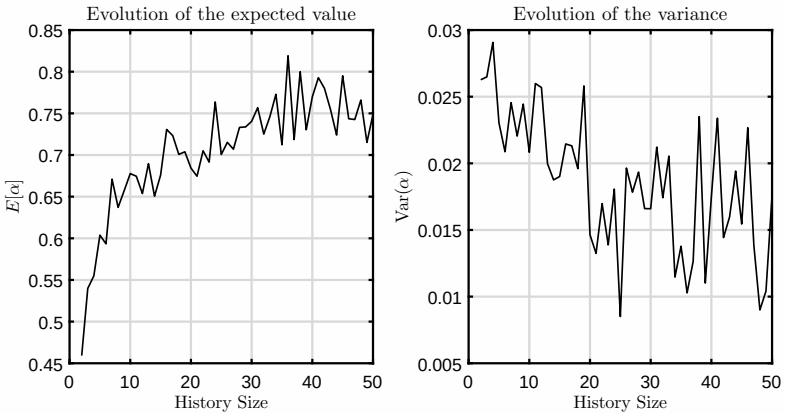

Figure 8.8: Relationship between the expected value of α (left) and its variance (right) with the History Size

Algorithm	Memory	Sums	Products	Other operations
Fixed-Step	0	1	1	0
Variable-Step	0	2	1	0
Adaptive-Step	1	1	2	1
Adaptive-Step-and-Damping	N	2 N + 3	N + 4	2

Table 8.3: Memory and computation complexities of the presented PCAs

The number of operations in the ASAD algorithm increases linearly with N using an inefficient calculation of the mean value and the standard deviation where at each iteration the whole stored array is swept. However, there are more efficient implementations that may reduce the complexity to $\mathcal{O}(\log N)$. Furthermore, depending on the number of remote nodes handled within the TDMA scheme, the memory requirements may turn this algorithm not feasible. In that case, the history size should be decreased.

Algorithm with wavelength switching capabilities

The proposed Adaptive-Step-and-Damping algorithm presented the better performance during the last subsection. In order to test the advantages of the commented wavelength switching for multi-color emitters, a decision stage is included. The interrogation period of the wavelength-switching stage was 10 iterations. Figure 8.9 depicts the behavior of the output power showing in blue lines the period of blue emission and in red the complementary period. The used channel gain distribution for the blue channel is the one used at Scenario #2, whilst the red channel distribution is is of the type $GEV(5 \cdot 10^{-5}, 2.5 \cdot 10^{5}, 0.3)$. Note that the red channel response is slightly better than the blue response (close-range scenario). The efficiencies of the blue and red emitters are related by 0.3:1. It can be observed that the algorithm starts in blue but quickly decides to switch to red. The interrogation period is clearly observed each 10 iterations. Finally, the resulting output power of the algorithm at red is much lower that in the case of the blue one.

The energy saving $\mathcal{E}$ of the PCA can be calculated as:

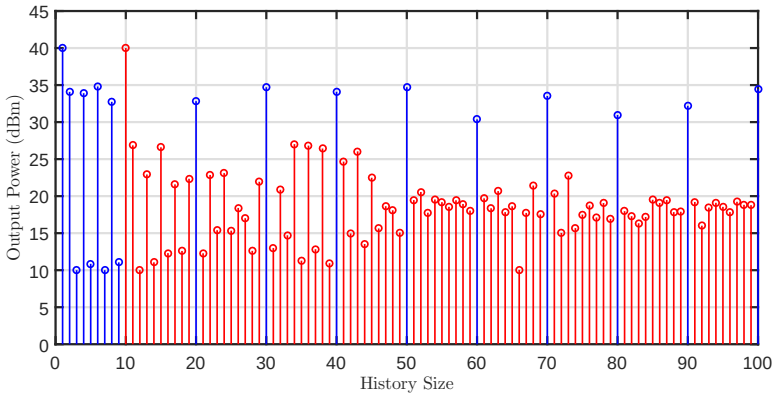

Figure 8.9: Output power using the wavelength-switching stage

$$\mathcal{E} = 1 - \frac{1}{\eta_{min} P_{max}} \lim_{N \to \infty} \frac{1}{N} \sum_{i=1}^{N} \eta(\lambda_i) P^{(i)} \tag{8.30}$$

Using this equation, the average energy savings of the ASAD algorithm and the same algorithm with wavelength switching for the presented scenario are presented in Table 8.4

Algorithm	$\mathcal{E}$
Only Blue	50.47 %
With Switching	89.41 %

Table 8.4: Energy saving

It can be observed that the sole fact of including a PCA, produces an energy saving in the communications interface of a 50.47 %. Furthermore, after introducing a wavelength-switching stage, the energy saving raises up to almost a 90 % respect to the static case.

8.4 Pulse Width Modulated Optical OFDM

From the first works devoted to the research on visible light communications, there has been a growing interest on the use of spectrally-efficient modulations to be used in optical data transmission [149]. Even after the publication of IEEE 802.15.7 standard [150], several research groups continued exploring this possibility [151] [152], which is now under consideration to be included in further versions of this proposals. OFDM modulations offer astonishing capabilities on scarce-spectrum environments or when transmitting through non-stationary channels, as in underwater applications. Many different variations from the basic OFDM transmission scheme have been developed in order to adapt them to the special characteristics of the optical transmitter as only positive signals are allowed. The resulting signal after the IFFT calculation must be clipped [153] or biased [154]. Furthermore, optical OFDM systems usually are baseband transmitted. There is also a standard procedure to generate an only-real signal, taking advantage of the Hermitian symmetry of real-valued Fourier transforms. Regarding spectral efficiency, optical OFDM implies reducing by a factor of 2 when compared to radio systems, as both real and imaginary parts cannot be simultaneously transmitted. Comparing ACO-OFDM and DCO-OFDM, the first is less bandwidth-efficient since only odd subcarriers are loaded with information while the latter is less power-efficient as a bias level is needed.

8.4.1 Optical OFDM schemes

As a matter of fact, Orthogonal Frequency Division Multiplexing (OFDM) is broadly employed in optical communications owing to its robustness against dispersion effects in the channel, such as inter symbol interference [155]. However, in OFDM, signals are both bipolar and complex which cannot be transmitted over an IMDD scheme. For this reason, Hermitian symmetry is used to guarantee that a real signal is to be transmitted, but halves the available bandwidth. The essential difference among the different schemes of optical OFDM is how they transform this bipolar signal into a unipolar one as depicted in Figure 8.10. To most common techniques are DC biased optical OFDM (DCO-OFDM) and asymmetrically clipped optical OFDM (ACO-OFDM) [154]. Nonetheless, it is worth to consider another strategies such as asymmetrically clipped DC biased optical OFDM (ADO-OFDM) and Flip- OFDM [156].

DCO-OFDM scheme

The most straightforward way of converting the bipolar OFDM signal into a pure positive one is to add a DC bias, yet the needed amplitude to make all samples positive depends on the PAPR, which is very high. This high DC bias makes DCO-OFDM inefficient in terms of optical power. In the event of using an insufficient DC bias, the samples that remain negative are clipped. As a result, clipping noise arises, affecting all subcarriers.

ACO-OFDM scheme

A capital idea is used in this technique. By making the signal not only real but also odd symmetric, it is possible to clip it without any loss of information. Instead of using a DC bias, only odd subcarriers hold actual information, sacrificing another half of the bandwidth. To put it another way, clipping the transmitted time domain signal equals a half-wave rectifier where harmonics appear on the even subcarriers. This fact is key for understanding the strategy used in the next scheme.

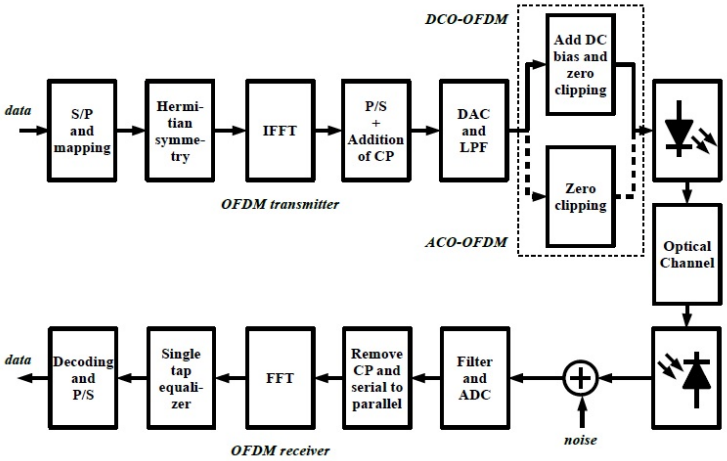

Figure 8.10: Block diagram of different optical OFDM schemes

ADO-OFDM scheme

We have pointed out succinctly DCO-OFDM is inefficient in terms of optical power and so does ACO-OFDM regarding bandwidth. In Flip-OFDM, even though the complexity at the receiver is augmented, the overall performance takes advantage of the strengths of each technique. On the even subcarriers, DCO-OFDM is transmitted whilst on the odd ones ACOOFDM is used; consequently, the optical power efficiency is better than DCO and all the subcarriers are employed enhancing bandwidth efficiency with respect to ACO. At the receiver, the ACO symbols are extracted in the same way as conventional ACO, at the same time, DCO symbols require an interference cancellation method due to both clipping noises, odd and even, fall in the even subcarriers. Hence, the constellation sizes in the DCO subcarriers are smaller than usual.

Flip-OFDM scheme

As an alternative approach, this scheme splits the signal into positive and negative parts which then are serialized in two consecutive OFDM subframes. Regardless of the fact that it is a patent [157], which has not succeeded in the literature, several works analyze its goodness facing ACO-OFDM. The authors introduce a modification for a fair comparison. On the whole, Flip-OFDM performs almost identically when compared to ACO-OFDM saving 50% in receiver hardware complexity now that all subcarriers carry data. The penalty of transmitting two subframes per N samples brings the possibility of demodulating N symbols per IFFT operation, while ACO-OFDM needs two N-IFFT operations to achieve the same N samples.

8.4.2 Proposed scheme

Optical OFDM is limited by the transmission of only positive signals. As it has been shown, this restriction has been solved using several methods, ranging from bias addition to intelligent mapping on the FFT block taking advantage of the predictable harmonics after a clipping operation. Another important issue in optical OFDM is the implicit nonlinearity of the emitters versus the necessity of linear drivers to handle the emission. If the LED devices were operated in a linear region, the dynamic range would be significantly diminished to avoid nonlinear distortion on the OFDM frame. A previous distortion to compensate the inherent LED behavior may be used, adding complexity to the design. In this thesis, a PWM encoding of the OFDM frame is proposed. By adding this operation, the linearity requirement is avoided and the use of nonlinear and efficient power drivers is allowed. Furthermore, this kind of codification is less sensitive to temperature variations on the emitter, because the information is encoded in the duty cycle of each PWM symbol. In the following subsections the advantages and disadvantages of the introduction of this block are discussed.

Figure 8.11 depicts the block diagram of the proposed scheme. A PWM modulator has been added at the output stage of the emitter. This modulator is one of the main parts of a class D amplifier. However, the low pass filter has been removed from the emitter and placed at the receiver's front end. From LTI systems theory, this simple change generates the same waveform at the receiver whilst dramatically increases the energy efficiency at the transmitter. However, the SNR is decremented adding an extra noise source derived from the N-bits quantization of the output OFDM waveform. Furthermore, the output waveform needs a sampling frequency 2^N times higher than the linear version if it is digitally generated. In addition, as the real-valued optical OFDM samples are normally distributed, a predistortion block such as a μ-law may be used to increase the distance between symbols before the ADC block. It may be also considered that all the subcarriers are used to carry information, as in DCO-OFDM, but with

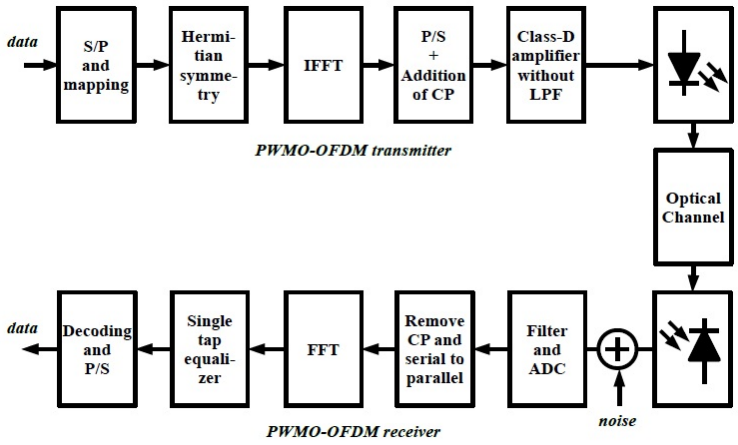

Figure 8.11: Block diagram of the proposed scheme

Advantages	Disadvantages
Allows the use of nonlinear drivers	Needs sampling frequency 2^N times higher
Eases synchronization	Decreases SNR
Reduces the cost	
Presents a higher dynamic range	

Table 8.5: Summary of the characteristics of the proposed scheme

the advantage of reducing the PAPR of the modulation to 3 dB because the peak power is fixed to a known and controlled value. The pulsed nature of a PWM signal allow an easier synchronization respect to traditional OFDM schemes. Furthermore, the advantages of OFDM against multipath dispersion and fading are conserved. Table 8.5 summarizes the main advantages and disadvantages of the proposed scheme.

Mathematical description

Using the signal $y_{OFDM}[n]$ as starting point, the driving current signal at the LED is shown at Equation 8.31.

$$I_{LED}(t) = I_{max} \sum_{i=0}^{N-1} \Pi\left(\tau(y_{OFDM}[i], t - i \cdot T_{sym}\right) \tag{8.31}$$

Where $\tau(\cdot)$ is a linear mapping function between the desired duty cycle and the OFDM samples, T_{sym} is the PWM symbol duration and $\Pi(\cdot)$ is the pulse function. If a predistorted version were carried out, $\tau(\cdot)$ would represent the nonlinear mapping commented above. The mean electrical power of a PWM-OFDM frame may be expressed as follows.

$$P_{elec} = I_{max} V\left(I_{max}\right) E[\tau] \tag{8.32}$$

Introducing the definition of PAPR, which is the ratio between the maximum and the average power, it can be easily shown that this scheme would present a PAPR of 3 dB for every frame. Optical OFDM techniques present a lower spectral efficiency regarding radio systems, because both real and imaginary parts cannot be transmitted simultaneously. ACO-OFDM uses half the subcarriers in order to produce a fully-recoverable clipped frame. Furthermore, as optical OFDM scheme only transmit the real part of the FFT, Hermitian symmetry must be applied resulting in a halving of the efficiency. This scheme is the less spectral-efficient of the common traditional optical OFDM techniques, but is also the most energy efficient. The spectral efficiency of ACO-OFDM is determined by Equation 8.33.

$$\xi_{ACO} \approx \frac{\log_2(M) N_{sc}}{4(N_{sc} + N_{cp})} \tag{8.33}$$

Where M is the number of symbols of the constellation, N_{sc} is the number of subcarriers and finally N_{cp} is the number cyclic prefix samples. In the case of PWMO-OFDM, the spectral efficiency is directly affected by the bandwidth of the PWM signal that encodes each IFFT sample, but it uses all the available subcarriers to transmit information. Both information density and bandwidth increase result in a spectral efficiency which is reduced by a factor of 2^{N-1}. Therefore, this scheme dramatically increases the energy saving but reduces the spectral efficiency, being only suitable for medium-speed communication scenarios such as UWSN.

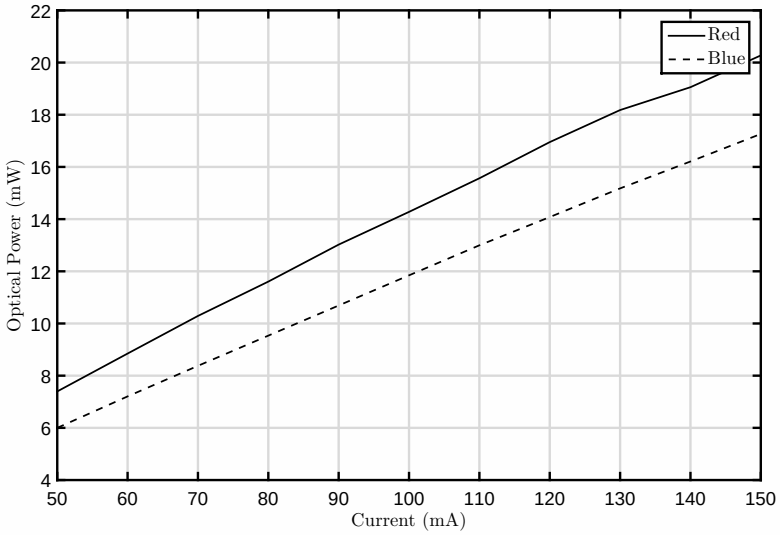

Figure 8.12: Optical emitted power vs driving current

The main advantage of ACO-OFDM against DCO-OFDM is the power reduction due to the clipping, which transforms it into one of the current most energy-efficient optical OFDM schemes. Taking into account that the probability density function of each sample within a sufficiently large OFDM frame is defined by a normal process, the clipped frame reduces the frame optical power to the half.

Regarding DCO-OFDM, the frame energy must be increased in order to transmit it. The frame optical power, in this case, tends to the DC-bias optical power. When considering PWMO-OFDM, the mean transmitted optical power is defined by the PWM signal amplitude and the mean duty cycle as it has been already shown. Lets assume a same-electrical power scenario between ACO-OFDM and PWMO-OFDM.

$$E[\tau]I_{max}V(I_{max}) = E[I_{ACO}V(I_{ACO})] = P_{elec} \tag{8.34}$$

ACO-OFDM needs a linear driver, which is sensitive to temperature variations and to the operation region. On the other hand, PWMO-OFDM uses a nonlinear power driver which is immune to the operation point and temperature, regarding nonlinear distortions on the signal. Generally, the output optical power of an LED has a linear behavior respect to the driving current. Defining the luminous efficiency as:

$$\eta(\lambda) = \frac{\phi(I_{LED}) \cdot I_{LED}}{I_{LED} \cdot V(I_{LED})} = \frac{\phi(I_{LED})}{V(I_{LED})} \tag{8.35}$$

As it was commented at the beginning of the chapter, linear LED drivers may present an electrical-to-electrical efficiency up to 80%, whilst class D amplifiers (which are the ones used for PWM signals) have efficiencies up to 95% [158]. In addition, using the proposed efficiency formula, it must be taken into account that the driver power will be determined by the commutation of the MOSFET driver transistor, which implies a small fixed power payback at a given P_{max}.

8.4.3 Experimental curves

During the measurements of Chapter 7, the used optical emitters were characterized using an integrating sphere. The obtained power-current curves are depicted in Figure 8.12. Furthermore, the voltage-intensity curves of both emitters are shown in Figure 8.13.

The current at which a nonlinear driver is more energy-efficient than a linear one, taking into account the consideration stated in Equation 8.34, is defined by:

$$\eta_{linear}\frac{\phi(I_{ACO})}{V(I_{ACO})} \leq \eta_{nonlinear}\frac{\phi(I_{max})}{V(I_{max})} \tag{8.36}$$

Rearranging the terms of Equation8.36 and defining relative measurements between fluxes and voltages, it yields:

$$\frac{\eta_{linear}}{\eta_{nonlinear}} \leq \frac{\Delta\phi}{\Delta V} \tag{8.37}$$

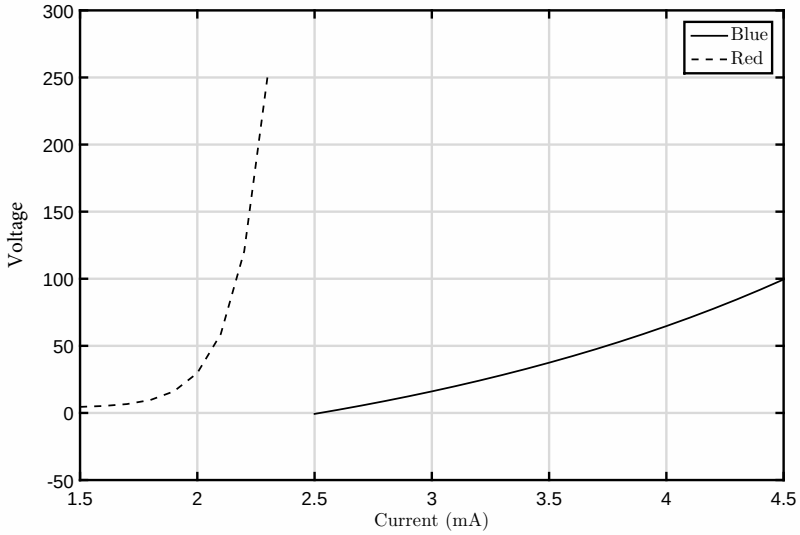

Figure 8.13: V-I curve of the used emitters

After including the measured efficiencies in the above Equations, the ratio $\frac{\Delta\phi}{\Delta V}$ for a range of electrical powers has been obtained. The same emitted power condition of Equation 8.34 has been included. Figure 8.14 depicts this curve and compares it to the ratio of driver efficiencies. In order to obtain the mean current of an ACO-OFDM scheme, the probability density function of the OFDM samples should be considered. In ACO-OFDM, each sample follows a Half Gaussian distribution where the variance depends on the used mapping. For a QAM mapping, this variance is unitary and the expected value of each sample is $1/\sqrt{2\pi}$ as is commented in [153].

It can be observed that for almost every electrical power, nonlinear drivers are more energy efficient than linear drivers. Notice that these curves correspond to a single LED emitter. In the case of a LED array where the currents are divided, the use of PWM is recommended in terms of energy. From the data, only very efficient linear drivers (more that 80%) justify the use of continuous waveforms.

8.4.4 Comments on the BER performance

As it was commented above, the pulse width modulation of the OFDM waveform introduces an extra noise term due to quantization, which affects the SNR in the following way:

$$SNR_{PWMO-OFDM} \approx \frac{S^2}{\sigma^2 + \sigma_Q^2} \tag{8.38}$$

Where σ_Q^2 is the quantization noise power, which depends on the quantization step $\Delta V = (V_{max} - V_{min})/2^N$. It implies that there is a maximum achievable SNR bounded by this always-present noise source. The BER curve of the proposed scheme would be right-shifted respect to a non-quantized scheme, as shows Figure 8.15. It must be taken into account that incrementing the number of bits to enhance the BER performance has several harmful implications:

- The spectral efficiency is reduced. The product $\Delta SNR \cdot \Delta\xi$ is conserved in this type of system. Hence, an increment on the SNR is directly translated to a decrement of the same amount in the efficiency. Nevertheless, the value of N can be optimized.
- The power consumption of the switching components is increased. As it was commented in the drivers Section, the power consumption of the MOS-based components increases linearly with the frequency. In this case, the ratio $\Delta SNR/\Delta P_{MOSFET}$ is constant.
- The nonlinear driver efficiency is reduced because of the previous effect. Depending on the parasitic capacitance of the used device, this effect may be neglected. As it was commented at the beginning of the chapter, there is a switching frequency f_s at which the linear driver surpasses the nonlinear driver efficiency, which is defined by:

$$f_s = \frac{2\,P_{OPA}(f_s/2^N)}{CV^2} \tag{8.39}$$

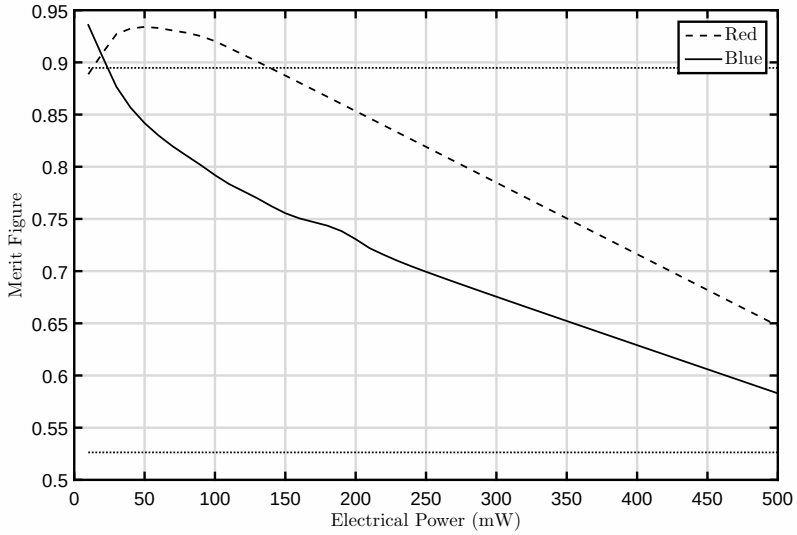

Figure 8.14: Merit figure of Equation 8.37 for the LED devices used in Chapter 7. The horizontal dotted lines correspond to the ratio of driver efficiencies. The upper one is for a linear driver efficiency of 85%, whilst the lower corresponds to an efficiency of 50%. In both cases, the nonlinear efficiency is 95%

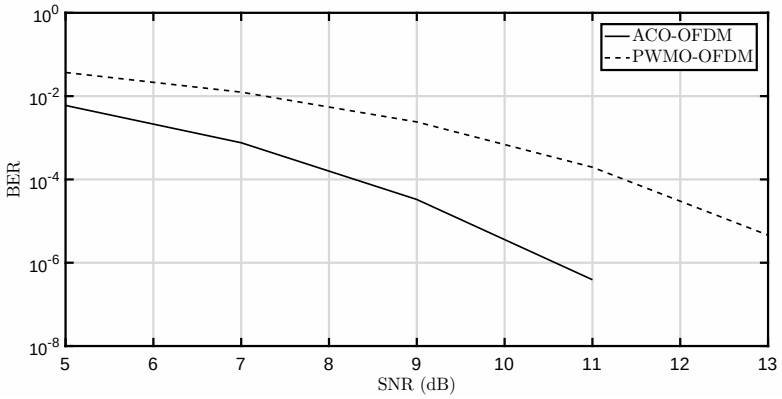

Figure 8.15: BER vs SNR curves for an ACO-OFDM (512 subcarriers with QAM) scheme and a PWMO-OFDM (1024 subcarriers with QAM) scheme. Note the right 3 dB shift of the PWM-based scheme.

Generally, the parasitic capacitance is very small (a few pF) and the switching voltage V is determined by the used LED array. Moreover, the power consumption of an OPA-based linear driver also increments with the signal's bandwidth, turning even higher the critical frequency. In conclusion, a compromise between power consumption and BER performance should be defined in order to optimize the number of bits of the transmitter's DAC.

Chapter 9

Conclusions and Future Research

During this thesis, several contributions have been made regarding different aspects of channel modeling and energy efficiency in UWOC. After analyzing the state-of-the-art research lines in Chapter 3, two clear conclusions were extracted. On the one hand, channel modeling in UWOC has been primarily directed by contributions at physical level, regarding different phenomena such as turbulences and multiple scattering. Traditionally, Beer-Lambert's law has been used to describe extinction in UWOC, but Cochenour et al. demonstrated in [16] that scattering produces beam spreading and in consequence, the effective extinction is smaller than the sum of $\alpha(\lambda)$ and $b(\lambda)$. Furthermore, there are different simulation engines using Monte Carlo schemes in the literature. Nonetheless, these algorithms use the Henyey-Greenstein scattering phase function to model the photon deviation due to particles, which is an oversimplification of a more realistic approach such as Mie scattering. The main advantages of Henyey-Greenstein are the easy parametrization of the scattering broadening with a single parameter and the fast calculation of random angles using this distribution, but the accuracy is reduced as it is commented in [38]. On the other hand, the contributions addressing applications range from very specific scenarios such as providing feedback to swimmers in a pool [109], to long-distance UWOC links in actual scenarios during ocean monitoring campaigns [86]. There are different works addressing hybrid opto-acoustic transceivers for UWSN [82]. These kind of devices take advantage of the high inherent energy efficiency and bandwidth of UWOC, whilst maintaining the possibility of long range communication using UAC. However, statistical approximations of the UWOC channel have been focused on providing a faster method to obtain channel gain estimations [47], but there are no statistical channel models for UWOC links in terms of channel gain or bandwidth. Finally, there is an evident lack of contributions regarding energy efficiency in UWOC even though it is of capital importance taking into account the replacement cost of underwater nodes.

The UWOC channel is a linear and time variant channel, but its time variability is subject to different phenomena such as turbulences, misalignment and scattering. In FSO, turbulences are normally subject to Kolmogorov's spectrum under weak turbulence regimes. Nonetheless, the optical properties of seawater present variability not only due to temperature gradients, but also because of salinity variations. In the literature, Kolmogorov's spectrum has proven to be inaccurate, and Nikishov's spectrum is widely used in the literature [122]. This approximation includes the two dependencies in the spatial frequency spectrum. It was proven during Chapter 4, that the UWOC scintillation index depends on the distance with an exponent ranging from 3/2 to 11/6, and not strictly on FSO's traditional 11/6 exponent. The exponent is defined by the spectrum's parameters.

In Chapter 4, the impulse response of different UWOC scenarios was obtained using a Modified Monte Carlo Ray Tracing algorithm. Unlike other authors, Mie scattering was used as phase function in this work. Consequently, the complexity of the ray generation is increased in exchange for the enhanced accuracy. However, using the modified approach, a direct ray to the receiver is calculated after each scattering, reducing the volume of rays and the convergence time of the algorithm respect to the impact-testing conditions used in the literature. Furthermore, the algorithm was parallelized using both multiprocessor and GPU schemes. Speedups up to 42 were obtained using a NVidia Tesla M2050 GPU, allowing calculations of full impulse responses with 10^5 rays in less than 2 seconds. The economical efficiency of both parallelization technologies was analyzed, showing that GPU implementations are more cost-effective than multiprocessor schemes. Moreover, the impact of the channel parameters into the received impulse response was analyzed. The following effects were observed:

- The link range reduces exponentially the channel gain and the bandwidth. As the distance increases, the optical paths followed by the arriving rays is greater. Therefore, the absorption losses and the number of impacts with particles also increase.
- Directive emitters concentrate energy in narrow solid angles, whilst other emitters disperse light. Taking into account the effect of multiple scattering, although the energy were collimated, a significant amount of energy may arrive the receiver. For perfectly aligned links, the higher the directivity, the higher the bandwidth and the channel gain.

- The emission wavelength has two main effects. Firstly, the seawater absorption and the loss due to particles are wavelength dependent. Secondly, the normalized dimension of the suspended matter depends on the wavelength, and therefore, for a given particle size, the Mie scattering phase function may widely vary from a wavelength to another.

- As it was commented above, the particle radius defines the shape of the scattering, but for a given concentration of particles per cubic meter, the number of scatterings increases with the particle radius. Therefore, the particle radius effect increments the number of scatterings but turns the phase function more forward-dominant. The observed simulated results suggests that the channel gain is reduced with the particle radius, due to the increasing number of impacts, whilst the bandwidth is increased due to the reduction of the average cosine of the phase function.

- The concentration of particles has two effects. The first one is the same as the particle radius. As the concentration increases, the collision probability also increases and the channel gain is reduced. The other effect is to contribute to the broadening of the BSF, allowing greater misalignment errors between emitter and receiver. Depending on the distance and the particle radius, the concentration of particles may contribute to a greater light collection since a bigger solid angle has influence on the receiver.

- The distance to seabed was demonstrated to have a very reduced effect on the channel gain. Nonetheless, the bandwidth is slightly reduced in horizontal deep links. Since the distance to seabed may be neglected in UWOC channel estimation, the seabed albedo has also negligible influence.

- For near-surface links, the contributions due to surface reflections cannot be obviated since they present a significant importance. However, this effect is dispersed as the link range increases due to the effect of extinction. Depending on the depth and for a still water scenario, the illuminated surface area with greater influence on the received power is modified. Therefore, as the depth increases, the channel gain is reduced and the bandwidth increased.

- Wind speed produces a random slope variation on the seawater surface. This random variation turns each point of the surface in a potential scatterer, where the overall average contribution of the illuminated surface is incremented. Regarding the bandwidth, the multipath component is strong in still water scenarios, whilst the random agitation of seawater disperses this component along the impulse response, increasing the average bandwidth.

In Chapter 5, underwater-to-air links were studied. This type of vertical links are suitable for shallow water node deployment where the data acquisition is performed without submerging the transceiver, for instance, an operator in a ship or a drone. The sealing process of a transceiver to make it submersible usually increments fabrication costs. This possibility is a cost-effective solution for shallow water UWSN applications. The underwater-to-air problem was addressed form a geometrical point of view, associating the received power to the optical power that impacts on the surface and is forwarded to the photodetector. This way, the analysis is based on calculating how much energy arrives a certain area of the seawater surface. To simplify the analysis, only surfaces with shapes that ensure the bijectivity of a spatial transformation were considered. This transformation related the XY positions of a ray on the surface and the position at the receiver's plane. After imposing several conditions regarding the sea wave spectrum, which was considered monochromatic, a numerical integration scheme was used to obtain simulations of the received power. It was observed that the received light intensity followed the shape of the sea waves, due to the lensing effect of a propagating plane wave. In addition, an analysis similar to the one made during Chapter 4 was performed to relate each channel parameter to the received intensity. Furthermore, the channel availability was studied in each scenario respect to the receiver sensitivity. The main obtained conclusions were:

- The emitter depth produces an exponential decay on the received power, following the extinction curve.

- The receiver height has a similar effect to the previous parameter, since the solid angle formed by the receiver and the emitter is reduced with the squared distance.

- The sea wave height has a direct impact on the seawater surface slope, which is critical on the calculation of the projected photodetector area. Steeper slopes generate deeper fadings, whilst low-height sea waves produce slight variations on the received power. The peak-to-peak variations of the received power can be higher than 10 dB, producing a notable impact on the channel availability and increasing the requirements of the receiver.

- The sea wave wavelength produces the same effect as the sea wave height. In this case, longer wavelengths imply more relaxed slopes and hence, smaller variations.

- Wind shear effect has a very interesting effect on the variation of the received power. As the wind speed increases, the peak-to-peak variation of the received signal is reduced (and also the maximum value). Therefore, windy scenarios may increase the channel availability when the receiver's sensitivity is within the variation range of the received optical power.

The statistical modeling of the UWOC channel response was addressed in Chapter 6. The main contributions made during this chapter were:

- Analyzing the most suitable probability distribution function for both channel gain and bandwidth.
- Defining a Fresnel zone attending to the 95 % of the impulse response energy, after performing a rectangular approximation.
- Proposing a model of the losses induced by big opaque particles.

A brief analysis of the impulse response formula showed the possibility of defining an *ad hoc* probability density function for the channel gain. Nonetheless, after performing a maximum likelihood estimation and several hypothesis tests on the simulated data, the Generalized Extreme Value distribution obtained the best results in the benchmark for both channel gain and bandwidth. This benchmark consisted on a set of scenarios covering a wide range of parameter combinations. Nonetheless, the proposed distribution only covered a few cases less than GEV. The obtained distribution showed how varies the received power at uncorrelated time instants. From the obtained data, it was observed that generally:

- The SNR increases with the directivity, since the variability of the received power is reduced. It is straightforward to notice that narrow emission cones are subject to a lower amount of possible scatterings.
- The link range reduce the effect of scattering-induced variability. However, the increment of the SNR due to distance respect to the impact with particles is countered by the effect of turbulences, which increase with a power law with distance.
- From the obtained data it can be inferred that for a given link range and concentration, there is a particle size that minimizes the SNR. As it has been commented several times during this document, large particle radii imply a high dominance of the forward direction of the scattering. This leads to an increasing SNR for decreasing particle radii.
- The particle concentration reduces the SNR. This occurs because for high concentrations there are more possible scatterers within the link's volume of influence.

The impulse response can be divided in the sum of two rectangles due to its abrupt shape. The first rectangle may be defined to contain the 95 % of the energy. Its width, or delay spread, is associated to those delays at which there is significant energy contributions. Therefore, the maximum delay defines through the space-time relation the maximum traveled distance of a single-scattered ray. Taking into account the geometry of the scenario, this maximum distance generates an ellipsoid that can be referred to as the volume of interest or Fresnel zone. This Fresnel zone has several implications:

- The definition of a volume of interest opens the possibility of time-dependent simulators where each particle is tracked within the ellipsoid. This kind of simulator would be able to model the time-frequency response of the channel, from which coherence time can be extracted.
- The Fresnel zone describes the volume at which any intersecting object produces an effect on the received power.

Furthermore, the impact of big opaque particles was also analyzed in Chapter 6. A big opaque particle is a particle that does not produce neither scattering nor diffraction, for instance, sand grains. Actually, sand grains would generate contributions due to their reflectivity, but this was obviated to isolate the shadowing effect of these particles. After statistically analyze the influence of these particles, it was found that big opaque particles produce an impact on the SNR that depends on their size, the link's range, the concentration of particles and the radii of emitter and receiver. Following the tendency of this thesis, the influence of each of the aforementioned parameters was analyzed, showing that:

- The SNR diminishes with the link range, since the average number of particles linearly depends on the distance. The higher the number of particles, the higher the probability to suffer fading.

- The SNR rapidly increases with the emission area up to a maximum that depends on the link's range, particle size and concentration. Above this optimum value, the SNR decreases as the area increments. The emission surface has two effects. When it increases, the truncated cone formed by emitter and receiver increments its volume and hence, the number of particles, but the particle size to emission surface ratio diminishes. These opposite effects equal at the optimum value.

- Regarding the receiver area, the SNR increments with it, but saturating. The saturation of the SNR is due to the residual impact of the parameter in the number of particles and the particle-to-surface ratio.

- The concentration of particles reduces the SNR because a bigger amount of particles within a volume produce shadowing with more degrees of freedom.

- The most harmful parameter of this analysis is the particle radius. The bigger the particle, the bigger the produced shadow and energy loss. In the studied scenarios, the SNR decreased at a rate of 10 dB/mm.

In Chapter 7, two experiments were carried out. The first one proved the influence of the movement of particles on the SNR, as well as the effect of the particle concentration. The second experiment analyzed how surface reflections affect a near-surface UWOC link. Furthermore, the WSSUS assumption in this type of link was demonstrated. The experiments were performed in a tap water-filled tank where chlorophyll-rich particles were dissolved. Regarding the particle movement experiment, it was found that it has a harmful effect on the SNR, and that it depends on the wavelength since scattering does. During the second experiment, the effect of wind speed was introduced using a wind generator on the tank's surface, showing that the greater the wind, the lower the coherence time of the channel.

Finally, Chapter 8 addressed energy-efficient strategies to reduce the power consumption of battery-powered nodes. Three contributions were made in this regard.

- Red wavelengths may be a better alternative to traditional blue-green emitters due to the higher energy efficiency at these wavelengths. Generally, low band gap emitters have greater wall-plug efficiencies due to the higher internal and external quantum efficiencies of these devices. Furthermore, silicon photodetectors, which are the most used in visible spectrum communications, present a better responsivity at longer wavelengths. These two characteristics can compensate the worse underwater propagation, generating a higher net input at the receiver.

- Power control algorithms dramatically reduce the power consumption. Traditionally, power control has been used in cellular networks to maximize the SINR, controlling the output power to generate the lowest possible interference. However, in UWSN the main objective is reducing the power consumption as much as possible, due to the elevated replacement costs. Several power control algorithms were tested under simulated conditions, and an Adaptive-Damping-Adaptive-Step power control algorithm was proposed to enhance the convergence time and reduce the variability of the output power. It was proven that this modification of the LMS algorithm can dramatically improve the energy efficiency respect to a constant power scheme adding very small complexity.

- Pulse-width modulating a waveform such as an optical OFDM reduces the power consumption since it allows the use of very energy-efficient nonlinear drivers. Optical OFDM schemes are subject to several constraints when used in IM/DD schemes. Optical emitters present a nonlinear behavior defined by the I-V curve of the device, limiting the linear working zone. Furthermore, the optical emitter power is not completely linear with the driving current, showing compression with the increasing current. Therefore, these two effects, which are multiplicative, drastically reduce the linear zone is several dB. Moreover, Optical OFDM needs linear drivers to convert the input voltages in currents in order to avoid extra distortion. These type of drivers are normally subject to high power consumptions, reducing the energy efficiency. On the other hand, nonlinear drivers such as class D amplifiers take advantage of the fast switching capability of LED and laser devices with a very large efficiency due to the use of MOSFET transistors. These transistors have a power consumption that increases linearly with frequency, but the frequencies at which these drivers surpass linear drivers in power consumption is very high. In Chapter 8, a proposal to reduce the consumption of OFDM schemes in UWOC was presented. The proposed modification consisted in a class D amplifier at the output stage of the emitter, whose low pass filter is removed and placed at the input stage of the receiver. This slight but effective modification allows a reduction on the power consumption of the emitter, the relaxation of the linear amplification at the receiver, and the ease to synchronize the received frames.

9.1 Future Research

The following lines summarize the future research lines derived from this thesis.

- During this thesis, only measurements in close-range scenarios have been obtained. Further research in actual UWOC scenarios must be performed in order to extend the valid range of the results of this thesis. For instance, there is no literature addressing simulation model validation, and this step is very important in order to clarify the relationship between channel parameters and link performance. Moreover, the obtained results may serve as input to generate more accurate statistical prediction models.

- The simulation of the influence of big opaque particles showed that there is an optimum emission area that maximizes the SNR. This fact needs experimental validation in actual scenarios in the presence of this kind of light-obstructing particles. In addition, this fact suggests the extrapolation of the results to scattering particles. Simulations with extended sources must be made in order to find if there is also an optimum value of the emitter's radius in scattered scenarios.

- The definition of Fresnel zones opened the possibility of time-dependent scenarios, since the volume of interest is reduced to an ellipsoid whose radius depends on the channel physical properties and the link distance. These type of simulators should track the particles positions within the volume during the simulation time. Without this volumetric restriction, the number of considered particles cannot be afforded. The use of time-frequency simulation in UWOC would give a new approach to the understanding of the variability of the channel.

- There is a lack of vertical link simulators in the bibliography. These type of links must be analyzed in order to obtain a better understanding of long range UWOC communications. Beam wandering due to turbulences and ray bending due to gradual changes on the refractive index hardens this type of analysis. However, this is the most typical scenario in UWSN and needs to be well-investigated.

- Energy efficiency has been shown to be a subject with great impact on real system implementations, but curiously has not received the attention it deserves by the scientific community. To lengthen the lifespan of underwater nodes is mandatory, and different strategies must be analyzed to achieve it. For instance, power control algorithms are an easy technique to increase energy efficiency, and further research is needed in this regard.

- Non-linearization of waveforms has been shown to be an easy way to enhance the efficiency of a transceiver. However, the spectral efficiency is reduced at the emitter and encodings on the pulsed-shape output can be performed to reduce the bandwidth requirements.

- In this thesis, medium access layer has not been addressed, but novel techniques in VLC such as OCC may be introduced in medium-range UWOC scenarios as a spatial division multiplexing strategy. If OCC were used, the analysis of the emission power requirements, as well as the resolution of the acquired images should be the starting point, since they would define the applicability range of the technique. Furthermore, in scenarios where the camera were mounted on a buoy, for instance, several aspects should be taken into account. In first place, since the nodes would be moving along the captured frame, tracking algorithms taking into account the measured acceleration and angular speeds of the receiver should be used. Moreover, the study of the probability density function of each point of the space, would reveal the effective coverage area of the camera. Finally, movement mitigation technology such as gimballs may be used to reduce the aforementioned harmful effect.

Appendices

Appendix A

Demonstrations of Chapter 5

In Chapter 5, a nonlinear transformation was proposed in order to obtain the projection of the photodiode over the seawater surface. This transformation was:

$$\begin{aligned} x' &= x + \Delta x(x,y) \\ y' &= y + \Delta y(x,y) \end{aligned} \tag{A.1}$$

Note that the terms $\Delta x(x,y)$ and $\Delta y(x,y)$ refer to the distance a ray travels in each direction before impacting the receiver's XY plane. This deviation depends on the receiver's height H and the refraction, as Equation set A.2 shows.

$$\begin{aligned} \Delta x(x,y) &= [H - S(x,t)]\,\frac{r_x}{r_z} \\ \Delta y(x,y) &= [H - S(x,t)]\,\frac{r_y}{r_z} \end{aligned} \tag{A.2}$$

The regions in which the change of basis is bijective directly imply that the photodiode's surface-projected area has a unique image on the transformed domain. In other case, several images of the photodiode may be projected on the seawater surface, complicating the analysis. In order to analyze this regions, the Jacobian matrix of the transformation is obtained as shows Equation A.3.

$$J = \begin{pmatrix} 1 + \Delta x(x,y)_{,x} & \Delta x(x,y)_{,y} \\ \Delta y(x,y)_{,x} & 1 + \Delta y(x,y)_{,y} \end{pmatrix} \tag{A.3}$$

The subindex $_{,\xi}$ denotes differentiation respect to ξ. The determinant of the Jacobian must be nonzero to assert bijectivity around a certain point (x_0, y_0). In order to analyze the critical point that make the rank of J less than 2, the next inequation must be solved.

$$(1 + \Delta x(x,y)_{,x})(1 + \Delta y(x,y)_{,y}) - \Delta x(x,y)_{,y}\Delta y(x,y)_{,x} > 0 \tag{A.4}$$

In order to ensure the bijectivity of the transformation in a sufficiently wide area, two main weak conditions must be satisfied. One of the cross partial derivatives ($\Delta x_{,y}$ or $\Delta y_{,x}$) must be negligible and both $\Delta x_{,x}$ and $\Delta y_{,y}$ must be bounded in the interval $(-1, \infty)$. Conditions must be imposed to satisfy $\Delta x_{,y} \approx 0$ or $\Delta y_{,x} \approx 0$. The most restrictive conditions will be assumed in the end. Equation A.5 shows the form of the condition of $\Delta x_{,y}$.

$$\Delta x_{,y} = (H - S(x,t))\,\frac{r_{x,y} r_z - r_{z,y} r_x}{(r_z)^2} \tag{A.5}$$

Working on the expression, it can be simplified to:

$$\Delta x_{,y} = (H - S(x,t))\,\frac{r_x}{r_z}\frac{\partial}{\partial y}\left(\ln \frac{r_x}{r_z}\right) \tag{A.6}$$

Introducing the vanishing requirement on this derivative, and assuming that $H - S(x,t) \neq 0$ and $r_z \neq 0$, for all (x,y) pair, it yields:

$$r_x \frac{\partial}{\partial y}\left(\ln \frac{r_x}{r_z}\right) = 0 \tag{A.7}$$

This equation has two solutions: the trivial solution $r_x = 0$ and $\ln \frac{r_x}{r_z}$ approximately constant in y. Performing the Taylor series of the latter around (0,0) up to the first derivative, and imposing that this derivative must be much lower than the constant term, it yields the following relation.

$$|y| << \left| \frac{r_x r_z}{r_{x,y} r_z - r_{z,y} r_x} \ln \frac{r_x}{r_z} \right|_{(0,0)} \tag{A.8}$$

Solving Equation A.8 it yields that there is no limitation on the y-axis, since $r_{x,y}$ and $r_{z,y}$ tend to zero. For $\Delta y_{,x}$ a similar condition can be obtained but in terms of x.

$$|x| << \left| \frac{r_y}{r_z(H-S)} \frac{\ln\left((H-S) r_z / r_y\right)}{(H-S)(r_{z,x} r_y - r_{y,x} r_z) - S_{,x} r_z r_y} \right|_{(0,0)} \tag{A.9}$$

It is straightforward to demonstrate that $r_{y,x}$ and $r_{z,x}$ linearly depend on $\partial\left(\hat{n} \cdot \hat{v}\right)/\partial x$. In order to vanish this last term (eliminate the dependency on X), the propagating sea wave must satisfy that:

$$\lambda >> \pi \sqrt{2 D \eta_0} \tag{A.10}$$

This last condition arises from the following approximation:

$$\begin{aligned}
\frac{\partial\left(\hat{n} \cdot \hat{v}\right)}{\partial x} &= \frac{\partial \hat{n}}{\partial x} \hat{v} + \frac{\partial \hat{v}}{\partial x} \hat{n} \\
\hat{v} &= \frac{(x, y, S)}{(x^2 + y^2 + S^2)^{1/2}} \rightarrow \hat{v}_{(0,0)} \approx (0, 0, 1) \\
\hat{n} &= \frac{(-S_{,x}, 0, 1)}{(1 + S_{,x}^2)^{1/2}} \\
\frac{\partial \hat{v}}{\partial x} &= \frac{(1, 0, S_{,x})}{(x^2 + y^2 + S^2)^{1/2}} - (x, y, S) \frac{x + S S_{,x}}{(x^2 + y^2 + S^2)^{3/2}} \rightarrow \frac{\partial \hat{v}}{\partial x}_{(0,0)} \approx (S^{-1}, 0, 0) \\
\frac{\partial \hat{n}}{\partial x} &= \frac{(-S_{,xx}, 0, 0)}{(1 + S_{,x}^2)^{1/2}} - (-S_{,x}, 0, 1) \frac{S_{,x} S_{,xx}}{(1 + S_{,x}^2)^{3/2}}
\end{aligned} \tag{A.11}$$

The term $S^{-1} \approx D^{-1}$ since $D >> \eta_0$. Taking this into consideration and considering the worst case, the previous equations can be reduced to:

$$S_{,xx} D << 1 \tag{A.12}$$

Finally, introducing the approximation on Equation A.9, the maximum x distance that assures that $\Delta y_{,x} \rightarrow 0$ is the same in the case of y, because $r_y = 0$ for $\hat{v} = (0, 0, 1)$. Hence, x and y do not limit the vanishing of the cross partial derivatives if condition A.10 is satisfied.

Finally, in order to ensure the presence of inverse, $\Delta x_{,x}$ and $\Delta y_{,y}$ must be bounded to the interval $(-1, \infty)$. These conditions are formulated in Equation set A.13.

$$\begin{aligned}
\Delta x_{,x} &> -1 \\
\Delta y_{,y} &> -1
\end{aligned} \tag{A.13}$$

Introducing the corresponding dependencies and assuming the same as before, it yields the following system of inequations:

$$\begin{aligned}
(r_z)^2 + (H - D) r_{x,x} r_z - (H - D) r_{z,x} r_x &> 0 \\
(r_z)^2 + (H - D) r_{y,y} r_z - (H - D) r_{z,y} r_y &> 0
\end{aligned} \tag{A.14}$$

Since the sea wave propagates along the x-axis, the limiting range is imposed by the maximum deviation of x. This maximum deviation δx is related to the x-axis itself ($y = 0$). Introducing the assumptions made during the previous steps into Equation set A.13 yields:

$$\begin{aligned}
D + (H - D) n_w \left(\frac{1}{D} - \eta_0 k \sin(\omega t - k \delta x) \right) &> 0 \\
D + (H - D) \frac{n_w}{D} &> 0
\end{aligned} \tag{A.15}$$

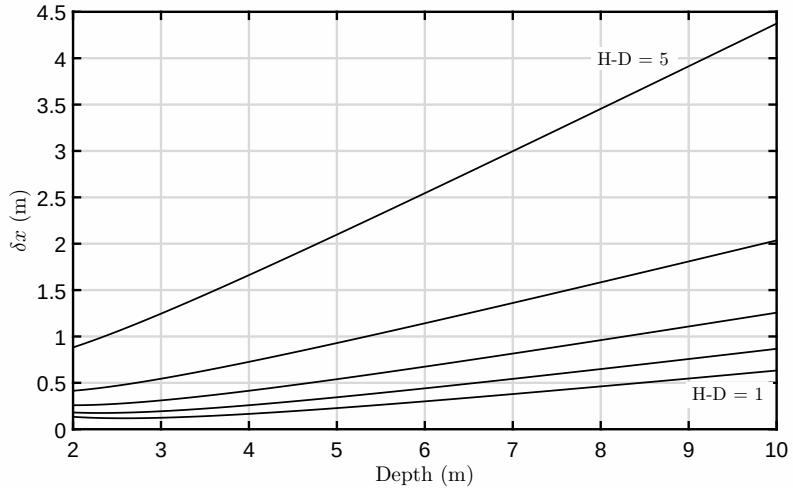

Figure A.1: Maximum deviation in the x-axis to assure bijectivity ($\eta_0 = 0.25\,m$).

The second inequation is satisfied for all D and H since $H > D$. Regarding the first inequation, the following condition can be obtained:

$$\sin(\omega t - k\delta x) < \frac{D^2 + (H-D)n_w}{n_w D\eta_0 k(H-D)} \tag{A.16}$$

This condition may be reduced to the worst case, which occurs when the sine tends to one. Making a second order approximation of the sine near to one, the maximum deviation of δx which assures the existence of inverse is:

$$|\delta x| < 2\frac{D^2 + (H-D)n_w\,(1 - D\eta_0 k)}{n_w D\eta_0 k^3(H-D)} \tag{A.17}$$

Finally, there is a minimum height over the still water level $(H-D)_{min}$ at which the last condition is satisfied.

$$(H-D)_{min} = \frac{D^2}{n_w(D\eta_0 k - 1)} \tag{A.18}$$

From the denominator of the last expression, an upper bound of the sea wave wavelength arises. Joint to condition A.10, to consider the approximations as valid, λ must be in the interval:

$$\pi\sqrt{2D\eta_0} << \lambda < 2\pi D\eta_0 \tag{A.19}$$

This last expression describes an absolute minimum of λ, which is defined by the intersection of the two boundary functions. The wavelength only complies with condition A.19 if $D\eta_0 > 1/2$, which is easily satisfied by a traveling sea wave under shallow water propagation. Figures A.1 and A.2 depict the last two limits in terms of $(H-D)$ and D for a sea wave satisfying condition A.10.

It can be observed that the area which assures bijectivity is wide enough compared to the photoreceiver's area.

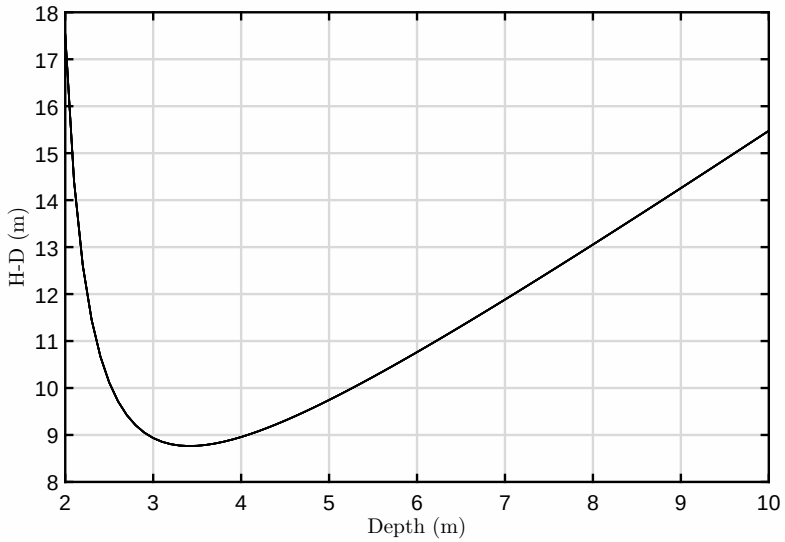

Figure A.2: Maximum height at which there is inverse ($\eta_0 = 0.25\,m$).

Appendix B

Received light intensity in partially obstructed links

In Chapter 6, a statistical approach of the received light intensity in a link partially obstructed by big opaque particles was presented. In this Appendix, the mathematical development from which the equations of Chapter 6 were derived is presented. In order to ease the analysis, the propagation medium will be considered lossless, the emitter will be considered as isotropic, and a single spherical particle will considered. Figure B.1 depicts the scenario under consideration.

Figure B.1: Particle obstructing a link comprising an extended source and a photodiode

Since the particle's position is important, the source will be considered as an extended source of light, where each point of the surface has the same emission pattern and radiance. Furthermore, to take advantage of cylindrical symmetry, both emitter and receiver are considered circular. Under the depicted situation, for a particle-free scenario, the received power can be expressed as four cascaded integrals of the form:

$$P_{rx} = \int_{r_{tx}} \int_{\varphi_{tx}} \int_{\theta} \int_{\varphi_{rx}} \frac{P_{tx}}{4\pi A_{tx}} r_{tx} \sin\theta \, \mathrm{d}r_{tx} \mathrm{d}\theta \mathrm{d}\varphi_{rx} \mathrm{d}\varphi_{tx} \tag{B.1}$$

The received power depends on the solid angle formed by the receiver and each point of the emitting surface. If there is no obstructing particle, the last integral presents symmetry on the emitter, and the solid angle subtended can be approximated by $\mathrm{d}\Omega \approx A_{rx}/d^2$, yielding:

$$P_{rx} = \frac{P_{tx}}{2A_{tx}} A_{rx} \int_0^{R_{tx}} \frac{r_{tx} d_{link}}{\left(d_{link}^2 + r_{tx}^2\right)^{3/2}} \, \mathrm{d}r_{tx} \tag{B.2}$$

Solving the integral:

$$P_{rx} = \frac{P_{tx}}{4\pi R_{tx}^2} A_{rx} \left(1 - \frac{d_{link}}{\sqrt{d_{link}^2 + R_{tx}^2}}\right) \tag{B.3}$$

For a small area emitter, which is a common consideration in OWC in general, the total received power depends on the following limit:

$$\lim_{R_{tx} \to 0} \frac{1}{R_{tx}^2} \left(1 - \frac{d_{link}}{\sqrt{d_{link}^2 + R_{tx}^2}}\right) = \frac{1}{d_{link}^2} \tag{B.4}$$

After analyzing the particle-free scenario, lets introduce a single particle of radius R amid the link. Now, in this situation, there would be certain angles at which the solid angle between emission point and receiver is reduced, as Figure B.1 showed. Now, the total received power can be integrated under two different intervals. An interval at which the particle does not produce any effect, and a particle-influenced interval. Figure B.2 shows this division of the integral.

Figure B.2: Division of the integration domain due to the presence of a particle

The integral of Equation B.2 can be rewritten as:

$$P_{rx} = \frac{P_{tx}}{2A_{tx}} \left(A_{rx} - A_{part}\right) \int_0^{R_0} \frac{r_{tx} d_{link}}{\left(d_{link}^2 + r_{tx}^2\right)^{3/2}} \, \mathrm{d}r_{tx} + \frac{P_{tx}}{2A_{tx}} A_{rx} \int_{R_0}^{R_{tx}} \frac{r_{tx} d_{link}}{\left(d_{link}^2 + r_{tx}^2\right)^{3/2}} \, \mathrm{d}r_{tx} \tag{B.5}$$

Naming I the integral of Equation B.3 and rearranging the terms of Equation B.5, the following expression is obtained:

$$P_{rx} = I - \frac{P_{tx}}{2A_{tx}} A_{part} \int_0^{R_0} \frac{r_{tx} d_{link}}{\left(d_{link}^2 + r_{tx}^2\right)^{3/2}} \, \mathrm{d}r_{tx} \tag{B.6}$$

The second part of the equation is similar to the one solved in Equation B.3, but in this case, the upper integration limit is defined by Equation B.7.

$$R_0 = \frac{d_{link} R + d_i R_{rx}}{d_{link} - d_i} \tag{B.7}$$

Where d_i is the z-axis position of the particle. Introducing Equation B.7 into Equation B.3, it yields.

$$P_{rx} = I - \frac{P_{tx}}{2A_{tx}} A_{part} \left(1 - \frac{d_{link}}{\sqrt{d_{link}^2 + R_0^2}}\right) \tag{B.8}$$

Finally, the expanded version of Equation B.8 is:

$$P_{rx} = \frac{P_{tx}}{4\pi R_{tx}^2} \left[A_{rx} \left(1 - \frac{d_{link}}{\sqrt{d_{link}^2 + R_{tx}^2}}\right) - A_{part} \left(1 - \frac{d_{link}}{\sqrt{d_{link}^2 + R_0^2}}\right)\right] \tag{B.9}$$

The loss term depending on A_{part} can be associated to the angle Ψ subtended by R_0 and d_{link}. Mathematically:

$$P_{rx} = I - \frac{P_{tx}}{4} \frac{A_{part}}{\pi R_{tx}^2 \left(1 - \cos \Psi(d_i)\right)^{-1}} \tag{B.10}$$

It can be shown that for $d_i = 0$, the power loss is a fraction of the emission surface, whilst for $d_i = d_{link}$ the power loss is defined by a reduction on the photodiode's illuminated area. Finally, for a given impact distance, the power loss is the quotient between the particle area and the area of the truncated cone formed by emitter and receiver at that distance.

Appendix C

Waveforms, Correlations and Probability Density Functions of Chapter 7

In this chapter, all the measurements obtained during the experiments commented in Chapter 7 are presented. In order to organize this appendix, the figures have been classified depending on the associated experiment. Section C.1 comprises the acquired waveforms and the obtained probability density functions, whilst Section C.2 presents the obtained correlation functions and the waveforms.

C.1 Movement of particles

This section presents all the captured waveforms. All the measurements were performed in a very low ambient noise environment, so as to reduce possible background extra noise. The amplified photodiode was configured with a gain of 60 dB, which implies a bandwidth of 11 KHz according to [138]. Furthermore, in this configuration, the RMS noise voltage is $800\mu V$. Figure C.1 depicts the noise of the receiver. Its standard deviation is 1.2 mV.

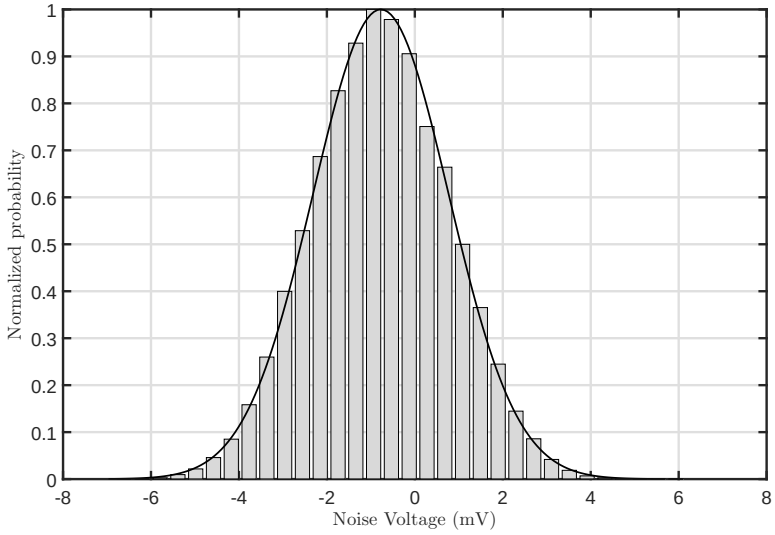

Figure C.1: Receiver noise under absolute darkness conditions. Note the small offset due to the effect of the transimpedance amplifier.

C.1.1 Blue emission

Blue suffers less extinction in pure seawater than red, but as the concentration of scatterers increases, the optimum transmission wavelength shifts to a redder value. However, due to the reduced length of the used water tank (91 cm), the red wavelength presents a better response for all cases. The following subsections present the obtained waveforms and PDFs for the used blue wavelength (470 nm) in the particle movement experiment.

Still water

In still water, the particle positions are practically invariant with time and the resulting variability is only due to Johnson and shot noises. However, comparing the variances of Figures C.4 and C.10, it can be observed that shot noise has a negligible influence. Furthermore, these variances are the same as the one shown in Figure C.1. In this case, the standard deviation of the still water capture was 1.15 mV. Note that the mean value of the blue emission is dramatically reduced as the concentration of chlorophyll increases.

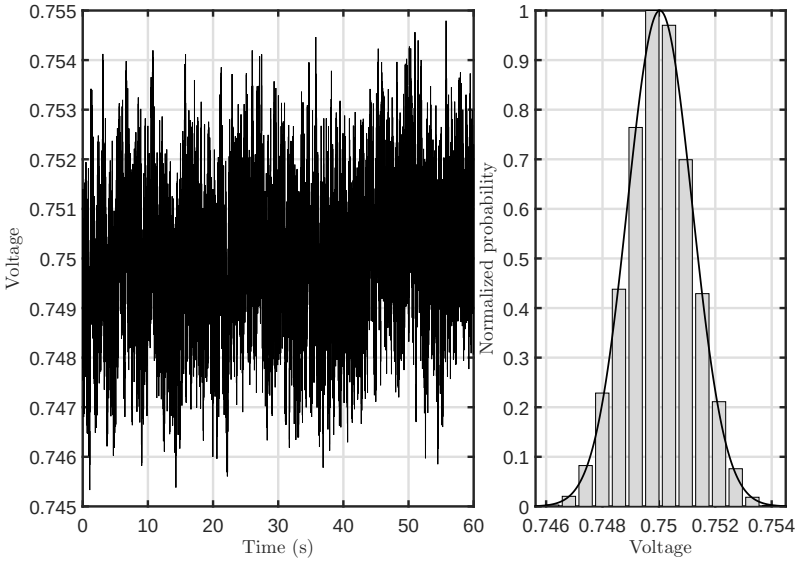

Figure C.2: Waveform and PDF for a blue emission in still tap water

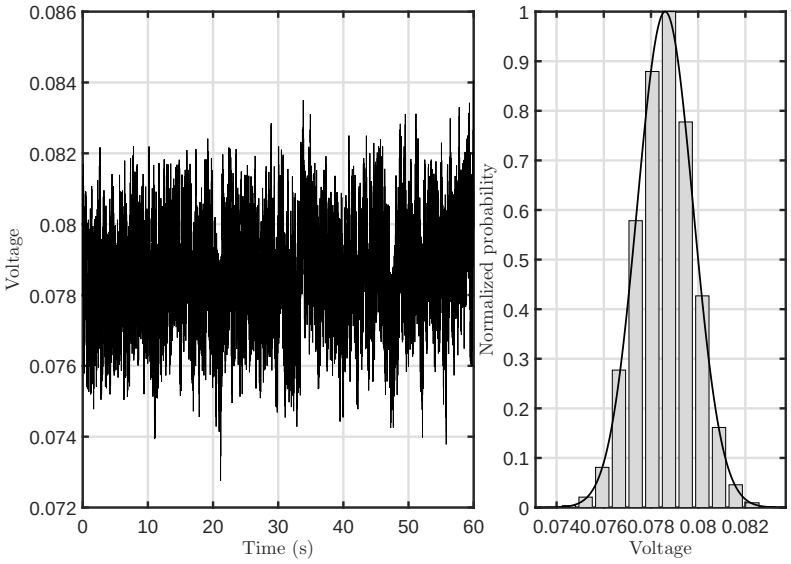

Figure C.3: Waveform and PDF for a blue emission in still water with 6.12 mg/l of particles

Moving water

For a moving environment, the changing positions of the suspended matter produce a variability on the received signal, since the incoming multiple-scattered energy varies with time. Comparing the two no-concentration figures (Figure C.4 and Figure C.7, it can be observed that the mean value of the received signal is decremented whilst the variance is slightly modified. This occurs because tap water has a certain amount of total dissolved solids, which is suspended matter that affects transmission as well. The mean value is decremented for all cases, and the variance increases with the concentration as it was commented in Chapter 7.

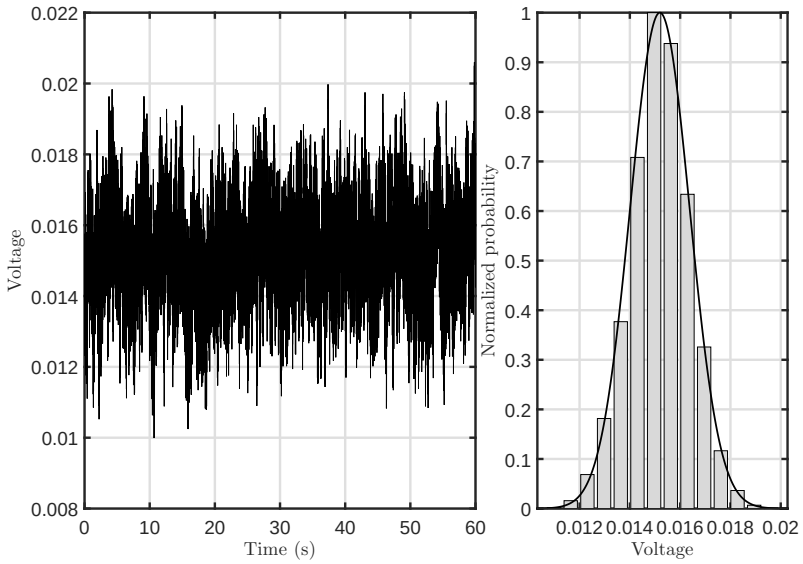

Figure C.4: Waveform and PDF for a blue emission in still water with 12.24 mg/l of particles

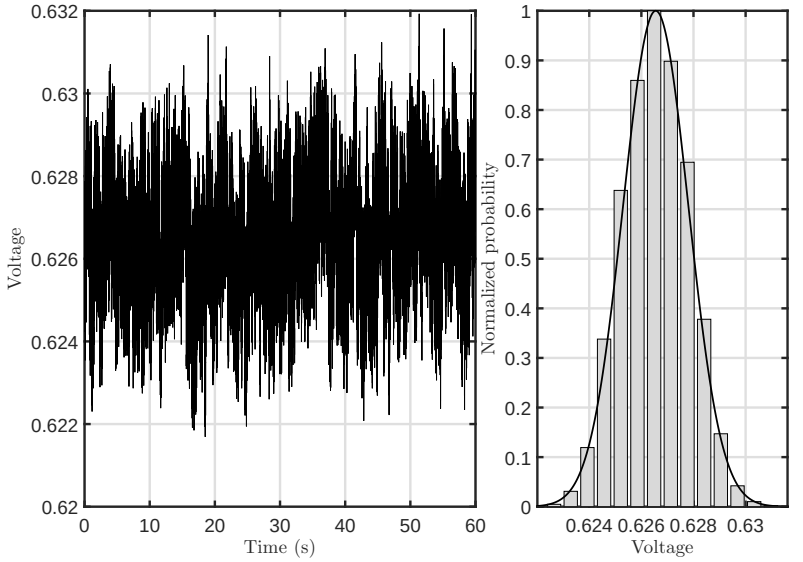

Figure C.5: Waveform and PDF for a blue emission in agitated tap water

C.1.2 Red emission

In this subsection, the captures of the red wavelength are presented. In this case, the induced voltage is higher than the generated using the blue wavelength. Taking into account the length of the tank, the effective optical output power at each wavelength (Table 7.2), and the responsivity of silicon, it is straightforward to notice this fact.

Still water

Chlorophyll's absorption spectrum has two fundamental peaks, one at blue and one at red. The blue peak may be higher depending on the relative concentrations of chlorophyll-a and chlorophyll-b, producing a red shift of the minimum absorption of water as the concentration is incremented. It can be observed that the difference of the mean values increases with the concentration level.

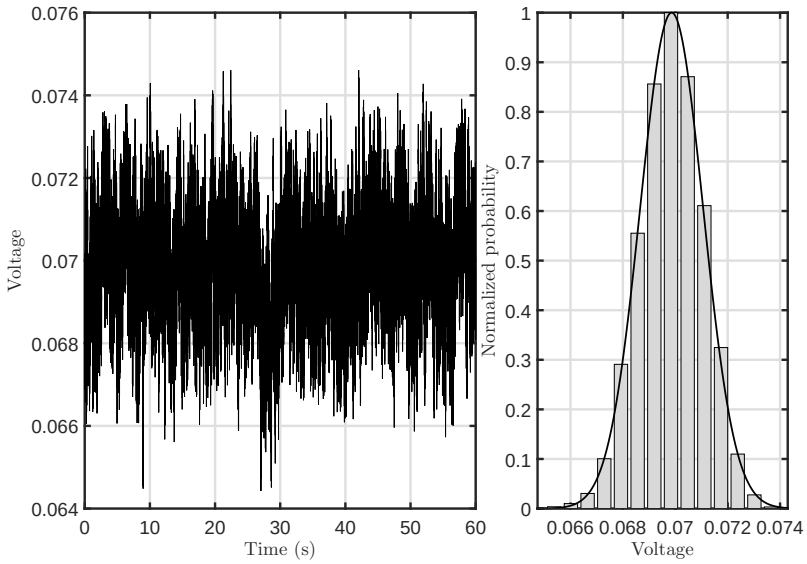

Figure C.6: Waveform and PDF for a blue emission in agitated water with 6.12 mg/l of particles

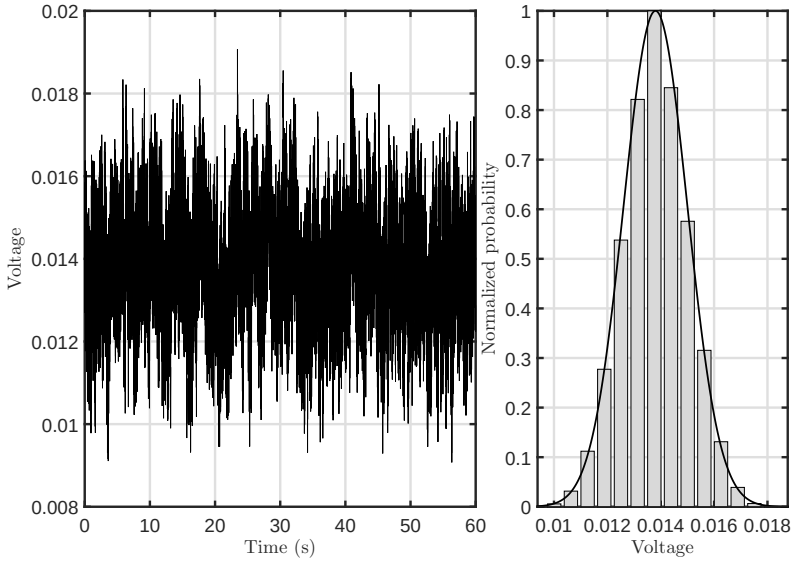

Figure C.7: Waveform and PDF for a blue emission in agitated water with 12.24 mg/l of particles

Moving water

In the case of red light, due to the better propagation of this wavelength, the particle-induced variability is greater than the associated to blue emissions at this distance. This effect is easily noticeable comparing the figures of moving water for a red emission and the same for a blue emission. Furthermore, the scattering phase function also differs in both cases, and probably it is much wider for a red emission.

C.2 Near-surface link measurements

In the case of the second experiment, the acquired waveforms and the obtained correlations are presented. The autocorrelation function of the acquired waveforms defined the coherence time as it was discussed during Chapter7. The results show variations with wavelength, depth and wind speed. At each wind speed, only the boundaries of the swept depths are shown (2 cm and 15 cm). The general trend of the results is that the deeper the higher the coherence time due to the decrement of the surface's influence. However, in the obtained results, the realizations at 15 cm have lower coherence times due to the increasing effect of total internal reflection. Beyond this limit for the used link range, the influence of the water surface decays abruptly. Regarding agitation, the more agitated the

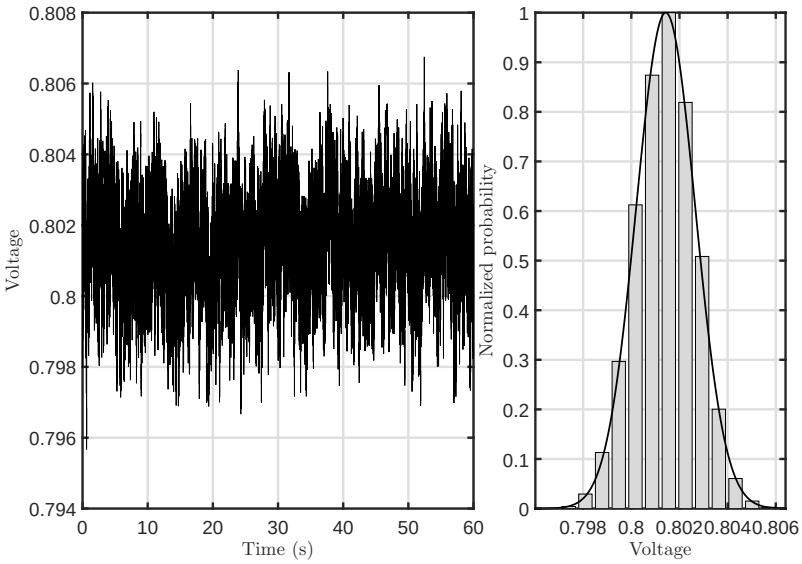

Figure C.8: Waveform and PDF for a red emission in still tap water

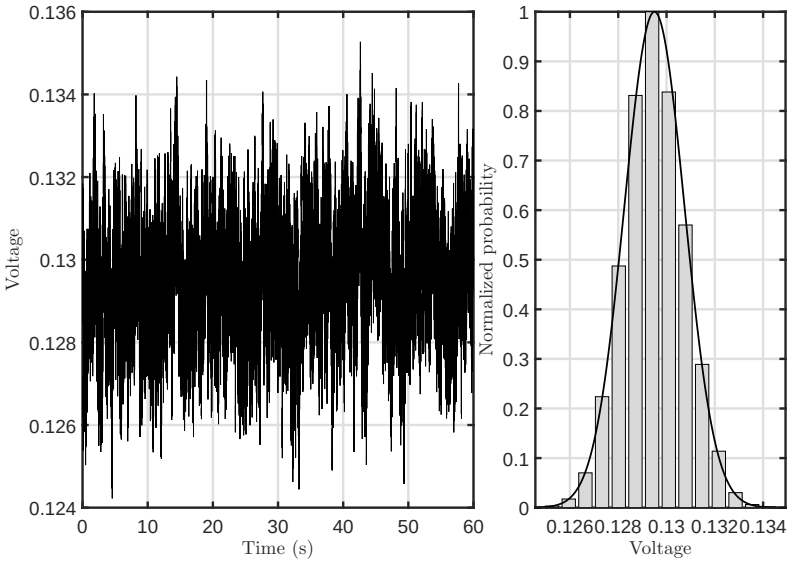

Figure C.9: Waveform and PDF for a red emission in still water with 6.12 mg/l of particles

surface, the lower the coherence time. Finally, the red emission presents a worse coherence time due to the better response of the system at very short distances.

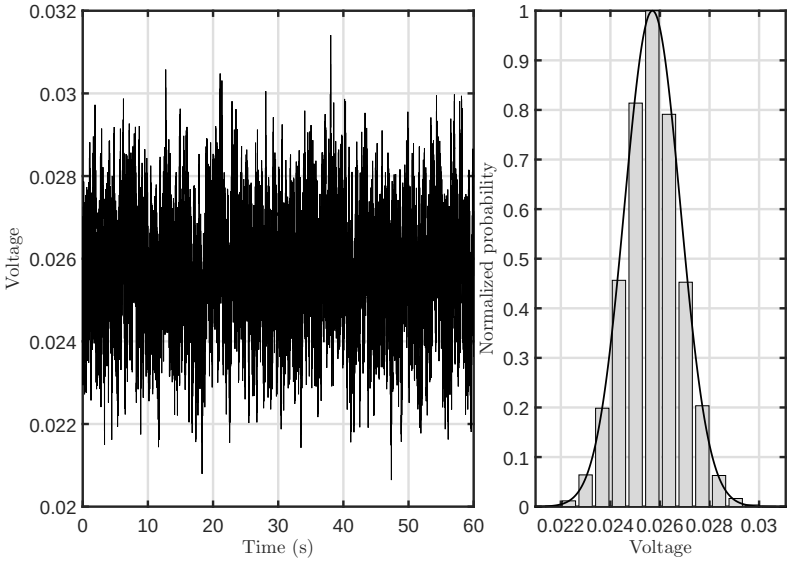

Figure C.10: Waveform and PDF for a red emission in still water with 12.24 mg/l of particles

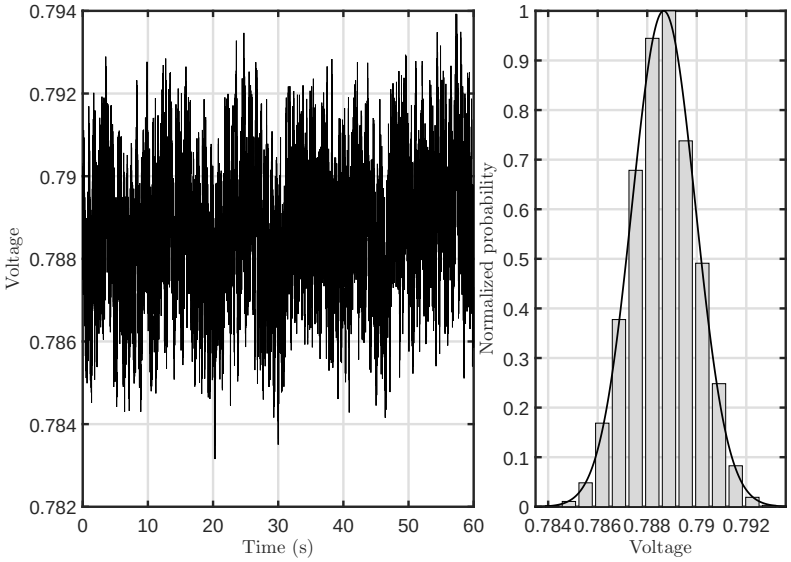

Figure C.11: Waveform and PDF for a red emission in agitated tap water

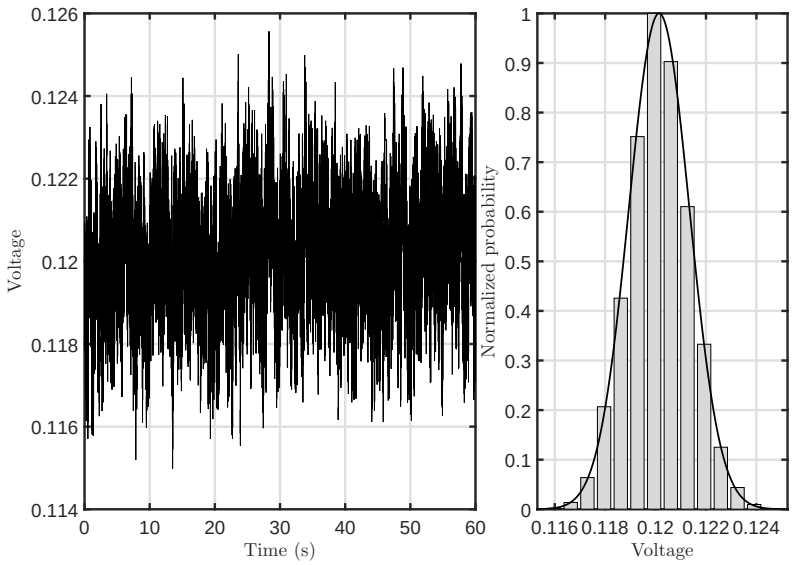

Figure C.12: Waveform and PDF for a red emission in agitated water with 6.12 mg/l of particles

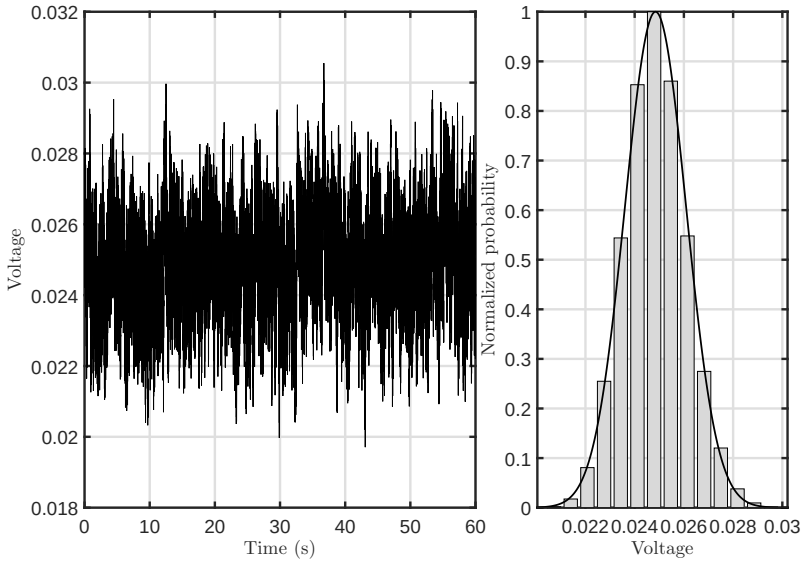

Figure C.13: Waveform and PDF for a red emission in agitated water with 12.24 mg/l of particles

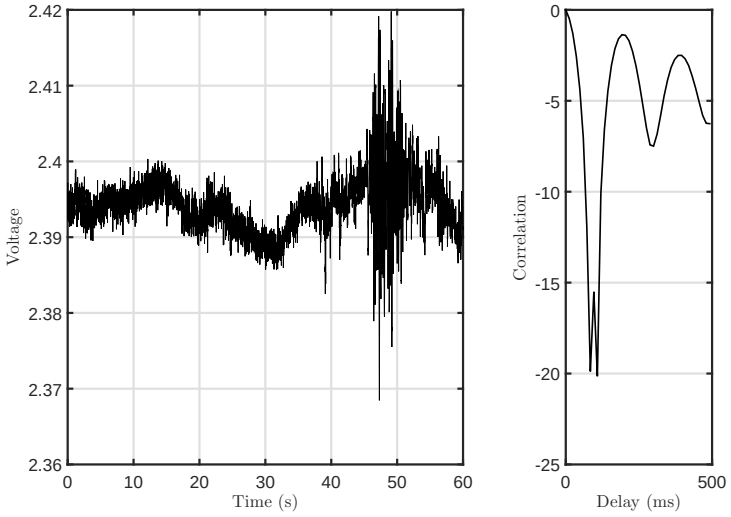

Figure C.14: Waveform and autocorrelation for a blue emission at 2 cm with still surface

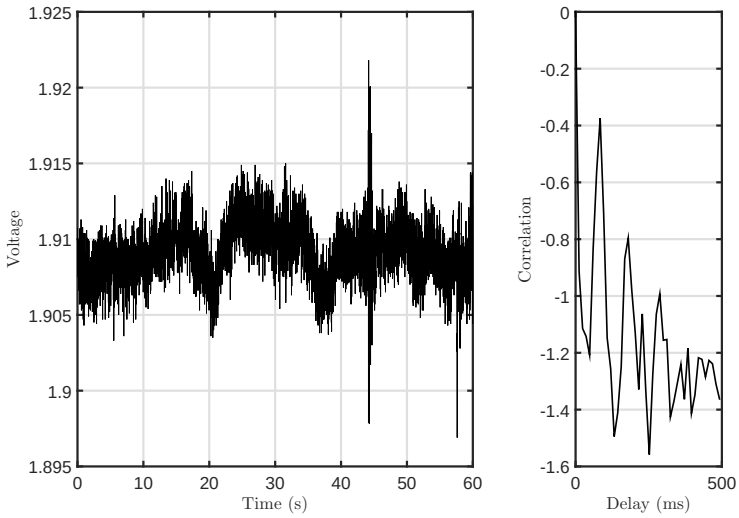

Figure C.15: Waveform and autocorrelation for a blue emission at 15 cm with still surface

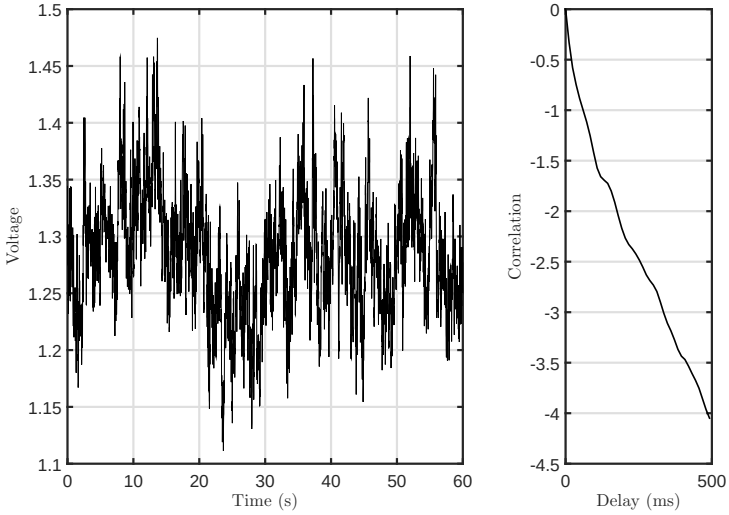

Figure C.16: Waveform and autocorrelation for a blue emission at 2 cm with moderate wind speed

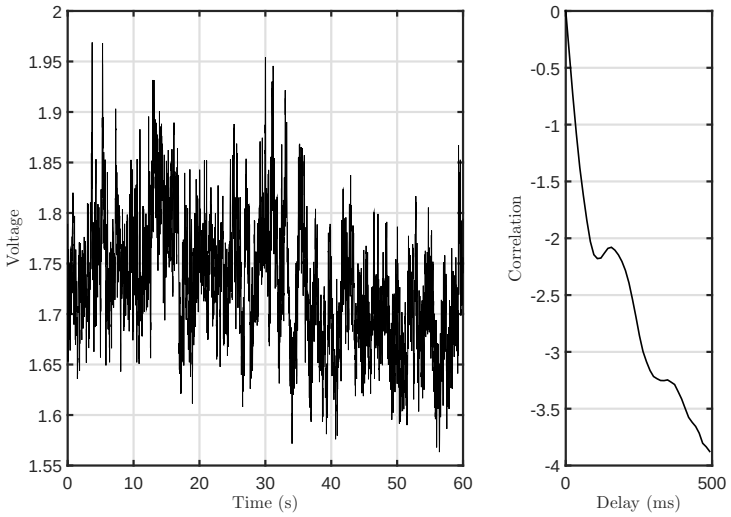

Figure C.17: Waveform and autocorrelation for a blue emission at 15 cm with moderate wind speed

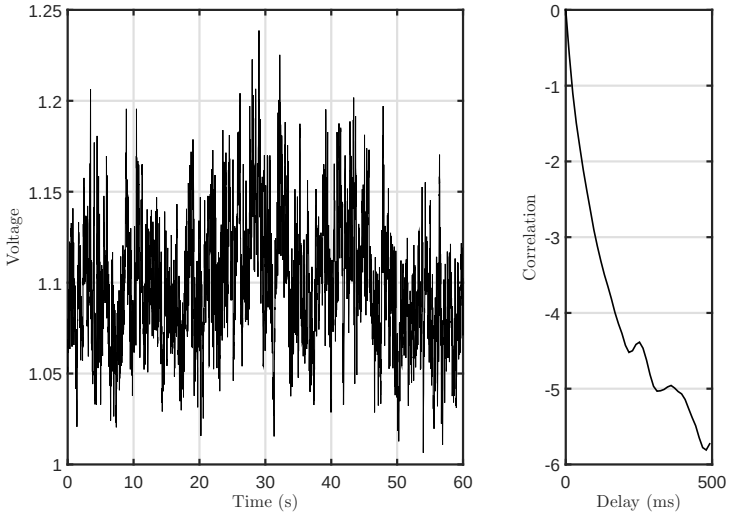

Figure C.18: Waveform and autocorrelation for a blue emission at 2 cm with high wind speed

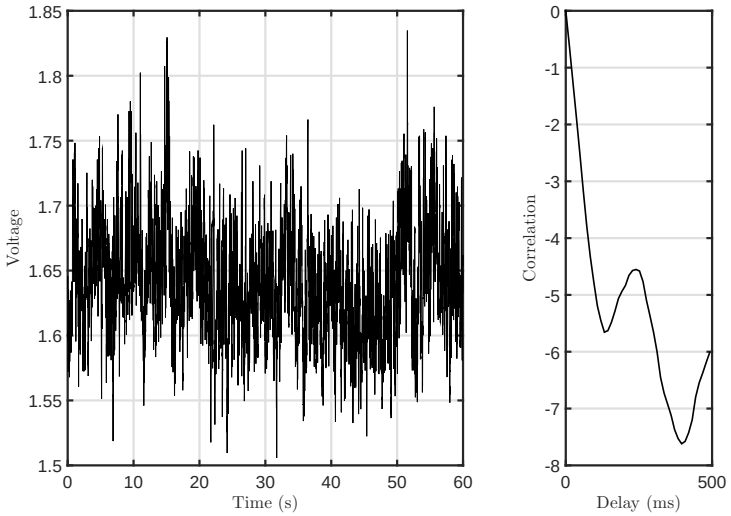

Figure C.19: Waveform and autocorrelation for a blue emission at 15 cm with high wind speed

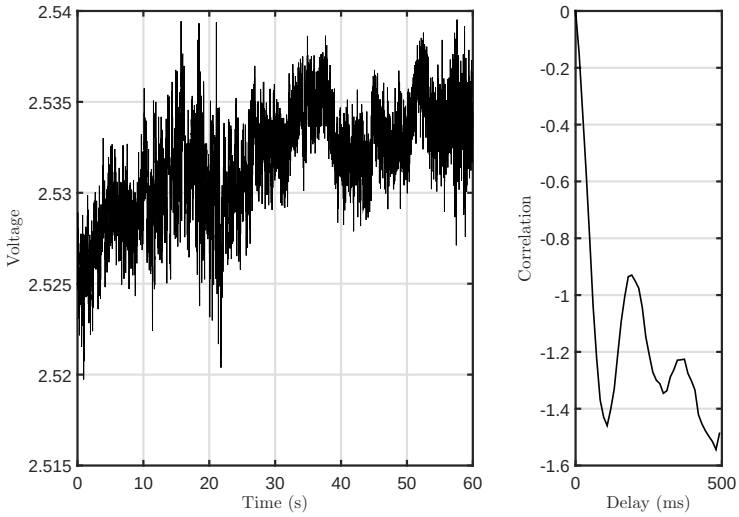

Figure C.20: Waveform and autocorrelation for a red emission at 2 cm with still surface

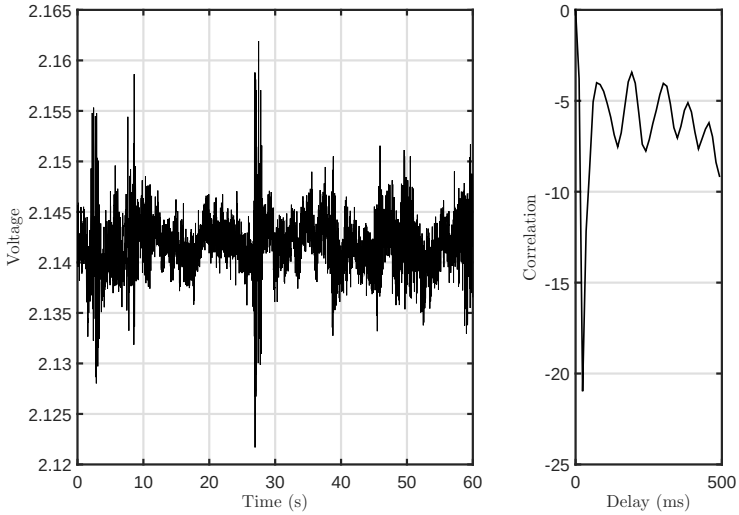

Figure C.21: Waveform and autocorrelation for a red emission at 15 cm with still surface

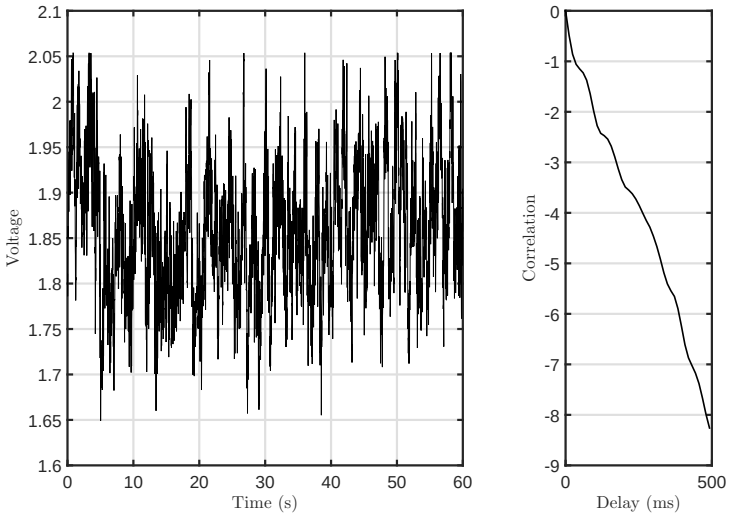

Figure C.22: Waveform and autocorrelation for a red emission at 2 cm with moderate wind speed

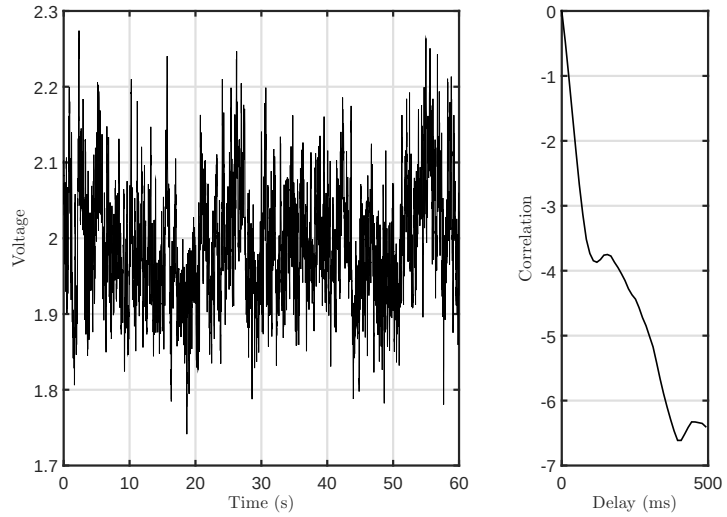

Figure C.23: Waveform and autocorrelation for a red emission at 15 cm with moderate wind speed

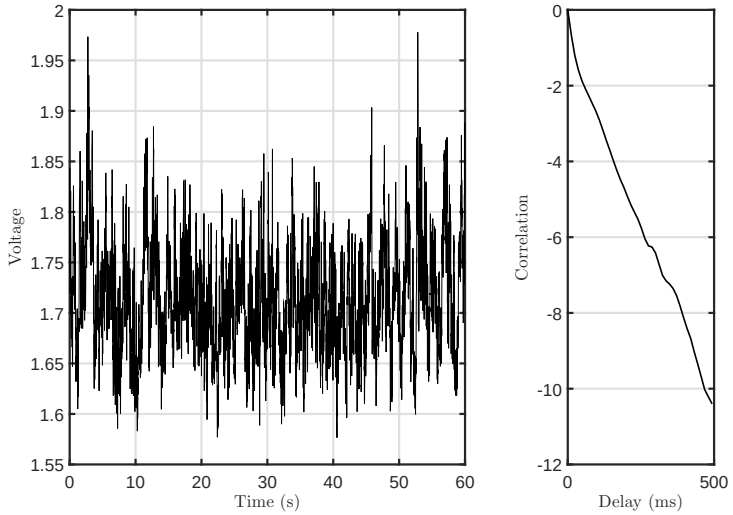

Figure C.24: Waveform and autocorrelation for a red emission at 2 cm with high wind speed

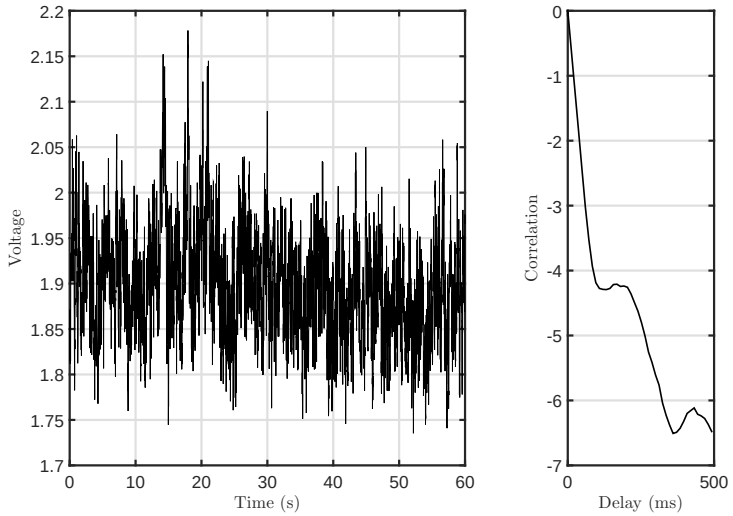

Figure C.25: Waveform and autocorrelation for a red emission at 15 cm with high wind speed

Appendix D

Summary in Spanish

D.1 Introducción

Los océanos cubren el 71 % de la superficie de La Tierra, y más del 90 % de la biosfera. Además de la gran importancia de los océanos en lo que se refiere a biodiversidad y ajuste climático, también son un medio que afecta a la economía global. El transporte por mar supone el 85 % de todo el tráfico mundial de mercancías, y casi el 35 $ de la extracción de hidrocarburos se lleva a cabo en el fondo marino. Además, una gran cantidad de alimentos son recogidos del mar a través de la pesca. Sin embargo, la industria pesquera está sometiendo actualmente al ecosistema marino a una sobre-explotación. Este hecho, junto a la polución, acidificación y el consecuente cambio climático, ha llevado a una más que notable redistribución de la clorofila, tal y como Boyce concluyó en [1]. La Figura 1.1 muestra la evolución de esta distribución desde 1900, basada en estimaciones tanto directas como indirectas. La concentración de clorofila esta directamente relacionada con la cantidad de fitoplankton, el cual es la base de la pirámide alimenticia marina. Cuanto menos es la cantidad de fitoplankton, menores son la cantidad de formas de vida más complejas (peces principalmente), de producción de oxigeno y de captación de carbono. Esta tendencia actual es la semilla de una posible retroalimentación devastadora si no se llevan a cabo tanto nuevos reglamentos más eficientes como estrategias de control. En esta última línea, existe un creciente interés en las aplicaciones referentes a la monitorización del océano, como medidas de concentración de oxígeno y de fitoplankton, las cuales están sujetas por lo general al despliegue de instrumentación *in situ*. Estos despliegues están basados en nodos aislados alimentación por baterías, y por tanto, se precisa de tecnologías inalámbricas de comunicación eficientes.

Controlar la industria pesquera parece obligatorio si se quiere revertir la presente situación. Las piscifactorías son la tendencia actual en lo que se refiere a control y mejora de la producción de pescado. Aunque el cultivo de especies carnívoras como el Salmón no reduce la presión sobre la pesca, ya que estos peces son alimentados con aceites derivados del pescado, existe una relajación tangible sobre las especies no carnívoras. Sin embargo, los cultivos marinos pueden producir efectos nocivos en las reservas salvajes de especies como la mencionada, reduciendo drásticamente la población. Este tipo de cultivos *offshore* necesitan infraestructuras de control y monitorización

de la producción. Las jaulas usadas en este tipo de granjes están normalmente localizadas a varias millas de la costa, precisando el despliegue de boyas que actúen como *hub* de comunicaciones.

Respecto a la extracción de hidrocarburos, ésta debe llevarse a cabo a profundidades muy elevadas, complicando las comunicaciones con superficie. Además, las operaciones deben realizarlas robot o vehículos no tripulados, ya que la presión no permite la presencia de buzos a no ser que se use un mini-submarino. Cuando se usan sistemas tele-robóticos, los cables umbilicales suponen un problema añadido, ya que las fuerzas de torsión y tensión pueden ser muy altas. En este caso, deberían emplearse tecnologías de comunicación inalámbricas de baja latencia.

Existe una actividad emergente relacionada con la mineria, la extracción de Deuterio. El Deuterio es un combustible esencial tanto en baterías Li-Hy como en los futuros reactores de fusión. Este isótopo del hidrogeno es creado de manera natural a altas presiones en el mar, lo cual implica grandes profundidades. Las instalaciones que se empleen en un futuro deberán estar dotadas de una infraestructura de comunicaciones que conecte la estación central con los sensores desplegados.

Todas las actividades anteriormente mencionadas tienen unos requisitos de comunicación muy estrictos. Las soluciones cableadas no son posibles en todos los escenarios, ya que limitan la movilidad y los cables pueden sufrir grandes fuerzas que pueden suponer un riesgo estructural. En situaciones donde se requiera movilidad o a profundidades donde no se puedan usar cables, las soluciones inalámbricas son la única alternativa. Actualmente hay tres tecnologías en comunicaciones submarinas inalámbricas: radiofrecuencia, comunicaciones acústicas y comunicaciones ópticas. A continuación se resumen las principales ventajas y desventajas de cada tecnología.

D.1.1 Radiofrecuencia

Las ecuaciones de Maxwell defines la propagación de ondas electromagnéticas en cualquier tipo de medio. Generalmente, la extinción de una onda plana esta relacionada con la tangente de pérdidas del medio, que es el cociente entre la parte imaginaria y la parte real de la permitividad eléctrica. Además, para materiales isótropos, el factor de atenuación α puede ser expresado en base a la tangente de pérdidas, tal y como muestra la Ecuación D.1.

$$\alpha^2 = \frac{\omega^2 \mu \epsilon}{2} \left(\sqrt{1 + \tan^2 \delta} - 1 \right) \tag{D.1}$$

Debe tenerse en cuenta que tanto σ como ϵ dependen de la frecuencia. Además, en la Figura 1.2 puede observarse que la tangente de pérdidas es muy alta a partir de la banda de HF, comparada con ELF o el espectro visible.

ELF (3 Hz - 30 Hz) y SLF (30 Hz - 300 Hz) son bandas de radiofrecuencia que fueron usadas durante la Segunda Guerra Mundial como una alternativa de comunicación con submarinos. Ya que la longitud de onda a frecuencias tan bajas es del orden de miles de kilómetros, no pueden implementarse dipolos a $\lambda/2$. Para poder radiar potencia útil, se usaron dipolos enterrados, los

cuales son parte de instalaciones gigantescas en las que dos electrodos son enterrados y separados decenas de kilómetros sobre estratos de baja conductividad. EEUU, Rusia e India son los únicos países con estaciones de ELF conocidas. Este tipo de sistemas tienen la ventaja de permitir comunicaciones virtualmente a cualquier punto del océano, pero tiene varias desventajas. El consumo de potencia para radiar unos pocos vatios es del orden de 800 MW, mientras que la tasa de datos obtenida no supera los pocos bits por minuto, además de ser un canal simplex.

El mencionado aumento de interés en aplicaciones submarinas, ha generado un momento en lo que a investigación en RF submarina se refiere. Varios autores han empezado a proponer HF como una alternativa a las tradicionales comunicaciones acusticas. Al-Shamma'a [2] llevó a cabo varias medidas a unos pocos MHz. Llevó a cabo dos experimentos utilizando antenas de espira. En el primero, realizó medidas de laboratorio en campo cercano, mientras que en el segundo, llevado a cabo en el puerto de Liverpool, alcanzó distancias de hasta 80 metros con bajas pérdidas.

El autor justificó sus observaciones diferenciando el comportamiento de las moléculas de agua expuestas a campo cercano y campo lejano. Para una excitación de campo cercano, dada la intensidad del campo eléctrica, existe ionización y por tanto, aparecen fenómenos de conducción produciendo altas atenuaciones. Para campo lejano, las moléculas de agua se comportan de manera diferente y la conducción no tiene tanta importancia. Estas afirmaciones no han sido probadas aún. Uribe y Grote [5] adaptaron el factor de atenuación α de las medidas de Al-Shamma'a, introduciendo una dependencia con la distancia. Sin embargo, la propuesta implica que el factor de atenuación decaiga exponencialmente con la distancia, lo cual supone que a distancias muy altas, no existiría atenuación.

D.1.2 Comunicaciones acústicas

La tecnología acústica es la tecnología más extendida en aplicaciones submarinas. La propagación de ondas mecánicas submarinas sufre una atenuación extremadamente baja en comparación a las ondas electromagnéticas. Sin embargo, estas buenas condiciones de propagación, combinadas con la baja velocidad en el medio (1500 m/s), generan effectos nocivos en el ancho de banda. Los canales acústicos submarinos adolecen the componentes multitrayecto muy importantes, produciendo dispersiones del retardo que van de decenas a varios cientos de miliseguntos. Además, el movimiento relativo entre emisor y receptor genera distorsión Doppler.

Respecto a la atenuación, la potencia de las ondas acústicas decae con la distancia debido a la absorción del medio, fenómeno que depende de la frecuencia. Además, como ocurre en cualquier proceso radiativo, este tipo de señal sufre de pérdidas por propagación esférica.

El ruido acústico ambiente, $N(f)$, tiene una distribución espectral como la presentada en la Figura 1.6. La dependencia del ruido ambiente con la frecuencia, unida a la atenuación del canal, tiene importantes implicaciones en el diseño de enlaces acústicas submarinos, ya que el ancho de banda disponible para una determinada SNR depende del término $(A(d,f)N(f))^{-1}$, tal y como

muestra la Ecuación 1.7.

$$SNR(d, f) = \frac{S(f)}{A(d, f)N(f)} \tag{D.2}$$

$S(f)$ es la densidad espectral de potencia de la señal transmitida y $A(d, f)$ es la atenuación del canal. El multitrayecto en UAC esta definido por dos efectos principales, las reflexiones y la refracción del sonido. Ésta última se debe a gradientes de temperatura, presión y salinidad, los cuales modifican el índice de refracción del sonido, desviando la dirección de propagación acorde a la Ley de Snell.

Respecto a la variabilidad temporal, la caracterización estadística de los canales UAC es un tema aún abierto. Esta variabilidad se debe a los cambios, en la escala temporal de la respuesta impulsiva, de los parámetros geométricos y físicos del enlace, como la agitación de la superficie por ejemplo. Generalmente, los tiempos de coherencia para este tipo de canales oscila alrededor de los cientos de milisegundos.

Adicionalmente a las restricciones fisicas inherentes a la propagación acústica, los módems acusticas añaden una restricción más al sistema. Las potencias requeridas en los transmisores para establecer la comunicación dependen de la distancia, pero generalmente en el rango de decenas de vatios, mientras que en el receptor las restricciones son mucho menores. El consumo de potencia es un aspecto importantísimo cuando se dispone de nodos aislados alimentados con baterías, y la eficiencia energética es también critica. Hay diferentes maneras de reducir el consumo de potencia en un nodo, pero las principales son los algoritmos de control de potencia, los esquemas de acceso al medio que impliquen un menor número de retransmisiones, y los sistemas adaptativos en ancho de banda.

Finalmente, los mamíferos marinos, como delfines y ballenas, disponen de sensibilidad hasta los 200 KHz. Estos animales utilizan el sonido con dos fines: uno social y otro de posicionamiento, por lo que UAC por debajo de los 200 KHz pueden ser altamente perjudiciales debido a las altas potencias implicadas. Además, aunque no se utilicen frecuencias *a priori* inocuas para la fauna marina, debido al efecto Doppler tan elevado, la densidad espectral de potencia realmente captada por estos mamíferos cuando están en movimiento, puede ser igualmente nociva en un océano lleno de transmisiones acústicas de alta potencia.

D.1.3 Comunicaciones ópticas

Las comunicaciones ópticas submarinas inalámbricas son un subgrupo de las comunicaciones ópticas inalámbricas. Al contrario que en FSO, el medio de propagación presenta absorción en UWOC. Esta absorción depende de las propiedades del agua y de las concentraciones relativas de algas y materia no algal. Además, mientras los aersoles y los gases producen scattering en FSO, UWOC sufre este dispersión espacial principalmente debido al fitoplankton. Respecto a las turbulencias, los modelos basados en gradientes de índices de refracción inducidos por cambios de

temperatura en FSO no son suficiente para modelar este fenómeno en UWOC, ya que el índice de refracción del agua marina depende de la temperatura, la salinidad y la presión. Además, la dependencia de la extinción con la longitud de onda, suele definir una ventana óptima de transmisión en la región verde-azul del espectro visible.

Como se comentó arriba, las comunicaciones RF estan limitadas tanto en potencia como en ancho de banda. El consumo de las estaciones ELF es absurfamente elevado y las tasas de datos obtenidas son muy pobres, pero ofrece un rango de comunicaciones elevadísimo. Respecto a UAC, el ancho de banda que ofrece esta tecnologia puede soportar una amplia variedad de servicios, pero sólo aquellos que requieran menos de unos pocos KHz. En los últimos años, UWOC ha demostrado poseer la mejor eficiencia energética en bits por Julio y un rango máximo de 100 metros. Además, el coste asociado a los transceptores ópticos es mucho menor que el asociado a los hidrófonos y drivers de UAC. Sin embargo, debido a la limitación de alcance de UWOC, la tendencia actual es usar soluciónes híbridas opto-acústicas, donde la telemetría a larga distancia se hace acústicamente, y las comunicaciones de baja latencia a alta velocidad, a través de un enlace óptico.

Las propuestas más recientes en UWOC como interfaz de comunicaciones para UWSN están fundamentadas en la posibilidad de descargar cantidades ingentes de datos recolectados durante largos períodos, en una fracción de tiempo respecto al caso acústico. Además, el uso de interfaces ópticos aumenta el tiempo de vida de los nodos desplegados. Sin embargo, aunque el máximo error de apuntamiento permitido no es tan restrictivo como se esperaba debido a la dispersión de la luz, sigue siendo menor que en UAC. También la baja latencia de los enlaces UWOC permite un manejo natural de vehículos submarinos. Ésta latencia puede llegar a ser incluso mejor que en el caso de un enlace por fibra, ya que el índice de refracción del agua es menor que el del plástico o el vidrio, pero ésta mejora esta normalmente compensada por la necesidad de retransmisiones en un escenario inalámbrico.

Existen varios problemas sin resolver todavía en UWOC, sobre todo en eficiencia energética y modelado de canal. Los autores generalmente modelan el canal como LTI, pero relamente es LTV y sólo unos pocos autores enfocan su estudio desde esta perspectiva para enlaces láser. Además, existe una notoria carencia de contribuciones en eficiencia energética, la cual es crítica en escenarios donde el reemplazo de baterías es prohibitivo en coste.

En esta tesis, se ha llevado a cabo un enfoque estadístico de los parámetros principales del canal (ancho de banda, ganancia y tiempo de coherencia). El análisis se ha basado tanto en aproximaciones teóricas como en resultados de simulación. Se han analizado dos escenario diferentes de aplicabilidad de UWOC en UWSN: enlaces agua-agua y enlaces agua-aire. Además, se propone un modelo estadístico para particulas opacas. La propuesta está dirigida a enlaces en aguas someras donde las corrientes costeras puede generar nubes de partículas en suelos arenosos. Respecto a la eficiencia energética, se propone el uso de algoritmos de control de potencia y de modulaciones

pulsadas capaces de reducir el consumo de potencia debido al uso de drivers no lineales.

D.2 Motivación, Hipótesis y Objetivos

El tema de esta tesis emergió como la evolución natural de las líneas de investigación de la *División de Fotónica y Comunicaciones* del *Instituto para el Desarrollo Tecnológico y la Innovación en Comunicaciones*, de la Universidad de Las Palmas de Gran Canaria.

El grupo ha estado enfocado durante los últimos años a comunicaciones IR y VLC, concretamente en algoritmos de trazado de rayos para obtener respuestas impulsivas en canales indoor [8] y en el desarrollo de prototipos para realizar pruebas de concepto en las mencionadas tecnologías, como video streaming usando VLC [9], o comunicaciones *in-flight* [10][11].

En este trabajo, ya que es el primero de un área novedosa para el grupo, se han tratado varios frentes. En primer lugar, era obligatorio realizar un análisis en profundidad del estado del arte a fin de detectar las debilidades principales, y por tanto, oportunidades para trabajar y poder realizar aportaciones significativas. Como se comenta en el capítulo 3 de la tesis, no se han estudiado aún en profundidad estrategias de reducción de consumo energético. Se comentarán varias contribuciones al respecto en la siguiente sección. Además, todavía no existen modelos de predicción estadísticos acorde a los parámetros de los enlaces UWOC.

Resumiendo, los principales objetivos de esta tesis son:

- Llevar a cabo un análisis en profundidad del estado del arte.
- Proponer estrategias para mejorar la eficiencia energetica en sistemas UWOC.
- Estudiar la posibilidad de realizar predicción de canal en UWOC.

D.2.1 Hipótesis

Ésta tesis se fundamenta en dos hipótesis principales, las cuales se enumeran abajo. La primera de ellas hace alusión al modelado del canal, mientras que la segunda contempla la eficiencia energética en UWOC.

- **Hipótesis 1. Sobre el canal.** El canal óptico submarino inalámbrico es linear y variante en el tiempo, but estacionario en sentido estricto con scattering incorrelado (WSSUS).
- La variabilidad del canal UWOC, descrita por la respuesta al impulso variante $h(t, \tau)$, está definida por los distintos fenómenos de reflexión y scattering que ocurren durante la propagación. Esta variabilidad, si el emisor y el receptor están en posiciones fijas, posee media constante. Además, las contribuciones de potencia que llegan de eventos de scattering están mutuamente incorreladas debido a la independencia de las localización donde dichos evento se producen.
- En un escenario con materia disuelta, el movimiento de las partículas a través del enlace genera una variabilidad en la potencia recibida que reduce la SNR. Para verificar esta hipótesis, se ha usado tanto un enfoque simulado como basado en medidas experimentales.

- Los enlaces agua-aire son también variables debido a la forma cambiante de la superficie del agua. Además, la potencia óptica que llega al receptor puede ser estimada como la energia de la superficie del mar iluminada que llega al receptor tras la refracción. Este área iluminada cambia con el tiempo, siguiendo la forma del espectro de olas del mar.

- **Hipótesis 2. Sobre la eficiencia energética.** La eficiencia energética de un enlace UWOC puede ser mejorada a través de algoritmos de control de potencia, el uso de la longitud de onda más apropiada en cada caso, y diferentes modulaciones y codificaciones eficientes.

- Generalmente, los enlaces UWOC se implementan en la región verde-azul del espectro visible, ya que en dicha región existe un mínimo de absorción. Sin embargo, teniendo en cuenta que la respuesta de los emisores y receptores ópticos de longitudes de onda más larga es mejor que la de los más azulados, la peor propagación en longitudes de onda rojas se compensa con estas mejores eficiencias, definiendo una distancia critica a la que es mejor realizar el enlace en rojo.

- Son algoritmos de control de potencia son una estrategia muy bien estudiada en la literatura, usada para optimizar la SNR en entornos con alta interferencia entre usuario. Además, los nodos submarinos, que están alimentados con baterias, tiene coste de reemplazo prohibitivos. Por tanto, se necesitan obligatoriamente estrategias de reducción de consumo, y los PCA puede ofrecer una optimización energética.

- Las modulaciones y codificaciones son el último nivel de la pila de comunicaciones. Teniendo en cuenta las caracteristicas eléctricas de los emisores ópticos, los drivers de corriente no lineales son una opción más eficiente que los lineales. Por consiguiente, modulaciones que precisen de una transmisión lineal puede ser cuantificadas para permitir el uso de driver energéticamente eficientes.

D.2.2 Aportaciones

Para servir de guía a aquellos que lean este trabajo, a continuación se presenta un resumen de las contribuciones que aporta esta tesis.

- **Capítulo 3.** Se presenta un análisis en detalle del estado del arte en UWOC. Dicho análisis se ha estructurado atendiendo a una taxonomía intuitiva y trata de ser el punto de partida de la tesis.

- **Capítulo 4.** Se presenta un algoritmo de Monte Carlo Ray Tracing para calcular la respuesta impulsiva de los canales UWOC. Al contrario que otros autores, los cuales emplean funciones de fase tipo Henyey-Greenstein para modelar el scattering por partículas, en este trabajo se ha decidido emplear el scattering de Mie ya que modela con mejor precisión dicho fenómeno. La influencia de cada parámetro del canal en la respuesta impulsiva también se analiza. Además,

el algoritmo se paralelizó usando tanto un enfoque multiprocesador como una implementación en GPU.

- **Capítulo 5.** Se presenta un modelo de comunicaciones agua-aire, centrado en el tiempo de disponibilidad del canal.
- **Capítulo 6**
  - Usando el algoritmo de Monte Carlo citado arriba, se hace una aproximación estadística de la ganancia del canal y del ancho de banda,
  - Se presenta una fórmula empírica para predecir la BSF del canal.
  - Tras realizar una aproximación rectangular de la respuesta impulsiva, se define una zona de Fresnel en términos de energía, permitiendo una reducción del volumen de interés de las simulaciones. Esta simplificación también lleva a poder realizar una predicción sencilla del ancho de banda.
  - También se presenta un estudio estadístico de la influencia de partículas opacas como granos de arena en el enlace. Esta propuesta está basada en relaciones geométricas y algunas aproximaciones, pero puede servir como línea de base para trabajos futuros.
- **Capítulo 7**
  - En este capítulo se demuestra la influencia del movimiento de las partículas en la SNR. El movimiento produce una variación aleatoria en la señal recibida que puede ser modelada como una distribución normal de varianza relacionada con la densidad de partículas.
  - Se obtiene el tiempo de coherencia de un canal agua-agua cercano a la superficie. Además de la velocidad del viento, se tienen en cuenta otros parámetros, como la profundidad y la longitud de onda.
  - Se demuestra la validez de la aproximación WSSUS en el canal submarino a través de medidas experimentales.
- **Capítulo 8**
  - Se justifica el uso de longitudes de onda rojas en lugar de azules bajo ciertas restricciones, como medida de mejora de la eficiencia energetica. Como los emisores rojos son más eficientes que los azules, y los receptores de Silicio son más sensibles también a estas longitudes de onda, por debajo de una distancia critica es mejor realizar la transmisión en rojo, a pesar de la mayor atenuación que se sufre a esta frecuencia.
  - Se presenta y evalua un algoritmo de control de potencia con capacidad de cambio de longitud de onda. El uso de PCA es muy recomendable para reducir el consumo de potencia en nodos submarinos. En este caso, varias mejoras son propuestas al clásico algoritmo iterativo de descenso (LMS).

– El uso de PWM se combina con el uso de driver no lineales para mejorar la eficiencia de la OFDM óptica. Se comentará en profundidad ya que la mayor eficiencia de los drivers no lineales puede ser una buena alternativa para reducir el consumo y por tanto, aumentar el tiempo de vida en nodos que usen este tipo de modulaciones.

D.3 Respuesta impulsiva del canal

En los últimos años ha habido un interés creciente en aplicaciones submarinas, como vigilancia, control a distancia de robotos, monitorización de océanos y comunicaciones militares. El desarrollo y mejora de los emisores y receptores en visible, ha llevado a un incremento de los trabajos de investigación relacionados con el uso de LED y láser para establecer enlaces submarinos. Hoy en dia, UWOC puede ser considerado como un tema independiente de FSO y VLC. Ésta independencia se justifica en las particularidades del canal subyacente.

La respuesta impulsiva de un canal lineal e invariante define la respuesta en frecuencia del mismo. Sin embargo, el canal UWOC no es invariante, y su varianza depende de las característica del medio. Aunque los canales variantes se caracterizan estadísticamente a través de la función de scattering, se presenta un algoritmo para obtener realizaciones estadísticamente independientes del proceso estocástico subyacente. Estas realizaciones podrían se empleadas como entrada de un motor de inferencia estadística en un esfuezo por encontrar las distribuciones de probabilidad tanto de la ganancia del canal, como del ancho de banda.

La propagación de la luz en el agua es un caso específico de transferencia radiativa. Normalmente, este medio es considerado homogéneo por simplicidad, pero esta aproximación es puramente estadistica. Las partículas no se estructuran como una red cristalina dentro del agua, sino que se distribuyen aleatoriamente siguiendo una distribución 3D-uniforme. Esta aproximación no tiene en cuenta ni los posibles efectos de floculación o el efecto de las turbulencias en la distribución de masa. Sin embargo, la aproximación sigue siendo válida para realizar estimaciones de canala, mientras que los fenómenos mencionados puede ser tenidos en cuenta superponiendo sus efectos al resultado obtenido.

D.3.1 Transferencia radiativa

La teoría de transferencia radiativa define el fundamento matemático de la propagación de radiación en medio absorbentes y dispersivos. Los primeros trabajos al respuesto fueron llevados a cabo por Lord Rayileigh en 1871 acerca de la iluminación y la polarización del cielo. Sin embargo, se tuvo que esperar 75 años por las ecuaciones que gobiernan la propagación. Este tema ha sido estudiado principalmente por astrofísicos, ya que los mismo problemas de dispersión aparecen en la difusión de neutrones. En UWOC, esta teoria juega un papel crucial en el modelado de canal, ya que el medio es tanto absorbente como dispersivo.

La ecuación de transferencia para medios isótropos con propagación en el eje Z es:

$$\frac{\cos\theta}{\kappa(\omega)\rho}\frac{\mathrm{d}I(\omega,z,\theta,t)}{\mathrm{d}z} = I(\omega,z,\theta,t) - \mathfrak{J}(\omega,z,\theta,t) \tag{D.3}$$

Donde:

$$\mathfrak{I}(\omega, z, \theta, t) = \frac{1}{2} \int_0^{\pi} p\left(\theta, \theta'\right) I(\omega, z, \theta', t) \sin\theta' \mathrm{d}\theta' \tag{D.4}$$

La última expresión es el resultado de la integración respecto a la componente azimutal. Debido a la simetría del problema, esta simplificación es directa.

D.3.2 Características del canal

El agua del mar es una mezcla de moléculas de agua, materia biológica y sales disueltas. Dependiendo de la concentración de cada tipo, los efectos en la propagación pueden variar.

Absorción

La absorción es un proceso dependiente de la longitud de onda, donde la energia electromagnética es convertida en otro tipo de energia, típicamente calor o energía química. Es muy importante ya que define el decaimiento de la energia que se propaga a través del agua, y por tanto, tiene un impacto directo en el número de fotones que llegan al receptor. La absorción total se puede expresar como la suma de las contribuciones parciales de cada elemento que compone el agua marina.

$$a(\lambda) = \sum_{i=1}^{N} C_i a_i(\lambda) \tag{D.5}$$

Generalmente, las contribuciones consideradas son: agua pura ($\alpha_w(\lambda)$), fitoplancton ($\alpha_\phi(\lambda)$), gelbstoff ($\alpha_g(\lambda)$, decaying organic matter) and materia no algal ($\alpha_n(\lambda)$).

Scattering

El scattering en un proceso físico por el cual la energia es dispersada espacialmente debido a la interacción luz-materia. Dependiendo del tamaño relativo de los dispersores, pueden usarse diferentes aproximaciones matemáticas para modelar el fenómeno.

Para tamaños de partícula muy pequeños se emplea el scattering de Rayleigh. Para tamaños de partícula cercanos a la longitud de onda se emplea el scattering de Mie. Por último, tamaños mayores pueden ser modelados con óptica geométrica.

El scattering de Mie es la solución más empleada en el problema de scattering elástico. Su aplicabilidad va desde los dominios del scattering de Rayleigh hasta los de la óptica geométrica, pero esta particularizado para esferas o cilindros principalmente.

Aunque la teoría de Mie tiene en cuenta el estado de polarización, y ya que este trabajo está orientado al uso de radiación no polarizada (LED), las dos polarizaciones pueden ser promedidas resultando en una formulación más manejable y compacta.

Índice de refracción

El índice de refracción de un material es la relación entre la velocidad de la luz en él y la velocidad de la luz en el vacío. Este parámetro define el retardo de la comunicaciones, y también juega un papel importante en el compartamiento de las reflexiones (Ley de Snell) y de las turbulencias. El índice de refracción depende de la temperatura, la salinidad y la longitud de onda. A continuación se presenta una aproximación empírica del mismo:

$$\begin{aligned} n_w(\lambda, S, T) =& 1.447824 + 3.011 \cdot 10^{-4} S - 1.8029 \cdot 10^{-5} T - 1.6916 \cdot 10^{-6} T^2 - 0.489\lambda + 0.728\lambda^2 - 0.384\lambda^3 - \\ & S\left(7.9362 \cdot 10^{-7} T - 8.06 \cdot 10^{-9} T^2 + 4.249 \cdot 10^{-4}\lambda - 5.847 \cdot 10^{-4}\lambda^2 + 2.812 \cdot 10^{-4}\lambda^3\right) \end{aligned} \tag{D.6}$$

Turbulencias

La turbulencia óptica es un cambio rápido del índice de refracción del agua de mar. Estos cambios bruscos pueden ocurrir a cualquier profundidad, y normalmente se atribuyen a las variaciones de temperatura. A diferencia de turbulencias en FSO, el espectro de potencia del índice de refracción depende de la temperatura y la salinidad. Por lo tanto, el espectro de potencia tradicional de Kolmogorov puede presentar errores de modelado en ambientes oceánicos, como Tang indica en [46]. Después de introducir el efecto de la salinidad, se obtiene el espectro de potencia propuesto por Nikishov [122]:

$$\Phi(\kappa) = C_0 \epsilon^{-1/3} \kappa^{-11/3} \frac{\chi_T}{\omega^2} \left[1 + 2.35(\kappa\eta)^{2/3}\right] \phi(\kappa) \tag{D.7}$$

Tras analizar el índice de centelleo, éste se puede aproximar por:

$$\sigma_I^2(L) \approx 8\pi^2 k^2 L \int_{\sqrt{\pi \frac{k}{L}}}^{\infty} \kappa \Phi(\kappa) \mathrm{d}\kappa \tag{D.8}$$

Analizando el espectro de Nikishov, se obtiene que la dependencia de la turbulencia es del tipo:

$$\sigma_I^2(L) \propto L^{\alpha} \quad / \alpha \in (3/2, 11/6) \tag{D.9}$$

Reflexiones en la superficie

La superficie del océano puede ser modelada como una superposición de ondas, por lo general modeladas por un espectro de olas del mar, además de un término ruidoso que depende de la fuerza del viento. Este estrés produce una variación aleatoria en la superficie del agua de mar, cuya distribución sigue una serie de Gram-Charlier como Cox y Munk demostraron en [21]. La variación de la superficie es generalmente modelada como una uniforme en la componente azimutal, y la varianza de la pendiente depende de la velocidad del viento. La relación que se puede obtener de trabajo Cox y de Munk con respecto a la velocidad del viento se presenta en la ecuación

D.10. En realidad, la varianza de la dirección de viento cruzado y la dirección contra el viento ligeramente diferentes, pero para los propósitos de este trabajo la aproximación omnidireccional es válida.

$$\sigma^2_{surf} = 0.003 + 0.00512 v_{wind} \;\; /1 < v_{wind} < 14\mathrm{m} \cdot \mathrm{s}^{-1} \tag{D.10}$$

En un escenario de comunicación agua-agua, los reflejos de la superficie aleatoria pueden introducir contribuciones adicionales de energía retardadas, aumentando la dispersión del retardo. Después de una reflexión, la dirección del rayo de salida $\hat{v}_{ref}$ se puede expresar como una combinación lineal de vector normal $\hat{n}_{norm}$ y la dirección incidente $\hat{v}_i$.

$$\hat{v}_{ref} = \hat{v}_i - 2 < \hat{v}_i, \hat{n}_{surf} > \hat{n}_{surf} \tag{D.11}$$

Después del impacto, una parte de la potencia incidente es reflejada y otra parte se transmite. La cantidad de energía que se refleja, $R_{Fresnel}(\theta_i)$, sigue la ecuación de Fresnel (Ecuación D.12). Además, para ángulos de incidencia por encima de cierto límite (ángulo crítico), no hay transmisión de energía y la ocurre reflexión total interna. Esto sucede porque los rayos de luz viajan a un medio con un índice de refracción más bajo, en el caso contrario, no hay ángulo crítico y siempre parte de la energía se transmite.

$$R_{Fresnel}(\theta_i) = \frac{1}{2}\left[\left(\frac{\sin(\theta_t - \theta_i)}{\sin(\theta_t + \theta_i)}\right)^2 + \left(\frac{\tan(\theta_t - \theta_i)}{\tan(\theta_t + \theta_i)}\right)^2\right] \tag{D.12}$$

Reflectividad del fondo marino

Los efectos difusivos son un fenómeno común que se produce debido a la dispersión de la luz en una superficie. Hay muchas funciones de dispersión que modelan la difusión respecto a la presencia o no de componentes especulares, como Phong o Torrance. Sin embargo, como el fondo del mar está normalmente compuesto por extensiones de arena, roca o coral, una aproximación lambertiana es una solución de compromiso.

Fouling óptico

El fouling óptico es la deposición de materia, normalmente algas y fitoplancton, en el blindaje transparente de los emisores ópticos en aplicaciones UWOC. Esta deposición tiene un efecto directo sobre la potencia efectiva radiada al medio. Dependiendo de la respuesta espectral de la materia depositada, la densidad de deposición y su espesor, la pérdida de potencia se pueden modelar como un decaimiento exponencial. La resistencia de ensuciamiento, β, es la velocidad a la que el espesor de las incrustaciones, $\tau(t)$ aumenta. α depende de la densidad del fouling y el tipo de partícula, mientras que β depende del tipo de partícula, la velocidad del agua, la temperatura de la superficie y la temperatura del agua [125].

Fauna

Los efectos de la fauna en el rendimiento de un enlace UWOC no han sido estudiados en profundidad aún. No obstante, sería presumiblemente dependerá de la concentración de la fauna, el tamaño de los individuos, su movilidad y su percepción de la longitud de onda utilizada.

D.3.3 Simulación de la respuesta al impulso

La ecuación RTT es difícil de resolver, y la tarea se hace aún más difícil cuando se introduce el carácter aleatorio de la dispersión de partículas. Sin embargo, la integración de Monte Carlo ofrece una alternativa simple y computacionalmente eficiente para obtener una solución a la ecuación de RTT dependiente del tiempo en cualquier escenario. Soluciones analíticas se pueden obtener sin tener en cuenta ni la aleatoriedad del medio ni el efecto de la superficie del agua o del fondo del mar, como Jaruwatanadilok llevó a cabo en [33]. El principal objetivo de este proceso de simulación es obtener una representación de la respuesta de impulso UWOC y realizar un análisis relacionando parámetros físicos con los parámetros de comunicación, tales como la ganancia de canal y el ancho de banda.

El escenario simulado consiste en un volumen tridimensional delimitado en los ejes Y y Z. Los límites del eje Y son el fondo del mar y la superficie del agua, mientras que los límites del eje Z son los planos de emisión y de recepción. Los fenómenos incluidos en el proceso de simulación son absorción, dispersión de partículas, efectos difusivos sobre el fondo marino y las reflexiones. Las turbulencias y la fauna no se han considerado debido a su naturaleza estocástica. En un modelo estocástico, estos efectos se pueden incluir como factores multiplicativos, ya que presentan independencia estadística. Por otra parte, se considera emisión LED y por lo tanto la polarización y la coherencia se obvian, lo que facilita el cálculo. La Figura 4.10 representa los efectos considerados en la simulación, así como la geometría del problema. Se puede observar que el punto de emisor es el origen de coordenadas. Por lo tanto, la profundidad del enlace es parametrizada como un valor positivo, mientras que la profundidad del fondo marino es un valor negativo.

El procedimiento de simulación propuesto realiza el cálculo de la respuesta de impulso a través de un algoritmo Monte Carlo Ray Tracing modificado (MMCRT). Los algoritmos MCRT tradicionales realizan la integración generando N rayos aleatorios en el punto de origen y propagando las contribuciones de cada rayo, pero cada rayo emitido genera contribución únicamente por "casualidad". A diferencia de MCRT, el algoritmo MMCRT genera un rayo determinista y N-1 rayos aleatorios, asegurando una convergencia más rápida a la solución. El rayo determinista se genera en la dirección definida por el punto de emisión y el receptor. Este procedimiento se ha utilizado en diferentes algoritmos de simulación en interiores [8] [126].

D.3.4 Resultados de simulación

Como características de rendimiento, se ha obtenido la ganancia de canal y el ancho de banda a partir de la respuesta $h(t)$ obtenida. No obstante, a diferencia de los canales en interiores, donde la respuesta al impulso puede considerarse fija; en el caso de UWOC, el escenario está variando continuamente debido al movimiento de las partículas y la superficie del agua del mar. Además, el apuntamiento entre emisores y receptores bajo el agua no es perfecto y presenta una variación que depende de las corrientes marinas. Este efecto ha sido despreciado por simplicidad, pero al igual que la turbulencia y la fauna, puede ser incluido como un factor multiplicativo en una descripción estocástica del canal UWOC.

Se ha observado que la ganancia del canal y el ancho de banda tienen las siguientes dependencias con los parámetros del enlace:

- El rango del enlace hace que tanto la potencia como el ancho de banda decaigan exponencialmente.
- Se ha observado que los dos parámetros estan influidos por la profundidad del enlace. A menor profundidad, más contribuciones llegan de las reflexiones superficiales.
- La velocidad del viento aumenta tanto la potencia recibida como el ancho de banda en un enlace cercano a la superficie.
- La distancia al fondo y la reflectividad no tienen influencia notable en enlaces a media distancia.
- La directividad del emisor aumenta tanto el ancho de banda como la potencia.
- En un escenario oceánico abierto, tanto el ancho de banda como la densidad de potencia son mayores en azul que en rojo.
- Partículas pequeñas producen BSF anchas, por tanto, reducen la potencia recibida y el ancho de banda. Por el contrario, partículas grandes tienen patrones de scattering con un fuerte dominio de la componente en la dirección de propagación. Estas partículas implican un ancho de banda y una potencia recibida más elevados.
- La concentración de partículas influye directamente en el número de "saltos" que da un rayo antes de llegar al receptor, por lo que reduce la potencia recibida. Además, al haber un mayor número de colisiones, la BSF se ensancha, aumentando la componente multitrayecto y reduciendo el ancho de banda.

La paralelización se ha llevado a cabo diviendo el cómputo en los rayos generados en el emisor. Los resultados de paralelización obtenidos se resumen a continuación:

- El esquema de planificación en OpenMP tiene una alta importancia, ya que el procesado de la contribución de cada rayo tiene duraciones diferentes. Por ello, la planificación que tiene mayor eficiencia es la dinámica. El mayor speedup conseguido ha sido de 3.904 para un sistema de 4 núcleos físicos.

- Usando CUDA en GPU, se obtienen eficiencias del hardware muy pobres, debido a la presencia de saltos condicionales en la implementación del código. Estos saltos son difíciles de evitar debido a la aleatoriedad de los fenómenos.

- El speedup obtenido en CUDA ha sido de 42 aproximadamente, y la eficiencia en coste de la implementación en GPU respecto a la de OpenMP se ha demostrado que es mucho mayor.

D.4 Canales agua-aire

Existen varias aplicaciones en las que es esencial un canal de comunicación entre vehículos submarinos (o sensores) y los dispositivos de superficie. Los parques eólicos, plantas de energía off-shore o instalaciones de acuicultura deben ser monitorizadas y se necesitan sensores submarinos. Estos sensores pueden recoger datos durante largos periodos de tiempo, cuyo volumen puede ser grande y se espera que crezca a medida que la tecnología de sensores se vuelve más compleja. Aunque las técnicas de comunicación acústica bajo el agua están bien establecidas y son prácticas en muchos casos, se limitan a la transmisión a baja velocidad, mientras que los enlaces ópticos tienen el potencial de proporcionar velocidades de datos más altas que las acústicas en varios órdenes de magnitud.

D.4.1 Propagación de ondas marinas

Los movimientos de las olas del mar pueden ser modelados por las ecuaciones de Navier-Stokes para fluidos newtonianos incompresibles, que representan la conservación de la masa y el momento. Condiciones de frontera de superficie libre que garantizan la continuidad del tensor de tensiones sobre la superficie son necesarias para determinar la localización de la superficie libre. Tanto las ecuaciones de Navier-Stokes y las condiciones de contorno de la superficie libre no son lineales. Por consiguiente, aún cuando los efectos de viscosidad y turbulencia pueden ser ignorados, el esfuerzo computacional requerido para resolver un problema de propagación de la onda tridimensional, es normalmente prohibitivo. Dado que este trabajo está orientado a la consecución de una relación entre la propagación de las olas del mar y su influencia en la potencia recibida en un enlace agua-aire, se presenta un modelo basado en la linealización de la aproximación de Boussinesq.

Únicamente se han considerado ondas planas monocromáticas, siendo la ecuación la siguiente.

$$\eta(t,x) = \eta_0 \cos(\omega t - kx) \tag{D.13}$$

D.4.2 Modelo de propagación

El escenario propuesto tiene una superficie que sigue la siguiente ecuación.

$$S(x,t) = D + \eta_0 \cos\left(\omega t - kx\right) \quad \forall y \tag{D.14}$$

El vector normal $\hat{n}(x,t)$ es de la forma:

$$\hat{n}(x,t) = \frac{\left(-\frac{\partial S(x,t)}{\partial x}, 0, 1\right)}{\sqrt{1 + \left(\frac{\partial S(x,t)}{\partial x}\right)^2}} \tag{D.15}$$

Este vector normal tiene una alta importancia en el desarrollo de la aproximación matemática de este trabajo, debido a su influencia en los ángulos refractados de la luz. Se presenta un cambio no lineal de la base de las posiciones de los rayos, donde se introduce este vector normal dentro del fenómeno de la refracción. Por otra parte, se harán algunas suposiciones para simplificar el análisis del problema.

Si se considera la fuerza del viento, un componente de ruido aditivo se añade a la ecuación. El comportamiento de este componente aleatorio se define por la serie de Gram-Charlier normal aproximada que se utilizó en el capítulo anterior.

Para el escenario propuesto, ya que hay un cambio de medio, la potencia óptica total sobre el área del fotodiodo A_{pd} situado en el plano del receptor es igual a la potencia óptica sobre un area A'_{pd} en la superficie, ya que la extinción del aire es insignificante.

Como se comentó anteriormente, se ha utilizado un cambio de base para calcular los límites de integración de un fotodiodo virtual localizado sobre la superficie. Se supone que no existen ni espuma ni partículas entre el agua del mar y el fotodiodo. La propuesta de cambio de base se presenta en la siguiente expresión.

$$\begin{aligned} x' &= x + \Delta x(x,y) \\ y' &= y + \Delta y(x,y) \end{aligned} \tag{D.16}$$

Donde $\Delta x(x,y)$ i $\Delta y(x,y)$ representan las desviaciones de un rayo tras salir de la superficie hasta llegar al plano del receptor.

Finalmente, el área proyectada del fotodiodo se puede obtener en base a la transformación inversa. En realidad, debido a las características de la superficie del agua del mar, la zona rectangular del fotodiodo no sería proyecta como un área rectangular sino como una curva. Sin embargo, debido a las restricciones impuestas en este trabajo, el error de una proyección rectangular será insignificante.

D.4.3 Simulación

A diferencia de la simulación de enlaces agua-agua, los enlaces agua-aire están definidos por la superficie. Como se comenta en el capítulo 4, cuando la luz impacta en la superficie, parte de la energía se refleja y se refracta la otra parte. La dirección del rayo refractado depende del vector normal a la superficie y la dirección del rayo incidente. Puesto que no hay efectos difusivos, el enfoque utilizado para acelerar la convergencia en escenarios agua-agua no se puede utilizar en este caso. Por lo tanto, se implementó un algoritmo tradicional MCRT para calcular la potencia recibida.

D.4.4 Resultados de simulación

Tras realizar varias simulaciones variando los parámetros del canal agua-aire, se han encontrado las siguientes dependencias.

- La profundidad del enlace reduce exponencialmente la potencia recibida debido a la mayor distancia que deben recorrer los rayos en el medio absorbente.
- La altura del receptor respecto al plano de la superficie del mar tiene un efecto parecido al anterior, ya que a mayor distancia, menor es el ángulo sólido entre emisor y receptor.
- Tanto la altura como la longitud de onda de la ola influyen directamente en la distancia pico-pico de la señal recibida. A mayor altura (o menor longitud de onda), la pendiente instantánea de la superficie marina se incrementa, desplazando el área proyectada del receptor una mayor distancia y por tanto, aumentando las pérdidas.
- La cizalladura del viento suaviza el efecto de la altura de ola, ya que aumenta el número de puntos de la superficie que pueden producir contribuciones significativas de potencia.
- La disponibilidad del canal aumenta con la velocidad del viento, mientras que se reduce con la altura de ola y las distancias del emisor y el receptor.

D.5 Análisis estadístico

Un enlace UWOC está totalmente caracterizo por su respuesta al impulso dependiente del tiempo. En general, los valores de la respuesta de impulso son muestras de un proceso aleatorio que se define en dos variables: tiempo y de retardos multitrayectoria. Por lo tanto, una respuesta al impulso realse representaría como $h(t, \tau)$, donde t es el tiempo y τ es el retardo. A partir de esta información, si el canal es WSSUS, la función de dispersión $S(f, \tau)$ del canal se puede extraer como:

$$S(f, \tau) = \mathfrak{F}_{\Delta t} \left\{ E \left[h(t, \tau) h^*(t + \Delta t, \tau) \right] \right\} \tag{D.17}$$

Donde $S(f, \tau)$ es la función de scattering del canal. A partir de esta función, se pueden obtener dos estadísticos muy importantes, el perfil Doppler y el perfil de potencia-retardo.

$$P(\tau) = \int_{-\infty}^{\infty} S(f, \tau) \, \mathrm{d}f = E \left[|h(t, \tau)|^2 \right] \tag{D.18}$$

$$S(f) = \int_{-\infty}^{\infty} S(f, \tau) \, \mathrm{d}\tau \tag{D.19}$$

A partir de $P(\tau)$, la dispersión del retardo se puede obtener como se realizó en el capítulo 4, y su inversa está relacionada con el ancho de banda de coherencia. En lo que respecta a $S(f)$, permite el cálculo del tiempo de coherencia a través de su transformada inversa de Fourier. En esta parte del trabajo, se asume un canal WSSUS, pero en el capítulo 7 se demuestra a través de la experimentación. Por otra parte, en este trabajo, se presentara un enfoque estadístico de la ganancia del canal y del ancho de banda, ya que el simulador implementado sólo ofrece muestras independientes de $h(t, \tau)$ (sin dependencia con t).

D.5.1 Análisis del problema

El simulador presentado en el capítulo 4 calcula la respuesta al impulso usando un algoritmo MM-CRT. La respuesta al impulso resultante se conforma por la suma de un número finito de deltas de Dirac ponderadas por un factor que depende de los fenómenos sufridos durante la trayectoria. La trayectoria seguida por cada rayo se determina aleatoriamente por la distribución de partículas. Esta distribución de partículas define el escenario y, por tanto, la potencia y el retardo de cada contribución. Sin embargo, en cada ejecución del algoritmo, las posiciones de las partículas varían al azar y no están correlacionadas entre iteraciones. Este hecho hace que una simulación dependiente del tiempo sea imposible, que es un requisito para obtener la función de dispersión $S(\tau, f)$. Sin embargo, este simulador permite el cálculo de las distribuciones de $H(0)$ y τ_{rms}.

Si se implementa un simulador dependiente del tiempo, la posición de cada partícula (despreciando el efecto de la superficie debido a su complejidad) debería almacenarse, siendo modificada

en cada iteración del algoritmo (sólo en una región de interés). En el caso representado en la figura 6.1, una distribución inicial de partículas uniformemente distribuidas sería generada, la respuesta de impulso obtenida a través de Monte Carlo y luego, la posición de cada partícula actualizada con la introducción de un efecto de transporte de masa. Para el escenario presentado, la cantidad de memoria se incrementaría con el cubo de la distancia de enlace. Si se considera solamente scattering simple, la paralelización en GPU sería sencilla, ya que cada rayo se rige por la misma ecuación de un salto. Este concepto no se explora en esta tesis doctoral y es parte de las futuras líneas de investigación.

Como se observó en los resultados del capítulo 4, la respuesta al impulso presenta una forma muy pronunciada, debido al predominio de la componente LOS. Este tipo de respuesta al impulso se puede aproximar a la suma de dos rectángulos. El primero y más estrecho contiene el 95 % de la energía mientras que el segundo representa la cola residual de la respuesta de impulso.

Usando esta aproximación e imponiendo restricciones de energía y ancho a los rectángulos, la ganancia del canal y el ancho de banda pueden aproximarse por:

$$H(0) \approx E_1 \tag{D.20}$$

$$B \approx \frac{\sqrt{12}}{5\Delta\tau_1} \tag{D.21}$$

Dado que las contribuciones importantes se definen dentro del intervalo de tiempo $\Delta\tau_1$, la región de interés de un enlace estaría determinada por los retardos inferiores a ese valor. Este límite se asocia a una distancia máxima d_{lim} descrita por:

$$d_{lim} = \Delta\tau_1 \frac{c_0}{n_w} \tag{D.22}$$

Esta distancia limita la región de interés a un elipsoide análogo a una zona de Fresnel. Al contrario que las zonas de Fresnel definidas en RF, en este caso el radio del elipsoide no implica un cambio de fase menor a cierto valor, sino una zona de interés en contribuciones energéticas. El radio del elipsoide tiene la forma:

$$r_{ellip} = \frac{1}{2}\sqrt{d_{lim}^2 - d_{link}^2} = \frac{1}{2}\sqrt{\left(\Delta\tau_1 \frac{c_0}{n_w}\right)^2 - d_{link}^2} \tag{D.23}$$

Esta zona se puede introducir en el simulador dependiente del tiempo mencionado con el fin de reducir el volumen de simulación y, por tanto, reducir el número de partículas y los requisitos de memoria. Además, este elipsoide se puede utilizar para predecir la influencia o no de un obstáculo en medio del enlace. Sin embargo, es necesario un enfoque estadístico de $\Delta\tau 1$ en términos de los parámetros del canal para llevar a cabo una predicción de la zona de Fresnel.

D.5.2 Procedimiento estadístico

Como se ha mencionado ya, uno de los principales objetivos de este trabajo es realizar una aproximación estadística de $H(0)$ y B para proporcionar una herramienta de predicción preliminar durante la etapa de planificación de enlaces UWOC. Este tipo de información es muy importante, ya que permite un mejor cálculo del balance de potencia y una estimación de máxima velocidad de datos. Uno de los parámetros más importantes de un problema de inferencia estadístico es el tamaño de la muestra. Este tamaño de la muestra depende de la varianza del proceso de debajo, que es *a priori* desconocido.

El procedimiento aplicado se basa en los siguientes pasos.

1. Generar N respuestas al impulso aleatorias.
2. Obtener los valores de la ganancia del canal y del ancho de banda.
3. Hacer una estimación de máxima verosimilitud con cada distribución de la base de datos.
4. Rechazar o aceptar el ajuste en base a un test de Kolmogorov-Smirnovt.

El tamaño de la muestra N depende de la varianza de la distribución subyacente. En lugar de imponer un tamaño de muestra sobredimensionado computacionalmente ineficiente, se ha realizado un proceso iterativo dentro de los pasos 1 y 2 del procedimiento anterior. Este proceso iterativo se basa en una minimización de errores de la función de distribución acumulada experimental.

Las distribuciones probadas se muestran en la tabla D.1.

Distribución	**Parámetros**
Gamma	a, b
Birnbaum-Saunders	β, γ
Burr Type XII	α, c, k
Exponential	μ
Generalized Extreme Value	k, σ, μ
Log-Normal	μ, σ
Nakagami	μ, ω
Normal	μ, σ
Rayleigh	b
Rician	s, σ
Student's T	ν
Wald	μ, λ
Weibull	a, b
Proposed distribution	a, b, x_{min}

Table D.1: Tested distributions

D.5.3 Resultados de simulación

Después de aplicar el procedimiento anterior a la base de datos. Se ha observado que tanto la ganancia del canal como el ancho de banda quedan bastante bien descritos por una distribución GEV. La PDF de esta distribución es:

$$f_x(x) = \frac{1}{\sigma} t(x)^{1+\xi} e^{-t(x)}$$
$$t(x) = \begin{cases} \left(1 + \left(\frac{x-\mu}{\sigma}\right)\xi\right)^{-1/\xi} & \xi \neq 0 \\ \\ e^{-(x-\mu)/\sigma} & \xi = 0 \end{cases} \tag{D.24}$$

Y su media y varianza son:

Its mean value and variance are defined in Equation set 6.24.

$$E[x] = \mu + \frac{\sigma}{\xi}(\Gamma(1-\xi) - 1) \tag{D.25}$$

$$\mathrm{Var}(X) = \left(\frac{\sigma}{\xi}\right)^2 \left(\Gamma(1-2\xi) - \Gamma^2(1-\xi)\right) \tag{D.26}$$

Donde μ es el parámetro de localización, σ el parámetro de escala y ξ el parámetro de forma. Este último parámetro define el soporte de la distribución. Dado que la ganancia del canal puede solo tener valores en $\mathbb{R}^+$, y según las propiedades de la función GEV, el parámetro de forma está limitada también en $\mathbb{R}^+$. A través del teorema de Fisher-Tippett, el máximo de una sucesión de variables aleatorias igualmente distribuidas sigue una distribución GEV. Por lo tanto, la ganancia del canal sigue una distribución GEV porque su valor puede ser considerado como el máximo de la respuesta de impulso, debido a su forma abrupta.

Analizando los parámetros de la distribución para distancias de enlace crecientes (Figura 6.7), se puede observar que tanto μ y σ, que definen principalmente la media y la varianza de la distribución, presentan un decaimiento exponencial tal y como la potencia recibida hace. Sin embargo, a distancias muy cortas, el modelo no se ajusta a los datos de forma adecuada, como el valor negativo de ξ sugiere. Tanto μ y σ son incrementados con la directividad. Sin embargo, ξ disminuye con la directividad y, por tanto, una directividad más alta implica una mejor SNR (Figura 6.8). El efecto de la BSF se puede observar en los máximos locales de μ y σ obtenidos para diferentes radios de partículas (Figura 6.9). Por encima de este valor máximo, la varianza disminuye a medida que el efecto de dispersión también se reduce. Por último, el efecto de la concentración de partículas se muestra en la Figura 6.10. Recordando que el radio de las partículas del escenario base era de 100 nm, un aumento en el número de partículas por metro cúbico produce no solo un incremento en la media de la potencia recibida, sino también una disminución en la SNR.

D.5.4 Zonas de Fresnel y Beam Spread Function

Durante la sección de análisis del problema, el concepto de zona de Fresnel fue descritp. En RF, las zonas de Fresnel son los volúmenes que son asociados a cambios de fase por debajo de un cierto límite. De esta manera, la primera zona de Fresnel se limita a cambios de fase de menos de π, el

segundo a los cambios por debajo de 2π y así sucesivamente. Por otra parte, en la misma sección de la zona de Fresnel se definió como el volumen iluminado en el que su contribución de potencia está relacionada con el 95 % de la energía total recibida.

Si se conociese la BSF del canal, la potencia total recibida podria aproximarse por:

$$P_{rx}(\theta') \approx 2\pi \int_0^{\theta'} P_{tx}(\theta)\xi(d_{link}\cos\theta, d_{link}\sin\theta)\left(\frac{A_{pd}\cos\theta}{d_{link}}\right)^2 \mathrm{d}\theta \tag{D.27}$$

Además, el ángulo máximo para el cual la anterior formula supone el 95 % de la energía de la respuesta impulsiva se puede calcular como:

$$\theta_{max} = \arg_{\theta} \{P_{rx}(\theta) = 0.95 P_{rx}\} \tag{D.28}$$

Bajo las restricciones geométricas del problema, este θ_{max} implica una distancia máxima recorrida hipotética igual a $d_{link}\,(\cos\theta + \sin\theta)$. La introducción de esta distancia en el estudio da lugar a la siguiente aproximación del radio de la zona de Fresnel.

$$r_{ellip} \approx \frac{d_{link}}{2}\tan\theta_{max} \tag{D.29}$$

Se ha realizado un ajuste de curvas basado en la expresión analítica de la BSF [16]. El resultado es el siguiente.

$$\xi(d,0) \approx 8.231 e^{-b(\lambda)(1-0.13g)\,d} \tag{D.30}$$

$$\eta \approx (1 - 6.6\cdot 10^{-3} b(\lambda)) e^{\left(1-e^{5\cdot 10^{-4} g\, b(\lambda)}\right) d^2} \tag{D.31}$$

$$\sigma_1^2 \approx 4.6\cdot 10^{-3} + 2.22\cdot 10^{-4} b(\lambda) + 1.74\cdot 10^{-4} e^{0.169 g\, b(\lambda)\, d} \tag{D.32}$$

$$\sigma_2^2 \approx (3.87 g + 0.976 b(\lambda)^2) e^{(0.39 b(\lambda) - 0.663 g) d} \tag{D.33}$$

With:

$$\xi(d,r) \approx \xi(d,0)\left(\eta e^{-\frac{r^2}{2\sigma_1^2}} + (1-\eta) e^{-\frac{r^2}{2\sigma_2^2}}\right) \quad /\sigma_1 < \sigma_2 \tag{D.34}$$

La BSF se ha modelado como la superposición de dos gaussianas. Los coeficientes de determinación obtenidos están todos por encima del 95%.

Respecto al valor de θ_{max}, también se ha realizado un ajuste, obteniendo el siguiente resultado con un $R^2 = 0.96$.

$$\theta_{max} \approx 0.2971 b(\lambda)\, g\, m\, d_{link}\left(1 - 6.8\cdot 10^{-3} b(\lambda)\, g^2\right) e^{-0.157 m\, d_{link}} + 9\cdot 10^{-4} m\, d_{link}\, b(\lambda)^2 \tag{D.35}$$

Esta aproximación tiene tres aplicaciones principales. Conociendo la zona de Fresnel a un 95 % de la potencia recibida y teniendo en cuenta las abruptas respuestas al impulso, el máximo

ancho de banda puede ser directamente calculado utilizando el radio del elipsoide y la ecuación D.21. Por otra parte, esta aproximación permite al diseñador del enlace considerar si un obstáculo afecta a la transmisión o no. Por último, la simulación de enlaces UWOC se reduce a un volumen muy pequeño si se considera solamente el elipsoide significativo.

D.5.5 Modelo de partículas opacas

En general, la literatura sólo trata el problema del scattering. No obstante, en ciertos escenarios, partículas opacas tales como granos de arena son parte del medio heterogéneo. En escenarios costeros, en regímenes de aguas poco profundas, las fuerzas del transporte de masa en el fondo del mar generan una distribución aleatoria de partículas opacas en medio del enlace. En esta sección, se presenta un modelo puramente geométrico para predecir la influencia de estas partículas.

Una partícula opaca grande es una pieza de materia cuya absorción es lo suficientemente alta como para considerar que no hay transmisión y cuya dimensión asegura que la difracción es despreciable.

Considerando una situación en la exista un emisor considerado de área extensa y un receptor, la potencia recibida podria aproximarse por:

$$P_{rx} = P_{tx}\frac{m+1}{2\pi}\frac{A_{pd}}{d_{link}^2}e^{-c(\lambda)d_{link}}\zeta \tag{D.36}$$

Donde ζ es una variable aleatoria que expresa la reducción del área aparente del fotodiode por ensombrecimiento. Esta variable tiene la siguiente forma.

$$\zeta = 1 - \pi R^2 \sum_{i=1}^{n} \frac{\gamma_i}{A(d_i)} \tag{D.37}$$

Donde $A(d_i)$ es el área de la intersección del cono a la distancia de impacto con partícula d_i, tal que:

$$A(d_i) = \pi\left(R_{tx} + \frac{d_i}{d_{link}}\left(R_{rx} - R_{tx}\right)\right)^2 \tag{D.38}$$

Donde γ_i es una variable que indica el grado de solapamiento de cada partícula con el resto. Este análisis no tiene en cuenta el efecto de la BSF y deben ser incluido en futuras investigaciones. Probablemente, el análisis sería análogo a la propuesta actual. Pero en ese caso, se deberia aumentar el volumen considerado a un elipsoide truncado definido por la zona de Fresnel anteriormente estudiada y el emisor. Por otra parte, $A(d_i)$ debería ser transformado a la intersección del elipsoide por un plano en d_i.

Asumiendo un número alto de partículas en el volumen definido por el emisor y el receptor, ζ puede ser aproximdo por una distribución normal, cuya media y varianza quedarían definidas por:

$$\mu \approx 1 - \pi R^2 E[n] \cdot E[x]$$
$$\sigma^2 \approx \left(\pi R^2\right)^2 \left(E[n]\sigma_x^2 + E[x]^2\sigma_n^2\right) \tag{D.39}$$

Esta aproximación presenta un error que aumenta a medida que el número de partículas disminuye. Además, puesto que γ_i ha sido despreciado, la pérdida estimada puede llegar a ser negativa. Por lo tanto, esta aproximación es válida para un densidad de partículas intermedia.

Influencia de los parámetros del enlace en la SNR

Para poder analizar únicamente el efecto de este tipo de partículas, se ha despreciado tanto el ruido Johnson como el ruido shot. De esta manera, la SNR puede estimarse mediante el cociente $E^2[\zeta]/\sigma_\zeta^2$. Los resultados obtenidos sugieren que:

- A mayor distancia la SNR disminuye, ya que el volumen del enlace crece, y con él el número de partículas.
- Existen un radio óptimo de emisor, donde la influencia del tamaño de las partículas frente al tamaño del emisor se compensa con el efecto de aumentar el volumen del enlace.
- A mayor área de recepción, mayor SNR. Sin embargo, existe aparentemente un valor de saturación en el cual incrementos de área implican incrementos de volumen. Además, para área muy grandes, la relación entre la sección de las partículas y el área del receptor es prácticamente nula.
- La SNR disminuye con el número de partículas.

D.6 Medidas experimentles

En este capítulo, se presenta una caracterización experimental de un enlace óptico inalámbrico bajo el agua cerca de la superficie (o en aguas poco profundas). La suposición de estacionariedad en sentido amplio, que se ha utilizado en los capítulos anteriores, se discute y demuestra para este canal. Además, los tiempos de coherencia estimados para diferentes configuraciones se presentan sobre mediciones reales. Estas pruebas se han realizado en un escenario de laboratorio con una solución controlada de materia suspendida *(Arthrospira platensis)* [136]. La partícula utilizada es una cianobacteria que presenta fluorescencia para excitaciones por debajo de 450 nm. Sin embargo, los experimentos se realizaron a longitudes de onda por encima de este límite. El efecto de las partículas en la SNR recibida y su varianza, así como el efecto de la componente reflejada de la superficie también se calcula.

Hoy en día, hay muchas aplicaciones que requieren comunicaciones inalámbricas subacuáticas de baja velocidad en aguas poco profundas, como podría ser la interconexión de sensores en zonas de alta vegetación marina, la acuicultura o el tratamiento de aguas residuales. Para estas instalaciones, los sistemas de RF no son adecuados, ya que requieren antenas grandes dimensiones y consumos de energía elevados. Las UWOC también se han examinado en la literatura con el fin de resolver este problema, a pesar de que están sujetas a la variabilidad de la canal óptico submarino. Las corrientes submarinas, la falta de alineación entre el emisor y el receptor, la fuerza del viento sobre la superficie del agua o la fauna de los alrededores, son factores que afectan directamente a la atenuación del canal. La ecuación D.40 muestra el comportamiento independiente y dependiente del tiempo de cada término que afecta a la respuesta de impulso.

$$\begin{aligned} h(t,\tau) &= G(t,\tau)L_G(t,\tau) + R(t,\tau)L_R(t,\tau) \\ L_i(t,\tau) &= F_i(t,\tau)\cdot M_i(t,\tau)\cdot T_i(t,\tau)\ /i = \{G,R\} \end{aligned} \tag{D.40}$$

Donde $h(t,\tau)$ es la respuesta al impulso del canal, $G(t,\tau)$ es la componente de línea de visibilidad directa (LOS) del enlace y $R(t,\tau)$ es el término que modela las componentes reflejadas. $L_i(t,\tau)$ es una función variable en el tiempo que comprende los otros fenómenos presentes. $F_i(t,\tau)$ es el efecto de fauna en la potencia recibida, $T_i(t,\tau)$ es el efecto de turbulencia, y $M_i(t,\tau)$ es el término de desapuntamiento. Debe tenerse en cuenta que el subíndice indica que cada fenómeno afecta a la LOS o a la componente NLOS

Como se sugirió en el capítulo 6, $G(t,\tau)$ presenta una variabilidad muy pequeña , produciendo un término casi constante. Gabriel estudió el desapuntamiento en cite6607990, así como Tang en [17]. Es sencillo demostrar que esta variabilidad depende de la tensión mecánica sufrida por los nodos de comunicación debido al transporte de masa, como Dong hizo en [20]. Por último, la fauna es un efecto impredecible. Para los escenarios libees de fauna libres como la vigilancia en

las instalaciones de tratamiento de aguas residuales, $F(t,\tau)$ se puede despreciar. De lo contrario, el paso de la fauna en medio del enlace produciría una sombra intensa que sere traduciría en una pérdida infinita durante un periodo de tiempo aleatorio. No hay literatura que aborde esta cuestión.

La introducción de estas consideraciones en la ecuación D.40, genera una versión simplificada en la que sólo las componentes reflectantes tienen un comportamiento dependiente del tiempo (Ecuación D.41). Esta componente sólo es importante para los enlaces cercanos a la superficie, lo cual es la situación que se refiere a este trabajo. Por otra parte, se ha considerado un ancho de banda muy alto, como sugieren los resultados de los Capítulos 4 y 6. Esta simplificación es válida si el ancho de banda del receptor es mucho menor que el ancho de banda físico del canal, lo cual es cierto para la mayoría de las aplicaciones de monitorización en redes de sensores.

$$h(t,\tau) \approx (G + R(t))\,\delta\left(\tau - d_{link}\frac{n_w}{c_0}\right) \tag{D.41}$$

Como criterio general, el canal UWOC no puede suponerse que es WSSUS si todos los términos de la ecuación D.40 poseen un peso importante. Sin embargo, teniendo en cuenta la ecuación D.41, ambas condiciones (estacionariedad y de dispersión no correlacionada) son satisfechas, lo que se demuestra a continuación.

En este trabajo, se presenta un montaje experimental para medir la variabilidad de canal de un enlace UWOC. Además, se obtienen varios resultados en cuanto a SNR y tiempo de coherencia para diferentes configuraciones. Un ancho de banda muy alto se ha considerado tal y como la literatura sugiere, lo que simplifica el cálculo de los resultados.

D.6.1 Descripción del experimento

Los principales objetivos de este trabajo son: la demostración de la validez de la suposición WSSUS en los enlaces UWOC cerca de la superficie, medir el tiempo de coherencia del canal en diferentes configuraciones y establecer una relación entre la movilidad de la materia en suspensión y la SNR. Esta configuración depende de dos variables: velocidad del viento sobre la superficie del agua y la profundidad (distancia a la superficie).

Las mediciones se han llevado a cabo dentro de un tanque de agua, cuyas paredes han sido ópticamente aisladas con una cubierta de color negro mate. Además, se utilizaron tres bombas sumergidas en el agua para generar movimiento en las partículas. Teniendo en cuenta la dispersión del retardo insignificante de la respuesta al impulso del canal para un enlace de corta distancia, las mediciones se han realizado con un nivel de corriente continuo aplicada a la lámpara LED emisora.

El emisor fue implementado utilizando una fuente de corriente y una configuración de 16 LED distribuídos en cuatro ramas. Los LED RGB empleados son CREE CLX6C-FKB [139].

El front-end óptico utilizado es un fotodiodo amplificado [138], que comprende un fotodiodo de silicio de 13 mm ^{2} seguido de un amplificador de transimpedancia de ganancia ajustable. Por otra parte, un osciloscopio InfiniiVision 7012A [144] fue utilizado como ADC. Esto permitió la implementación de un sencillo software control basado en comandos SCPI.

Para evaluar la influencia de la materia en suspensión en la potencia recibida, dos variables han sido barridas: concentración de partículas y la movilidad. La movilidad se ha conseguido utilizando las ya mencionadas bombas de agua. El experimento de la velocidad del viento se realizó con agua de abastecimiento, ya que la presencia de partículas no era parte del diseñao. La velocidad del viento se midió utilizando un anemómetro digital a mitad de la superficie del agua. El generador de viento únicamente disponía de dos velocidades diferentes: 8.1 $\mathrm{m \cdot s^{-1}}$ y 13 $\mathrm{m \cdot s^{-1}}$. Tanto la velocidad del viento como la profundidad del enlace fueron barridas para obtener formas de onda de larga duración en el receptor. Utilizando los datos recuperados del osciloscopio, se obtuvo el tiempo de coherencia y la demostración de la aproximación WSSUS.

D.6.2 Resultados experimentales

La materia en suspensión contribuye a la extinción de potencia del canal de dos maneras diferentes. Si las partículas son estables debido a un escenario de flujo de nulo, cada punto del espacio sufre los mismos eventos de dispersión antes de llegar al receptor. Por otro lado, si las partículas presentan cierta movilidad, el comportamiento casi determinista queda reemplazado por un comportamiento aleatorio cuyo valor medio y varianza dependerán de la evolución de la densidad volumétrica de las partículas. Con el fin de probar estos efectos, se utilizaron dos movilidades de partículas y tres concentraciones diferentes. La siguiente tabla resume los resultados:

Wavelength (nm)	**Concentration** ($\mathrm{mg\,l^{-1}}$)	α	σ^2_{ch}
660	0	0.99	$6.67 \cdot 10^{-18}$
660	6.12	0.92	$1.08 \cdot 10^{-15}$
660	12.24	0.96	$3.6 \cdot 10^{-15}$
470	0	1	$4.25 \cdot 10^{-12}$
470	6.12	0.89	$116.3 \cdot 10^{-12}$
470	12.24	0.91	$138.5 \cdot 10^{-12}$

Table D.2: Values of α and σ^2_{ch} for each concentration and wavelength for a mobility of $1\,\mathrm{cm\,s^{-1}}$

Esta reducción de la relación señal ruido en los canales con partículas en movimiento puede ser importante en el cálculo de los balances de enlace en UWOC. Con el fin de evitar este efecto, un margen de potencia extra según el término de ruido presentado anteriormente debería ser considerado. Estos resultados son la suma de los efectos de turbulencia (sin concentración) y la influencia de la densidad de las partículas. Puesto que este experimento se realizó en el laboratorio, la microescala de Kolmogorov sería mayor que la esperada en un entorno en mar abierto. Sin embargo, el incremento de concentración genera una reducción de la SNR mucho mayor que el

esperado debido a la turbulencia en enlaces de corto alcance.

El componente reflectivo en un enlace cercano a la superficie es la suma de las contribuciones de todos los puntos de la superficie del agua. El plano de la superficie puede dividirse formando una unión disjunta de dispersores no correlacionados, cuyos comportamientos se rigen por sus vectores normales aleatorios. El tamaño de cada región no correlacionada depende de la velocidad del viento y las ondas que se propagan.

Como se comentó en el capítulo 5, $\hat{n}(x, y)$ depende de la velocidad del viento y comúnmente se aproxima mediante una distribución normal. Además, la componente NLOS sigue una distribución normal, ya que puede ser entendida como la suma de una gran cantidad de procesos independientes de Bernoulli (cada dispersor tiene una probabilidad p_{xy} de contribuir a la potencia recibida total), pero su evolución en función del tiempo es desconocida.

De acuerdo con la ecuación D.41, el término $R(t)$ puede aislarse ya que el componente LOS no varía significativamente como ya se demostró. Cuatro profundidades diferentes, tres velocidades de viento diferentes y dos longitudes de onda se ensayaron en este experimento. La señal resultante $R(t)$ se calculó y su distribución de probabilidad se ajusta a una distribución normal. Por otra parte, la media, la varianza y el tiempo de coherencia se muestran en la siguiente tabla.

λ (nm)	**Profundidad** (cm)	**Viento** ($\mathrm{m\,s^{-1}}$)	μ	σ^2	T_c (ms)
660	2	8.1	$0.231 \cdot 10^{-4}$	$0.116 \cdot 10^{-11}$	140
660	2	13	$0.21 \cdot 10^{-4}$	$0.064 \cdot 10^{-11}$	85.2
660	5	8.1	$0.256 \cdot 10^{-4}$	$0.164 \cdot 10^{-11}$	178.4
660	5	13	$0.222 \cdot 10^{-4}$	$0.075 \cdot 10^{-11}$	73.3
660	10	8.1	$0.247 \cdot 10^{-4}$	$0.176 \cdot 10^{-11}$	98
660	10	13	$0.233 \cdot 10^{-4}$	$0.1 \cdot 10^{-11}$	70.7
660	15	8.1	$0.25 \cdot 10^{-4}$	$0.132 \cdot 10^{-11}$	58.4
660	15	13	$0.237 \cdot 10^{-4}$	$0.078 \cdot 10^{-11}$	50.9
470	2	8.1	$0.294 \cdot 10^{-4}$	$0.25 \cdot 10^{-11}$	267
470	2	13	$0.24 \cdot 10^{-4}$	$0.1 \cdot 10^{-11}$	79.5
470	5	8.1	$0.355 \cdot 10^{-4}$	$0.475 \cdot 10^{-11}$	255.4
470	5	13	$0.321 \cdot 10^{-4}$	$0.215 \cdot 10^{-11}$	93.2
470	10	8.1	$0.417 \cdot 10^{-4}$	$0.331 \cdot 10^{-11}$	90.6
470	10	13	$0.375 \cdot 10^{-4}$	$0.226 \cdot 10^{-11}$	74.1
470	15	8.1	$0.424 \cdot 10^{-4}$	$0.326 \cdot 10^{-11}$	209.3
470	15	13	$0.398 \cdot 10^{-4}$	$0.165 \cdot 10^{-11}$	49.2

Table D.3: Media, varianza and tiempo de coherencia de $R(t)$ para cada configuración

La reducción del tiempo de coherencia con la velocidad del viento se debe a que el número de regiones no correlacionadas en la superficie se incrementa. En otras palabras, la correlación espacial entre los puntos de la superficie se reduce a medida que aumenta la velocidad del viento, incrementando el número de contribuciones no correlacionadas en el receptor. Teniendo en cuenta esto, suponer que el enlace UWOC cerca de la superficie es WSUS supone obvio, ya que los dispersores (puntos en la superficie) varían en una región limitada, y el emisor y el receptor están

en posiciones fijas, pero la demostración experimental se puede encontrar a continuación.

En una proceso WSSUS, el valor esperado es constante. Para demostrar esta propiedad en un enlace cerca de la superficie, se realizó una test ANOVA. Las muestras que se introdujeron en el test fueron elegidas aleatoriamente a partir de la serie original de muestras de 50 segundos como una concatenación de muestras separadas un valor múltiplo del tiempo de coherencia (para crear un vector no correlacionado). El resultado se puede ver en la figura 7.12 para el rojo a 10 cm de profundidad y un viento de 13 m/s. Como era de esperar, el valor medio del proceso puede considerarse constante (p-value mayor que 0.9 para todos los casos). La incorrelación del scattering (US) se puede interpretar como estacionariedad en el dominio de la frecuencia. En este caso, como el ancho de banda es considerado muy alto para todos los escenarios, esta propiedad es directamente satisfecha.

D.7 Estrategias para la mejora de la eficiencia energética

La eficiencia energética es uno de los aspectos más importantes en UWSN. El consumo de energía de los nodos aislados que funcionan con baterías define su vida útil, y teniendo en cuenta los altos costos de reemplazo, es un objetivo de minimización primario. En general, el consumo de energía de un nodo es la suma de las contribuciones parciales. Los principales consumos están relacionados con el procesamiento (CPU y control), interfaces de comunicación y la carga útil. Este último aspecto puede variar ampliamente dependiendo de la finalidad del nodo desplegado. Para el aplicaciones de monitorización, la carga útil comprende sensores y circuitos de adquisición, que pueden ser normalmente despreciados en cosumo energetico respecto a las comunicaciones. Sin embargo, para aplicaciones donde se necesita accionamiento de mecanismos, el consumo de potencia de la carga útil puede ser la fuente primaria de uso de energía. En cuanto a las comunicaciones, para los enlaces de corto alcance, UWOC ha demostrado presentar la mejor eficiencia, pero para los enlaces de largo alcance, UAC sigue siendo la tecnología por excelencia.

La eficiencia energética se puede mejorar de distintas maneras. Haciendo un enfoque por capas, las mejores opciones para mejorar la eficiencia son la capa física y la capa de acceso al medio. En cuanto a la capa física, modulaciones pulsadas son normalmente mejores alternativas que las formas de onda continuas como OFDM o CSK. Sin embargo, estos tipos de señales pueden cuantificadas y remoduladas con el fin de aprovechar la alta eficiencia de los drivers no lineales. Por otra parte, los emisores y receptores ópticos presentan una mejor respuesta a las longitudes de onda largas que a los cortas. A pesar de que las mejores ventanas de transmisión generalmente se encuentran en la región azul-verde, la respuesta comentada de los dispositivos hace que las transmisiones en rojo sean más eficientes por debajo de una distancia crítica d_{crit}. Por otro lado, entre capas PHY y MAC, los algoritmos de control de potencia son una opción interesante para adaptar la potencia emitida de los nodos aislados y, por tanto, reducir el consumo de energía.

D.7.1 SNR en canales UWOC

La SNR en un canal UWOC se puede definir como:

$$SNR(\lambda) = \frac{\left(P_{tx}H(0,\lambda)R(\lambda)\right)^2}{2q(P_{tx}H(0,\lambda)R(\lambda) + I_d + I_b)B + \frac{4KTB}{R_L}F_n} \tag{D.42}$$

Sin embargo, añadiendo la eficiencia óptica de la fuente, que relaciona el consumo eléctrico con la potencia óptica radiada, se obtiene que:

$$SNR(\lambda) = \frac{\left(\eta(\lambda)P_{tx}|_{elec}H(0,\lambda)R(\lambda)\right)^2}{2q(\eta(\lambda)P_{tx}|_{elec}H(0,\lambda)R(\lambda) + I_d + I_b)B + \frac{4KTB}{R_L}F_n} \tag{D.43}$$

Analizando el cociente entre las SNR a dos longitudes de onda diferentes, se obtiene la siguiente expresión.

$$\frac{SNR(\lambda_1)}{SNR(\lambda_0)} = \left(\frac{\eta(\lambda_1)H(0,\lambda_1)R(\lambda_1)}{\eta(\lambda_0)H(0,\lambda_0)R(\lambda_0)}\right)^2 \frac{2q\eta(\lambda_0)P_{tx}|_{elec}H(0,\lambda_0)R(\lambda_0) + \frac{4KT}{R_L}F_n}{2q\eta(\lambda_1)P_{tx}|_{elec}H(0,\lambda_1)R(\lambda_1) + \frac{4KT}{R_L}F_n} \tag{D.44}$$

Téngase en cuenta que para los escenarios dominados por ruido shot (corta distancia) esta figura de mérito es lineal, pero para situaciones dominadas por el ruido térmico (larga distancia), la relación se convierte en parabólica. Sin embargo, en cualquiera de los dos casos, la distancia crítica d_{crit} se define como la distancia a la que la figura de mérito se convierte en uno. Teniendo en cuenta las conclusiones de los capítulos 4 y 6, la relación entre las ganancias de canal dependerá de la diferencia de los coeficientes de extinción eficaces, como se muestra en la ecuación D.45.

$$\frac{H(0,\lambda_1)}{H(0,\lambda_0)} \approx e^{-(c(\lambda_1)-c(\lambda_0)d_{link}} \tag{D.45}$$

Introduciendo esto en las ecuaciones anteriores, se obtiene que la distancia crítica queda definida por:

$$d_{crit} = -\frac{1}{c(\lambda_1)-c(\lambda_0)} \ln\left(\frac{\eta(\lambda_0)R(\lambda_0)}{\eta(\lambda_1)R(\lambda_1)}\right) \tag{D.46}$$

D.7.2 Emisores y receptores ópticos

La topología del transmisor, la codificación utilizada y la eficiencia cuántica de la fuente son aspectos críticos de los transmisores ópticos. Por otra parte, los receptores ópticos se determinan por la NEP opto-eléctrica, la responsividad del sustrato y la figura de ruido de los amplificadores.

Los transmisores ópticos comprenden generalmente una lámpara LED y un driver de corriente, cuya eficiencia depende de los requisitos de linealidad de la señal transmitida. En teoría, un driver de corriente realiza una amplificación de transconductancia ya que convierte un voltaje de entrada en una corriente de conducción. Los drivers lineales se implementan normalmente utilizando transistores bipolares de unión, mientras que los drivers no lineales por lo general comprenden dispositivos MOSFET. Los primeros necesitan polarización en los componentes activos, y que el punto de polarización supone una fuga de energía que puede hacer caer la eficiencia del sistema por debajo de 50 % fácilmente. Por otro lado, los transistores MOSFET sólo consumen energía durante las transiciones de estado, permitiendo drivers de alta velocidad con rendimientos de hasta el 95 % [146]. No obstante, estos dispositivos de alta impedancia aumentan su consumo de energía linealmente con la frecuencia de acuerdo con el almacenamiento de energía en los condensadores parásitos de la unión puerta-fuente.

La eficiencia energética de los emisores ópticos se mide como relación entre la potencia óptica total radiada y la potencia eléctrica consumida. Matemáticamente:

$$\eta_{opt}(\lambda) = \frac{P_{tx}}{V_D I_D} = \eta_{ext}(\lambda)\frac{hc}{q\lambda V_D} \tag{D.47}$$

$\eta_{ext}(\lambda)$ es la eficiencia cuántica externa del dispositivo, que es la relación del flujo de fotones de salida y el flujo de electrones inyectados. Esta relación depende del sustrato y la fabricación. Sin embargo, la eficiencia cuántica interna es normalmente mayor en los dispositivos de AlGaInP (naranja, rojo) que en los de GaN (azul), tal como muestra la Figura 8.2. Hay que tener en cuenta que $\eta_{opt}(\lambda)$ no es una constante, ya que V_D depende de la corriente de excitación I_D y $\eta_{ext}(\lambda)$ también presenta no-linealidades para valores altos de I_D.

D.7.3 Algoritmos de control de potencia

El control de potencia es la selección de la potencia de salida de transmisión en un sistema de comunicaciones, atendiendo a un criterio de optimización. Este criterio es normalmente una combinación de un minimización de la energía y la satisfacción de un rendimiento mínimo en el receptor. Tradicionalmente, los PCAs se han utilizado para maximizar la SNR manteniendo la interferencia global por debajo de un umbral en los canales de comunicación inalámbricos, tales como UMTS [148]. En este caso, ya que todas las señales se transmiten al mismo tiempo, cada una ensanchada por su código ortogonal correspondiente, si no hay un control de potencia, el nivel de interferencia puede aumentar hasta niveles perjudiciales, reduciendo drásticamente la BER.

En el caso de UWSN, los PCA no se proponen como técnica de mejora de la SNR, sino como algoritmos de ahorro de energía. La BER es importante ya que define parcialmente el número de retransmisiones de paquetes, lo cual consume mucha energia. Sin embargo, la posibilidad de adaptar la potencia de transmisión a un valor óptimo en términos de energía, tiene más peso en el diseño de nodos UWSN ópticos. Casi cualquier protocolo o técnica de ahorro de energía se justifica en UWSN, debido a que la extensión de vida útil de los nodos reduce drásticamente los costos de reemplazo.

Hay diferentes taxonomías de los algoritmos de control de potencia, en función del criterio de clasificación. Por ejemplo, si cada nodo toma sus propias decisiones el algoritmo es distribuido mientras que en el otro caso es centralizado. Si hay intercambio del estado del canal entre los nodos, *ergo*, hay una retroalimentación de la información, el algoritmo es en bucle cerrado. En caso contrario, es en lazo abierto. Finalmente, dependiendo de cómo se calcula el tamaño del paso del proceso iterativo de control de potencia, los algoritmos pueden ser de paso fijo, paso variable o paso adaptativo.

En este trabajo, se ha considerado una topología de red en forma de estrella. Este tipo de red es un enfoque muy general, pero es suficiente para estudiar el impacto de los PCA. Además, un protocolo MAC TDMA se ha considerado el fin de simplificar la optimización de la SNR y para aislar el estudio de los N canales posibles de un esquema general. La Figura 8.3 representa el escenario en cuestión, que puede comprender un nodo principal de ilimitada energía y un conjunto de nodos remotos. Esta topología puede ajustarse tanto a un escenario boya-nodos o un escenario UAV-nodos, en función de la movilidad del nodo principal.

Además, los algoritmos estudiados son centralizados y de bucle cerrado. La centralización de los algoritmos se ha propuesto para reducir la complejidad del nodo remoto. Además, la estimación del rendimiento del enlace se lleva a cabo en el lado del nodos maestro, mientras que el enlace ascendente (nodo principal al nodo remoto) siempre se lleva a cabo a la máxima potencia. La retroalimentación de la información del canal es necesaria para estimar con un error menor la potencia de salida de transmisión necesaria, pero también añade una fuente de error que debe ser tomada en cuenta.

Generalmente, los algoritmos de control de potencia optimizan el siguiente problema convexo.

$$\begin{aligned} &\min \sum_i P_i \\ &\text{subject to:} \\ &\frac{(P_i g_{ii})^2}{\sigma_N^2 + 2qB\sum_j P_j g_{ij} + \sum_{j\neq i}(P_j g_{ij})^2} \geq K_i \end{aligned} \tag{D.48}$$

Los términos dependientes de los otros usuarios del sistema pueden ser depreciados si se emplea un esquema de acceso TDMA, obtiendo el siguiente problema simplificado.

$$\begin{aligned} &\min P_i \\ &\text{subject to:} \\ &\frac{(P \cdot g)^2}{\sigma_N^2 + 2qBP \cdot g} \geq K \end{aligned} \tag{D.49}$$

La potencia puede ser minimizada iterativamente, obteniendo un algoritmo recursivo del tipo:

$$P^{(i+1)} = P^{(i)} + \Delta P^{(i)} \tag{D.50}$$

Los siguientes algoritmos han sido probados, el último de ellos es una de las propuestas de esta tesis.

- Paso fijo. Este tipo de algoritmo se caracteriza por su bajo tiempo de coherencia y por su dificultad para tener a un nivel de potencia estable tras la convergencia.
- Paso variable. Estos algoritmos son la evolución natural de los anteriores. En este caso, si la potencia recibida no es suficiente, el paso en dicha dirección se incrementa en cada iteración, reduciendo el tiempo de convergencia. Sin embargo, debido a este mismo efecto, la estabilidad es menor.
- Paso adaptativo. Modifican el paso de potencia con cada iteración, dependiendo de la potencia recibida estimada y la distancia hasta el valor óptimo. Normalmente se obtienen a través

de un método de descenso por gradiente, como Newton-Raphson, el cual da lugar a un algoritmo LMS. Poseen mejor tiempo de convergencia que los dos anteriores generalmente. Pero el rendimiento del algoritmo está muy condicionado por el valor del coeficiente de relajación α predeterminado. Este coeficiente se emplea para amortiguar las posibles variaciones del canal.

- Paso adaptativo con factor de amorguamiento adaptativo. Este algoritmo propuesto es una mejora del anterio. Se ha incluido un proceso iterativo de ajuste del factor de relajación que elimina la dependencia del rendimiento con este factor. Es el algoritmo que obtiene mejores resultados tanto en tiempo de convergencia como en variabilidad.

La Tabla D.4 muestra los resultados obtenidos en tres escenarios diferentes (corta distancia, media distancia con baja variabilidad y media distancia con alta variabilidad).

Escenario	**FS**	**VS**	**AS** ($\alpha = 0.25$)	**AS** ($\alpha = 1$)	**ADAS**
#1	$101/3.13 \cdot 10^{-4}$	46/0.001	$24/8 \cdot 10^{-7}$	$6//3.13 \cdot 10^{-6}$	$2/10^{-13}$
#2	107/0.016	55/0.1	59/0.115	6/0.48	2/0.0026
#3	45/0.05	30/0.024	9/0.103	4/0.445	$2/9.6 \cdot 10^{-4}$

Table D.4: Resumen de resultados

Se puede observar que el algoritmo de paso fijo y el de paso variable presentan una variabilidad muy reducida, sin embargo, su iteración de convergencia es varias veces mayor que los algoritmos adaptativos. En cuanto al de paso adaptativo, los resultados sugieren que el compromiso entre la variabilidad y la velocidad depende de α. Esta dependencia se elimina utilizando el algoritmo propuesto. Además, los valores bajos de α pueden necesitar una gran cantidad de muestras para recuperarse de un cambio en la ganancia del canal media (un aumento o disminución de la distancia del enlace en una comunicación de UAV a nodo por ejemplo). El algoritmo propuesto presenta la variabilidad más baja, a pesar de que se llevó a cabo el cálculo del parámetro de variabilidad usando sólo 5 muestras.

D.7.4 Cambio de longitud de onda

Anteriormente, se presentó una figura de mérito para decidir si una longitud de onda es más eficientes que otra. Suponiendo emisores rojos y azules en los nodos remotos UWSN, se podria añadir un código de color en la cabecera de la trama transmitida y una etapa de comparación entre los consumos de energía a cada longitud de onda entre iteraciones del algoritmo. Si el emisor rojo tuviese una eficiencia $\eta(\lambda_1)$ y el azul una eficiencia $\eta(\lambda 0)$, la mejor longitud de onda de emisión se podría extraer de la siguiente desigualdad.

$$\eta(\lambda_1)^{-1} P(\lambda_1)|_{opt} g(\lambda_1) < \eta(\lambda_0)^{-1} P(\lambda_0)_{opt} g(\lambda_0) \tag{D.51}$$

Al algoritmo propuesto se le ha añadido la capacidad de elegir la longitud de onda. Para medir el ahorro energético, se ha empleado la siguiente fórmula.

$$\mathcal{E} = 1 - \frac{1}{\eta_{min} P_{max}} \lim_{N \to \infty} \frac{1}{N} \sum_{i=1}^{N} \eta(\lambda_i) P^{(i)} \tag{D.52}$$

Usando esta ecuación, para un escenario a corta distancia en entorno costero se obtuvieron los ahorros de energia de la Tabla D.5.

Algoritmo	$\mathcal{E}$
Solo azul	50.47 %
Con elección de λ	89.41 %

Table D.5: Ahorro energético

D.7.5 OFDM modulada en PWM

Desde los primeros trabajos dedicados a la investigación en comunicaciones en luz visible, ha habido un creciente interés en el uso de modulaciones espectralmente eficaces para ser utilizadas en la transmisión óptica de datos [149]. Incluso después de la publicación del estándar IEEE 802.15.7 [150] , varios grupos de investigación continúan explorando esta posibilidad [151] [152], que ahora está bajo consideración para ser incluido en próximas versiones del estándar. OFDM ofrece una capacidad sorprendente en entornos con espectro reducido o cuando se transmiten a través de canales no estacionarios, como en aplicaciones bajo el agua. Muchas variaciones diferentes del esquema de transmisión OFDM básico se han desarrollado con el fin de adaptarlos a las características especiales del transmisor óptico, ya que tan sólo se permiten las señales positivas. La señal resultante después del cálculo de IFFT puede ser recortada [153] o referida a un nivel medio de DC [154]. Además, los sistemas OFDM ópticos por lo general son transmitidos en banda base. También hay un procedimiento estándar para generar una señal puramente real, haciendo uso de la simetría hermitiana. En cuanto a la eficiencia espectral, la OFDM óptica implica la reducción por un factor de 2 en comparación con los sistemas de radio, ya que ambas partes, real e imaginaria, no se pueden transmitir simultáneamente. Comparando ACO-OFDM y DCO-OFDM, la primera es menos eficiente en ancho de banda ya que sólo las subportadoras impares están cargadas de información, mientras que el segundo caso es menos eficiente en energía ya que se necesita de un nivel de polarización.

La OFDM óptica está limitada por la transmisión de señales solamente positivas. Como se ha demostrado, esta restricción se ha resuelto utilizando varios métodos, que van de la adición de polarización a un mapeo inteligente en el bloque FFT para aprovechar los armónicos predecibles después de una operación de recorte. Otro tema importante en OFDM óptica es la no linealidad implícita de los emisores frente a la necesidad de los drivers lineales para llevar a cabo la emisión. Si los dispositivos LED se hicieran funcionar en su región lineal, el rango dinámico se vería disminuido significativamente para evitar la distorsión no lineal en el frame OFDM. Una distorsión previa para compensar el comportamiento inherente de LED suele ser utilizada, añadiendo complejidad

Ventajas	Desventajas
Permite el uso de drivers no lineales	Necesita una frecuencia de muestra 2^N veces mayor
Facilita la sincronización	Reduce la SNR
Reduce el coste	
Tiene un rango dinámico mayor	

Table D.6: Características del sistema propuesto

al diseño. En esta tesis, se propone una codificación PWM del frame OFDM. Mediante la adición de esta operación, el requisito de linealidad se evita y se permite la utilización de los drivers de potencia no lineales y eficientes. Además, este tipo de codificación es menos sensible a las variaciones de temperatura en el emisor, ya que la información se codifica en el ciclo de trabajo de cada símbolo PWM. A continuación se discuten las ventajas y desventajas de la introducción de este bloque.

El esquema propuesto consiste en la adición de un modulador PWM en la etapa de salida del emisor. Este modulador es una de las partes principales de un amplificador de clase D. Sin embargo, el filtro de paso bajo se ha eliminado en el emisor y se ha colocadoaen la entrada del receptor. Según la teoría de sistemas LTI, este simple cambio genera la misma forma de onda en el receptor, mientras que aumenta drásticamente la eficiencia energética en el transmisor. Sin embargo, la SNR se decrementa agregando una fuente de ruido adicional derivada de la cuantificación de N bits. Además, la forma de onda de salida necesita una frecuencia de muestreo 2^N veces mayor que la versión lineal si se genera digitalmente. Además, como las muestras de la OFDM óptica se distribuyen normalmente, un bloque de predistorsión tal como una ley μ podría utilizarse para aumentar la distancia entre símbolos antes del bloque ADC. Se puede considerar también que todas las subportadoras se utilizan para transportar información, como en DCO-OFDM, pero con la ventaja de reducir la PAPR de la modulación a 3 dB debido a que la potencia de pico se fija a un valor conocido y controlado. La naturaleza pulsada de una señal PWM permite una sincronización más fácil que en los sistemas OFDM tradicionales. Además, las ventajas de OFDM contra dispersión multitrayecto y desvanecimiento se conservan. La Tabla D.6 resume las principales ventajas y desventajas del esquema propuesto.

Resultados

Después de incluir las eficiencias medidas en las ecuaciones correspondientes, la relación $\frac{\Delta\phi}{\Delta V}$ entre la ACO-OFDM y la DCO-OFDM modulada en PWM se ha obtenido para un conjunto de potencias desde 10 mW hasta 500 mW. La Figura 8.14 presenta esta curva y la compara con la relación de eficiencias de los drivers.

Se puede observar que para casi todos los valores de potencia eléctrica, los drivers no lineales son más eficientes que los drivers lineales. Téngase en cuenta que estas curvas corresponden a un único emisor LED. En el caso de una matriz de LED en la que se dividen las corrientes, el uso de PWM es aún más recomendable en términos de energía.

La SNR de la modulación obtenida está definida por la siguiente expresión, donde el ruido de cuantificación σ_Q^2 se incluye

$$SNR_{PWMO-OFDM} \approx \frac{S^2}{\sigma^2 + \sigma_Q^2} \tag{D.53}$$

La adición de este ruido que siempre está presente debido a la cuantificación define un máximo de SNR alcanzable. Sin embargo, comparando las curvas de BER (Figura 8.15) para una PWMO-OFDM de 10 bits y una ACO-OFDM, se observa que la curva se desplaza únicamente 3 dB aproximadamente. Además, aumentar el número de bits para reducir este gap tiene las siguientes consecuencias.

- La eficiencia espectral se reduce. El producto $\Delta SNR \cdot \Delta\xi$ se conserva en este tipo de sistema. Por lo tanto, un incremento en la SNR se traduce directamente en una disminución de la misma cantidad en la eficiencia. No obstante, el valor de N puede ser optimizado.

- El consumo de energía de los componentes de conmutación se incrementa. Como se comentó en la Sección de drivers, el consumo de energía de los componentes basados en MOS aumenta linealmente con la frecuencia. En este caso, la relación $\Delta SNR/\Delta P_{MOSFET}$ es constante.

- La eficacia del driver no lineal se reduce debido al efecto anterior. Dependiendo de la capacidad parásita del dispositivo utilizado, este efecto puede despreciarse.Existe una frecuencia de conmutación f_s a la que el conductor lineal supera la eficacia del conductor no lineal, que se define por:

$$f_s = \frac{2\,P_{OPA}(f_s/2^N)}{CV^2} \tag{D.54}$$

Generalmente, la capacidad parásita es muy pequeña (unos pocos pF) y la tensión de conmutación V está determinada por la matriz de LED utilizada. Por otra parte, el consumo de energía de un driver lineal basado en OPA también incrementa con el ancho de banda de la señal, haciendo aún más alta la frecuencia crítica. En conclusión, un compromiso entre el consumo de energía y el BER debe definirse con el fin de optimizar el número de bits del DAC del transmisor.

D.8 Conclusiones

Durante esta tesis, se han hecho varias contribuciones en relación con diferentes aspectos de modelado del canal y la eficiencia energética en UWOC. Después de analizar las líneas de investigación del estado del arte en el capítulo 3, se extrajeron dos conclusiones claras. Por un lado, el modelado de canales en UWOC ha estado dominado principalmente por contribuciones a nivel físico, con respecto a diferentes fenómenos tales como turbulencias y la scattering múltiple. Tradicionalmente, la ley de Beer-Lambert se ha utilizado para describir la extinción en UWOC, pero Cochenour demostraó en [16] que el scattering por particulas produce la dispersión del haz y en consecuencia, la extinción efectiva es menor que la suma de $\alpha(\lambda)$ y $b(\lambda)$. Por otra parte, existen diferentes motores de simulación basados en Monte Carlo en la literatura. No obstante, estos algoritmos utilizan una función de fase del scattering tipo Henyey-Greenstein para modelar la desviación de fotones debido a las partículas, que es una simplificación excesiva de un enfoque más realista, tal como la dispersión de Mie. Las principales ventajas de Henyey-Greenstein son la parametrización sencilla de la dispersión con un solo parámetro y el cálculo rápido de ángulos aleatorios usando esta distribución, pero la precisión se reduce como se comenta en [38]. Por otra parte, las contribuciones que abordan aplicaciones van desde escenarios muy específicos como el suministro de feeback a los nadadores en una piscina [109], hasta enlaces de larga distancia en escenarios reales durante campañas de monitorización del océano [86]. Existen diferentes trabajos que abordan transceptores opto-acústica híbridos para UWSN [82]. Este tipo de dispositivos se aprovechan de la alta eficiencia energética inherente y ancho de banda de las comunicaciones ópticas submarinas, manteniendo al mismo tiempo la posibilidad de comunicación de largo alcance usando UAC. Sin embargo, las aproximaciones estadísticas del canal UWOC se han centrado en proporcionar un método más rápido para obtener estimaciones de ganancia del canal [47], pero no hay modelos estadísticos para el enlaces UWOC en términos de ganancia de canal o ancho de banda. Por último, existe una evidente falta de contribuciones relativas a la eficiencia energética en UWOC a pesar de que es de alta importancia teniendo en cuenta el coste de reposición de los nodos bajo el agua.

El canal UWOC es lineal y variante en el tiempo, pero su variabilidad en el tiempo está sujeta a diferentes fenómenos tales como turbulencias, desalineación y la dispersión. En FSO, las turbulencias están normalmente sujetas al espectro de Kolmogorov bajo regímenes de turbulencia débiles. Sin embargo, las propiedades ópticas del agua del mar presentan variabilidad no sólo debido a los gradientes de temperatura, sino también debido a las variaciones de salinidad. En la literatura, el espectro de Kolmogorov ha demostrado ser inexacto, y el espectro de Nikishov es ampliamente usado en la literatura [122]. Esta aproximación incluye las dos dependencias en el espectro de frecuencia espacial. Durante el capítulo 4, quedó demostrado que el índice de centelleo depende de la distancia con un exponente que va desde 3/2 a 11/6, y no estrictamente

en el tradicional 11/6 de FSO. El exponente se define por los parámetros del espectro.

En el capítulo 4, se obtuvo la respuesta al impulso de diferentes escenarios UWOC usando un algoritmo de Monte Carlo Ray Tracing modificado. A diferencia de otros autores, la dispersión de Mie se utilizó como función de fase en este trabajo. En consecuencia, la complejidad de la generación de rayos se incrementó a cambio de la exactitud. Sin embargo, utilizando el enfoque modificado, un rayo directo al receptor se calcula después de cada dispersión, reduciendo el volumen de los rayos y el tiempo de convergencia del algoritmo respecto a los algoritmos utilizados en la literatura. Por otra parte, el algoritmo se paralelizó utilizando tanto un enfoque multiprocesador como una implementación en GPU. Aceleraciones de hasta 42 se obtuvieron utilizando una GPU NVidia Tesla M2050, lo que permitió el cálculo de las respuestas al impulso completas con 10^5 rayos en menos de 2 segundos. Se analizó la eficiencia económica de ambas tecnologías de paralelización, mostrando que las implementaciones sobre GPU son más rentable que los sistemas multiprocesador. Por otra parte, se analizó el impacto de los parámetros del canal en la respuesta al impulso. Se observaron los siguientes efectos:

- La distancia de enlace reduce exponencialmente la ganancia del canal y el ancho de banda. A medida que aumenta la distancia, los caminos ópticos seguidos por los rayos que llegan al receptor son mayores. Por lo tanto, las pérdidas por absorción y el número de impactos con partículas también aumentan.

- Los emisores directivos concentran la energía en ángulos sólidos más pequeños, mientras que otros emisores dispersan la luz. Teniendo en cuenta el efecto del scattering múltiple, aunque la energía se colima, una cantidad significativa de energía puede llegar al receptor. Para los enlaces perfectamente alineados, a mayor directividad, mayor es el ancho de banda y la ganancia del canal.

- La longitud de onda de emisión tiene dos efectos principales. En primer lugar, la absorción de agua de mar y la pérdida debido a las partículas dependen de la longitud de onda. En segundo lugar, la dimensión normalizada del partículas depende también de la longitud de onda, y por lo tanto, para un tamaño de partícula dado, la función de fase de dispersión de Mie puede variar ampliamente de una longitud de onda a otra.

- Como se comentó anteriormente, el radio de la partícula define la forma de la dispersión, pero para una concentración dada de partículas por metro cúbico, el número de colisiones aumenta con el radio de la partícula. Por lo tanto, el radio de las partículas aumenta el número de colisiones pero la función de fase se vuelve más directiva. Los resultados simulados observados sugieren que la ganancia del canal se reduce con el radio de la partícula, debido ala creciente número de impactos, mientras que se aumenta el ancho de banda debido a la reducción del coseno promedio de la función de fase.

- La concentración de partículas tiene dos efectos. El primero es el mismo que el radio de la partícula. A medida que aumenta la concentración, la probabilidad de colisión también aumenta y la ganancia del canal se reduce. El otro efecto es el de contribuir al ensanchamiento de la BSF, permitiendo mayores errores de desalineación entre el emisor y el receptor. Dependiendo de la distancia y el radio de la partícula, la concentración de partículas puede contribuir a una mayor captación de luz desde un ángulo sólido más grande.

- La distancia al fondo del mar tiene un efecto muy reducido sobre la ganancia del canal. No obstante, el ancho de banda se reduce ligeramente en enlaces profundos horizontales. Dado que la distancia al fondo marino puede despreciarse en la estimación de canal UWOC, el albedo del lecho marino tiene también una influencia insignificante.

- Para los enlaces cercanos a la superficie, las contribuciones debidas a las reflexiones de la superficie no se puede obviar ya que presentan una importancia significativa. Sin embargo, este efecto se dispersa a medida que el rango de enlace aumenta debido al efecto de la extinción. Dependiendo de la profundidad y para un escenario de agua en reposo, se modifica la superficie iluminada con mayor influencia en la potencia recibida. Por lo tanto, a medida que aumenta la profundidad, la ganancia del canal se reduce y el ancho de banda aumenta.

- La velocidad del viento produce una variación aleatoria en la pendiente de la superficie del agua de mar. Esta variación aleatoria convierte cada punto de la superficie en un dispersor potencial, donde se incrementa la contribución media global de la superficie iluminada. En cuanto a la anchura de banda, la componente multitrayectoria es fuerte para escenarios de mar en calma.

En el capítulo 5, se estudiaron los enlaces agua-aire. Este tipo de enlaces verticales son apropiados para el despliegue de nodos en aguas poco profundas, donde se lleva a cabo la adquisición de datos sin sumergir el transceptor, por ejemplo, un operador en un barco o un avión no tripulado. El proceso de sellado de un transceptor para que sea sumergible generalmente incrementa los costes de fabricación. Esta posibilidad es una solución rentable para aplicaciones UWSN en aguas someras. El problema se abordó desde un punto de vista geométrico, asociando la potencia recibida a la potencia óptica que incide en la superficie y que impacta en el fotodetector. De esta manera, el análisis se basa en el cálculo de la cantidad de energía que llega un área determinada de la superficie del agua. Para simplificar el análisis, sólo las superficies con formas que aseguren la biyectividad de una transformación espacial fueron consideradas. Esta transformación relaciona las posiciones XY de un rayo en la superficie y la posición en el plano del receptor. Después de imponer una serie de condiciones en relación al espectro de ola, que se consideró monocromático, se utilizó un esquema de integración numérica para obtener simulaciones de la potencia recibida. Se observó que la intensidad de luz recibida sigue a la forma de las olas del mar, debido al efecto

de lente de una onda plana que se propaga. Además, un análisis similar al realizado durante el capítulo 4 se llevó a cabo para relacionar cada parámetro de canal con la intensidad recibida. Además, la disponibilidad de canales se estudió en cada escenario respecto a la sensibilidad del receptor. Las principales conclusiones del estudio fueron:

- La profundidad del emisor produce en decaimiento exponencial en el receptor.
- La altura del receptor tiene un efecto similar al anterior, ya que el ángulo solido que ve el emisor hacia el receptor, disminuye con el cuadrado de la distancia.
- Tanto la altura de ola como la longitud de onda del espectro de ola tiene una influencia importante en la variación pico-pico de la señal recibida. A mayor altura de ola (o menor longitud de onda), la pendiente de la superficie marina se vuelve más abrupta, reduciendo la potencia mínima recibida.
- El efecto de cizalladura del viento tiene un efecto muy interesante en la variación de la potencia recibida. A medida que aumenta la velocidad del viento, se reduce la variación de pico a pico de la señal recibida (y también el valor máximo). Por lo tanto, los escenarios ventosos pueden aumentar la disponibilidad de canales cuando la sensibilidad del receptor se encuentra dentro del rango de variación de la potencia óptica recibida.

El modelado estadístico de la respuesta del canal UWOC se abordó en el capítulo 6. Las principales contribuciones realizadas durante este capítulo fueron:

- Analizar la distribución de probabilidad que mejor se ajustase a la ganancia del canal y al ancho de banda.
- Definir una zona de Fresnel atendiendo al 95 % de la energia de la respuesta impulsiva, después de realizar una aproximación rectangular.
- Proponer un modelo de pérdidas por partículas opacas grandes, como granos de arena.

Un breve análisis de la fórmula de la respuesta al impulso mostró la posibilidad de definir una la función de densidad de probabilidad *ad hoc* para la ganancia del canal. Sin embargo, después de realizar una estimación de máxima verosimilitud y varias pruebas de hipótesis sobre los datos simulados, la distribución GEV obtuvo los mejores resultados tanto para la ganancia del canal y como para el ancho de banda. Este estudio consistió en un conjunto de escenarios que abarcaron una amplia gama de combinaciones de parámetros. Sin embargo, la propuesta de distribución cubría sólo unos pocos casos de menos que GEV. La distribución obtenida mostró cómo varía la potencia recibida en instantes de tiempo no correlacionados. De los datos obtenidos, se observó que, en general:

- La SNR aumenta con la directividad, ya que se reduce la variabilidad de la potencia recibida. Es fácil darse cuenta de que los conos de emisión más estrechos están sujetos a una menor cantidad de posibles dispersiones.
- El rango del enlace reduce el efecto de la variabilidad inducida. Sin embargo, el incremento de la SNR debido a la distancia es contrarrestado por el efecto de las turbulencias, que aumentan con una ley de potencias con la distancia.
- De los datos obtenidos se puede inferir que para un determinado rango de enlace y concentración, hay un tamaño de partícula que minimiza la SNR. Como se ha comentado varias veces durante este documento, los radios de partículas grandes implican una alta directividad en la dispersión. Esto conduce a un aumento de SNR para la disminución de los radios de partículas.
- La concentración de partículas reduce la SNR. Esto se debe a que para altas concentraciones hay más dispersión posible dentro del volumen del enlace.

La respuesta al impulso se puede dividir en la suma de dos rectángulos debido a su forma abrupta. El primer rectángulo se puede definir para contener el 95 % de la energía. Su anchura, o dispersión de retardo, se asocia a los retrasos en las que hay contribuciones de energía significativos. Por lo tanto, el retardo máximo se define a través de la relación espacio-tiempo de la máxima distancia recorrida por un rayo que haya sufrido únicamente un evento de scattering. Teniendo en cuenta la geometría del escenario, esta distancia máxima genera un elipsoide que se puede denominar como el volumen de interés o la zona de Fresnel. Esta zona de Fresnel tiene varias implicaciones diferentes:

- La definición de un volumen de interés abre la posibilidad de simuladores dependientes del tiempo, donde cada partícula se traza dentro del elipsoide. Este tipo de simulador sería capaz de modelar la respuesta de tiempo-frecuencia del canal, de la que tiempo de coherencia se puede extraer.
- La zona de Fresnel describe el volumen en el que un objeto de intersección produce un efecto en la potencia recibida.

Por otra parte, el impacto de partículas opacas grandes también se analizó en el capítulo 6. Una partícula opaca es una partícula que no produce ni dispersión ni difracción, por ejemplo, granos de arena. En realidad, los granos de arena generan contribuciones debidas a su reflectividad, pero esto fue obviado para aislar el efecto de sombreado de estas partículas. Después de analizar estadísticamente la influencia de estas partículas, se encontró que las partículas opacas grandes producen un impacto en la SNR que depende de su tamaño, el alcance del enlace, la concentración de partículas y los radios de emisor y receptor. Siguiendo la tendencia de esta tesis, se analizó la influencia de cada uno de los parámetros antes mencionados, que muestra que:

- La SNR disminuye con el rango de enlace, ya que el número medio de partículas depende linealmente de la distancia. Cuanto mayor sea el número de partículas, mayor es la probabilidad de sufrir desvanecimiento.

- La SNR aumenta rápidamente con el área de emisión, hasta un máximo que depende de la distancia, el tamaño de las partículas y la concentración. Por encima de este valor óptimo, la SNR disminuye a medida que se incrementa el área de emisión. La superficie de emisión tiene dos efectos. Cuando se aumenta, el tronco de cono formado por emisor y receptor incrementa su volumen y, por tanto, el número de partículas, pero el tamaño de partícula respecto a la superficie de emisión disminuye. Estos efectos contrarios se igualan en el valor óptimo.

- En cuanto al área de receptor, la SNR aumenta con ella, pero hasta un valor de saturación. La saturación de la SNR es debido al impacto residual del parámetro en el número de partículas y la relación partículas-superficie.

- La concentración de partículas reduce la relación señal ruido debido a que hay una mayor cantidad de partículas dentro del volumen que producen sombra, con lo que hay más grados de libertad.

- El parámetro más perjudicial de este análisis es el radio de la partícula. Cuanto más grande sea la partícula, más grande es la sombra producida y la pérdida de energía. En los escenarios estudiados, la SNR disminuye a una tasa de 10 dB/mm.

En el capítulo 7, dos experimentos se llevaron a cabo. El primero demostró la influencia del movimiento de las partículas en la SNR, así como el efecto de la concentración de partículas. El segundo experimento analizó cómo las reflexiones superficiales afectan al enlace UWOC cerca de la superficie. Además, se demostró la hipótesis de WSSUS en este tipo de enlace. Los experimentos se realizaron en un tanque lleno de agua de abastecimiento, donde se disolvieron partículas ricas en clorofila. En cuanto al experimento del movimiento de las partículas, se ha descubierto que tiene un efecto perjudicial sobre la SNR, y que depende de la longitud de onda. Durante el segundo experimento, para observar el efecto de la velocidad del viento se introdujo un generador de viento en la superficie del tanque, lo que demuestra que cuanto mayor es el viento, más bajo es el tiempo de coherencia del canal.

Por último, el capítulo 8 abordó estrategias de eficiencia energética para reducir el consumo de energía de los nodos que funcionan con baterías. Tres contribuciones se hicieron en este sentido.

- Las longitudes de onda rojas pueden ser una mejor alternativa a los emisores tradicionales azul-verde debido a la mayor eficiencia energética asociadas a estas longitudes de onda. En general, los emisores de menor gap tienen una mayor eficiencia debido a sus eficiencias cuánticas internas y externas más elevadas. Por otra parte, los fotodetectores de silicio,

que son los más utilizados en las comunicaciones de espectro visible, presentan una mejor respuesta a longitudes de onda más largas. Estas dos características pueden compensar la propagación peor bajo el agua, generando una corriente neta superior en el receptor.

- Los algoritmos de control de potencia reducen drásticamente el consumo de energía. Tradicionalmente, el control de potencia se ha utilizado en las redes celulares para maximizar la SINR. Sin embargo, en UWSN el objetivo principal es reducir el consumo de energía tanto como sea posible, debido a los costes de sustitución elevados. Varios algoritmos de control de potencia se probaron bajo condiciones simuladas, y se propuso un algoritmo de control de potencia adaptable con amortiguación adaptativa para mejorar el tiempo de convergencia y reducir la variabilidad de la potencia de salida. Se comprobó que esta modificación del algoritmo LMS puede mejorar sobremanera la eficiencia energética respecto a un esquema de potencia constante añadiendo muy pequeña complejidad.

- Modular en PWM una forma de onda tal como una OFDM óptica reduce el consumo de energía, ya que permite el uso de drivers no lineales muy eficientes energéticamente. Los esquemas OFDM ópticos están sujetos a varias limitaciones cuando se utilizan en los sistemas de IM/DD. Los emisores ópticos presentan un comportamiento no lineal definido por la curva I-V del dispositivo, lo que limita la zona de trabajo lineal. Además, la potencia del emisor óptico no es lineal completamente con la corriente del driver, que muestra cierta compresión con el aumento de la corriente. Por lo tanto, estos dos efectos, que son multiplicativos, reducen drásticamente la zona lineal en varios dB. Por otra parte, La OFDM óptica necesita drivers lineales para convertir las tensiones de entrada en corrientes con el fin de evitar la distorsión adicional. Este tipo de conductores están normalmente sujetos a altos consumos de energía, reduciendo la eficiencia energética. Por otro lado, los drivers no lineales, tales como amplificadores de clase D se aprovechan de la capacidad de conmutación rápida de dispositivos LED y láser con una gran eficacia debido a la utilización de transistores MOSFET. Estos transistores tienen un consumo de energía que aumenta linealmente con la frecuencia, pero las frecuencias a las que estos dispositivos superan a los drivers lineales en el consumo de energía es muy alta. En el capítulo 8, se presentó una propuesta para reducir el consumo en esquemas OFDM en UWOC. La modificación propuesta consiste en un amplificador de clase D en la etapa de salida del emisor, cuyo filtro de paso bajo se elimina y se coloca en la etapa de entrada del receptor. Esta ligera pero eficaz modificación permite una reducción en el consumo de potencia del emisor, la relajación de la amplificación lineal en el receptor, y la facilidad para sincronizar las tramas recibidas.

Bibliography

[1] D. G. Boyce, M. R. Lewis, and B. Worm, "Global phytoplankton decline over the past century," *Nature*, vol. 466, July 2006.

[2] A. I. Al-Shamma'a, A. Shaw, and S. Saman, "Propagation of electromagnetic waves at mhz frequencies through seawater," *IEEE Transactions on Antennas and Propagation*, vol. 52, pp. 2843–2849, Nov 2004.

[3] "Conduction and magnetic signalling in the sea a background review," *Radio and Electronic Engineer*, vol. 42, pp. 447–452, October 1972.

[4] H. Yoshida, N. Iwakiri, T. Fukuda, M. Deguchi, and S. Onogi, "Measurements of underwater electromagnetic wave propagation," in *Underwater Technology (UT), 2015 IEEE*, pp. 1–5, Feb 2015.

[5] C. Uribe and W. Grote, "Radio communication model for underwater wsn," in *New Technologies, Mobility and Security (NTMS), 2009 3rd International Conference on*, pp. 1–5, Dec 2009.

[6] M. Stojanovic and J. Preisig, "Underwater acoustic communication channels: Propagation models and statistical characterization," *IEEE Communications Magazine*, vol. 47, pp. 84–89, January 2009.

[7] M. Siderius and M. B. Porter, "Modeling techniques for marine-mammal risk assessment," *IEEE Journal of Oceanic Engineering*, vol. 31, pp. 49–60, Jan 2006.

[8] J. F. Lopez-Hernandez and R. Perez-Jimenez, "Ray-tracing algorithms for fast calculation of the channel impulse response on diffuse ir-wireless indoor channels," *Optical engineering*, vol. 39, no. 10, pp. 2775–2780, 2000.

[9] J. Rufo, J. Rabadan, F. Delgado, C. Quintana, and R. Perez-Jimenez, "Experimental evaluation of video transmission through led illumination devices," *IEEE Transactions on Consumer Electronics*, vol. 56, pp. 1411–1416, Aug 2010.

[10] C. Quintana, V. Guerra, J. Rufo, J. Rabadan, and R. Perez-Jimenez, "Reading lamp-based visible light communication system for in-flight entertainment," *IEEE Transactions on Consumer Electronics*, vol. 59, pp. 31–37, February 2013.

[11] C. Quintana, J. Rabadan, J. Rufo, F. Delgado, and R. Perez-Jimenez, "Time-hopping spread-spectrum system for wireless optical communications," *IEEE Transactions on Consumer Electronics*, vol. 55, pp. 1083–1088, August 2009.

[12] Z. Islam, S. Faruque, and S. Faruque, "Experimental investigation of underwater turbulence effect on ber for orthogonal ook modulation," in *Electro/Information Technology (EIT), 2014 IEEE International Conference on*, pp. 608–611, June 2014.

[13] W. Hou and S. Matt, "Eo signal propagation in a simulated underwater turbulence environment," in *OCEANS 2014 - TAIPEI*, pp. 1–6, April 2014.

[14] Z. Wang, A. C. Bovik, H. R. Sheikh, and E. P. Simoncelli, "Image quality assessment: From error visibility to structural similarity," *IEEE Transactions on Image Processing*, pp. 600–612, April 2004.

[15] B. Cochenour, L. Mullen, A. Laux, and T. Curran, "Effects of multiple scattering on the implementation of an underwater wireless optical communications link," in *OCEANS 2006*, pp. 1–6, Sept 2006.

[16] B. Cochenour, L. Mullen, and A. Laux, "Characterization of the beam-spread function for underwater wireless optical communications links," *Oceanic Engineering, IEEE Journal of*, vol. 33, pp. 513–521, Oct 2008.

[17] S. Tang, Y. Dong, and X. Zhang, "On link misalignment for underwater wireless optical communications," *Communications Letters, IEEE*, vol. 16, pp. 1688–1690, October 2012.

[18] C. Gabriel, M.-A. Khalighi, S. Bourennane, P. Leon, and V. Rigaud, "Misalignment considerations in point-to-point underwater wireless optical links," in *OCEANS - Bergen, 2013 MTS/IEEE*, pp. 1–5, June 2013.

[19] R. Hagem, D. V. Thiel, S. O'Keefe, and T. Fickenscher, "Optical wireless link budget calculations for real time swimmers feedback," in *Computer and Communication Engineering (ICCCE), 2012 International Conference on*, pp. 180–184, July 2012.

[20] Y. Dong, S. Tang, and X. Zhang, "Effect of random sea surface on downlink underwater wireless optical communications," *Communications Letters, IEEE*, vol. 17, pp. 2164–2167, November 2013.

[21] C. Cox and W. Munk, "Measurement of the roughness of the sea surface from photographs of the sun's glitter," *J. Opt. Soc. Amer.*, vol. 44, no. 11, p. 838–850, 1954.

[22] H. Zhang, Y. Dong, and L. Hui, "On capacity of downlink underwater wireless optical mimo systems with random sea surface," *Communications Letters, IEEE*, vol. 19, pp. 2166–2169, Dec 2015.

[23] H. Zhang, L. Hui, and Y. Dong, "Angle of arrival analysis for underwater wireless optical links," *Communications Letters, IEEE*, vol. 19, pp. 2162–2165, Dec 2015.

[24] W. Liu, D. Zou, P. Wang, Z. Xu, and L. Yang, "Wavelength dependent channel characterization for underwater optical wireless communications," in *Signal Processing, Communications and Computing (ICSPCC), 2014 IEEE International Conference on*, pp. 895–899, Aug 2014.

[25] M. Tabacchiera, S. Betti, and S. Persia, "Underwater optical communications for swarm unmanned vehicle network," in *Photonics Technologies, 2014 Fotonica AEIT Italian Conference on*, pp. 1–3, May 2014.

[26] S. Arnon and D. Kedar, "Non-line-of-sight underwater optical wireless communication network," *J. Opt. Soc. Amer. A*, vol. 26, no. 3.

[27] S. Tang, Y. Dong, and X. Zhang, "On path loss of nlos underwater wireless optical communication links," in *OCEANS - Bergen, 2013 MTS/IEEE*, pp. 1–3, June 2013.

[28] A. Choudhary, V. Jagadeesh, and P. Muthuchidambaranathan, "Pathloss analysis of nlos underwater wireless optical communication channel," in *Electronics and Communication Systems (ICECS), 2014 International Conference on*, pp. 1–4, Feb 2014.

[29] L. Johnson, R. Green, and M. Leeson, "The impact of link orientation in underwater optical wireless communication systems," in *Oceans - St. John's, 2014*, pp. 1–8, Sept 2014.

[30] R. G. Laura Johnson and M. Leeson, "Underwater optical wireless communications : depth dependent variations in attenuation," *Applied Optics*, vol. 52 (Number 33).

[31] D. Rashkin, I. Cardei, M. Cardei, F. Dalgleish, and T. Giddings, "Detector noise model verification for undersea free space optical data links," in *Oceans, 2012*, pp. 1–7, Oct 2012.

[32] H. Dy and R. Gustilo, "Characterization of signal response for surface water movements in underwater optical wireless communications," in *TENCON 2012 - 2012 IEEE Region 10 Conference*, pp. 1–6, Nov 2012.

[33] S. Jaruwatanadilok, "Underwater wireless optical communication channel modeling and performance evaluation using vector radiative transfer theory," *Selected Areas in Communications, IEEE Journal on*, vol. 26, pp. 1620–1627, December 2008.

[34] C. Li, K.-H. Park, and M.-S. Alouini, "On the use of a direct radiative transfer equation solver for path loss calculation in underwater optical wireless channels," *Wireless Communications Letters, IEEE*, vol. 4, pp. 561–564, Oct 2015.

[35] C. Gabriel, M. Khalighi, S. Bourennane, P. Leon, and V. Rigaud, "Channel modeling for underwater optical communication," in *GLOBECOM Workshops (GC Wkshps), 2011 IEEE*, pp. 833–837, Dec 2011.

[36] C. D. Mobley, *Light and Water: Radiative Transfer in Natural Waters*. IEEE, 1994.

[37] C. Gabriel, M. Khalighi, S. Bourennane, P. Leon, and V. Rigaud, "Monte-carlo-based channel characterization for underwater optical communication systems," *Optical Communications and Networking, IEEE/OSA Journal of*, vol. 5, pp. 1–12, Jan 2013.

[38] G. Zhao and X. Sun, "Error analysis of using henyey-greenstein in monte carlo radiative transfer simulations," in *Progress in Electromagnetics Research Symposium Proceedings, Xi'an, China*, March 2010.

[39] F. Jasman and R. Green, "Monte carlo simulation for underwater optical wireless communications," in *Optical Wireless Communications (IWOW), 2013 2nd International Workshop on*, pp. 113–117, Oct 2013.

[40] V. Jagadeesh, A. Choudhary, F. Bui, and P. Muthuchidambaranathan, "Characterization of channel impulse responses for nlos underwater wireless optical communications," in *Advances in Computing and Communications (ICACC), 2014 Fourth International Conference on*, pp. 77–79, Aug 2014.

[41] S. Tang, X. Zhang, and Y. Dong, "On impulse response for underwater wireless optical links," in *OCEANS - Bergen, 2013 MTS/IEEE*, pp. 1–4, June 2013.

[42] S. Tang, Y. Dong, and X. Zhang, "Impulse response modeling for underwater wireless optical communication links," *Communications, IEEE Transactions on*, vol. 62, pp. 226–234, January 2014.

[43] Y. Dong, H. Zhang, and X. Zhang, "On impulse response modeling for underwater wireless optical mimo links," in *Communications in China (ICCC), 2014 IEEE/CIC International Conference on*, pp. 151–155, Oct 2014.

[44] B. Cochenour, L. Mullen, and J. Muth, "Temporal response of the underwater optical channel for high-bandwidth wireless laser communications," *Oceanic Engineering, IEEE Journal of*, vol. 38, pp. 730–742, Oct 2013.

[45] X. Dai, S. Sheard, D. O'Brien, S. Russell, and L. Carswell, "Propagation and scattering model of infrared and ultraviolet light in turbid water," in *Wireless and Optical Communication Conference (WOCC), 2013 22nd*, pp. 601–606, May 2013.

[46] S. Tang, X. Zhang, and Y. Dong, "Temporal statistics of irradiance in moving turbulent ocean," in *OCEANS - Bergen, 2013 MTS/IEEE*, pp. 1–4, June 2013.

[47] H. Zhang, Y. Dong, and X. Zhang, "On stochastic model for underwater wireless optical links," in *Communications in China (ICCC), 2014 IEEE/CIC International Conference on*, pp. 156–160, Oct 2014.

[48] H. Zhang and Y. Dong, "General stochastic channel model and performance evaluation for underwater wireless optical links," *Wireless Communications, IEEE Transactions on*, vol. PP, no. 99, pp. 1–1, 2015.

[49] B. Cochenour, L. Mullen, and A. Laux, "Phase coherent digital communications for wireless optical links in turbid underwater environments," in *OCEANS 2007*, pp. 1–5, Sept 2007.

[50] M. Sui, X. Yu, and F. Zhang, "The evaluation of modulation techniques for underwater wireless optical communications," in *Communication Software and Networks, 2009. ICCSN '09. International Conference on*, pp. 138–142, Feb 2009.

[51] S. Meihong, Y. Xinsheng, and Z. Zhangguo, "The modified ppm modulation for underwater wireless optical communication," in *Communication Software and Networks, 2009. ICCSN '09. International Conference on*, pp. 173–177, Feb 2009.

[52] X. Yu, W. Jin, M. Sui, and Z. Lan, "Evaluation of forward error correction scheme for underwater wireless optical communication," in *Communications and Mobile Computing (CMC), 2011 Third International Conference on*, pp. 527–530, April 2011.

[53] P. Minev, C. Tsimenidis, and B. Sharif, "Short-range optical ofdm," in *OCEANS, 2012 - Yeosu*, pp. 1–5, May 2012.

[54] C. Gabriel, M. Khalighi, S. Bourennane, P. Leon, and V. Rigaud, "Investigation of suitable modulation techniques for underwater wireless optical communication," in *Optical Wireless Communications (IWOW), 2012 International Workshop on*, pp. 1–3, Oct 2012.

[55] F. Akhoundi, J. Salehi, and A. Tashakori, "Cellular underwater wireless optical cdma network: Performance analysis and implementation concepts," *Communications, IEEE Transactions on*, vol. 63, pp. 882–891, March 2015.

[56] B. Srinivasan and V. Rodoplu, "Energy-efficient joint source-channel coding for optical wireless underwater networks," in *OCEANS 2007*, pp. 1–5, Sept 2007.

[57] N. BaniHassan, F. Akhoundi, and J. A. Salehi, "Adaptive power control algorithms in underwater wireless optical cdma cellular networks," in *Optical Wireless Communications (IWOW), 2015 4th International Workshop on*, pp. 107–111, Sept 2015.

[58] L. Liu, "A topology recovery algorithm of underwater wireless sensor networks," in *Communication Technology (ICCT), 2010 12th IEEE International Conference on*, pp. 64–67, Nov 2010.

[59] T. Hu and Y. Fei, "Murao: A multi-level routing protocol for acoustic-optical hybrid underwater wireless sensor networks," in *Sensor, Mesh and Ad Hoc Communications and Networks (SECON), 2012 9th Annual IEEE Communications Society Conference on*, pp. 218–226, June 2012.

[60] A. Mora, D. Ganger, G. Wells, J. Zhang, X. Hu, C. Zhou, A. Richa, and C. Youngbull, "Ad-hoc multi-hop underwater optical network for deep ocean monitoring," in *Oceans - San Diego, 2013*, pp. 1–5, Sept 2013.

[61] A. Vavoulas, H. Sandalidis, and D. Varoutas, "Underwater optical wireless networks: A k -connectivity analysis," *Oceanic Engineering, IEEE Journal of*, vol. 39, pp. 801–809, Oct 2014.

[62] D. Anguita, D. Brizzolara, and G. Parodi, "Optical communication for underwater wireless sensor networks: a vhdl-implementation of a physical layer 802.15.4 compatible," in *OCEANS 2009 - EUROPE*, pp. 1–2, May 2009.

[63] D. Anguita, D. Brizzolara, and G. Parodi, "Vhdl modeling of phy and mac layer modules for underwater optical wireless communication," in *Circuits and Systems for Communications (ECCSC), 2010 5th European Conference on*, pp. 185–188, Nov 2010.

[64] D. Anguita, D. Brizzolara, and G. Parodi, "Optical wireless communication for underwater wireless sensor networks: Hardware modules and circuits design and implementation," in *OCEANS 2010*, pp. 1–8, Sept 2010.

[65] M. Doniec and D. Rus, "Bidirectional optical communication with aquaoptical ii," in *Communication Systems (ICCS), 2010 IEEE International Conference on*, pp. 390–394, Nov 2010.

[66] M. Doniec, A. Xu, and D. Rus, "Robust real-time underwater digital video streaming using optical communication," in *Robotics and Automation (ICRA), 2013 IEEE International Conference on*, pp. 5117–5124, May 2013.

[67] A. Destrez, Z. Toffano, and P. Leon, "Underwater high bit-rate optical free-space communication system," in *Optical Wireless Communications (IWOW), 2012 International Workshop on*, pp. 1–3, Oct 2012.

[68] P. Swathi and S. Prince, "Designing issues in design of underwater wireless optical communication system," in *Communications and Signal Processing (ICCSP), 2014 International Conference on*, pp. 1440–1445, April 2014.

[69] S. Tang, Y. Dong, and X. Zhang, "Receiver design for underwater wireless optical communication link based on apd," in *Communications and Networking in China (CHINACOM), 2012 7th International ICST Conference on*, pp. 301–305, Aug 2012.

[70] B. Tian, F. Zhang, and X. Tan, "Design and development of an led-based optical communication system for autonomous underwater robots," in *Advanced Intelligent Mechatronics (AIM), 2013 IEEE/ASME International Conference on*, pp. 1558–1563, July 2013.

[71] G. Cossu, R. Corsini, A. Khalid, S. Balestrino, A. Coppelli, A. Caiti, and E. Ciaramella, "Experimental demonstration of high speed underwater visible light communications," in *Optical Wireless Communications (IWOW), 2013 2nd International Workshop on*, pp. 11–15, Oct 2013.

[72] N. Farr, A. Chave, L. Freitag, J. Preisig, S. White, D. Yoerger, and P. Titterton, "Optical modem technology for seafloor observatories," in *OCEANS, 2005. Proceedings of MTS/IEEE*, pp. 928–934 Vol. 1, 2005.

[73] J. Simpson, W. Cox, J. Krier, B. Cochenour, B. Hughes, and J. Muth, "5 mbps optical wireless communication with error correction coding for underwater sensor nodes," in *OCEANS 2010*, pp. 1–4, Sept 2010.

[74] D. Anguita, D. Brizzolara, G. Parodi, and Q. Hu, "Optical wireless underwater communication for auv: Preliminary simulation and experimental results," in *OCEANS, 2011 IEEE - Spain*, pp. 1–5, June 2011.

[75] N. Farr, J. Ware, C. Pontbriand, and M. Tivey, "Demonstration of wireless data harvesting from a subsea node using a ship of opportunity," in *Oceans - San Diego, 2013*, pp. 1–5, Sept 2013.

[76] L. Johnson, R. Green, and M. Leeson, "Hybrid underwater optical/acoustic link design," in *Transparent Optical Networks (ICTON), 2014 16th International Conference on*, pp. 1–4, July 2014.

[77] Y. F. Fung, M. Dai, and M. Ercan, "Underwater short range free space optical communication for a robotic swarm," in *Autonomous Robots and Agents, 2009. ICARA 2009. 4th International Conference on*, pp. 529–532, Feb 2009.

[78] M. Doniec, C. Detweiler, I. Vasilescu, and D. Rus, "Using optical communication for remote underwater robot operation," in *Intelligent Robots and Systems (IROS), 2010 IEEE/RSJ International Conference on*, pp. 4017–4022, Oct 2010.

[79] B. Gao and S. Guo, "Development of an infrared sensor-based wireless intelligent fish-like underwater microrobot," in *Information and Automation (ICIA), 2010 IEEE International Conference on*, pp. 1314–1318, June 2010.

[80] I. Rust and H. Asada, "A dual-use visible light approach to integrated communication and localization of underwater robots with application to non-destructive nuclear reactor inspection," in *Robotics and Automation (ICRA), 2012 IEEE International Conference on*, pp. 2445–2450, May 2012.

[81] A. Bowen, M. Jakuba, N. Farr, J. Ware, C. Taylor, D. Gomez-Ibanez, C. Machado, and C. Pontbriand, "An un-tethered rov for routine access and intervention in the deep sea," in *Oceans - San Diego, 2013*, pp. 1–7, Sept 2013.

[82] S. Han, Y. Noh, R. Liang, R. Chen, Y.-J. Cheng, and M. Gerla, "Evaluation of underwater optical-acoustic hybrid network," *Communications, China*, vol. 11, pp. 49–59, May 2014.

[83] S. Liu, C. Zhang, and Y. Huang, "Research on acoustic source localization using time difference of arrival measurements," in *Measurement, Information and Control (MIC), 2012 International Conference on*, vol. 1, pp. 220–224, May 2012.

[84] M. Sun, B. Zheng, L. Zhao, and J. Yu, "Paying a way of the rov equipped with a function of underwater laser communication," in *OCEANS 2014 - TAIPEI*, pp. 1–4, April 2014.

[85] M. Sun, B. Zheng, L. Zhao, X. Zhao, and F. Kong, "A design of the video transmission based on the underwater laser communication," in *Oceans - St. John's, 2014*, pp. 1–4, Sept 2014.

[86] N. Farr, J. Ware, C. Pontbriand, T. Hammar, and M. Tivey, "Optical communication system expands cork seafloor observatory's bandwidth," in *OCEANS 2010*, pp. 1–6, Sept 2010.

[87] F. Campagnaro, F. Favaro, P. Casari, and M. Zorzi, "On the feasibility of fully wireless remote control for underwater vehicles," in *Signals, Systems and Computers, 2014 48th Asilomar Conference on*, pp. 33–38, Nov 2014.

[88] C. Moriconi, G. Cupertino, S. Betti, and M. Tabacchiera, "Hybrid acoustic/optic communications in underwater swarms," in *OCEANS 2015 - Genova*, pp. 1–9, May 2015.

[89] P. W. Zhai, G. W. Kattawara, and P. Yang, "Impulse response solution to the three-dimensional vector radiative transfer equation in atmosphere-ocean systems i. monte carlo method," *Applied Optics*, vol. 47, No. 8, March 2008.

[90] P. W. Zhai, G. W. Kattawar, and P. Yang, "Impulse response solution to the three-dimensional vector radiative transfer equation in atmosphere–ocean systems. ii.the hybrid matrix operator—monte carlo method," *Applied Optics*, vol. 47, No. 8.

[91] Z. Jin, T. P. Charlock, K. Rutledge, K. Stamnes, and W. Yingjian, "Analytical solution of radiative transfer in the coupled atmosphere-ocean system with a rough surface," *Applied Optics*, vol. 45, No. 28.

[92] K. Gjerstad, J. Stamnes, B. Hamre, J. Lotsberg, Y. Banghua, and K. Stamnes, "Monte carlo and discrete-ordinate simulations of irradiances in the coupled atmosphere–ocean system," *Applied Optics*, vol. 42, No. 15.

[93] L.Bo, Z. Hai, and C. Weibiao, "Simulation of laser communication channel from atmosphere to ocean," in *ACTA OPTICA SINICA, China*, July 2007.

[94] Y. Dong and X. Qingji, "Atmosphere-ocean laser communication channel simulation and modeling," in *Computing, Communication, Control, and Management, 2009. CCCM 2009. ISECS International Colloquium on*, vol. 4, pp. 554–557, Aug 2009.

[95] R. Stokes, M. Bermal, C. Griffith, R. Blair, E. Marttila, and G. Mooradian, "An adaptive data rate controller (adrc) for the through cloud, undersea laser communications channel," in *Photonics Society Summer Topical Meeting Series, 2012 IEEE*, pp. 107–108, July 2012.

[96] G. Baiden and Y. Bissiri, "High bandwidth spherical optical wireless communication for subsea telerobotic mining," in *OCEANS 2011*, pp. 1–4, Sept 2011.

[97] A. Barroso, G. Baiden, and J. Johnson, "Teleoperation of mining equipment using optical wireless communications," in *Ubiquitous and Future Networks (ICUFN), 2015 Seventh International Conference on*, pp. 727–733, July 2015.

[98] R. Hagem, D. Thiel, S. O'Keefe, and T. Fickenscher, "Real-time swimmers' feedback based on smart infrared (ssir) optical wireless sensor," *Electronics Letters*, vol. 49, pp. 340–341, February 2013.

[99] R. Hagem, S. O'Keefe, T. Fickenscher, and D. Thiel, "Self contained adaptable optical wireless communications system for stroke rate during swimming," *Sensors Journal, IEEE*, vol. 13, pp. 3144–3151, Aug 2013.

[100] R. Hagem, D. V. Thiel, S. O'Keefe, A. Wixted, and T. Fickenscher, "Low-cost short -range wireless optical fsk modem for swimmers feedback," in *Sensors, 2011 IEEE*, pp. 258–261, Oct 2011.

[101] W. Cox, J. Simpson, and J. Muth, "Underwater optical communication using software defined radio over led and laser based links," in *MILITARY COMMUNICATIONS CONFERENCE, 2011 - MILCOM 2011*, pp. 2057–2062, Nov 2011.

[102] I. Mizukoshi, N. Kazuhiko, and M. Hanawa, "Underwater optical wireless transmission of 405nm, 968mbit/s optical im/dd-ofdm signals," in *Optical Fibre Technology, 2014 OptoElectronics and Communication Conference and Australian Conference on*, pp. 216–217, July 2014.

[103] T. Szili, B. Matolcsy, and G. Fekete, "Water pollution investigations by underwater visible light communications," in *Transparent Optical Networks (ICTON), 2015 17th International Conference on*, pp. 1–4, July 2015.

[104] A. Lin, W. Lu, J. Xu, H. Song, F. Qu, J. Han, X. Gu, and J. Leng, "Underwater wireless optical communication using a directly modulated semiconductor laser," in *OCEANS 2015 - Genova*, pp. 1–4, May 2015.

[105] J. Giles and I. N. Bankman, "Underwater optical communications systems. part 2: basic design considerations," in *Military Communications Conference, 2005. MILCOM 2005. IEEE*, pp. 1700–1705 Vol. 3, Oct 2005.

[106] D. Anguita, D. Brizzolara, and G. Parodi, "Building an underwater wireless sensor network based on optical: Communication: Research challenges and current results," in *Sensor Technologies and Applications, 2009. SENSORCOMM '09. Third International Conference on*, pp. 476–479, June 2009.

[107] R. Camilli, A. Bowen, and N. Farr, "Bright blue: Advanced technologies for marine environmental monitoring and offshore energy," in *OCEANS 2010 IEEE - Sydney*, pp. 1–7, May 2010.

[108] V. Lyatkher, "Low-speed hydro-kinetic turbines, in tidal power: Harnessing energy from water currents," *John Wiley & Sons*, 2014.

[109] R. Hagem, D. Thiel, S. O'Keefe, and T. Fickenscher, "Optical wireless communication for real time swimmers feedback: A review," in *Communications and Information Technologies (ISCIT), 2012 International Symposium on*, pp. 1080–1085, Oct 2012.

[110] L. Johnson, R. Green, and M. Leeson, "A survey of channel models for underwater optical wireless communication," in *Optical Wireless Communications (IWOW), 2013 2nd International Workshop on*, pp. 1–5, Oct 2013.

[111] M.-A. Khalighi, C. Gabriel, T. Hamza, S. Bourennane, P. Leon, and V. Rigaud, "Underwater wireless optical communication; recent advances and remaining challenges," in *Transparent Optical Networks (ICTON), 2014 16th International Conference on*, pp. 1–4, July 2014.

[112] S. Chandrasekhar, *Radiative Transfer*. Dover Publications, Inc., New York.

[113] W. M. Irvine, "Multiple scattering by large particles. ii. optically thick layers," *The Astrophysical Journal*, vol. 152, p. 823, 1968.

[114] R. M. Pope and E. S. Fry, "Absorption spectrum (380–700 nm) of pure water. ii. integrating cavity measurements," *Appl. Opt.*, vol. 36, pp. 8710–8723, Nov 1997.

[115] C. S. Roesler, M. J. Perry, and K. L. Carder, "Modeling in situ phytoplankton absorption from total absorption spectra in productive inland marine waters," *Limnology and Oceanography*, vol. 34, no. 8, pp. 1510–1523, 1989.

[116] R. Doerffer and J. Fischer, "Concentrations of chlorophyll, suspended matter, and gelbstoff in case ii waters derived from satellite coastal zone color scanner data with inverse modeling methods," *Journal of Geophysical Research: Oceans*, vol. 99, no. C4, pp. 7457–7466, 1994.

[117] A. Ferreira, V. M. Garcia, and C. A. Garcia, "Light absorption by phytoplankton, non-algal particles and dissolved organic matter at the patagonia shelf-break in spring and summer," *Deep Sea Research Part I: Oceanographic Research Papers*, vol. 56, no. 12, pp. 2162 – 2174, 2009.

[118] V. I. Haltrin, "Chlorophyll-based model of seawater optical properties," *Appl. Opt.*, vol. 38, pp. 6826–6832, Nov 1999.

[119] G. T. McNeil, "Metrical fundamentals of underwater lens system," *Optical Engineering*, vol. 16, no. 2, 1977.

[120] W. Matthäus, "Empirische gleichungen für den brechungsindex des meerwassers," *Beiträge zur Meereskunde*, vol. 33, pp. 73–78, 1974.

[121] L. J. Johnson, R. J. Green, and M. S. Leeson, "Underwater optical wireless communications: depth-dependent beam refraction," *Applied Optics*, vol. 53, no. 31, pp. 7273–7277, 2014.

[122] V. V. Nikishov and V. I. Nikishov, "Spectrum of turbulent fluctuations of the sea-water refraction index," *International Journal of Fluid Mechanics Research*, vol. 27, no. 1, pp. 82–98, 2000.

[123] O. Korotkova, N. Farwell, and E. Shchepakina, "Light scintillation in oceanic turbulence," *Waves in Random and Complex Media*, vol. 22, no. 2, pp. 260–266, 2012.

[124] N. Farwell, "Optical beam propagation in oceanic turbulence," *PhD dissertation*, 2014.

[125] M. M. Awad, *Heat Transfer - Theoretical Analysis, Experimental Investigations and Industrial Systems, Prof. Aziz Belmiloudi (Ed.)*, ch. 20. Fouling of Heat Transfer Surfaces. InTech, 2011. ISBN: 978-953-307-226-5.

[126] O. Gonzalez, S. Rodriguez, R. Perez-Jimenez, B. R. Mendoza, and A. Ayala, "Comparison of monte carlo ray-tracing and photon-tracing methods for calculation of the impulse response on indoor wireless optical channels," *Optics express*, vol. 19, no. 3, pp. 1997–2005, 2011.

[127] "Bohren-huffman scattering calculation algorithm source code." `http://code.google.com/p/scatterlib/wiki/Spheres`. Spheres.wiki, Google Source Code Archive.

[128] "The openmp api specification for parallel programming." `http://openmp.org`. OpenMP's website.

[129] "Tesla m2050 documentation." `http://www.nvidia.com/docs/io/43395/bd-05238-001_v03.pdf`. NVidia's website.

[130] G. Marsaglia, "Random numbers fall mainly in the planes," in *National Academy of Science, Proceedings of the*, vol. 61, pp. 25–28, 1968.

[131] "Intel xeon e5620 documentation." `http://ark.intel.com/es-es/products/47925/Intel-Xeon-Processor-E5620-12M-Cache-2_40-GHz-5_86-GTs-Intel-QPI`. Intel website.

[132] D. H. Peregrine, "Long waves on a beach," *Journal of Fluid Mechanics*, vol. 27, pp. 815–827, 3 1967.

[133] M. A. Tayfun, "Narrow-band nonlinear sea waves," *Journal of Geophysical Research: Oceans*, vol. 85, no. C3, pp. 1548–1552, 1980.

[134] J. R. Barry, J. M. Kahn, W. J. Krause, E. A. Lee, and D. G. Messerschmitt, "Simulation of multipath impulse response for indoor wireless optical channels," *IEEE Journal on Selected Areas in Communications*, vol. 11, pp. 367–379, Apr 1993.

[135] B. Basrak, *International Encyclopedia of Statistical Science*, ch. Fisher-Tippett Theorem, pp. 525–526. Berlin, Heidelberg: Springer Berlin Heidelberg, 2011.

[136] M. A. u. H. S. M. Peter, A. Phaninatha Sarma and I. H. Attitalla, "Studies on the impact of nitrogen starvation on the photosynthetic pigments through spectral proprties of cyanobacterium, spirulina platensis;: Identification of target phycobiliprotein under nitrogen chlorosis," *Botany Research International*, vol. 3, no. 2, pp. 38–42, 2010.

[137] P. Bello, "Characterization of randomly time-variant linear channels," *IEEE Transactions on Communications Systems*, vol. 11, pp. 360–393, December 1963.

[138] "Pda36a - silicon switchable gain detector datasheet." http://www.thorlabs.de/thorProduct.cfm?partNumber=PDA36A. Thorlabs' website.

[139] "Clx6c-fkb smd rgb led datasheet." http://www.cree.com/~/media/Files/Cree/LED-Components-and-Modules/HB/Data-Sheets/1281-CLX6C-FKB.pdf. CREE's website.

[140] "Fa-851 power supply datasheet." http://www.promax.es/downloads/products/esp/FA-851.pdf. Promax's website.

[141] "Volume 1: Syntax and style," *Standard Commands for Programmable Instruments (SCPI)*, 1999. Ivi Foundation, http://www.ivifoundation.org/docs/scpi-99.pdf.

[142] "30 mm barium-coated integrating sphere." https://www.gigahertz-optik.de/en-us/product/UMBB-300. Gigahertz Optik's website.

[143] "Bts256 led tester datasheet." https://www.gigahertz-optik.de/en-us/product/BTS256-LED. Gigahertz Optik's website.

[144] "Dso7012a oscilloscope." http://www.keysight.com/en/pd-1586532-pn-DSO7012A/oscilloscope-100-mhz-2-analog-channels?cc=ES. Keysight's website.

[145] "Description of openfoam." http://www.openfoam.com/. OpenFOAM's website.

[146] F. Che, L. Wu, B. Hussain, X. Li, and C. P. Yue, "A fully integrated ieee 802.15.7 visible light communication transmitter with on-chip 8-w 85 efficiency boost led driver," *Journal of Lightwave Technology*, vol. 34, pp. 2419–2430, May 2016.

[147] A. Khan, "Semiconductor photonics: Laser diodes go green," *Nature Photonics*, vol. 3, no. 8, pp. 432–434, 2009.

[148] "Umts definition." http://www.3gpp.org/technologies/keywords-acronyms/103-umts. 3GPP website.

[149] O. Gonzalez, R. Perez-Jimenez, S. Rodriguez, J. Rabadan, and A. Ayala, "Ofdm over indoor wireless optical channel," *IEE Proceedings - Optoelectronics*, vol. 152, pp. 199–204, Aug 2005.

[150] "Ieee standard for local and metropolitan area networks–part 15.7: Short-range wireless optical communication using visible light," *IEEE Std 802.15.7-2011*, pp. 1–309, Sept 2011.

[151] S. Dimitrov and H. Haas, "Information rate of ofdm-based optical wireless communication systems with nonlinear distortion," *Journal of Lightwave Technology*, vol. 31, pp. 918–929, March 2013.

[152] A. H. Azhar, T. A. Tran, and D. O'Brien, "A gigabit/s indoor wireless transmission using mimo-ofdm visible-light communications," *IEEE Photonics Technology Letters*, vol. 25, pp. 171–174, Jan 2013.

[153] J. Armstrong, "Ofdm: From copper and wireless to optical," in *Optical Fiber communication/National Fiber Optic Engineers Conference, 2008. OFC/NFOEC 2008. Conference on*, pp. 1–27, Feb 2008.

[154] S. D. Dissanayake and J. Armstrong, "Comparison of aco-ofdm, dco-ofdm and ado-ofdm in im/dd systems," *Journal of Lightwave Technology*, vol. 31, pp. 1063–1072, April 2013.

[155] J. Armstrong, "Ofdm for optical communications," *Journal of Lightwave Technology*, vol. 27, pp. 189–204, Feb 2009.

[156] N. Fernando, Y. Hong, and E. Viterbo, "Flip-ofdm for optical wireless communications," in *Information Theory Workshop (ITW), 2011 IEEE*, pp. 5–9, Oct 2011.

[157] Y. Jun, "Modulation and demodulation apparatuses and methods for wired/wireless communication system." http://www.google.com/patents/WO2007064165A1?cl=en, June 7 2007. WO Patent App. PCT/KR2006/005,140.

[158] H. J. Chiu, Y. K. Lo, J. T. Chen, S. J. Cheng, C. Y. Lin, and S. C. Mou, "A high-efficiency dimmable led driver for low-power lighting applications," *IEEE Transactions on Industrial Electronics*, vol. 57, pp. 735–743, Feb 2010.